

**Cenozoic Palaeoceanographic evolution
of the southwestern South Atlantic:
indications from the Falkland/Malvinas Plateau**

Dissertation

in partial fulfillment of the requirements for the
doctoral degree of Natural Sciences (Dr. rer. nat.)

Submitted to the
Department of Geosciences-University of Bremen

Banafsheh Najjarifarizhendi

Bremen, den 20.02.2023

PhD colloquium 16.11.2023



Seismic data acquisition was funded within the core program METEOR/MERIAN by the German Research Foundation (DFG). This work was funded by the DFG under grant no. Ue 49/23.

Supervisor

Dr. Gabriele Uenzelmann-Neben

Alfred Wegener Institute, Helmholtz Center for Polar and Marine Research,
Am Alten Hafen 26, 27568 Bremerhaven, Germany

Assessors

Prof. Dr. Karsten Gohl

Alfred Wegener Institute, Helmholtz Center for Polar and Marine Research,
Am Alten Hafen 26, 27568 Bremerhaven, Germany

University of Bremen, Bibliothekstraße 1, 28359 Bremen, Germany

Prof. Dr. Sebastian Krastel

University of Kiel, Research Group Marine Geophysics und Hydroacoustics,
Otto-Hahn-Platz 1, 24118 Kiel, Germany

Versicherung an Eides Statt / Affirmation in lieu of an oath

**gem. § 5 Abs. 5 der Promotionsordnung vom 18.06.2018 / according to § 5 (5) of the
Doctoral Degree Rules and Regulations of 18 June, 2018**

Ich / I, Banafsheh, Najjarifarizhendi, Am Lehester Deich [REDACTED], 28357 Bremen, 3246146

(Vorname / First Name, Name / Name, Anschrift / Address, ggf. Matr.-Nr. / student ID no., if applicable)

versichere an Eides Statt durch meine Unterschrift, dass ich die vorliegende Dissertation selbständig und ohne fremde Hilfe angefertigt und alle Stellen, die ich wörtlich dem Sinne nach aus Veröffentlichungen entnommen habe, als solche kenntlich gemacht habe, mich auch keiner anderen als der angegebenen Literatur oder sonstiger Hilfsmittel bedient habe und die zu Prüfungszwecken beigelegte elektronische Version (PDF) der Dissertation mit der abgegebenen gedruckten Version identisch ist. / *With my signature I affirm in lieu of an oath that I prepared the submitted dissertation independently and without illicit assistance from third parties, that I appropriately referenced any text or content from other sources, that I used only literature and resources listed in the dissertation, and that the electronic (PDF) and printed versions of the dissertation are identical.*

Ich versichere an Eides Statt, dass ich die vorgenannten Angaben nach bestem Wissen und Gewissen gemacht habe und dass die Angaben der Wahrheit entsprechen und ich nichts verschwiegen habe. / *I affirm in lieu of an oath that the information provided herein to the best of my knowledge is true and complete.*

Die Strafbarkeit einer falschen eidesstattlichen Versicherung ist mir bekannt, namentlich die Strafandrohung gemäß § 156 StGB bis zu drei Jahren Freiheitsstrafe oder Geldstrafe bei vorsätzlicher Begehung der Tat bzw. gemäß § 161 Abs. 1 StGB bis zu einem Jahr Freiheitsstrafe oder Geldstrafe bei fahrlässiger Begehung. / *I am aware that a false affidavit is a criminal offence which is punishable by law in accordance with § 156 of the German Criminal Code (StGB) with up to three years imprisonment or a fine in case of intention, or in accordance with § 161 (1) of the German Criminal Code with up to one year imprisonment or a fine in case of negligence.*



Bremen, 19.02.2023

Ort / Place, Datum / Date

Unterschrift / Signature

Acknowledgement

My sincerest thanks go to...

Dr. Gabrielle Uenzelmann-Neben, my supervisor, for entrusting me with the project she conceived and for her scientific guidance, unwavering patience and constant moral support over the duration of this work.

Prof. Dr. Karsten Gohl and Prof. Dr. Sebastian Krastel for agreeing to assess my thesis.

Dr. Jens Gruetzner for helping me improve the clarity of my thesis by test-reading it and giving me insightful comments.

Dr. Gabrielle Uenzelmann-Neben, Prof. Dr. Karsten Gohl, and Dr. Jens Gruetzner, my thesis advisory committee, for their constructive input and productive discussions during our biannual meetings.

Dr. Claudia Hanfland and Dr. Claudia Sprengel from the POLMAR office for offering a unique graduate program.

Constance Oberdieck for her dependable assistance in countless office matters.

German Research Foundation (DFG) for providing the financial support of this work.

Friends and colleagues in the geophysics and bathymetry sections at AWI for creating a warm and friendly atmosphere, both in the office and during expeditions.

I. Table of contents

I.	Table of contents	i
II.	List of Figures.....	iv
III.	List of Tables	ix
IV.	List of Abbreviations	x
V.	Thesis outline	xi
CHAPTER 1.	Abstract.....	1
1.1	Summary.....	1
1.2	Zusammenfassung.....	2
CHAPTER 2.	Introduction	3
2.1	Falkland/Malvinas Plateau: present and past peculiarities	3
2.2	Preceding investigation of the Falkland/Malvinas Plateau	7
2.3	Thesis motivation and central questions	9
CHAPTER 3.	Technique, datasets, and analysis.....	11
3.1	Technique/ Reflection seismology	11
3.1.1	Marine reflection seismics.....	11
3.1.2	Essentials of reflection seismology.....	12
3.1.3	Propagation model in reflection seismology.....	13
3.2	Datasets.....	14
3.2.1	High resolution 2D seismic reflection data from expedition MSM81	14
3.2.2	Scientific borehole data	17
3.3	Analysis	18
3.3.1	Seismic data processing	18
3.3.2	Qualitative and quantitative seismic interpretation	23
3.3.3	Target features	24
CHAPTER 4.	Contributions to scientific journals.....	29
4.1	Footprints of palaeocurrents in sedimentary sequences of the Cenozoic across the Maurice Ewing Bank.....	29
4.2	Fossilized silica diagenetic fronts: Implications for palaeoceanographic evolution across the Falkland/Malvinas plateau.....	29
4.3	Falkland/Malvinas Trough: Indications for Cenozoic tectonic and oceanographic evolution in the southwestern South Atlantic	30
CHAPTER 5.	Footprints of palaeocurrents in sedimentary sequences of the Cenozoic across the Maurice Ewing Bank.....	31
5.1	Abstract.....	31

5.2	Introduction.....	31
5.3	Geological and oceanographic background.....	33
5.4	Data and methods.....	36
5.4.1	Seismic reflection data acquisition and processing.....	36
5.4.2	Interpretation scheme	38
5.5	Results	40
5.5.1	Basement	40
5.5.2	Seismic units	41
5.6	Discussion.....	51
5.6.1	Pre-Tertiary circulation (seismic units SU1, SU2, and SU3)	51
5.6.2	Paleocene and early Eocene circulation (seismic unit SU4)	52
5.6.3	Oligocene-Quaternary circulation (seismic unit SU5)	53
5.7	Conclusions.....	57
CHAPTER 6.	Fossilized silica diagenetic fronts: Implications for palaeoceanographic evolution across the Falkland/Malvinas plateau.....	58
6.1	Abstract	58
6.2	Introduction.....	58
6.3	Geological and oceanographic background.....	61
6.4	Data and methods.....	63
6.4.1	Seismic reflection data	63
6.4.2	Drilling data and age model	64
6.5	Results	67
6.5.1	Stratigraphic context.....	67
6.5.2	Cross-cutting reflectors.....	67
6.5.3	Distinctive features associated with cross-cutting reflectors	71
6.6	Discussion.....	71
6.6.1	Diagenetic origin of cross-cutting reflectors.....	71
6.6.2	Cross-cutting reflectors as fossilized silica diagenetic fronts	73
6.6.3	Implications for regional palaeoceanographic evolution	76
6.7	Conclusions.....	78
CHAPTER 7.	Falkland/Malvinas Trough: Indications for Cenozoic tectonic and oceanographic evolution in the southwestern South Atlantic	84
7.1	Abstract	84
7.2	Introduction.....	84
7.3	Geological and tectonic settings.....	87
7.4	Present oceanographic setting.....	88
7.5	Seismic data and seismostratigraphy	89
7.6	Discussion of observations	91
7.7	Conclusions.....	98

CHAPTER 8.	Conclusion.....	99
CHAPTER 9.	Future direction	104
CHAPTER 10.	References.....	105
CHAPTER 11.	Data availability	117
CHAPTER 12.	Seismic profiles	119

II. List of Figures

Figure 2.1: (a). Bathymetric map of the Southern Ocean (Dorschel et al., 2022). Colored lines are the paths for the Antarctic Circumpolar Current fronts from Orsi et al. (1995), including the Subtropical Front-STF (yellow), Subantarctic Front-SAF (red), Polar Front (green), and Southern Antarctic Circumpolar Current Front-SACCF (blue). (b). Bathymetric features of the Scotia Sea and Falkland/Malvinas Plateau. BB = Burdwood Bank; FE = Falkland Escarpment ; F/MB = Falkland/Malvinas Basin; F/MI = Falkland/Malvinas Islands; F/MT = Falkland/Malvinas Trough; FP = Falkland/Malvinas Passage; IOR = Islas Orcadas Rise; MEB = Maurice Ewing Bank; NGP = North Georgia Passage; SG = South Georgia; SO = South Orkney Islands; SRP = Shag Rocks Passage.	4
Figure 2.2: (a). Bathymetric map of the southwest South Atlantic (Dorschel et al., 2022). Colored dotted lines are the paths for the Antarctic Circumpolar Current fronts from Orsi et al. (1995), including the Subtropical Front-STF (yellow), Subantarctic Front-SAF (red), Polar Front (green), and Southern Antarctic Circumpolar Current Front-SACCF (blue). Colored thick lines show the schematic pathway of the deep water masses in the area after Naveira Garabato et al. (2002) (see legend for the definition). Dashed lines are the sporadic or undefined pathways. Black circles are the station position of ALBATROSS hydrographic cruise, part of the results is shown in Figure 2.2b. BB = Burdwood Bank; FE = Falkland Escarpment ; F/MB = Falkland/Malvinas Basin; F/MI = Falkland/Malvinas Islands; F/MT = Falkland/Malvinas Trough; FP = Falkland/Malvinas Passage; IOR = Islas Orcadas Rise; MEB = Maurice Ewing Bank; NGP = North Georgia Passage; SG = South Georgia; SO = South Orkney Islands; SRP = Shag Rocks Passage. (b). Schematic of the spatial distribution of water masses along the ALBATROSS cruise track (black dots in Figure 2.2.a) after Arhan et al. (2002), where black dashed-lines represent the water mass isopycnal limits (surfaces of constant density). Arrows show the location of the Antarctic Circumpolar Current fronts after Orsi et al. (1995) and (Arhan et al., 2002).	5
Figure 2.3: Summary of the depositional environment and evolution of the Falkland/Malvinas Plateau, based on borehole information from DSDP Leg 36, Sites 327, 329, and 330, and Leg 71 Site 511 (Shipboard_Scientific_Party, 1974a, c, d, 1980a), in addition to interpretation of regional seismic profiles acquired during the 60s-80s (e.g. Barker, 1977a; Cunningham and Barker, 1996; Lorenzo and Mutter, 1988; Ludwig, 1983; Shipboard_Scientific_Party, 1977, 1980a).	7
Figure 3.1: Schematic of marine seismic surveying.	11
Figure 3.2: Propagation pattern and reflection elements.	12
Figure 3.3: Convolution model in reflection seismology.	13
Figure 3.4: Logo of cruise leg MSM81 (Uenzelmann-Neben, 2019a).	14
Figure 3.5: Bathymetric map of the Falkland/Malvinas Plateau in the Southern Ocean (Dorschel et al., 2022). (a). Lines show the location of the seismic profiles from survey MSM81. (b). Location of DSDP Leg 36 Sites 327, 329, 330 and Leg 71 Site 511, as well as the seismic lines crossing these drill sites (see Table 3.3 for details). Appendix A includes the information on the intersection points among the seismic profiles.	17
Figure 3.6: Flow chart of seismic data processing implemented in this work (For details see section 3.1.1. and Table 3.4).	20
Figure 3.7: Velocity measurements on cores versus depth for DSDP Sites 327, 329, 330, and 511. The characteristic reflectors from the seismostratigraphic model are marked along with the calculated two-way travel-times for these boundaries using the average interval velocities.	22

Figure 5.1: (a) Bathymetric map of the Falkland/Malvinas Plateau and western South Atlantic sector of the Southern Ocean (Smith and Sandwell, 1997). Arrows schematically show the pathways of the southern-sourced deep/bottom water masses in the present oceanic scheme (Arhan et al., 1999; Arhan et al., 2002; Orsi et al., 1999; Shipboard_Scientific_Party, 1980a): Upper Circumpolar Deep Water (UCDW) in orange, Lower Circumpolar Deep Water (LCDW) in yellow, South Pacific Deep Water (SPDW) in green, Weddell Sea Deep Water (WSDW) in pink, and Antarctic Bottom Water (AABW) in blue. BB = Burdwood Bank; DP = Drake Passage; FI = Falkland Islands; FP = Falkland Passage; FPB = Falkland Plateau Basin; IOR = Islas Orcadas Rise; MEB = Maurice Ewing Bank; NGP = North Georgia Passage; SRP = Shag Rocks Passage. The green box indicates the study area shown in Figure 5.1b, and stars show the location of DSDP Sites in the study area. (b) Bathymetric map of the Maurice Ewing Bank (Smith and Sandwell, 1997). Superimposed are the locations of the seismic profiles used for the study. Dark red lines illustrate the location of profiles shown in the figures. Stars mark the location of DSDP Leg 36 Sites 327, 329, and 330 and Leg 71, Site 511 in the study area. The dotted line represents the location of the Agulhas-Falkland Fracture Zone (AFFZ). 32

Figure 5.2: Outline of DSDP Leg 36 Sites 327, 329, and 330 and Leg 71, Site 511 in the study area (Shipboard_Scientific_Party, 1974a, c, d, 1980a). Schematically shown are the lithological units and hiatuses (and the attributable geological event) reported at each Site against the geological ages for the total drill depths. The rightmost column summarizes the depositional environment and the evolutionary history recorded at DSDP Sites. The marker horizons and seismic units defined in the seismostratigraphic model are also color marked (for more details, refer to Table 5.1 and Section 5.5). 34

Figure 5.3: Information from DSDP Leg 36 Sites 327, 329, and 330 and Leg 71, Site 511 used for integration with seismic data (Bayer, 1980; Shipboard_Scientific_Party, 1974a, c, d, 1980a). Velocity functions and lithological results are shown against depth (below seafloor) for each site. The marker horizons and seismic units defined in the seismostratigraphic model are also color marked (for more details, refer to Table 5.1 and Section 5.5). 37

Figure 5.4: Interpreted seismic profile AWI-20190002. Location of profile is shown in Figure 5.1b. Superimposed are the seismic stratigraphy and the marker horizons (for more details, refer to Table 5.1 and Section 5.5). 42

Figure 5.5: Interpreted seismic profile AWI-20190025. Location of profile is shown in Figure 5.1b. Superimposed are the seismic stratigraphy and the marker horizons (for more details, refer to Table 5.1 and Section 5.5). 44

Figure 5.6: Interpreted seismic profile AWI-20190019. Location of profile is shown in Figure 5.1b. Superimposed are the seismic stratigraphy and the marker horizons (for more details, refer to Table 5.1 and Section 5.5). Arrow shows the location of the crossing seismic profile. 44

Figure 5.7: Interpreted seismic profile AWI-20190001. Location of profile is shown in Figure 5.1b. Superimposed are the defined seismic stratigraphy and the marker horizons (for more details, refer to Table 5.1 and Section 5.5). Arrow shows the location of the crossing seismic profile. 46

Figure 5.8: Interpreted seismic profile AWI-20190017. Location of profile is shown in Figure 5.1b. Superimposed are the defined seismic stratigraphy and the marker horizons (for more details, refer to Table 5.1 and Section 5.5). Arrow shows the location of the crossing seismic profile. 46

Figure 5.9: Interpreted seismic profile AWI-20190014. Location of profile is shown in Figure 5.1b. Superimposed are the seismic stratigraphy and the marker horizons (for more details, refer to Table 5.1 and Section 5.5). Arrows show the location of the crossing seismic profile. 47

Figure 5.10: Evolution of the palaeocirculation in the study area. Erosional and depositional features for the labeled seismic subunits SU4-a, SU4-b, SU5-a, SU5-b, SU5-c, and SU5-d, as observed along the

seismic profiles are color-marked (see the legend). For each subunit, respectively corresponding to Paleocene, Eocene, late Eocene-Oligocene, early Miocene, middle Miocene, and late Miocene times, the arrows schematically show the inferred flow paths of water masses (arrow thickness qualitatively shows the postulated acceleration/deceleration). Also illustrated in the bottom right, is the bathymetry map of the Maurice Ewing Bank (Smith and Sandwell, 1997), superimposed by the location of the seismic profiles and DSDP Leg 36 Sites 327, 329, and 330 and Leg 71, Site 511....50

Figure 5.11: Schematic representation of contourite sedimentary features' distribution across the Maurice Ewing Bank within different seismic subunits, color-marked by their depth of occurrence below the sea surface as intermediate (<2000 m) in pink, deep (3000 m < < 2000 m) in green, and abyssal (> 3000 m) in blue. The width of the bars qualitatively depicts the increased/decreased buildup of the sedimentary features. The rightmost column summarizes the main tectonic and climatic events and the reconstructed palaeoceanography. Refer to Figure 5.10 and section 5.6 for details. [A: (Lawver and Gahagan, 2003; Scher et al., 2015)], [B: (Brown et al., 2006; Eagles and Jokat, 2014), [C: (Goldner et al., 2014; Katz et al., 2011)], [D: (Flower and Kennett, 1994; Zachos et al., 2001)], [E:(Gruetzner and Uenzelmann-Neben, 2016; Gruetzner et al., 2014; Nisancioglu et al., 2003)].....54

Figure 6.1: (a) Bathymetric map showing the location of the Falkland/Malvinas Plateau in the Southern Ocean (General Bathymetric Chart of the Oceans (Dorschel et al., 2022). Arrows schematically show the pathways of the southern-sourced deep/bottom water masses in the present oceanic scheme (Arhan et al., 1999; Arhan et al., 2002; Orsi et al., 1999; Shipboard_Scientific_Party, 1980a).Upper Circumpolar Deep Water (UCDW) in orange, Lower Circumpolar Deep Water (LCDW) in yellow, South Pacific Deep Water (SPDW) in orange, Weddell Sea Deep Water (WSDW) in pink, and Antarctic Bottom Water (AABW) in blue. BB=Burdwood Bank; DP=Drake Passage; F/MB=Falkland/Malvinas Basin; F/MI=Falkland/Malvinas Islands; F/MT=Falkland/Malvinas Trough; MEB=Maurice Ewing Bank; SRP=Shag Rocks Passage. Stars mark the location of DSDP Leg 36 Sites 327, 329, and 330 and Leg 71, Site 511 and the commercial borehole Loligo-1 in the study area. (b). Superimposed are the locations of the seismic profiles used for this study, shown as solid lines. Dark red lines illustrate the location of profiles shown in figures. Light dashed lines illustrate part of the dataset across the MEB, which have been the focus of the publication by Najjarifarizhendi and Uenzelmann-Neben (2021). Stars mark the location of DSDP Leg 36 Sites 327, 329, and 330 and Leg 71, Site 511 in the study area.....62

Figure 6.2: Summary of results from DSDP Leg 36 Sites 327, 329, and 330 and Leg 71, Site 511 (Shipboard_Scientific_Party, 1974a, c, d, 1980a). Schematically shown are the lithological information, hiatuses, and geological ages reported at each site plotted against depth below seafloor. WD, DC (C or I), PD, and CRF values stated for each site respectively represent Water Depth, Drilled Core (Continuously Cored or Intermittently Cored), penetration depth, and Core Recovery Factor. The marker horizons defined in the seismostratigraphic model are also color marked (for details, see Figure 6.4, Section 6.5.1, and Appendix B).65

Figure 6.3: Interpreted composite seismic profile (from profiles AWI-20190001, AWI-20190008, AWI-20190004). Location of profile is shown in Figure 6.1b. Superimposed are the marker horizons defined in the seismostratigraphic model (for details, see Figure 6.4, Section 6.5.2, and Appendix B). The location of DSDP Sites 327, 329, and 330 and Leg 71, Site 511 crossed by the seismic lines are marked with thick black lines. The pink and purple triangles respectively mark the cross-cutting reflectors XR-F/MB and XR-F/MT (for details, see Section 6.5.2). The black box marks the zoomed section shown in Figure 6.8. Arrow shows the location of crossing seismic profile.66

Figure 6.4: Summary of the seismostratigraphic model for the Falklands/Malvinas Plateau, showing units and marker horizons (at left), generalized reflection characteristics (middle column) and relative thickness variations (right-hand column). Left column is the seismostratigraphic model and seismic units across the Falkland/Malvinas Plateau . The marker horizons and seismic units for the eastern sector of the Falkland/Malvinas Plateau, after Figure 2 in Najjarifarizhendi and Uenzelmann-Neben (2021) have been modified to include the new seismic unit SU3' in the F/MB (for more details, see Figure

6.5, section 6.5.1 and Appendix B.2) and the new seismic unit SU6 in the F/MT (for details, see Figure 6.3 and 6.5, section 6.5.1 and Appendix B.2). Unit SU3' is introduced to represent late Cretaceous strata in the F/MB, which unlike its coeval strata on the MEB (SU3), comprises 5 distinct subunits. Unit SU6, has been introduced to include the strata of post-Oligocene with a unique mounded morphology, restricted to F/MT, and differentiable from underlying unit SU5 elsewhere on the Falkland/Malvinas Plateau. 68

Figure 6.5: (a) Interpreted seismic profile AWI-20190007. Location of profile is shown in Figure 6.1b. Superimposed is the defined seismic stratigraphy and the marker horizons (for details, see Figure 6.4, Section 6.5.2 and Appendix B). The pink and purple triangles respectively mark the cross-cutting reflectors XR-F/MB and XR-F/MT (for details, see Sections 6.5.2 and 6.5.3). Black boxes mark the zoomed sections shown in (b), (c), and (d). Arrow shows the location of crossing seismic profile. (b) and (c) Zoomed sections respectively showing the cross-cutting reflectors XR-F/MB and XR-F/MT; schematically shown are the polarity of the cross-cutting reflector compared to the seafloor reflector, typical of a positive polarity (for details, see Sections 6.5.2 and 6.5.3). (d) Zoomed section showing the seismic attribute “energy” (for details, see Section 6.5.3). Arrows show the location of crossing seismic profile. 69

Figure 6.6: (a) Interpreted seismic profile AWI-20190011. Location of profile is shown in Figure 6.1b. Superimposed is the defined seismic stratigraphy and the marker horizons (for details, see Figure 6.4, Section 6.5.1 and Appendix B). The gray and violet triangles respectively mark the seafloor reflector (R-SF) and the early-middle Miocene unconformity (R-EMM). The pink and purple triangles respectively mark the cross-cutting reflectors XR-F/MB and XR-F/MT (for details, see Sections 6.5.2 and 6.5.3). The black boxes mark the zoomed sections shown in (b) and (c). Arrows show the location of crossing seismic profiles. (b) and (c) Zoomed sections respectively showing the peculiar structural features in proximity of the cross-cutting reflectors XR-F/MB and XR-F/MT (for details, see Section 6.5.3). 70

Figure 6.7: (a) Seismic profile AWI-20190011. Location of profile is shown in Figure 6.1b. The pink and purple triangles respectively mark the cross-cutting reflectors XR-F/ MB and XR-F/MT (for details, see Section 6.5.2). Superimposed on the seismic profiles is the interval velocity section calculated from the seismic stacking velocity data, where the color scale gives the velocity values. Dashed cyan lines show the location of CDP 1200 and 9800. (b) and (c) respectively show the CDP gather 1200 and 9800 in gray scale (right) and the corresponding semblance profile (left). The pink and purple triangles respectively show the extent of reflectors XR-F/MB and XR-F/ MT on the CDP gathers and semblance profiles. (for details, see Sections 6.5.2 and 6.5.3). Arrows show the location of crossing seismic profiles 74

Figure 6.8: Section from seismic profile AWI-20190004. Location of profile is shown in Figure 6.1b. The pink and purple triangles respectively mark the cross-cutting reflectors XR-F/MB and XR-F/MT (for details, see Section 6.5.2). (a) and (b) Superimposed on the seismic profiles are respectively the instantaneous frequency and the first envelope derivative attribute section calculated from the seismic data, where the color scale gives the corresponding values (for details, see Sections 6.5.2 and 6.5.3). Arrows show the location of crossing seismic profiles. 75

Figure 7.1: (a). Bathymetric map of the southwestern South Atlantic (Dorschel et al., 2022). Colored dotted lines are the paths for the Antarctic Circumpolar Current fronts from Orsi et al. (1995), including the Subtropical Front-STF (yellow), Subantarctic Front-SAF (red), Polar Front (green), and Southern Antarctic Circumpolar Current Front-SACCF (blue). Colored thick lines show the schematic pathway of the deep water masses in the area after Naveira Garabato et al. (2002) (see legend for the definition). Dashed lines are the sporadic or undefined pathways. Blue triangles are the CTD stations for the North Scotia Ridge Overflow Project, results are shown in Figure 7.2 (Smith et al., 2010). Black circles and purple diamonds are the station position of ALBATROSS hydrographic cruise, results are shown in Figure 7.2 (Arhan et al., 2002). Arrows show the location of the Antarctic Circumpolar Current fronts after Orsi et al. (1995) and (Arhan et al., 2002; Naveira Garabato et al.,

2002). BB = Burdwood Bank; F/MB = Falkland/Malvinas Basin; F/MI = Falkland/Malvinas Islands; F/MT = Falkland/Malvinas Trough; FP = Falkland/Malvinas Passage; IOR = Islas Orcadas Rise; MEB = Maurice Ewing Bank; NGP = North Georgia Passage; SG = South Georgia; SO = South Orkney Islands; SRP = Shag Rocks Passage.	85
Figure 7.2: Schematic of the spatial distribution of water masses along the stations for the North Scotia Ridge Overflow Project after (Smith et al., 2010) and the ALBATROSS cruise track after Arhan et al. (2002). See Figure 7.1 for the location of these hydrographic stations. The black dashed-lines represent the water mass isopycnal limits (surfaces of constant density).....	87
Figure 7.3: Part of the interpreted seismic profile AWI-20190004. Location of section is shown in Figure 7.1b. Superimposed is the seismic stratigraphy and the marker horizons. The pink and purple triangles respectively mark the cross-cutting reflectors XR-F/MB and XR-F/MT (for details, see Section 7.5)	90
Figure 7.4: Part of the interpreted seismic profile AWI-20190006. Location of section is shown in Figure 7.1b. Superimposed is the seismic stratigraphy and the marker horizons. The pink and purple triangles respectively mark the cross-cutting reflectors XR-F/MB and XR-F/MT (for details, see Section 7.5).	93
Figure 7.5: Part of the interpreted seismic profile AWI-20190012. Location of section is shown in Figure 7.1b. Superimposed is the seismic stratigraphy and the marker horizons. The pink and purple triangles respectively mark the cross-cutting reflectors XR-F/MB and XR-F/MT (for details, see Section 7.5).	96

III. List of Tables

Table 3.1: Survey and acquisition parameters (Uenzelmann-Neben, 2019a).....	15
Table 3.2: 2D seismic profiles from survey MSM81.....	16
Table 3.3: Location and drilling information of DSDP Leg 36 Sites 327, 329, 330 and Leg 71 Site 511 (Shipboard_Scientific_Party, 1974a, c, d, 1980a), as well as the seismic lines crossing these drill sites (see Figure 6.2 for details).....	18
Table 3.4: Processing modules and parameters used from paradigm-ECHOS software for processing of the seismic data in this work. See appendix B for the parameter tests performed to reach the optimum processing parameters for each seismic sequence.....	19
Table 5.1: Seismostratigraphic model. Defined seismic stratigraphy and reflector nomenclature at DSDP Leg 36 Site 327, 329, 330, and Leg 71 Site 511.....	39
Table 6.1: Summary of the features used for discerning the status of a silica diagenetic front (active vs. arrested), modified from Varkouhi et al. (2022) (for details, see sections 6.5.2 and 6.6.2. The colors indicate the degree of reliability attributed to each feature for characterizing an active vs. an arrested silica diagenetic front; red (low reliability), yellow (reliability), and green (high reliability).....	59

IV. List of Abbreviations (in alphabetical order)

AABW	<u>A</u> ntarctic <u>B</u> ottom <u>W</u> ater
AAIW	<u>A</u> ntarctic <u>I</u> ntermediate <u>W</u> ater
ACC	<u>A</u> ntarctic <u>C</u> ircumpolar <u>C</u> urrent
AWI	<u>A</u> lfred <u>W</u> ege <u>n</u> er <u>I</u> nstitute
BGHS	<u>B</u> ase of <u>G</u> as- <u>h</u> ydrate <u>S</u> tability-zone
BSR	<u>B</u> ottom <u>S</u> imulating <u>R</u> eflector
CDP	<u>C</u> ommon <u>D</u> epth <u>P</u> oint
CDW	<u>C</u> ircumpolar <u>D</u> eep <u>W</u> ater
DFG	<u>D</u> eutsche <u>F</u> orschungsgemeinschaft
DSDP	<u>D</u> eep <u>S</u> ea <u>D</u> rilling <u>P</u> roject
F/MB	<u>F</u> alkland/ <u>M</u> alvinas <u>B</u> asin
F/MI	<u>F</u> alkland/ <u>M</u> alvinas <u>I</u> slands
F/MP	<u>F</u> alkland/ <u>M</u> alvinas <u>P</u> lateau
F/MT	<u>F</u> alkland/ <u>M</u> alvinas <u>T</u> rough
GH	<u>G</u> as <u>H</u> ydrate
GH_BSR	<u>G</u> as <u>H</u> ydrate <u>B</u> ottom <u>S</u> imulating <u>R</u> eflector
GI-gun	<u>G</u> enerator- <u>I</u> njector <u>G</u> un
LCDW	<u>L</u> ower <u>C</u> ircumpolar <u>D</u> eep <u>W</u> ater
mbsf	<u>m</u> eters <u>b</u> elow <u>s</u> eafloor
MEB	<u>M</u> aurice <u>E</u> wing <u>B</u> ank
ms TWT	<u>m</u> illisecond <u>s</u> <u>T</u> wo- <u>w</u> ay <u>T</u> ravel- <u>t</u> ime
msbsf TWT	<u>m</u> illisecond <u>s</u> <u>T</u> wo- <u>w</u> ay <u>T</u> ravel- <u>t</u> ime <u>b</u> elow <u>s</u> eafloor
NADW	<u>N</u> orth <u>A</u> tlantic <u>D</u> eep <u>W</u> ater
NBSR	<u>N</u> on- <u>B</u> ottom <u>S</u> imulating <u>R</u> eflector
NMO	<u>N</u> ormal <u>M</u> ove <u>o</u> ut
NSR	<u>N</u> orth <u>S</u> cotia <u>R</u> idge
O _A /CT_BSR	<u>O</u> pal- <u>A</u> to <u>O</u> pal- <u>CT</u> <u>T</u> ransition <u>B</u> ottom <u>S</u> imulating <u>R</u> eflector
O _A /CT_NBSR	<u>O</u> pal- <u>A</u> to <u>O</u> pal- <u>CT</u> <u>T</u> ransition <u>N</u> on- <u>B</u> ottom <u>S</u> imulating <u>R</u> eflector
PF	<u>P</u> olar <u>F</u> ront
RMS	<u>R</u> oot- <u>M</u> ean- <u>S</u> quare
SACCF	<u>S</u> outhern <u>A</u> ntarctic <u>C</u> ircumpolar <u>C</u> urrent <u>F</u> ront
SAF	<u>S</u> ub <u>a</u> ntarctic <u>F</u> ront
SPDW	<u>S</u> outh <u>P</u> acific <u>D</u> eep <u>W</u> ater
TZ _A /CT	<u>O</u> pal- <u>A</u> to <u>O</u> pal- <u>CT</u> <u>T</u> ransition <u>Z</u> one
UCDW	<u>U</u> pper <u>C</u> ircumpolar <u>D</u> eep <u>W</u> ater
WSDW	<u>W</u> eddell <u>S</u> ea <u>D</u> eep <u>W</u> ater

V. Thesis outline

For the aim of this thesis, ca. 5300 km of 2D high-resolution seismic data, acquired by the Alfred Wegener Institute in 2019 across the Falkland/Malvinas Plateau, were analyzed in order to investigate the Cenozoic oceanographic evolution in the southwestern south Atlantic. The seismic palaeoceanographic investigation of the Falkland/Malvinas Plateau contributes to a better understanding of the onset and evolution of the Antarctic Circumpolar Current in association with tectonics of the development of the Drake Passage-Scotia See zone and the subsequent climatic modifications. This cumulative doctoral thesis comprises a total of twelve chapters.

Chapter 1 includes the abstract of the thesis. Chapter 2 serves to introduce the Falkland/Malvinas Plateau, its importance with respect to the Palaeoceanography of the southwestern South Atlantic, and the central questions which are addressed. The technique and analysis used for the study are elaborated in chapter 3. The findings and results relevant to the central research questions are presented as three articles for peer-reviewed scientific journals. An overview of these articles, including my contributions to each, is included in chapter 4. Detailed results and discussions of the observations with respect to the central questions of this thesis outline chapters 5- 7. Chapter 8 summarized and concludes the finding of the three articles, while suggestions for future direction are given in chapter 9. Links to the references and the data availability are respectively provided in chapters 10 and 11. Migrated seismic profiles from expedition MSM81 are included in chapter 12.

CHAPTER 1. Abstract

1.1 Summary

Today a submarine plateau in the southwest South Atlantic, the Falkland/Malvinas Plateau had its origin in the southwest Gondwana in between South America, Africa, Antarctica, and Antarctic Peninsula. With the separation of Gondwana into individual continents, the Falkland/Malvinas Plateau has a history associated with the development of the South Atlantic since the late Mesozoic and the growth of the Drake Passage-Scotia Sea zone since the early Cenozoic. These tectonic developments paved the way for the abyssal connections between the south Atlantic and the Pacific, which enabled the establishment of the modern-style oceanic circulation setting. The inception of the Antarctic Circumpolar Current conditioned the thermal isolation of Antarctica, the perennial glaciation, and the vast climatic modifications of the Cenozoic. The imprints of these oceanographic modifications in the southwestern South Atlantic are to be archived within the sedimentary strata at Falkland/Malvinas Plateau. This thesis focuses on the onset and variations in pathways and intensities of southern-sourced oceanic water masses flowing in the Antarctic Circumpolar Current, in response to the Cenozoic tectonic and climatic events. To this end, a new set of 2D high-resolution seismic reflection data acquired by the Alfred Wegener Institute in 2019 is presented here. Defining a seismic-stratigraphic framework, through the integration of borehole information from Deep Sea Drilling Project Leg 36 Sites 327, 329, and 330 and Leg 71 Site 511 allowed me to interpret the seismic data. In this study, the sedimentary and structural peculiarities across the Falkland/Malvinas Plateau, which link to the regional tectonic evolution and the corresponding oceanographic modifications are investigated. In specific, I look into the current-controlled depositional - and erosional features of contourite drifts as footprints of palaeocurrents across different bathymetric sectors of the Falkland/Malvinas Plateau, namely the Maurice Ewing Bank, the Falkland/Malvinas Basin, and – Trough. The findings highlight that the Falkland/Malvinas Plateau has been acting as a barrier to the southern-sourced deep and bottom water masses on their way into the Argentine Basin since Paleocene times. A precursor of Circumpolar Deep Water overspilled the Falkland/Malvinas plateau in a highly dynamic circulation regime already in late Eocene/Oligocene times as the growth of the Drake Passage-Scotia Sea zone favored deep circulations. Persistent erosional action of these deep water masses commenced the geometry of the present seafloor in Falkland/Malvinas Basin. Vast erosion and removal of tens of meters of overburden sediments led to the fossilization of a silica-diagenetic front across the Falkland Malvinas Basin and – Trough. Since the middle Miocene, with the full development of the Drake Passage and the enhanced bottom water mass production below the Antarctic ice shelves, a precursor of Weddell Sea Deep Water has escaped the Georgia Basin and entered the Falkland/Malvinas Trough.

1.2 Zusammenfassung

Das Falkland/Malvinas-Plateau hat seinen Ursprung im südwestlichen Gondwana zwischen Südamerika, Afrika, der Antarktis und der Antarktischen Halbinsel und bildet heute ein submarines Plateau im südwestlichen Südatlantik. Seit der Aufspaltung Gondwanas in einzelne Kontinente dokumentiert das Falkland/Malvinas-Plateau die Entwicklung des Südatlantiks seit dem späten Mesozoikum und die Bildung der Drake Passage-Scotia See seit dem frühen Känozoikum. Diese tektonischen Ereignisse ermöglichen tiefe Verbindungen der Becken des Pazifiks und des Atlantiks, welche die Entwicklung der modernen ozeanischen Zirkulation erlaubten. Die Bildung des antarktischen Zirkumpolarstroms führte zur thermischen Isolierung der Antarktis, der Vereisung der Antarktis- und enormen klimatischen Veränderungen während des Känozoikums. Die ozeanographischen Modifikationen im südwestlichen Südatlantik sind in den Sedimentschichten des Falkland/Malvinas-Plateaus archiviert. Diese Arbeit untersucht die Entstehung und die Modifikationen in Pfaden und Intensitäten der südlichen Wassermassen des antarktischen Zirkumpolarstroms in Relation zu den tektonischen Bewegungen und klimatischen Veränderungen des Känozoikums. Zu diesem Zweck werden hochauflösende reflexionsseismischen Daten präsentiert, die 2019 vom Alfred-Wegener-Institut im Gebiet des Falkland/Malvinas-Plateaus akquiriert wurden. Die Definition eines seismostratigraphischen Modells durch die Integration von Bohrlochsinformation aus Deep Sea Drilling Project Leg 36 Sites 327, 329 und 330 und Leg 71 Site 511 ermöglichte mir die Interpretation der seismischen Daten. In dieser Studie werden die Sedimentstrukturen des Falkland/Malvinas-Plateaus untersucht, die auf die regionale tektonische Entwicklung und die entsprechenden ozeanographischen Veränderungen hinweisen. Insbesondere untersuche ich die bodenströmungsgesteuerten Ablagerungs- und Erosionsstrukturen von Sedimentdriftkörpern, die Spuren von Paläoströmungen in den Sektoren des Falkland/Malvinas-Plateaus, nämlich der Maurice Ewing Bank, dem Falkland/Malvinas-Becken und der -Rinne dokumentieren. Die Ergebnisse zeigen, dass das Falkland/Malvinas-Plateau seit dem Paläozän eine Barriere für die südlichen Tiefen- und Bodenwassermassen darstellt, die Richtung des Argentinischen Beckens fließen. Ein proto-zirkumpolares Tiefenwassers überfloß das Falkland/Malvinas-Plateau in einem hochdynamischen Zirkulationsregime bereits im späten Eozän/Oligozän, als die Öffnung der Drake Passage-Scotia See tiefozeanische Zirkulationen begünstigte. Die anhaltende Erosionwirkung dieser Bodenwassermassen initiierten die heutige Morphologie des Meeresbodens des Falkland/Malvinas-Beckens. Erosion von Dutzenden von Metern an Sedimenten führte zur Fossilisierung/Arrestierung einer Silikat-Diagenesefront in Falkland/Malvinas-Becken und -Rinne. Seit dem mittleren Miozän, mit der vollständigen Öffnung der Drake Passage und der verstärkten Produktion von Bodenwassermassen unter den antarktischen Schelfeisen kann ein Proto-Weddellmeer-Tiefenwasser aus dem Georgia-Becken in die Falkland/Malvinas-Rinne fließen.

CHAPTER 2. Introduction

2.1 Falkland/Malvinas Plateau: present and past peculiarities

The present. Today, the Falkland/Malvinas Plateau (F/MP) is a prominent submarine plateau offshore Argentina in the southwest South Atlantic (Figure 2.1), having its origin in the Gondwana prior to the breakup. The F/MP is a transform marginal plateau (de Lépinay et al., 2016; Schimschal and Jokat, 2018) at the westernmost end of the Agulhas-Falkland Fracture Zone, which is a ca. 1200 km trans-Atlantic transform zone extending eastwards towards to the Agulhas margin near South Africa (Ben Avraham et al., 1997).

The Falkland/Malvinas Islands (F/MI) constitute the elevated western sector of the plateau, whereas the Falkland/Malvinas Basin (F/MB) with average water depths of 2600 constitutes the central part. This 500 km-wide basin gives way eastwards to a bathymetric high with an average water depth of 1000 m, known as the Maurice Ewing Bank (MEB). Towards the south, the F/MP is bound by the Falkland/Malvinas Trough (F/MT), a bathymetric depression with an average water depth of 3000 m.

The F/MP lies downstream of the Drake Passage on the pathway of the Antarctic Circumpolar Current (ACC) and is influenced by the southern-sourced water masses flowing within the ACC on their way into the Argentine Basin and the South Atlantic. Today, the ACC is the strongest zonal oceanic current system on earth, to which the estimations attribute ca. 140 Sv ($140 * 10^6 \text{ m}^3/\text{s}$) of eastward water transport in the Southern Ocean (Orsi et al., 1995; Rintoul et al., 2001; Smith et al., 2010). The ACC contributes to the distribution of heat, fresh water, etc. throughout the Pacific, Atlantic, and the Indian Oceans. Thereby, the ACC contributes to the Atlantic Meridional Overturning Circulation (Kuhlbrodt et al., 2007; Orsi et al., 1995), and as well responds on a global scale to climatic variations (Talley, 2013).

The ACC comprises three deep-reaching circumpolar fronts (Figure 2.1), which in the terminology of physical oceanography correspond to large meridional density gradients (e.g. Belkin and Gordon, 1996; Nowlin and Klinck 1986; Orsi et al., 1995). As both the ship-based and satellite-based physical oceanography suggest, these fronts include a number of narrow jets of fast flowing water which present rather quiescent water in between (e.g. Gille, 1994; Orsi et al., 1995). In the geological sense, the ACC is imprinted with co-existence of biosiliceous fauna to its south and biocalcarous fauna to its north, while the main activity axis is marked with erosional or non-depositional features (Barker et al., 2007).

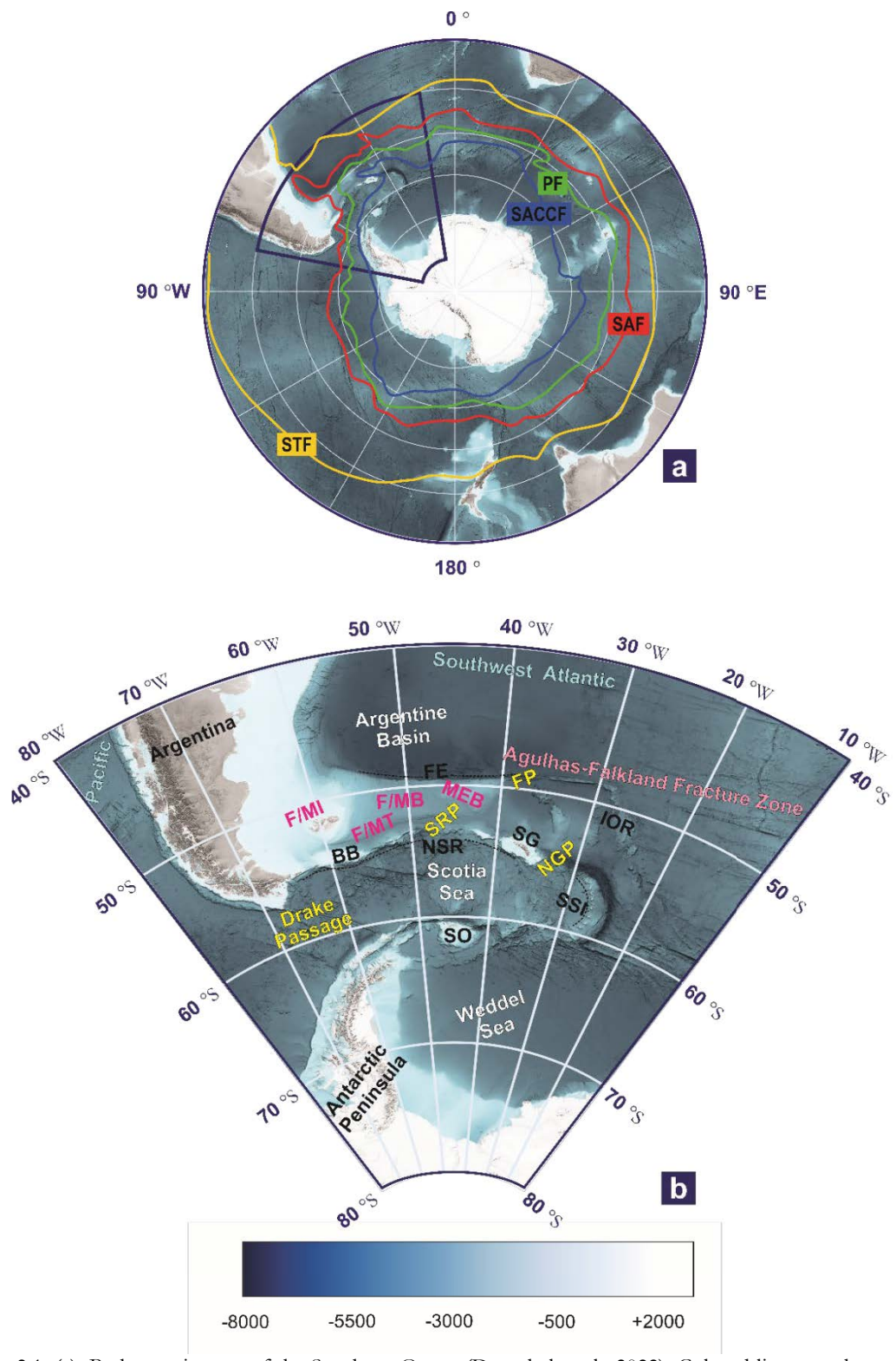


Figure 2.1: (a). Bathymetric map of the Southern Ocean (Dorschel et al., 2022). Colored lines are the paths for the Antarctic Circumpolar Current fronts from Orsi et al. (1995), including the Subtropical Front-STF (yellow), Subantarctic Front-SAF (red), Polar Front (green), and Southern Antarctic Circumpolar Current Front-SACCF (blue). (b). Bathymetric features of the Scotia Sea and Falkland/Malvinas Plateau. BB = Burdwood Bank; FE = Falkland Escarpment ; F/MB = Falkland/Malvinas Basin; F/MI = Falkland/Malvinas Islands; F/MT = Falkland/Malvinas Trough; FP = Falkland/Malvinas Passage; IOR = Islas Orcadas Rise; MEB = Maurice Ewing Bank; NGP = North Georgia Passage; SG = South Georgia; SO = South Orkney Islands; SRP = Shag Rocks Passage.

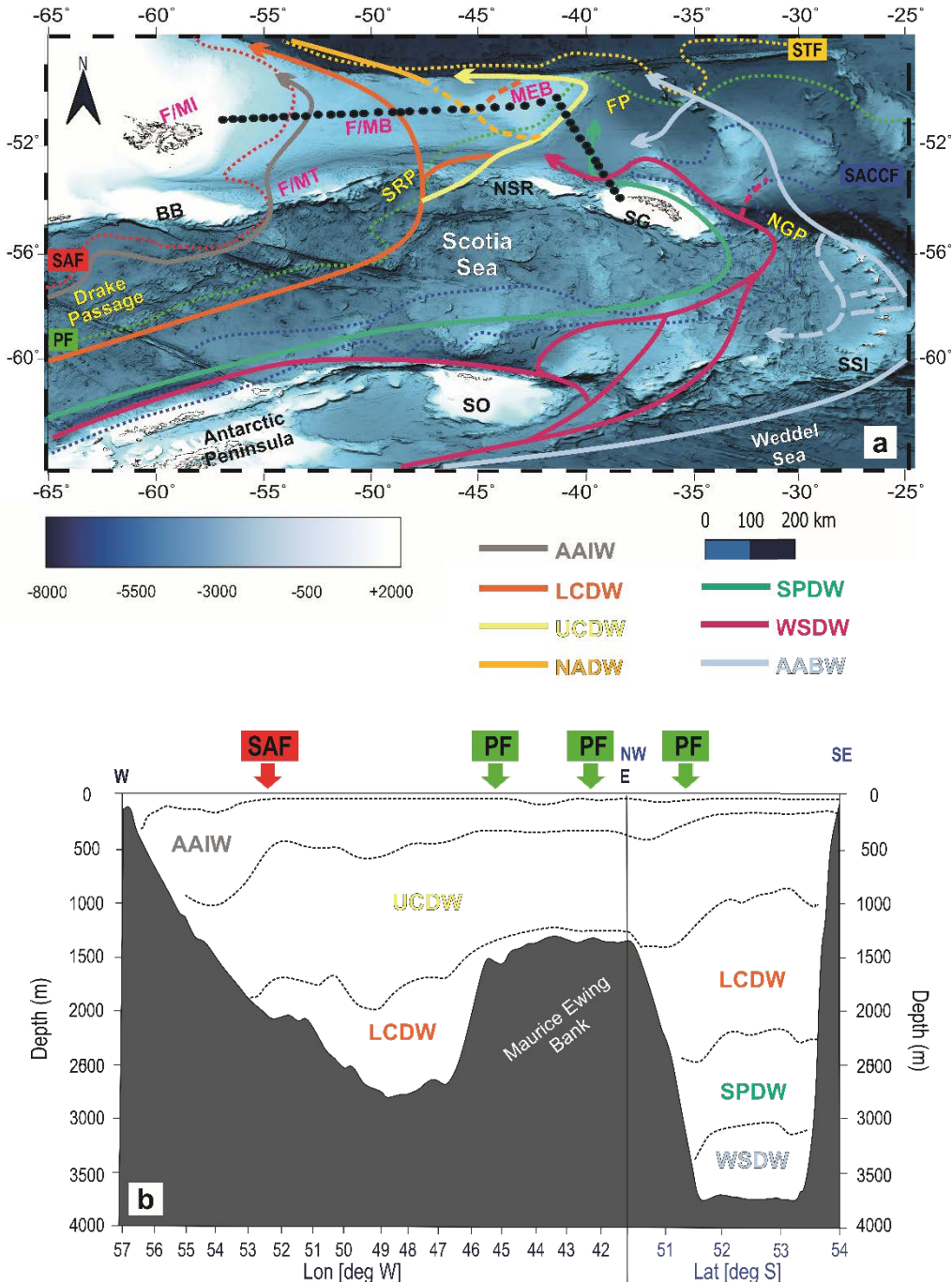


Figure 2.2: (a). Bathymetric map of the southwest South Atlantic (Dorschel et al., 2022). Colored dotted lines are the paths for the Antarctic Circumpolar Current fronts from Orsi et al. (1995), including the Subtropical Front-STF (yellow), Subantarctic Front-SAF (red), Polar Front (green), and Southern Antarctic Circumpolar Current Front-SACCF (blue). Colored thick lines show the schematic pathway of the deep water masses in the area after Naveira Garabato et al. (2002) (see legend for the definition). Dashed lines are the sporadic or undefined pathways. Black circles are the station position of ALBATROSS hydrographic cruise, part of the results is shown in Figure 2.2b. BB = Burdwood Bank; FE = Falkland Escarpment ; F/MB = Falkland/Malvinas Basin; F/MI = Falkland/Malvinas Islands; F/MT = Falkland/Malvinas Trough; FP = Falkland/Malvinas Passage; IOR = Islas Orcadas Rise; MEB = Maurice Ewing Bank; NGP = North Georgia Passage; SG = South Georgia; SO = South Orkney Islands; SRP = Shag Rocks Passage. (b). Schematic of the spatial distribution of water masses along the ALBATROSS cruise track (black dots in Figure 2.2.a) after Arhan et al. (2002), where black dashed-lines represent the water mass isopycnal limits (surfaces of constant density). Arrows show the location of the Antarctic Circumpolar Current fronts after Orsi et al. (1995) and (Arhan et al., 2002).

Downstream of the Drake Passage, the majority of the transport is associated with, from north to south, the Subantarctic Front (SAF), the Polar Front (PF), and the Southern ACC Front (SACCF) (Figure 2.1). These three frontal systems continue unbroken on a circumpolar path around Antarctica (Orsi et al., 1995). After passing through the Drake Passage, the SAF and the PF deflect north towards the North Scotia Ridge (NSR), which acts as a barrier to the water masses. Due to its oceanographic importance, the area downstream of the Drake Passage and the F/MP has been subject to a number of hydrographic studies (Arhan et al., 1999; Arhan et al., 2002; Naveira Garabato et al., 2002). The northward flowing water masses downstream of the Drake Passage have been described and quantified, based on full-depth hydrographic and lowered acoustic Doppler current profiler measurements in a transect between the F/MI and the South Georgia by (Arhan et al., 2002). This includes the complete overflow of the Falkland/Malvinas Plateau (See Figure 2.2 for a summary of the circulation patterns and the stratification of the water masses.)

The crust. Samples from outcrops, drillings, and dredging provided ground truth information of Precambrian continental basement rocks on the F/MP (Lorenzo and Mutter, 1988; Shipboard_Scientific_Party, 1974d). Geophysical surveys (aeromagnetic, gravity, refraction - and reflection seismology) however, vouch for a thick (10-12 km) oceanic crust in the F/MB. West of the MEB and east of the F/MI are described as Continent-Ocean Transition Zones (Eagles and Eisermann, 2020; Kimbell and Richards, 2008; Schimschal and Jokat, 2018, 2019).

The Mesozoic. The palaeo-geographical location of the F/MI in-between South America, Africa, and Antarctica is of importance for tectonic reconstructions of the southwest Gondwana in the Mesozoic. The F/MP as a transform margin is considered a key to deciphering continental fragmentations and dispersal and to the evolution of the South Atlantic. However, there is still ongoing debate as to relative position of the F/MI prior to the breakup of Gondwana. A palaeo-location close to southeast South Africa is suggested for the F/MI in rotational models, mostly on the grounds of the stratigraphic and structural correlation and micropalaentological studies (e.g. Adie, 1952; Mitchell et al., 1986; Stanca et al., 2019; Stone et al., 2009). Whereas an opposing hypothesis postulates the F/MI to be an extension of the South American continent, situated south of South Africa in the pre-Paleozoic (Du Toit, 1927; Eagles and Eisermann, 2020; Lovecchio et al., 2019; Ramos et al., 2017).

The Cenozoic. The Cenozoic history of the F/MP is entangled with the Cenozoic inception of the Scotia Sea, attributed to an extension behind a subduction zone at the South American-Antarctic plate boundary (Barker, 2001a). This in turn is linked with the opening of the Drake Passage, which is considered as a final phase in the breakup of southwest Gondwana as the South America and Antarctic Peninsula separated. In the oceanographic setting of the Southern Ocean, the opening of the Drake Passage (in addition to the Tasman Gateway) is considered as a principle final phase in the completion of a full circumpolar path and the establishment of the ACC (e.g. Barker, 2001a; Dalziel, 2014).

The establishment of the ACC is suggested to have served as a thermohaline boundary, hindering the meridional geostrophic flow across the circumpolar frontal system (Naveira Garabato et al., 2011). It has led to the separation of the mid-latitude warm subtropical regimes from the high-latitude cold subpolar regimes and contributed to the thermal isolation of the Antarctic continent. The latter is considered as a prerequisite for the stabilized continental-wide Antarctic glaciation (e.g. Barker and Thomas, 2004; Gordon et al., 2001; Rintoul et al., 2001; Scher et al., 2015; Zachos et al., 2001).

The Cenozoic history of the ACC is hence important in terms of glaciation of Antarctica and the subsequent enhanced production of the Antarctic Bottom Water (AABW) below the expanding ice shelves (Goldner et al., 2014). Despite its extreme importance in understanding the Cenozoic oceanographic and climatic conditions and modifications, the timing of the opening of the Drake Passage for shallow and deep water transport is yet under debate. Estimations based on tectonic reconstructions and geo-environmental analysis give a very wide span between 41 and 6 Ma for this event (reviewed by Barker et al., 2007).

2.2 Preceding investigation of the Falkland/Malvinas Plateau

The reflection seismology. The extensional and rifted system of the plateau, known to embed late Jurassic organic-rich source rocks has been the target of petroleum exploration and exploitation, primarily offshore F/MI (e.g. Foschi and Cartwright, 2016; Hillier, 2000; Levashov et al., 2014; Platt and Philip, 1995; Richards, Gatliff, Quinn and Fannin, 1996). Therefore, the nearby area offshore F/MI has vastly been explored by means of 2D and 3D seismic surveys. The seismic datasets across the majority of the F/MP, is however low-quality and relatively sparse.

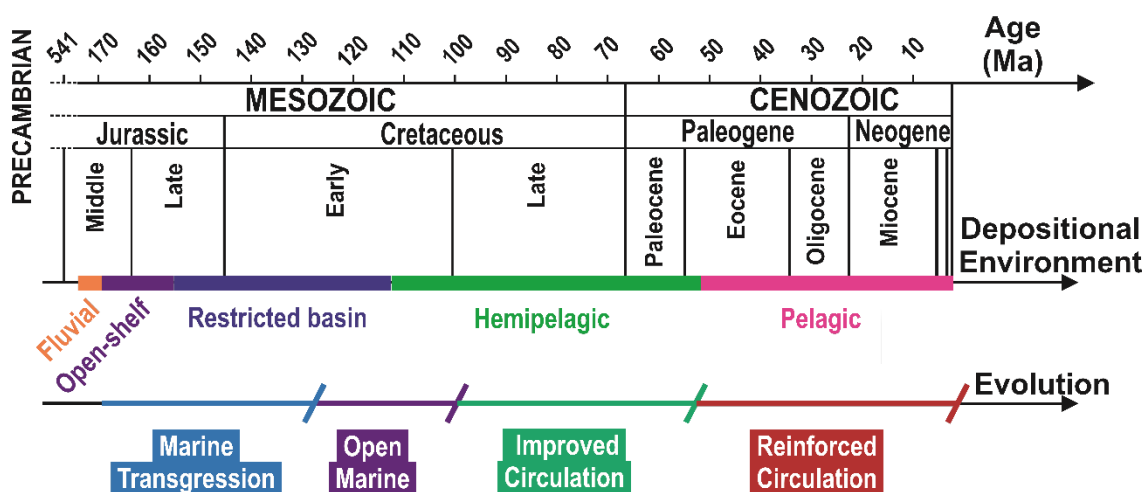


Figure 2.3: Summary of the depositional environment and evolution of the Falkland/Malvinas Plateau, based on borehole information from DSDP Leg 36, Sites 327, 329, and 330, and Leg 71 Site 511 (Shipboard_Scientific_Party, 1974a, c, d, 1980a), in addition to interpretation of regional seismic profiles acquired during the 60s-80s (e.g. Barker, 1977a; Cunningham and Barker, 1996; Lorenzo and Mutter, 1988; Ludwig, 1983; Shipboard_Scientific_Party, 1977, 1980a).

Disperse single-channel seismic tracks were collected between 1973 and 1978 by the Lamont Doherty Earth Observatory during RV Robert D. Conrad RC cruise 1606 and 2106. Later, between 1974 and 1993, the British Antarctic Survey ran single-channel seismic tracks during RRS Shackleton cruises 734, 756 and 881, RRS Bransfield cruise 778, RRS Discovery cruise 172, RRS Charles Darwin cruise 37 and RRS James Clark Ross cruise 04. For the first time in 1988, during RSS Discovery Cruise 172, the British Antarctic Survey collected 6 regional 2D multi-channel (24-Fold) across the NSR and the F/MP. These works in addition to the Deep Sea Drilling Project (DSDP) drillings of Leg 36, Sites 327, 329, and 330 in 1974, and Leg 71 Site 511 in 1980 led to the general understanding of the geological history and structure of the F/MP (e.g. Barker, 1977a; Cunningham and Barker, 1996; Lorenzo and Mutter, 1988; Ludwig, 1983; Shipboard_Scientific_Party, 1977, 1980a). Figure 2.3 presents the concluded evolutional model for the F/MP based on these regional studies. To the scientific community, the F/MP has never stopped to be a subject of interest.

The paleoceanography. Apropos of the palaeoceanographic reconstructions via investigation of sedimentary features in the area, Cunningham and Barker (1996) discussed bottom-current control on the sedimentation in the eastern F/MT. From a single seismic profile MCS I95167b, acquired by the Italian National Program for Antarctic Research (PNRA) in 1995, Del Ben (2004) reported current-controlled deposition to the south of MEB. Based on evidences from sediment cores, sub-bottom profiler, and seismic data, Howe et al. (1997), Koenitz et al. (2008), and Pérez et al. (2015) discussed contourites at the westernmost sector of the F/MT, between the F/MI and the Burdwood Bank. To the south of the F/MI, Nicholson and Stow (2019) associated the erosional and depositional sedimentary features with the action of the Subantarctic Front jet since ca. 34 Ma. Nicholson et al. (2020) discussed the erosional action of currents flowing along the Subantarctic Front of the northern flank of the Burdwood Bank, where rapid sedimentation of the Burdwood sediment drift has been preconditioning tsunamigenic submarine landslides. Esteban et al. (2020) analyzed the structure of the sedimentary fill of the westernmost sector of the F/MT, to the north of the Burdwood Bank, and presented an evolutionary model about the area and its links to the onset of the Antarctic Intermediate Water (AAIW).

Through analysis of the Albian benthic foraminiferal fauna at DSDP Site 327, Lopes et al. (2017) characterized conditions of the bottom-water oxygenation in association with the action of abyssal currents. Dummann, Hofmann, et al. (2020) evaluated new proxy records from DSDP Site 511 and discussed an early Cretaceous palaeo-environmental evolution of the plateau accompanied by earliest connections of the Atlantic and the Southern Ocean, which according to Dummann, Steinig, et al. (2020) allowed for the development of the early intra-oceanic circulation patterns.

IODP expedition 382 drilled Sites U1534 and U1535 into a contourite drift below the Subantarctic Front at the continental shelf ca. 600 KM east of Strait of Magellan to investigate the evolution of the AAIW and the history of the prevailing Southern Hemisphere Westerlies (Weber et al., 2021).

2.3 Thesis motivation and central questions

It can be expected that the mighty ACC has left recognizable erosional and depositional footprints on the sedimentary strata across the F/MP, spilling over into the Argentine Basin. The ACC is mainly driven by south-westerly winds, however the surface shear strength extends down to the seafloor and accommodates intermediate as well as deep and abyssal water masses (Barker and Thomas, 2004). The pathway of the ACC is controlled by the topography of the seafloor (e.g. Kim and Orsi, 2014; Lazarus and Caulet, 1993; Trathan et al., 2000). The water masses flowing within the ACC are constrained to the bathymetric contours (continental shelves, submarine plateaus, etc.), thereby leaving behind sedimentary footprints. As a pronounced submarine plateau downstream of the Drake Passage, the F/MP hinders the northward flow of the water masses flowing within the ACC.

Long-term action of the water masses at the seafloor governs the sediment distribution with respect to the bulk density, porosity, grain size and sorting, compaction and reworking; hence affects the physical properties of the sediments (Rack, 1993). At larger scales, these water masses create erosional and/or non-depositional manifestations across the sedimentary strata along their pathways. These contouritic depositional and erosional patterns are known as sediment drifts, which can be imaged and mapped using reflection seismology.

The genesis and the evolutional history of the oceanic currents in terms of intensity (vigorousness/sluggishness) as well the pathway modifications are archived as sedimentary features at the seafloor. These oceanographic modifications are essentially associated with the tectonic or climatic events. Across the F/MP, these current-related sedimentary features would hint at the early onset of the ACC and allow for constraining its response to the tectonic, climatic events (e.g. Barker and Thomas, 2004; Pfuhl and McCave, 2005; Pudsey and Howe, 2002).

The invaluable potential of the sedimentary strata across the F/MP as archive of palae-oceanographic and palaeo-climatic variations in the southwestern South Atlantic is however hardly investigated. In 2019, ca. 5300 km of 2D high-resolution seismic reflection data were acquired during expedition MSM81 by the Alfred Wegener Institut (AWI), with the aim to contribute to better understand the development of oceanic circulation in the Southern Ocean (Uenzelmann-Neben, 2019a). Using this dataset, this thesis addresses the following questions.

- When do the earliest current-related sedimentary traces appear across the F/MP? If and how do these sedimentary manifestations link to the early phase of the evolution of the Southern Ocean?
- When and how do sedimentary manifestations of a multi-layered ocean appear on the F/MP? When and how has sedimentation on the F/MP recorded the overspill of the Upper- and Lower Circumpolar Deep Water (UCDW and LCDW)?

-
- When and how do the Cenozoic sedimentary structures on the F/MP reveal the onset of the ACC and the transition to a modern ocean? Does it correlate with the tectonic development of the Southern Ocean, and if so, in what way?
 - According to the contouritic features on the F/MP, how have the characteristics, pathways, and intensities of the water masses flowing within the ACC varied during the Cenozoic?

Chapter 5-7 are dedicated to the relevant observations, results, and discussions approaching these questions. Chapter 8 concludes the findings.

CHAPTER 3. Technique, datasets, and analysis

3.1 Technique/ Reflection seismology

Reflection seismology is a branch of seismology for deep (a few kilometers) subsurface investigation which was first carried out in the early 1920s and was primarily aimed for the petroleum exploration and development. This active geophysical method is based on the principle of acoustic wave propagation, where a synthetic acoustic source produces and emits controlled, very short, high-energy pulses of sound. Acoustic waves propagate away from the source point into the surrounding environment until they get reflected as near-normal incidence at boundaries, traveling back to be recorded by the receivers. Raw seismic data are processed using complex data-processing steps to produce seismic sections, representing subsurface pseudo-images used for geological and structural studies. Reflection seismology has a wide range of application to land (on-shore) and marine (off-shore) studies and can vary in terms of the extent of survey activity from rather simpler 2D acquisition geometries to highly extensive 3D and 4D acquisition surveys. Some highlights on the principles, acquisition methodology, processing and interpretation of reflection seismology are brought here from principle bibliographic references (Aminzadeh and Dasgupta, 2013; Badley, 1985; Dondurur, 2018; Gadallah and Fisher, 2008; Kearey et al., 2002; Yilmaz, 1987).

3.1.1 Marine reflection seismics

Acquisition of marine seismic reflection data requires a compatible and synchronous function of multiple systems in real-time, including the source controller, the navigation and positioning units, the recording unit and the QC/processing unit. Seismic acquisition system uses complex navigation software systems which combine data from several navigation sources to derive reference positions for the vessel, source, receivers, etc. The seismic vessel runs at a nearly constant speed for (un)deployment of acquisition equipment and during data acquisition, to ensure measurements according to the designed survey parameters. A general setup for a 2D marine seismic survey is shown in Figure 3.1.

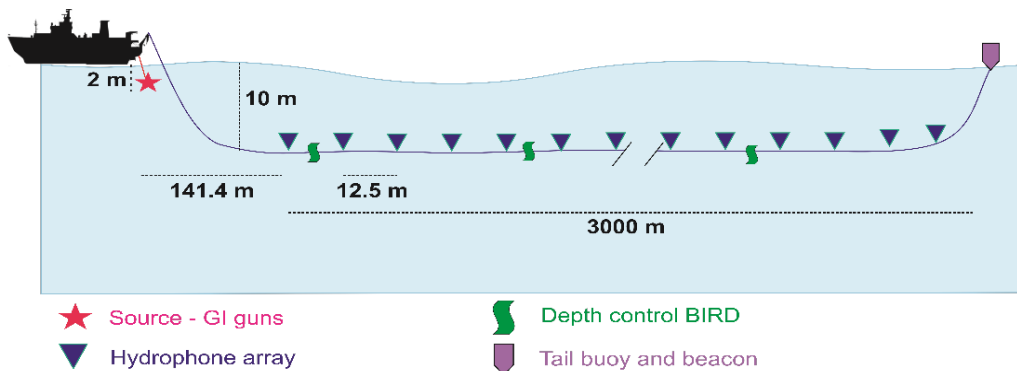


Figure 3.1: Schematic of marine seismic surveying.

A lead-in cable couples the streamer to the seismic vessel and ensures a constant tow distance. The streamer is a long (tens of meters to - kilometers) towed cable, within which hydrophones are located at regular spacing. Hydrophones are pressure sensors, made from piezoelectric elements, acting as receivers in marine seismology to detect the pressure variations in the water column and convert them into electric voltages being recorded as reflections. Streamers are towed ideally at a constant depth below the water surface to avoid sea-surface noises. This is done by implementing the remotely controlled buoyant objects, called birds, mounted at regular intervals onto the streamer. The streamer is also kept afloat at the end by a tail buoys, accommodating a Global Positioning System (GPS) transponder and a beacon. A single recording channel in marine surveys is the output of several adjacent hydrophones in order to improve the data quality. The seismic recording system receives and stores all seismic amplitudes from the streamer.

Airgun is the most common marine seismic energy source. It generates a high-amplitude positive acoustic signal through an abrupt discharge of high-pressurized air into the water. In practice, an array of airguns are used to improve the source signal. GI-guns (Generator/Injector-gun) have a specific configuration with two chambers, as the name implies, which work independently. GI-guns offer the advantage of preventing the collapse of the primary air bubble, hence minimizing the noise from the bubble burst as a secondary source.

3.1.2 Essentials of reflection seismology

As the acoustic waves propagate from the source, they vary continuously based on the properties of the surrounding medium, primarily relevant to the density and body waves (P-wave and S-wave) velocities; the latter being a function of elastic moduli in homogeneous and isotropic material. In terminology of the reflection seismics, acoustic impedance $Z = \text{density} * \text{velocity}$, is a measure of the medium's hardness. Seismic waves are reflected at acoustic impedance boundaries, referred to as seismic reflectors. The magnitude and polarity of acoustic energy which is reflected back at an acoustic impedance boundary is proportional to the reflection coefficient given by $R = \frac{Z_2 - Z_1}{Z_2 + Z_1}$, whereas the magnitude and polarity of the transmitted/refracted energy is defined by $T = 1 - R$.

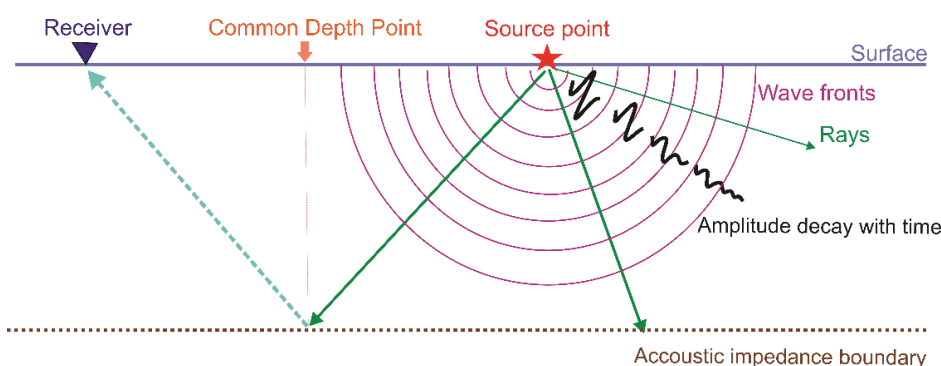


Figure 3.2: Propagation pattern and reflection elements.

In a homogeneous medium, the transmitted energy from the seismic source becomes distributed over a spherical area (radius r) as the propagation goes on. Therefore, the energy drops off to r^{-2} and the amplitude drops off to r^{-1} ; this is known as the effect of the geometrical spreading. Furthermore, during propagation, the amplitude of seismic waves gets lost by scattering and absorption; where shorter wavelengths are more attenuated than longer ones. A seismic source produces ideally a sharp spike signal with a wide frequency range. However, the source signal loses higher frequency waves as it travels through the earth, hence the source signal becomes ringy and low frequency in content.

In reflection seismology, the vertical resolution provides a sense of how close two acoustic impedance boundaries can be, while still being discerned separately on seismic sections. According to Sheriff and Geldart (1983), vertical resolution is proportional to $\frac{1}{8}$ to $\frac{1}{4}$ of the dominant wavelength (λ) of the source pulse. A measure of how closely two reflecting points can be next to each other, yet being identified as two separate points on seismic data is defined by the horizontal resolution. This is proportional to the width of the Fresnel Zone, the area of the acoustic impedance boundary impinged by the wavefront, which is given by $W = \sqrt{2Z\lambda}$, where Z and λ respectively represent depth and dominant wavelength of the source.

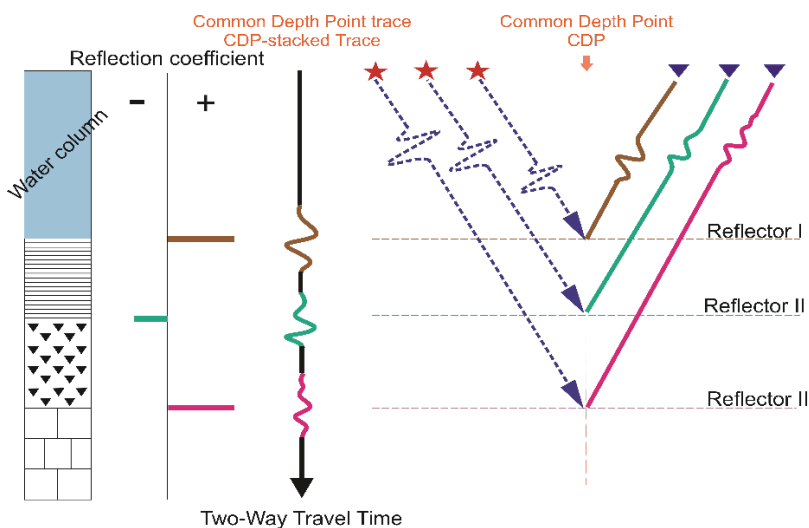


Figure 3.3: Convolution model in reflection seismology.

3.1.3 Propagation model in reflection seismology

Seismic reflection surveying records the two-way travel-time at an offset distance, which is a measure of the delay time to the reflector and the amplitude of the received waves which relates to the reflection coefficient. Seismic trace is the graphical representation of the response of the layered subsurface and recording system to a seismic pulse at a single receiver. Mathematically, a seismic trace is defined as the convolution of a reflection coefficient series in two-way travel-time domain (R_t) with a source wavelet (w_t), i.e. $y_t = w_t * R_t = \sum w_{t-\tau} R_{t-\tau}$. A collection of traces is called a seismogram; which could subsequently be resorted into shot-, receiver-, or common depth point (CDP)-gathers, respectively

representing the traces corresponding to one specific shot, receiver, or common depth point (CDP) (Figure 3.2 and 3.3). A CDP-gather include all traces which represent reflections from a certain reflection location from the subsurface; where the number of traces is termed fold. Via the stacking process, traces within a CDP-gather are summed-up linearly to produce a stacked trace, leading to an increased signal to noise ratio.

For the simple case of one reflection from a single acoustic impedance reflector in a homogeneous medium, the two-way travel-time is given by the length of the travel path to the medium velocity, i.e. $t = \frac{\sqrt{X^2+4Z^2}}{v}$. In reflection seismology, propagation models include several simplifying assumptions to allow for an analytical solution of the wave propagation. For zero offset from the source-point, meaning $X=0$, $t_0 = \frac{2Z}{v}$ is the two-way travel-time of a vertical ray path. The two-way travel-time equation could be rewritten as $t = t_0 \left(1 + \left(\frac{X}{v t_0}\right)^2\right)^{1/2}$, which using a binomial expansion for small offset/depth ratios, i.e. $(\frac{X}{Z} \ll 1)$, would give $t = t_0 + \frac{X^2}{2t_0 v^2}$. This time-distance equation for reflection is widely used in processing and interpretation. By definition, the normal moveout (NMO) at offset x is the difference in travel-time for the reflection received at offset X from the source and the zero offset, i.e. $\Delta T = t_X - t_0 = \frac{x^2}{2t_0 v^2}$. In a multi-layer model, the NMO for the n^{th} reflector is given by $\Delta T_n = \frac{x^2}{2t_0 V_{rms,n}^2}$, where $V_{rms,n}$ is the root-mean-square velocity of the media down to reflector n . $V_{rms,n}$ is defined by Dix (1955) as $V_{rms,n} = \sqrt{\frac{\sum_{i=1}^n V_i^2 \tau_i}{\sum_{i=1}^n \tau_i}}$; τ_i and V_i are respectively the one-way travel-time and interval velocity of layer i .

3.2 Datasets

3.2.1 High resolution 2D seismic reflection data from expedition MSM81

Thirty 2D high-resolution reflection seismic profiles (ca. 2 Terabyte of raw data) were acquired by the Alfred Wegener Institute (AWI) during February-March 2019 during cruise leg MSM81 (Figure 3.4) with the research vessel Maria s. Merian across the Falkland/Malvinas Plateau (F/MP) (Uenzelmann-Neben, 2019a). A total of ca. 5300 km of 2D seismic reflection data were collected, covering the eastern, central and southern sectors of the F/MP. The survey was designed to cross DSDP Leg 36 Sites 327,

329, 330 and Leg 71 Site 511 to enable correlation of seismic data with the boreholes. Figure 3.5 shows the location of the seismic profiles from cruise MSM81 along with DSDP boreholes. Table 3.1 summarizes the acquisition parameters and Table 3.2 includes the general information on the seismic profiles of survey MSM81. See appendix A for the intersection points of the 2D seismic profiles.

Figure 3.4: Logo of cruise leg MSM81 (Uenzelmann-Neben, 2019a).



Table 3.1: Survey and acquisition parameters (Uenzelmann-Neben, 2019a).

Acquisition Parameters		
Source specification	Air guns	4 GI-guns (4*2.4 l)
	Generator capacity	0.72 l (45 in ³)
	Injector capacity	1.68 l (105 in ³)
	Depth	2 m
	Offset from vessel	20 m
	Shot interval	25 m ~10 s
	Gun controller	Teledyne BigShot TM
Receiver specification	Hydrophone	Sercel Flexible Hydrophone (SFH)
	Lead-in	141.4 m
	Nominal capacity	32.5 nF ± 10% @ 20° C
	Nominal sensitivity	-192.9 dB ref to 1 V/µPa ± 1.5 dB (22.65 V/bar) @
	Active spread Length	3000 m
	Number of channels	240
	Hydrophone array spacing	12.5 m
	Number of active sections	20
	Cut-off frequency	2 Hz
	Groups per section	12
	Hydrophones per group	8
	Nominal streamer depth	10 m
Recording and navigation	Depth control system	Model 5010/5011 DigiBIRD TM & CompassBIRD TM
	Data format	SEGD
	Sample rate	1 ms
	Record length	9 s
	Dominant frequency	80 Hz
	Maximum frequency	500 Hz
	Navigation system	Sercel SeaPro Nav TM
	Coupling	Fiber-optic tow leader + deck lead 141.4 m
	Digitizer	Field Digitizing Unit (FDU2F) 24-Bit
	Onboard connection	Deck Cable Crossing Unit (DCXU)
	Communication & synchronization	Ethernet links / T0 signal

Table 3.2: 2D seismic profiles from survey MSM81.

Profile	Direction	Length (m)~	No. of CDPs	1 st CDP		Last CDP	
				Longitude	Latitude	Longitude	Latitude
AWI-20190001	SW-NE	371950	14879	52.45359	-50.49607	-50.63857	-46.04921
AWI-20190002	SE-NW	285325	11414	50.62089	-46.06997	-49.72722	-49.77379
AWI-20190003	NW-SE	385150	15407	-49.72499	-49.72976	-52.88898	-47.53786
AWI-20190004	SW-NE	234775	9392	-52.87340	-47.57948	50.83521	-46.76869
AWI-20190005	E-W	268975	10760	-50.87279	-46.75879	-50.90089	-50.56600
AWI-20190006	NW-SE	239625	9586	-50.92631	-50.55893	-52.87888	-49.15359
AWI-20190007	SW-NE	361225	14450	-52.86337	-49.17290	-49.77918	-47.62064
AWI-20190008	SSE- NNW	189700	7589	-49.80445	-47.63611	-51.36041	-46.60823
AWI-20190009	SE-NW	267450	10699	-51.3807	-46.6296	-50.3127	-50.0106
AWI-20190010	NNE-SSW	129200	5169	-50.3324	-50.0308	-51.4691	-50.3669
AWI-20190011	SE-NW	310675	12428	-51.5281	-50.3123	-52.8453	-46.3298
AWI-20190012	SW-NE	244425	9778	-52.8634	-46.3681	-50.9474	-44.7317
AWI-20190013	SW-NE	82675	3308	-50.9638	-44.7446	-50.358	-44.0862
AWI-20190014	WSW-ENE	204100	8165	-50.3349	-43.9886	-49.9099	-41.2588
AWI-20190015	WSW-ENE	67100	2685	-49.9188	-41.2351	-49.7632	-42.1182
AWI-20190016	NNE- SSW	67275	2692	-49.739	-42.123	-50.326	-42.1538
AWI-20190017	SSE-NNW	77925	3118	-50.3408	-42.122	-49.7407	-42.6463
AWI-20190018	NNE- SSW	59875	2396	-49.7294	-42.6101	-50.2163	-42.9207
AWI-20190019	SSE-NNW	62775	2512	-50.2183	-42.8865	-49.7468	-43.3431
AWI-20190020	NNE-SSW	76675	3068	-49.7327	-43.3199	-50.4081	-43.4429
AWI-20190021	SSE-NNW	89525	3582	-50.4123	-43.4143	-49.7016	-43.9686
AWI-20190022	NNE-SSW	110525	4422	-49.6893	-43.9425	-50.6571	-44.2044
AWI-20190023	SSE-NNW	117550	4703	-50.7141	-44.1590	-49.6970	-44.5231
AWI-20190024	NNE-SSW	120475	4820	-49.6881	-44.4916	-50.6919	-45.0692
AWI-20190025	SSE-NNW	122275	4892	-50.7338	-45.0541	-49.7348	-45.7203
AWI-20190026	NNE-SSW	175325	7014	-49.7037	-45.6808	-51.1091	-46.7270
AWI-20190027	SE-NW	65725	2630	-51.1226	-46.6916	-50.5495	-46.8881
AWI-20190028	SSW-NNE	91225	3650	-50.5603	-46.886	-49.7689	-46.5895
AWI-20190029	WNW-ESE	212450	8499	-49.7937	-46.6298	-49.9007	-43.7056
AWI-20190030	ENE-WSW	213300	8533	-49.8779	-43.6891	-50.1686	-46.6040

3.2.2 Scientific borehole data

Four boreholes were drilled as part of the Deep Sea Drilling Project (DSDP) Legs 36 and 71 on the easternmost sector of the Falkland/Malvinas Basin (F/MB), including Sites 327, 329, 330, and 511 (Shipboard_Scientific_Party, 1974a, c, d, 1980a). Seismic survey MSM81 was designed to cross these four boreholes (Figure 3.5b) (Uenzelmann-Neben, 2019a). Table 3.3 summarizes drilling information related to these boreholes, the lithologic information, the oldest drilled sediments, and the seismic profiles crossing the location of these DSDP Sites (see Figure 6.2)

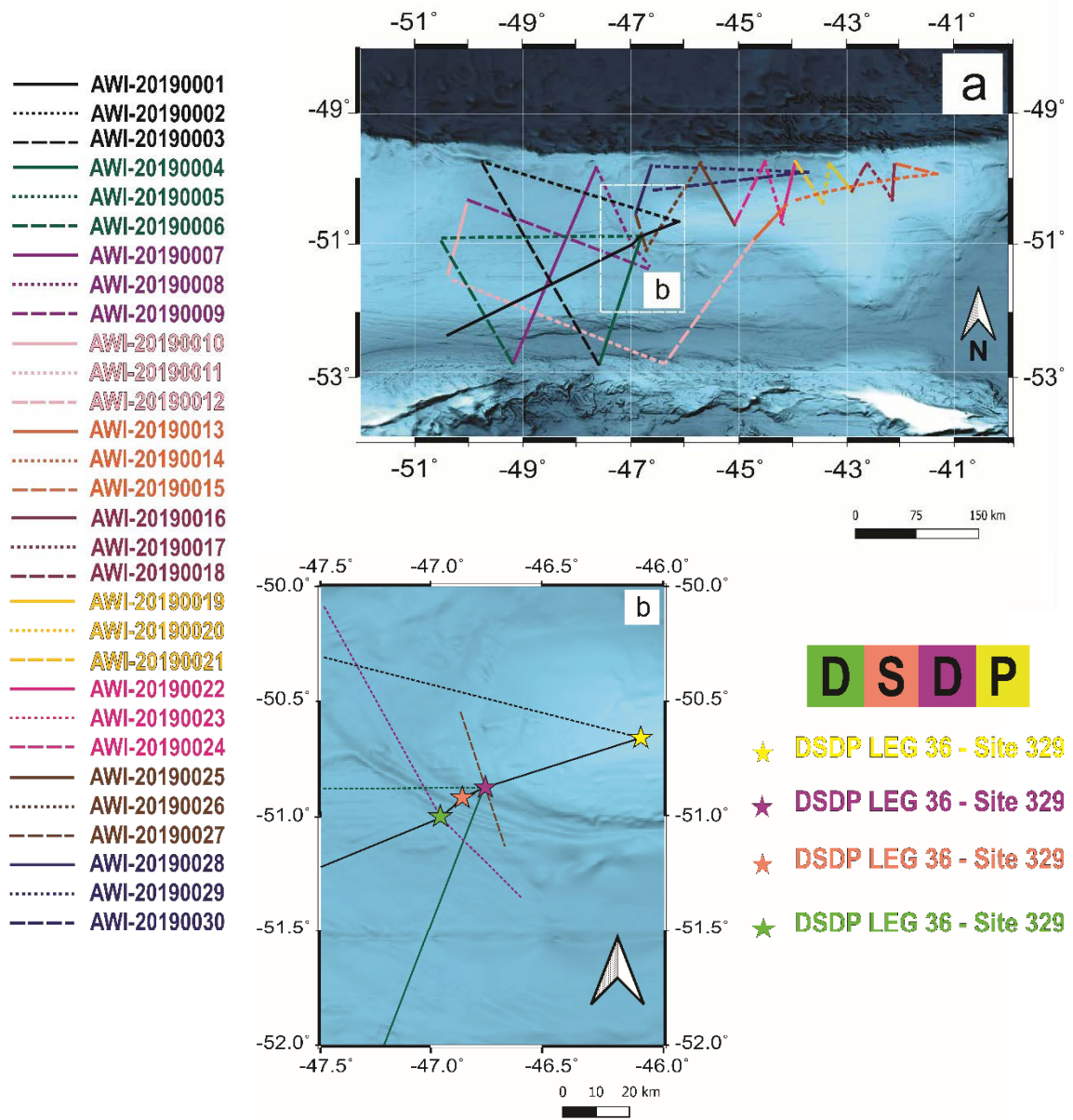


Figure 3.5: Bathymetric map of the Falkland/Malvinas Plateau in the Southern Ocean (Dorschel et al., 2022). (a). Lines show the location of the seismic profiles from survey MSM81. (b). Location of DSDP Leg 36 Sites 327, 329, 330 and Leg 71 Site 511, as well as the seismic lines crossing these drill sites (see Table 3.3 for details). Appendix A includes the information on the intersection points among the seismic profiles.

Table 3.3: Location and drilling information of DSDP Leg 36 Sites 327, 329, 330 and Leg 71 Site 511 (Shipboard_Scientific_Party, 1974a, c, d, 1980a), as well as the seismic lines crossing these drill sites (see Figure 6.2 for details).

LEG / Date	Site	Latitude Longitude	Water depth (m) / Total drilled depth below seafloor (mbsf)	Recovery rate (%) / Coring / No. lithological units / Oldest recovery	Available logs -Ex situ-	Crossing seismic profiles/CDP Number
36 / 1974	327	-50.8713 -46.7837	2400 469.5	50 Intermittent 8 Neocomian	Water Content Porosity	AWI-20190001 / 12589 AWI-20190004 / 9177 AWI-20190005 / 10 AWI-20190027 / 1124
	329	-50.6552 -46.0955	1519 464.5	69 Intermittent 6 Paleocene	Water Content Porosity Bulk Density Sonic Velocity	AWI-20190001 / 14757
	330	-50.9198 -46.8833	2626 575.5	53 Intermittent 7 Precambrian basement	Water Content Porosity Bulk Density Sonic Velocity	AWI-20190001 / 12230
71 / 1980	511	-51.0047 -46.9717	2589 632	61 Continuous 2 Late Jurassic	Water Content Porosity Bulk Density Sonic Velocity Vane Shear Strength Natural Gamma Ray Neutron Log	AWI-20190001 / 11776 AWI-20190008 / 5693

3.3 Analysis

3.3.1 Seismic data processing

A seismic section, which is the conventional product of reflection seismology, provides a meaningful image of the earth in time-domain, which can further be used for seismostratigraphic and structural interpretation. To produce such sections from raw seismic data of field recordings, several seismic processing sequences need to be implemented. No unique work-flow exists for processing of seismic data; the processing sequence needs to be adapted based on the needs of the project. Figure 3.6 presents the seismic processing flow applied to this work. As a result, chapter 12 includes all migrated sections for survey MSM81. Emerson E&P software (Paradigm-ECHOS) from Emerson Automation Solutions

was used for seismic processing and mapping in the scope of the Emerson Academic program. Table 3.4 summarizes the modules used in paradigm-ECHOS software along with the appointed parameters.

Besides acquisition design and surveying methodology, seismic data processing contributes significantly to improving the seismic signal (reflections from acoustic impedance boundaries) and attenuating random as well as systematic noise. Common-Depth-Point processing is the prevailing processing scheme for multi-channel seismic reflection imaging, aiming for signal improvement using signal processing methods.

The initiation stage in processing of seismic data included conversion of data from field format (SEGD) to internal format of the processing system ECHOSTTM. Source and receiver points and their geometrical relation were defined based on their distances and navigational data. This was followed by sorting the data from shot into CDP-gather with a designed bin size of 25 m. These flows were performed subsequent to data acquisition by the chief scientist Dr. Uenzelmann-Neben, onboard the Maria s. Merian (Uenzelmann-Neben, 2019a).

Multi-channel seismic reflection data provides information on velocity distribution along the seismic profiles vs. the time/depth axis. Semblance analysis or the velocity spectrum analysis is commonly used to extract velocity functions from multichannel seismic data. Semblance method is based on the correlation of traces within a CDP-gather and the goal is to find the proper velocity function for NMO-correction of the CDP-gather.

Table 3.4: Processing modules and parameters used from paradigm-ECHOS software for processing of the seismic data in this work. See appendix B for the parameter tests performed to reach the optimum processing parameters for each seismic sequence

Processing sequence	Module Echos ®2017, 2019	Final applied parameters
Geometry load	GEOMLD	Keyname: shot
Velocity analysis	VELDEF	Semblance method, At least every 50 CDP, Supergathers of 3-9 CDPs
Normal moveout	NMO	Second Order, no Stretching applied
Amplitude correction	GAIN, SPHDIV	T ² , Scalar Factor 1
CDP stacking	STACK, ITER	1 Iteration, 80% admitted Samples, Threshold 20, Power scaling
Migration	MIGFX	Tau:32, Dipmode:80, Min and Max frequency 5-250, velocity smoothing along CDP and time 0-0
Filter	FILTER	Bandpass, Hanning Taper, 5-30/200-250
Top mute	MUTE	On, 10 ms Ramp length Water column

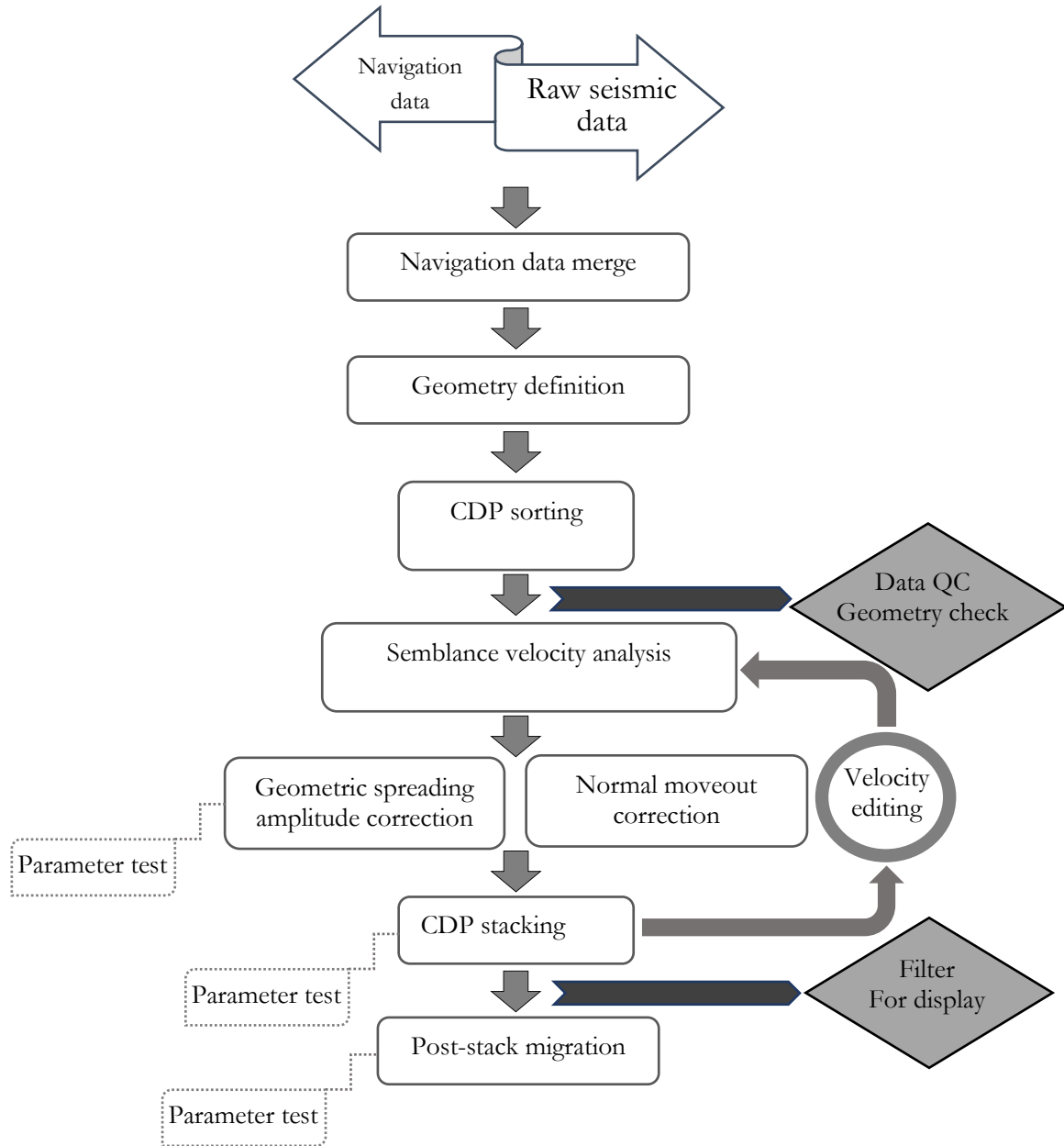


Figure 3.6: Flow chart of seismic data processing implemented in this work (For details see section 3.1.1. and Table 3.4).

The stacking velocity V_{st} is by definition the velocity value which produces the maximum amplitude of a reflection event, given by $t = t_0 \sqrt{1 + \left(\frac{x}{V_{st}t_0}\right)^2}$. For smaller source-receiver offsets compared to the reflector depth, stacking velocity approximates the Root Mean Square (RMS) velocity. The velocity spectrum is derived by calculating the NMO-corrections for narrow time-windows along the seismic trace using a velocity range and calculation of correlation among traces (semblance). Semblance contours are plotted, with X-axis showing velocity range and Z-axis showing the two-way travel-time (TWT) of the reflected events. The proper velocity is the one which gives the highest semblance value, these provide a velocity function for each CDP. In this work, after first round of velocity analysis, stacked sections were produced using velocities deviating $\pm 1\%$ and $\pm 2\%$ from the original picked

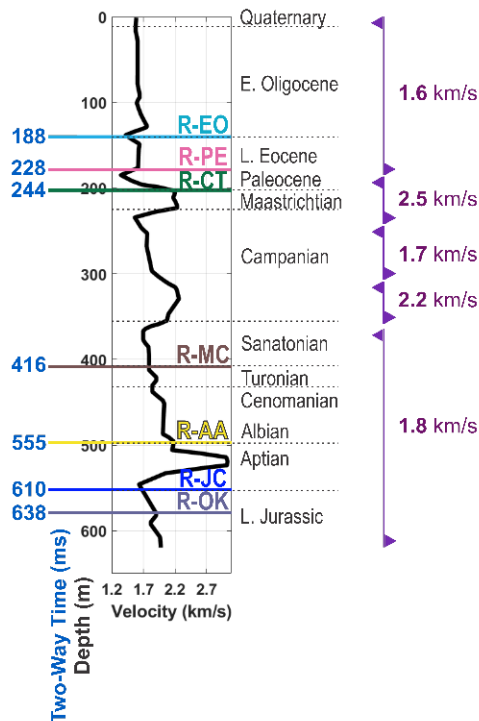
function. By comparing these stacked sections, the velocity functions were accordingly edited in subsequent rounds (if required) to reach an optimum result.

The physical properties of the media in which the seismic waves propagate on its way from the source to the receivers affect the seismic signal lead to absorption, scattering, and other phenomena, which causes the reduction in the amplitude. We aimed for an amplitude-preserved processing, therefore the amplitude recovery sequence was limited to accounting for the amplitude-decay due to spherical divergence. The energy contained in a unit of area is $\frac{E}{4\pi r^2}$ (r is the radius of the wave front). As the distance along a ray path increases, the energy that it contains falls off as r^2 . For a homogeneous and layered medium, this effect is accounted for by the gain function $g(t) = \frac{V_o^2(t)t}{V_o^2 t_0}$, where V_o is the reference velocity at time t_0 . However, to avoid overcorrection of amplitudes from multiple reflections, a velocity-independent scaling $g(t) = t^\alpha$ is preferred.

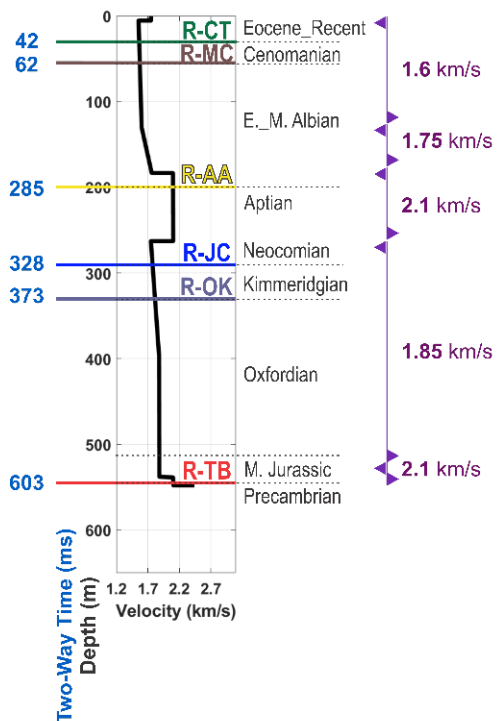
Simply put, the stacking process to calculate a stacked trace involves the sum-up and averaging of the NMO-corrected traces within a CDP-gather. The stacked section is then the display of these stacked traces side by side. In practice however, the classic averaging of all amplitudes for a sample is avoided due to the issue of noise imbedded in the seismic traces. Specific stacking methods such as partial stacking, median, trimmed, etc. are in practice tested and the one which best resolves the seismic events is implemented. Appendix B lists the parameter tests performed in this work to reach the optimum processing parameters for each seismic sequence. In trimmed stacking method, the amplitudes are sorted prior to the averaging and a certain percentage of the high- and low-amplitudes are ignored. The applied iterative stacking method is similar to the trimmed stacking, with the difference that the filtering of amplitudes is repeated in multiple iterations.

The ideal assumption of horizontal layering in reflection seismology is often not true in the subsurface. Migration processing strategies move reflections from dipping structure to their true subsurface positions. Migration methods differ in terms of the migration domains (i.e. pre-stack vs. post-stack and time vs. depth). The optimum migration strategy relies on the structural complexity of the area, the maximum dipping of the structures and the vertical and horizontal velocity variations in the present geological features. See chapter 4 in Yilmaz (1987) for an in-depth review of the seismic imaging and migration algorithms. The structures on the F/MP show smooth southwards dipping features (with gradients of up to 0.8 degrees), and no extensive horizontal velocity variation is seen on the seismic data, therefore a post-stack finite difference migration algorithm in time domain is applied. Finite-difference migration is based on the numerical solution of two-way wave equation in time/depth by finite-difference method. In a simple sense, the algorithm is in theory based on downward displacement of the recorded wavefield, where the receivers are moved in finite time/depth steps, while shortening the spread length (Claerbout and Doherty, 1972). Finite difference algorithms are sensitive to the time/depth step-size, as well as the implemented velocity models.

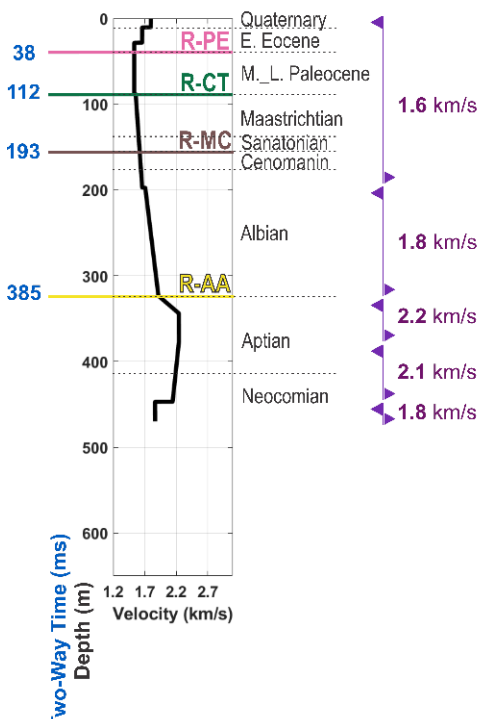
DSDP Site 511



DSDP Site 330



DSDP Site 327



DSDP Site 329

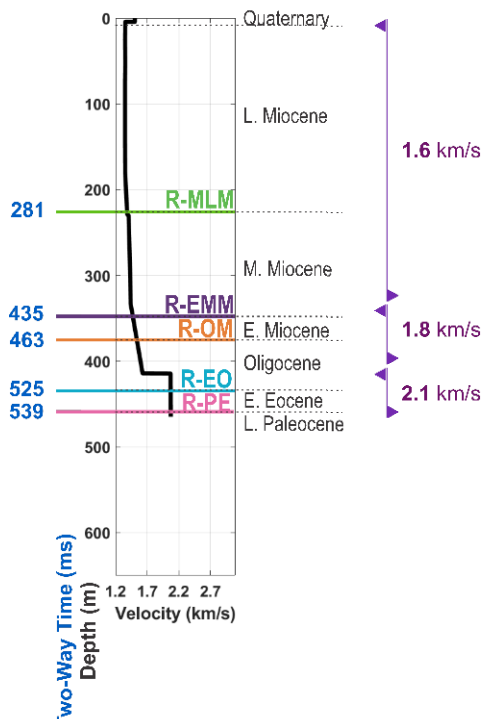


Figure 3.7: Velocity measurements on cores versus depth for DSDP Sites 327, 329, 330, and 511. The characteristic reflectors from the seismostratigraphic model are marked along with the calculated two-way traveltimes for these boundaries using the average interval velocities.

3.3.2 Qualitative and quantitative seismic interpretation

3.3.2.1 Borehole correlation and seismic stratigraphy

Borehole-seismic correlation or well-tie is an important part of seismic interpretation. DSDP boreholes on the F/MP were not logged, therefore the well-tie was established using the tops and times extracted from onboard velocity measurements. The reference datum for the seismic data was set to the mean sea-level and the stratigraphic and lithologic tops were converted from depth to time using average interval velocities, i.e. $V_{int} = \frac{z_2 - z_1}{t_2 - t_1}$. The velocity of water was set to 1500 m/s. Figure 3.7 shows the geological ages from drill holes, the onboard velocity measurements, the implemented average interval velocities for the well-tie, as well as the converted TWTs (see Figure 6.3 for the correlation with seismic data).

Seismic stratigraphy involves the analysis of seismic profiles based on the reflection units which correlate with lithologically-distinct depositional units. The principle of stratigraphic analysis is that the sedimentary strata of the same genesis generally appear as concordant strata, while showing discordance (angular unconformities) with over- and under-lying units. For description of our seismostratigraphic model, we adopted the terminology from Mitchum Jr et al. (1977), Vail et al. (1977), and Emery and Myers (2009) for different types of geological boundaries.

A seismic unit could be considered as the seismic representation of a depositional unit. Major seismic units can usually be correlated regionally. Once seismic units are distinguished on a seismic section, their reflection characteristics and internal structure could provide information at depositional conditions responsible for that unit. Internal bedforms within a seismic unit could form (sub)parallel, sigmoidal, oblique, hummocky or divergent reflection patterns (Sheriff, 1980). The seismostratigraphic structure defined across the F/MP is summarized in Figure 6.4 (see chapters 5 and 6 for detailed description of the model).

3.3.2.2 Interpretation

For the horizon tracking and interpretation, Paradigm EPOS software was used. In total, 12 reflectors were picked along the seismic profiles as far as the resolution allowed. Horizon tracking was set to start from the location of DSDP Sites on all crossing seismic profiles (Table 3.3). Horizon selection was based on the depth, TWT and assumed polarity primarily for the major unconformities which delineate the stratigraphic units at the top and bottom. The polarity of seismic sections was set to (SEG) normal, therefore it was expected that reflectors corresponding to an increased acoustic impedance should give a trough, whereas those representing decreased acoustic impedance give a peak (Veeken, 2006). For the horizon tracking, the focus was laid on tracing the characteristic reflections. To this end, the correlation polygon module in EPOS software was used, which enabled taking a snap of an outstanding reflector and moving it along the section for comparison of reflection characteristics. Intersecting

profiles were folded and tied in order to ensure tracking the same reflector along different profiles; this was done via the composite profile module of EPOS (intersections of the seismic profiles are shown in Appendix A).

3.3.2.3 Seismic attribute analysis

Seismic attributes are calculated from the original seismic data; these include mathematical manipulation of wave characteristics such as amplitude, frequency, phase, and velocity which continuously change during wave propagation in subsurface layers. Seismic attributes provide powerful tools to highlight specific geological and physical features of the subsurface. There are several categories of seismic attributes, each suitable for specific targets. For the Seismic attribute analysis, the open source version of OpendTect was used. The energy, instantaneous frequency, and the first envelope derivative attributes were calculated to investigate the origin of the cross-cutting reflectors on the F/MP (see chapter 6 for details). There, the main bibliography on this topic is as well presented.

3.3.3 Target features

3.3.3.1 Contourites

Contourites are associated with long-term action of abyssal contour currents. Contourite drifts are sedimentary features related to deposition by bottom currents, while moats and terraces are shaped by higher energy bottom currents. Co-occurring depositional and erosional features are common elements of contourite depositional systems. Contrary to turbidites, contourites are along-slope deposits. These sedimentary bodies have large-scale morphological expressions. Therefore, reflection seismology is able to image these features at the present sea-floor or buried beneath younger sedimentary strata.

Contourites are linked with persistent action of deep and bottom currents at geological time scales, hence their spatial (geographical) distribution as well as their temporal (in geological times) occurrence contributes to understanding the (palaeo)oceanographic settings. Chapters 5 and 7 studies the contouritic features and argues how these could be interpreted in terms of palaeoceanographic evolution in the southwestern South Atlantic subsequent to the opening of the Southern Ocean gateways. There, the main bibliography on this topic is as well presented.

3.3.3.2 Cross-cutting reflectors

Discordant reflectors which cross-cut the host strata are known to be associated with post-depositional/secondary processes in sedimentary basins. Two most well-known origins of cross-cutting reflectors are Gas-Hydrates (GH) and diagenesis; these are functions of temperature and pressure which are known to be depth-dependent. Hence, their resulting reflectors are usually linked with the Bottom simulating reflectors (BSRs), which geometrically replicate the seafloor. Reflection seismology is capable of distinguishing between gas-hydrate BSRs (GH-BSR) and diagenetic BSRs by means of

seismic diagnostic criteria such as reflection polarity, seismic velocity and frequency content. Identification of the origin of the cross-cutting reflectors and the processes leading to their genesis contributes to delineating the evolutional history of the sedimentary basins. Chapter 6 discusses how reflection seismology allows for differentiating between a GH-BSR and a diagenetic BSR and how this applies to understanding palaeo-environmental conditions within a basin. There, the main bibliography on this topic is as well presented.

3.3.3.3 Structural features

Reflection seismology is a powerful tool -taking the limits of the seismic resolution into account- for the structural analysis, that contributes to the study of the processes creating the sedimentary basins or deforming the basin's sedimentary infill (Misra and Mukherjee, 2018). The deformational structures such as folds and faults exist at all scales and are associated with various geological processes. In general, structural features can be categorized as those linked with extensional, compressional, and shear stress regimes or those resulting from magma intrusions, salt – or shale diapirs. Nanda (2021) provides a complete, yet concise review of the structural deformations which results in modifications of original sedimentary depositions. In chapter 6, examples of differential compaction folding and polygonal faults linked with extensional systems are presented and their significance with respect to the diagenetic processes are highlighted. There, the main bibliography on this topic is as well presented. Chapter 7 looks into the deformational folds and reactivated normal faults and discusses their origin with respect to the regional Cenozoic compressional tectonic system. There, the main bibliography on this topic is as well presented.

Appendices

Appendix A: Intersections of seismic profiles.

Seismic Profile	@ CDP	Seismic Profile	@ CDP	Longitude	Latitude
AWI-20190001	6711	AWI-20190003	9277	-51.6366	-48.4494
AWI-20190001	12542	AWI-20190004	9214	-50.8739	-46.7835
AWI-20190001	12549	AWI-20190005	65	-50.8731	-46.7813
AWI-20190001	2662	AWI-20190006	5968	-52.1336	-49.6752
AWI-20190001	6361	AWI-20190007	5551	-51.6801	-48.5543
AWI-20190001	11735	AWI-20190008	5702	-51.0043	-46.9671
AWI-20190001	10436	AWI-20190009	2233	-51.1694	-47.3463
AWI-20190001	4336	AWI-20190011	3658	-51.9295	-49.165
AWI-20190001	13543	AWI-20190026	5342	-50.7734	-46.4682
AWI-20190001	12548	AWI-20190027	1150	-50.8732	-46.7817
AWI-20190002	11245	AWI-20190003	79	-49.7411	-49.7194
AWI-20190002	5400	AWI-20190007	12382	-50.2211	-47.8317
AWI-20190002	3886	AWI-20190008	2571	-50.3463	-47.3407
AWI-20190002	796	AWI-20190026	4452	-50.5947	-46.3315
AWI-20190002	2408	AWI-20190028	433	-50.4663	-46.8592
AWI-20190003	15204	AWI-20190004	119	-52.8477	-47.5689
AWI-20190003	5624	AWI-20190005	6247	-50.8861	-48.9669
AWI-20190003	8943	AWI-20190007	6075	-51.5682	-48.4973
AWI-20190003	4171	AWI-20190009	8005	-50.5867	-49.1679
AWI-20190003	12615	AWI-20190011	7403	-52.3198	-47.9598
AWI-20190004	9217	AWI-20190005	70	-50.8732	-46.7832
AWI-20190004	8169	AWI-20190008	6212	-51.1007	-46.8708
AWI-20190004	7279	AWI-20190009	978	-51.2939	-46.9458
AWI-20190004	1739	AWI-20190011	9065	-52.4963	-47.4246
AWI-20190004	9227	AWI-20190027	1160	-50.871	-46.7824
AWI-20190005	3954	AWI-20190007	9270	-50.8861	-48.1557
AWI-20190005	807	AWI-20190008	5091	-50.8769	-47.0433
AWI-20190005	4174	AWI-20190009	5036	-50.8863	-48.2335
AWI-20190005	9685	AWI-20190010	2574	-50.8987	-50.1849
AWI-20190005	65	AWI-20190027	1150	-50.8731	-46.7814
AWI-20190006	9479	AWI-20190007	32	-52.8569	-49.1693
AWI-20190006	1607	AWI-20190010	4100	-51.2342	-50.2914
AWI-20190006	3622	AWI-20190011	1019	-51.6486	-50.0037
AWI-20190007	14317	AWI-20190008	18	-49.8076	-47.6341
AWI-20190007	9167	AWI-20190009	4824	-50.9081	-48.1667

AWI-20190007	3750	AWI-20190011	4946	-52.0642	-48.7517
AWI-20190011	12264	AWI-20190012	181	-50.2464	-47.8438
AWI-20190013	2543	AWI-20190023	1012	-50.4981	-44.2377
AWI-20190013	3075	AWI-20190022	3252	-50.4007	-44.1322
AWI-20190014	8059	AWI-20190015	187	-49.9136	-41.2947
AWI-20190014	5619	AWI-20190016	1198	-49.9952	-42.1231
AWI-20190014	4832	AWI-20190017	1600	-50.033	-42.3874
AWI-20190014	3433	AWI-20190018	1882	-50.105	-42.8567
AWI-20190014	3095	AWI-20190019	499	-50.1236	-42.9698
AWI-20190014	1823	AWI-20190020	2100	-50.195	-43.3953
AWI-20190014	1344	AWI-20190021	907	-50.2321	-43.5508
AWI-20190015	2642	AWI-20190016	161	-49.7658	-42.104
AWI-20190016	2555	AWI-20190017	232	-50.2957	-42.151
AWI-20190017	2990	AWI-20190018	185	-49.7654	-42.6246
AWI-20190018	2262	AWI-20190019	151	-50.1884	-42.9046
AWI-20190019	2368	AWI-20190020	191	-49.7738	-43.3166
AWI-20190020	2921	AWI-20190021	179	-50.3758	-43.4354
AWI-20190021	2599	AWI-20190029	8177	-49.9001	-43.8136
AWI-20190021	2582	AWI-20190030	380	-49.8968	-43.8163
AWI-20190021	3436	AWI-20190022	192	-49.7306	-43.9461
AWI-20190022	4247	AWI-20190023	455	-50.6188	-44.1936
AWI-20190022	921	AWI-20190029	7871	-49.8902	-43.9901
AWI-20190022	1053	AWI-20190030	922	-49.9191	-43.9981
AWI-20190023	4507	AWI-20190024	250	-49.7396	-44.5083
AWI-20190023	3900	AWI-20190029	8299	-49.8714	-44.462
AWI-20190023	3480	AWI-20190030	2190	-49.9626	-44.4299
AWI-20190024	4812	AWI-20190025	214	-50.6902	-45.0682
AWI-20190024	858	AWI-20190029	5950	-49.8664	-44.5817
AWI-20190024	1422	AWI-20190030	2835	-49.9839	-44.6502
AWI-20190025	4757	AWI-20190026	305	-49.7623	-45.7013
AWI-20190025	4412	AWI-20190029	2839	-49.8325	-45.6527
AWI-20190025	3277	AWI-20190030	5297	-50.0637	-45.4929
AWI-20190026	6857	AWI-20190027	208	-51.0776	-46.7025
AWI-20190026	637	AWI-20190029	2553	-49.8289	-45.7513
AWI-20190026	2036	AWI-20190030	8889	-50.1095	-45.9632
AWI-20190027	2617	AWI-20190028	37	-50.5523	-46.8872
AWI-20190028	433	AWI-20190002	2408	-50.4662	-46.8592
AWI-20190028	3529	AWI-20190029	89	-49.7951	-46.5994
AWI-20190029	8253	AWI-20190030	311	-49.8977	-43.7902

Appendix B: Parameter testing

Sequence	Method	Parameter Echos®2017 & 2019	Values
Amplitude correction	Spherical divergence	Domain	CDP, Stack
		Power function	T^2 , VT^2 , V^2T , V^2T^2
		Scalar factor	0.2, 0.5, 1
Stacking	Median stacking	Scaling method	Average, Norm
	Alpha-trimmed mean stacking	Trim rate (%)	20, 30, 40
		Scaling method	Power
		Min. Number of samples	1
	Iterative stacking	Max Number of samples	Max Number of Traces
		Rate (%)	50, 60, 80
		Number of iterations	1, 2, 3, 4
		Threshold level	20, 15, 10, 5
	Coherency-weighted stacking	Scaling method	Power
		Coherency window	250, 500, 1000
		Stabilizing exponent	1
Post-stack migration	F-X Migration	Stacking method	Mean, Median
		CDP bin size (m)	25
		Frequency range (Hz)	5-250
		Velocity smoothing	Along CDPs: 0, 5, 10, 25, 50 Along Time (ms): 0, 150, 300, 500
		Max. optimization angle	65, 80, 87, 90
		Step size (Tau)	20, 22, 24, 26, 32

CHAPTER 4. Contributions to scientific journals

In the framework of this dissertation, three scientific articles were prepared as summarized in this chapter in a chronological order.

4.1 Footprints of palaeocurrents in sedimentary sequences of the Cenozoic across the Maurice Ewing Bank

Authors: Banafsheh Najjarifarizhendi, Gabriele Uenzelmann-Neben
Affiliation: Alfred Wegener Institute, Helmholtz Centre for Polar and Marine Research, Bremerhaven, Germany
Journal: Marine Geology
Status: Published on 26th May 2021, doi: 10.1016/j.margeo.2021.106525

The paper (see chapter 5) presents new 2D seismic reflection data from 2019 RV Maria S. Merian cruise MSM81 across the Maurice Ewing Bank (MEB). A seismostratigraphic-age model is built with integration of borehole data from Deep Sea Drilling Project (DSDP) Leg 36, Sites 327, 329, and 330 and Leg 71 Site 511. Indications for current-related erosion and sedimentation are investigated within the seismic (sub)units across this bathymetric high. The temporal and the spatial distribution of the contouritic features are discussed with respect to the tectonic development of the southwestern South Atlantic. The onset of a modern circulation and the evolution of deep and abyssal water masses flowing within the Antarctic Circumpolar Current (ACC) are discussed in response to regional Cenozoic tectonic and climatic events.

The author was responsible for the processing and interpretation of 2D seismic data from cruise MSM81, conceptualization of the article, writing the paper and preparing the illustrations. The co-author, Dr. Uenzelmann-Neben, acquired funding for and led the 2019 cruise MSM81, acquired funding for and supervised the scientific work, and contributed to the manuscript by conceptualization as well as editing the text.

4.2 Fossilized silica diagenetic fronts: Implications for palaeoceanographic evolution across the Falkland/Malvinas plateau

Authors: Banafsheh Najjarifarizhendi, Gabriele Uenzelmann-Neben
Affiliation: Alfred Wegener Institute, Helmholtz Centre for Polar and Marine Research, Bremerhaven, Germany
Journal: Marine and Petroleum Geology
Status: Published on 19th November 2022, doi: 10.1016/j.marpetgeo.2022.106035

The paper (see chapter 6) presents new 2D seismic reflection data from 2019 RV Maria S. Merian cruise MSM81 across the Falkland/Malvinas Basin (F/MB) and Falkland/Malvinas Trough (F/MT). The study investigates two cross-cutting reflectors in the study area. Using their seismic characteristics, these reflectors are argued to be associated with silica diagenetic fronts. The geometrical and structural features accompanied by these discordant reflectors are discussed to link with the fossilization/arrest of the upward advancement of the Opal-A to Opal-CT transition zone. The presumed timing and plausible scenarios for the cessation of the silica diagenesis are discussed in response to the palaeoceanographic evolution in the southwestern South Atlantic.

The author was responsible for the processing and interpretation of 2D seismic data from cruise MSM81, conceptualization of the article, writing the paper and preparing the illustrations. The co-author, Dr. Uenzelmann-Neben, acquired funding for and led the 2019 cruise MSM81, acquired funding for and supervised the scientific work, and contributed to the manuscript by conceptualization as well as editing the text.

4.3 Falkland/Malvinas Trough: Indications for Cenozoic tectonic and oceanographic evolution in the southwestern South Atlantic

Authors: Banafsheh Najjarifarizhendi, Gabriele Uenzelmann-Neben, Jens Gruetzner

Affiliation: Alfred Wegener Institute, Helmholtz Centre for Polar and Marine Research, Bremerhaven, Germany

Status: To be submitted to Geochemistry, Geophysics, Geosystems (G3)

The paper (see chapter 7) presents new 2D seismic reflection data from 2019 RV Maria S. Merian cruise MSM81 across the F/MT. There, the Cenozoic sedimentary fill is investigated for evidences of the tectonics of the opening of the Drake-Passage-Scotia Sea zone. Furthermore, the current-controlled sedimentary features in this bathymetric depression are described and examined with respect to the Cenozoic oceanographic development of the southwestern South Atlantic. The onset and evolution of the abyssal circulation are discussed in response to the tectonic and climatic events of the southwestern South Atlantic.

The author was responsible for the processing and interpretation of 2D seismic data from cruise MSM81, conceptualization of the article, writing the paper and preparing the illustrations. The co-author, Dr. Uenzelmann-Neben, acquired funding for and led the 2019 cruise MSM81, acquired funding for and supervised the scientific work, and contributed to the manuscript by conceptualization as well as editing the text. Dr. Gruetzner provided a thorough review of the findings and offered valuable insights and suggestions to enhance the manuscript.

CHAPTER 5. Footprints of palaeocurrents in sedimentary sequences of the Cenozoic across the Maurice Ewing Bank

Najjarifarizhendi, Banafsheh*; Uenzelmann-Neben, Gabriele

Alfred Wegener Institute, Helmholtz Centre for Polar and Marine Research, Am Alten Hafen 26, 27568 Bremerhaven, Germany

- The formatting has been adapted to the dissertation and differs slightly from the publication.

5.1 Abstract

High-resolution seismic reflection data across the Maurice Ewing Bank, the easternmost section of the Falkland/Malvinas Plateau in the SW South Atlantic, is integrated with information from Deep Sea Drilling Project Leg 36, Sites 327, 329, and 330 and Leg 71 Site 511. Five seismic units were identified ranging in age from the middle Jurassic to Quaternary and are interpreted with respect to the evolution of the oceanic circulation in the Atlantic sector of the Southern Ocean in response to tectonic and climatic events. Sedimentary sequences of late Cretaceous and early Paleogene include little and restricted evidence of current activity, attributable to shallow/intermediate-depth connections between the developing South Atlantic and the Southern Ocean. In contrast, sedimentary sequences of the late Eocene/Oligocene and Neogene reveal a history of strong current-related erosion and deposition. These features are identified in specific water-depth ranges and interpreted to document proto-Upper and -Lower Circumpolar Deep Waters to have shaped the bank since the Oligocene. The Maurice Ewing Bank bathymetric high thus has been acting as a barrier for the deep and bottom water masses flowing within the Antarctic Circumpolar Current since its establishment at the Eocene-Oligocene boundary. This study provides evidence for a multi-layered ocean already in the Paleocene/early Eocene.

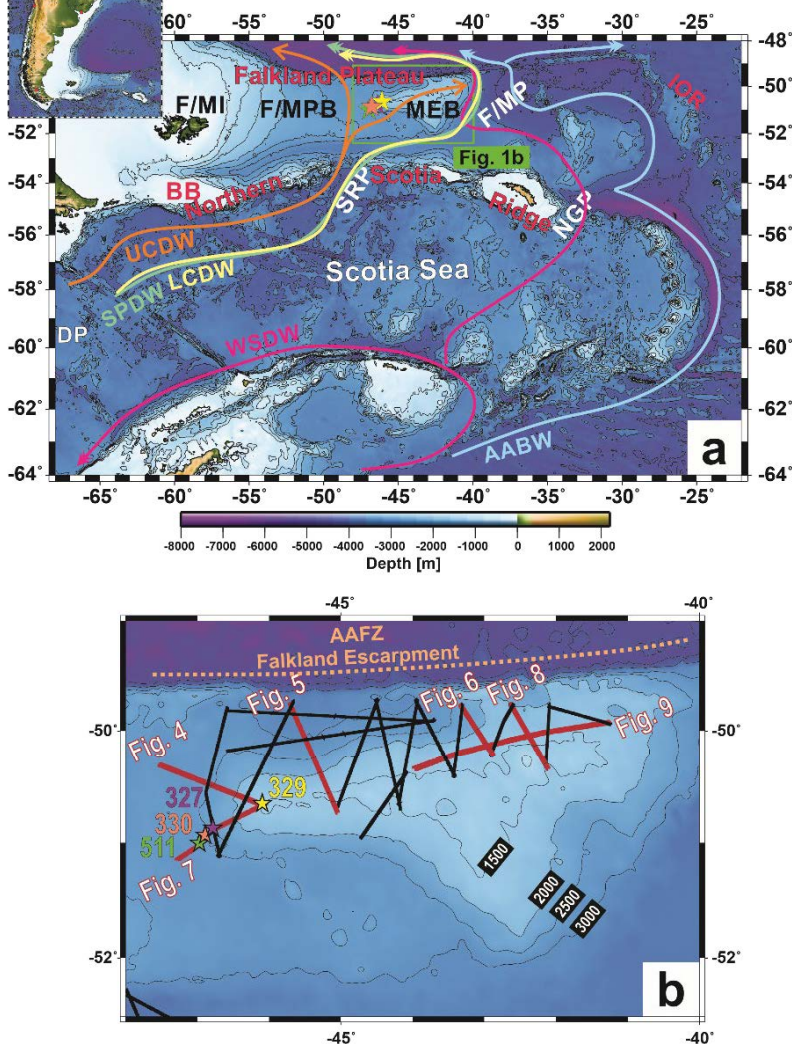
5.2 Introduction

In the present oceanic regime, the western South Atlantic forms a crucial gateway for the exchange of water masses between the Southern Ocean, South Pacific, and the South Atlantic; where the circulation is controlled by the complex topography of the Drake Passage and the Scotia Sea (Figure 5.1a). As a pronounced bathymetric high, the Maurice Ewing Bank (MEB), the easternmost extremity of the Falkland/Malvinas Plateau (F/MP), steers the deep and bottom water masses flowing within the Antarctic Circumpolar Current (ACC). On their journey around the bathymetric obstacles, the oceanic currents undergo acceleration and disruption, leaving behind erosional and depositional features. The so-called contourite drifts form an archive of pathways and intensities of the palaeocirculation, which

are in turn controlled by tectonic movements and climate modifications (Rebesco et al., 2007; Rebesco et al., 2014; Stow et al., 2002). Seismic reflection imaging allows studying of the modifications of the palaeocurrents' pathways and intensification through interpretation of the spatial distribution, morphological and structural characteristics of observed contourite drifts.

So far, the area south and east of the Falkland/Malvinas Islands (F/MI) and further west towards South America has been the subject of a number of studies (Koenitz et al., 2008; Nicholson and Stow, 2019; Pérez et al., 2015), but the available seismic reflection data across the MEB is sparse and yet low-resolution (Ciesielski and Weaver, 1980; Shipboard_Scientific_Party, 1977). So, little is known about the location and re-location of the water masses flowing within the ACC in the southwestern South Atlantic since the onset of Antarctica's glaciation at the Eocene-Oligocene boundary, which in turn has had a significant influence on climate.

Figure 5.1: (a) Bathymetric map of the Falkland/Malvinas Plateau and western South Atlantic sector of the Southern Ocean (Smith and Sandwell, 1997). Arrows schematically show the pathways of the southern-sourced deep/bottom water masses in the present oceanic scheme (Arhan et al., 1999; Arhan et al., 2002; Orsi et al., 1999; Shipboard_Scientific_Party, 1980a): Upper Circumpolar Deep Water (UCDW) in orange, Lower Circumpolar Deep Water (LCDW) in yellow, South Pacific Deep Water (SPDW) in green, Weddell Sea Deep Water (WSDW) in pink, and Antarctic Bottom Water (AABW) in blue. BB = Burdwood Bank; DP = Drake Passage; FI = Falkland Islands; FP = Falkland Passage; FPB = Falkland Plateau Basin; IOR = Islas Orcadas Rise; MEB = Maurice Ewing Bank; NGP = North Georgia Passage; SRP = Shag Rocks Passage. The green box indicates the study area shown in Figure 5.1b, and stars show the location of DSDP Sites in the study area. (b) Bathymetric map of the Maurice Ewing Bank (Smith and Sandwell, 1997). Superimposed are the locations of the seismic profiles used for the study. Dark red lines illustrate the location of profiles shown in the figures. Stars mark the location of DSDP Leg 36 Sites 327, 329, and 330 and Leg 71, Site 511 in the study area. The dotted line represents the location of the Agulhas-Falkland Fracture Zone (AFFZ).



We present newly collected high-resolution multichannel seismic reflection data across the MEB, acquired during RV *Maria S. Merian* expedition MSM81 in early 2019, including a direct crossing of the Deep Sea Drilling Project (DSDP) Leg 36 Sites 327, 329, and 330 and Leg 71 Site 511 (Figure 5.1b). Drilling data from DSDP boreholes are incorporated into the study to transfer the chronostratigraphic model into a seismostratigraphic model used for a qualitative seismic interpretation across the bank. The geometry of the identified current-related depositional and erosional features observed on the seismic profiles are mapped and translated into spatiotemporal variations of the palaeocurrents. We identify and interpret depositional and erosional features across the MEB in pursuit of understanding the evolution of the regional oceanic settings in response to tectonic and climatic events.

5.3 Geological and oceanographic background

The F/MP can be subdivided into three distinct provinces of the F/MI, the F/MB, and the MEB (e.g., Lorenzo and Mutter, 1988; Shipboard_Scientific_Party, 1974a, c, d, 1980a). The MEB constitutes the morphostructural elevated easternmost part of the plateau, located on the westernmost part of the Agulhas-Falkland Fracture zone in the southwestern Atlantic Ocean (Figure 5.1b). The MEB rises about 1500 m above the surrounding seafloor and has formed a barrier for the oceanic circulation since the separation of South America and Africa.

Although drilling into the gneissose and granitic basement at DSDP Leg 36 Site 330 on the western shoulder of the MEB, the area between the MEB and the Falkland/Malvinas Basin (F/MB), has attested to the continental origin of this part (Shipboard_Scientific_Party, 1974d), there remains ambiguity as to the nature of the plateau's underlying crust. Three prevailing schemes exist for the paleogeography of the F/MI microplate prior to the Gondwana breakup. The first explains the present location with a clockwise rotation from its origin southeast of South Africa and drift along the transform faults (e.g., Eagles and Eisermann, 2020; Marshall, 1994; Stone et al., 2009; Taylor and Shaw, 1989; Thomson, 1998). The second suggests a paleo-location between South America and South Africa (Du Toit, 1927; Du Toit, 1937), while the third concludes that the plateau has been a rigid part of the South American plate (Barker, 2001b; Borrello, 1963; Chemale Jr et al., 2018; Ramos et al., 2017).

DSDP drillings on the western shoulder of the MEB shed light on the sedimentation history on the F/MP, which includes a primary phase of shallow-water marine setting mainly in the Mesozoic and a second phase of pelagic sedimentation predominantly in the Cenozoic (Timofeev et al., 1980). Following a marine transgression, deposition took place in the middle to late Jurassic in an open shelf environment. Sapropelic claystone of the late Jurassic (mainly Oxfordian) through the Aptian gives evidence for the development under euxinic conditions in a restricted basin subject to sluggish oceanic circulations (Dummann, Steinig, et al., 2020; Shipboard_Scientific_Party, 1977). Rapid subsidence gave way to open marine conditions starting in Albian and going on through the late Cretaceous and Paleocene (Barker, 1977b; Ludwig, 1983; Shipboard_Scientific_Party, 1974a, d, 1980a; Thompson,

1977). This transition may have resulted from abyssal connections between the Indian and the developing South Atlantic oceans (Barker, 1977b; Dingle and Robson, 1992; Dummann, Steinig, et al., 2020; Ludwig, 1983; Shipboard_Scientific_Party, 1974a, d, 1980a).

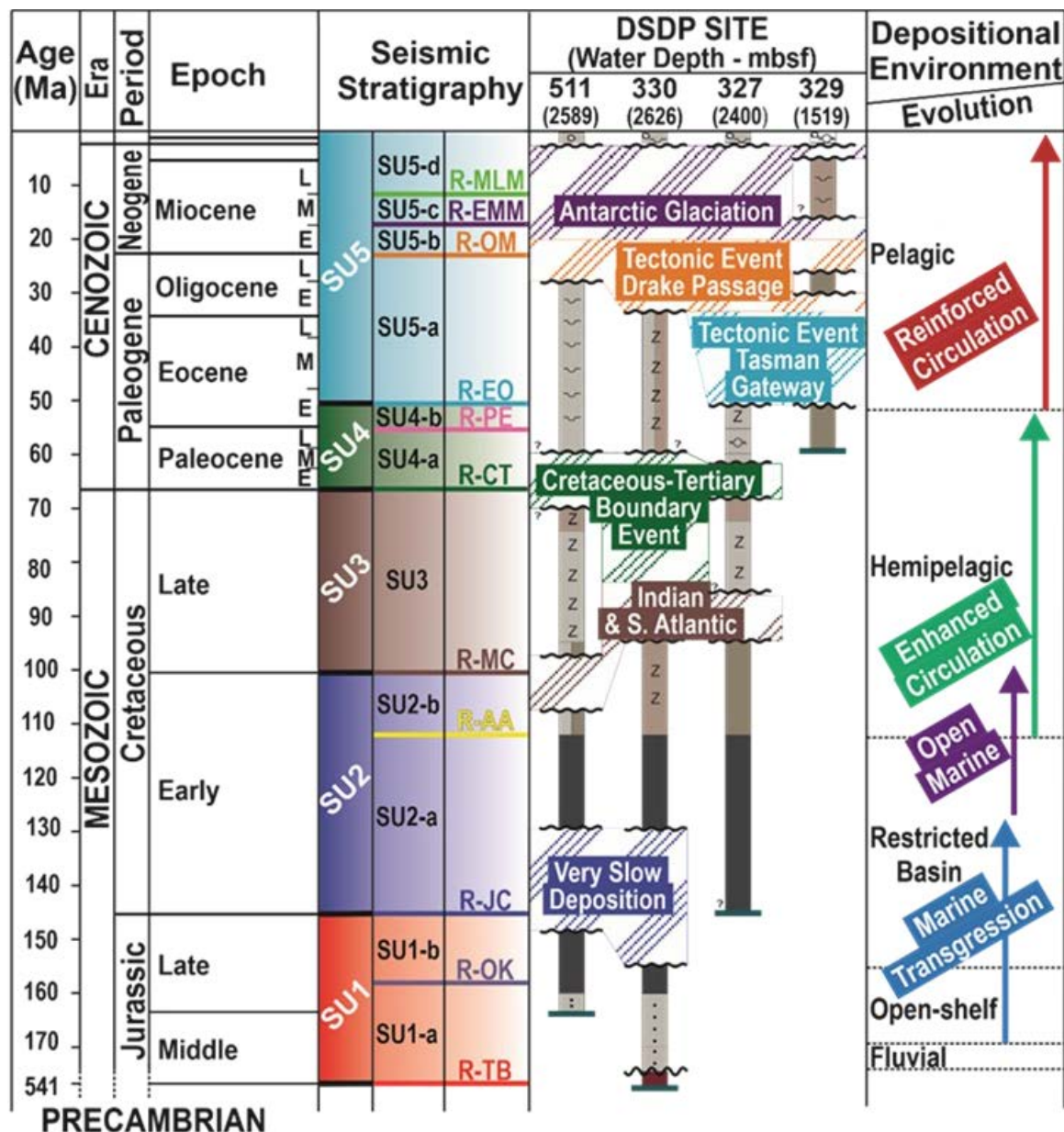


Figure 5.2: Outline of DSDP Leg 36 Sites 327, 329, and 330 and Leg 71, Site 511 in the study area (Shipboard_Scientific_Party, 1974a, c, d, 1980a). Schematically shown are the lithological units and hiatuses (and the attributable geological event) reported at each Site against the geological ages for the total drill depths. The rightmost column summarizes the depositional environment and the evolutional history recorded at DSDP Sites. The marker horizons and seismic units defined in the seismostratigraphic model are also color marked (for more details, refer to Table 5.1 and Section 5.5).

A major non-depositional to erosional hiatus across the late Cretaceous to Paleocene, known as the Cretaceous-Tertiary boundary event, is considered to be the product of a poor-carbonate ocean and a shallow Carbonate Compensation Depth (CCD) (Ciesielski and Wise Jr, 1977; Shipboard_Scientific_Party, 1974a, 1977; Worsley, 1974) as well as the arising changes in the bottom

circulation patterns (Barker, 1977b; Lorenzo and Mutter, 1988; Ludwig, 1983; Shipboard_Scientific_Party, 1977). Moreover, at this boundary abrupt biotic changes and a brief earliest Paleocene cooling have been associated with the Chixulub meteorite impact (Brett, 1992; Gulick et al., 2008; Schulte et al., 2010).

Reinforced bottom currents and higher productivity were the leading agents for the post-Eocene sediment accumulation on the MEB (Shipboard_Scientific_Party, 1974c, 1977). An early to middle Eocene hiatus is assumed to be a consequence of the distant tectonic event of the separation of East Antarctica and Australia (Tasman Gateway), which contributed to the development of a circumpolar current pathway (Shipboard_Scientific_Party, 1974c). A sudden surge in the bottom currents across the Eocene-Oligocene boundary subsequent to the regional tectonic evolution leading to the opening of the Drake Passage is accounted for the significant scouring and sediment removals throughout the Neogene (e.g., Barker, 1977b; Barker and Thomas, 2004; Ciesielski and Wise Jr, 1977; Nicholson and Stow, 2019; Scher and Martin, 2006a; Shipboard_Scientific_Party, 1974a, c, d, 1980a; Uenzelmann-Neben et al., 2017).

Reorganization of the oceanic currents and the establishment of the ACC following the opening of the Southern Ocean gateways prompted the vast glaciation of the Antarctic continent (Ciesielski and Wise Jr, 1977; Katz et al., 2011; Scher et al., 2015). This in turn led to increased Antarctic Bottom Water (AABW) production beneath the expanding Antarctic ice-shelves (Ciesielski and Weaver, 1980). Vigorous deep and bottom water circulation resulted in the most severe erosional event observed in the late Miocene and contributed to the complex erosional history of the MEB (Shipboard_Scientific_Party, 1974a, c). Based on evidence of ceased carbonate depositions, the Polar Front (PF) is suggested to have moved to the north of the bank in the Miocene, while abyssal currents kept scouring the sediments to shape the mounded MEB (Ciesielski and Wise Jr, 1977). The erosion of the older sediments was impeded by the accumulation of the glacial marine sediments throughout the Plio-Pleistocene, whereas a change towards local Carbonate deposition occurred in the late Pleistocene as the PF migrated to the south of the bank (Ciesielski and Wise Jr, 1977).

As the largest and strongest current system on Earth today contributing to mass and energy exchange in the Southern Ocean, the clockwise flowing ACC comprises three major jets coinciding with the Subantarctic Front (SAF), the PF, the Southern ACC Front, and Southern Boundary of the ACC (e.g., Orsi et al., 1995 (their Fig. 11); Sokolov and Rintoul, 2009 (their Figure 6)). Across the Drake Passage, at about 66°W, the ACC is divided into two branches as it rounds Burwood Bank (Figure 5.1a) (Fetter and Matano, 2008). The eastern branch flows eastwards and around the MEB, where it joins the western northward-flowing branch at about 48°S to form the Falkland/Malvinas Current. A total of ~100 SV (1 SV= 10^6 m³/s) of deep and bottom water from different origins crosses the F/MP and enters the Argentine Basin through three main north-south trending openings being the saddle of the F/MP (sill depth 2500 m), the Falkland/Malvinas Passage at 35-40°W (sill depth of 5100 m at the

narrow Falkland/Malvinas Gap at 36°W), and west of the Islas Orcadas Rise (sill depth >4500 m) (Figure 5.1a). These water masses comprise Weddell Sea Deep Water (WSDW), South Pacific Deep Water (SPDW), Lower Circumpolar Deep Water (LCDW), and Upper Circumpolar Deep Water (UCDW) (Arhan et al., 1999; Arhan et al., 2002; Orsi et al., 1999) (Figure 5.1a).

5.4 Data and methods

5.4.1 Seismic reflection data acquisition and processing

The presented study is based on a subset (ca. 2200 km²) of seismic reflection data acquired by the Alfred Wegener Institute (AWI) during RV Maria S. Merian cruise MSM81 in 2019 (Uenzelmann-Neben, 2019a) (Figure 5.1b). A 240-channel digital seismic streamer (SERCEL SEAL©) with a hydrophone array spacing of 12.5 m (total active length 3 km) in addition to a 141.4 m-long lead-in cable was used to record 9 s of data sampled at 1 ms. An array of 4 GI-guns (Generator/Injector-gun) with a total volume of ca. 9.6 l constituted the seismic source. Each individual GI-gun consisted of a generator chamber (0.72 l volume) producing the seismic signal and an injector chamber (1.68 l volume) triggered with a 33 ms delay to minimize the bubble effect. The GI-guns were fired every 25 m, producing signals with frequencies of up to 300 Hz.

Pre-processing of seismic data comprised navigation data merge, geometry definition, and common depth point (CDP)-sorting with a 25 m CDP spacing. For normal moveout (NMO) correction, a precise velocity analysis (at least) every 50 CDP (\sim 1.2 km) was carried out. Geometric spreading amplitude correction was applied before stacking. Furthermore, an Omega-X post-stack time migration was included to attain a correct seismic image of the underground in the areas with high inclination (Yilmaz, 2001a). Aiming for an amplitude preserved processing, no Automatic Gain Control filter (AGC) was applied neither throughout the processing sequence nor for display. A bandpass filter with a Hanning Window taper with low and high boundaries of 5-30 Hz and 200-250 Hz, respectively, was applied for the display of the sections.

5.4.1.1 DSDP Drilling Data

Borehole information from four DSDP Leg 36 and Leg 71 sites are integrated into this study. The seismic profiles of cruise MSM81 were designed to intersect Leg 36 Sites 327, 329, and 330 and Leg 71 Site 511 (Uenzelmann-Neben, 2019a) (Figure 5.1b). Figure 5.2 provides an overview of the four DSDP Sites in the study area.

5.4.1.2 DSDP Leg 36 Site 327

Including two boreholes, respectively 469.5 and 5.5 m deep, this site was drilled on the western shoulder of the MEB, at a water depth of 2400 m (Shipboard_Scientific_Party, 1974a). DSDP Site 327 was continuously cored up to 118 m and intermittently cored up to the bottom of the hole. In total 128.1

m core was recovered (50% core recovery). Eight lithological units were distinguished, ranging in age from Neocomian-late Aptian to Quaternary (Figures 5.2 and 5.3).

5.4.1.3 DSDP Leg 36 Site 329

DSDP Site 329, located ca. 55 km northeast of DSDP Site 327 on the MEB, includes one borehole drilled on the westernmost end of the MEB to a depth of 464.5 m, at a water depth of 1519 m. DSDP Site 329 was continuously cored up to 179.5 m and intermittently cored up to the bottom of the hole (Shipboard_Scientific_Party, 1974c). The section comprised two lithological units ranging in age from Paleocene to Pleistocene-recent (Figures 5.2 and 5.3).

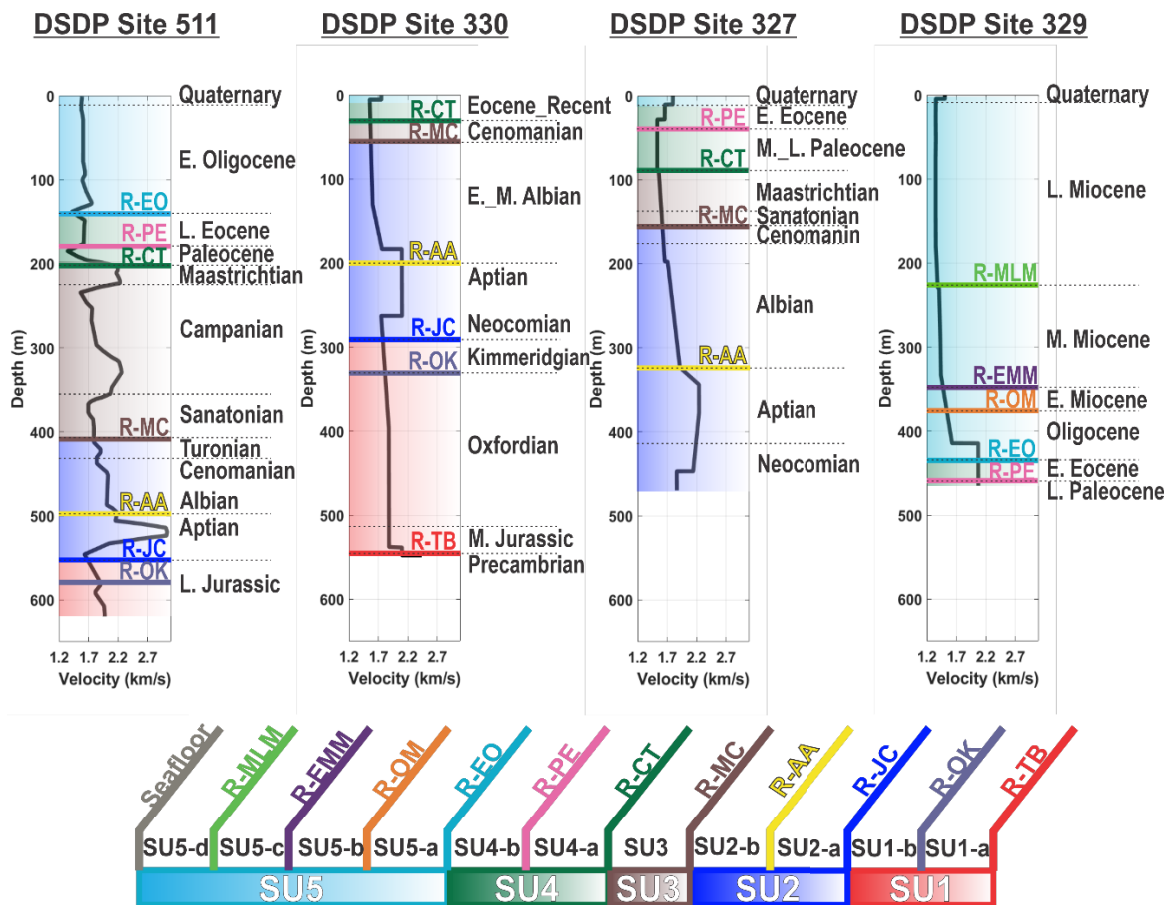


Figure 5.3: Information from DSDP Leg 36 Sites 327, 329, and 330 and Leg 71, Site 511 used for integration with seismic data (Bayer, 1980; Shipboard_Scientific_Party, 1974a, c, d, 1980a). Velocity functions and lithological results are shown against depth (below seafloor) for each site. The marker horizons and seismic units defined in the seismostratigraphic model are also color marked (for more details, refer to Table 5.1 and Section 5.5).

5.4.1.4 DSDP Leg 36 Site 330

Including two boreholes, respectively 575.5 and 47.5 m deep, this site was drilled at the western end of the MEB, ca. 10 km southwest of DSDP Site 327, at a water depth of 2626 m (Shipboard_Scientific_Party, 1974d). DSDP Site 330 was intermittently cored up to a depth of 575.5 m. In total 85.5 m core was recovered (53% core recovery). At a depth of 550 meters below seafloor

(mbsf), the hole drilled into the gneissose and granitic continental basement. The section recorded seven lithological units ranging in age from Pre-Cambrian to Recent (Figures 5.2 and 5.3).

5.4.1.5 DSDP Leg 71 Site 511

DSDP Site 511 was drilled and continuously cored 632 m within the basin province of the F/MP, ca. 10 km south of DSDP Site 330, at a water depth of 2589 m (Shipboard_Scientific_Party, 1980a). In total 385.62 m core was recovered (61% core recovery). The section comprises six lithological units ranging in age from early Albian to early Oligocene (Figures 5.2 and 5.3).

5.4.2 Interpretation scheme

5.4.2.1 Integration of DSDP well data into seismic sections

P-wave velocity models from measurements on the core material for the four DSDP Sites in the study area were adopted to convert geological information from depth into two-way travel-time domain since no downhole logging data was available. Velocity information for DSDP Sites 327, 329, and 330 were taken from Shipboard_Scientific_Party (1974a, b, c) and for DSDP Site 511 from Bayer (1980) (Figure 5.3). DSDP Site 511 is the only site with a continuous coring interval; however, the recovery rate lies by only 61%. Detailed information on shipboard sonic velocity measurement for Legs 36 and 71 inclusive of the methodology, limitations, potential sources of errors, and applied calibrations are explained by Lonardi (1974) and Bayer (1980). The velocity models from onboard measurements, integrated into this study, are assumed to be based on true values, with small errors. The depth-age conversion was applied for DSDP boreholes using the velocity information. Reflectors were first traced in-between the sites and afterward extended outwards as far as the reflectors' continuities allowed. The observations of the depths and thicknesses, according to the seismic data are all in Two-Way travel-time ms (ms TWT) or ms TWT below seafloor (msbsf TWT). The expressed thicknesses in ms TWT are converted to m using an average interval velocity for each (sub)unit.

5.4.2.2 Seismic stratigraphy

In principle, seismic stratigraphy is the technique of stratigraphic interpretation using seismic data within the limits of seismic resolution, where seismic images are divided into distinct stratigraphic packages through identification of prominent reflection terminations (Emery and Myers, 2009). Marking consistent reflector truncations against seismic surfaces allows for dividing the stratigraphy on seismic data into depositional packages with (semi-) conformable reflections with minor varying character. Categorization of reflection terminations is based on the geometric relationship between the reflections and the seismic surfaces against which they terminate. Reflection truncation terminology is here adopted from Mitchum Jr et al. (1977); Vail et al. (1977) and Emery and Myers (2009). The

unconformities, distinguished by their high-relief truncational characteristic, are considered as sequence boundaries across which the units' strata show discordance (Emery and Myers, 2009; Vail et al., 1977).

Table 5.1: Seismostratigraphic model. Defined seismic stratigraphy and reflector nomenclature at DSDP Leg 36 Site 327, 329, 330, and Leg 71 Site 511.

Geological record DSDP Site#			Age [Ma]	Geological Age	Seismic Unit	Reflector/su bunit name	Published stratigraphic model*	Depth at DSDP site [msbsf TWT]	Thickness (min/max) [ms TWT]	Seismic Character			
Q.			Recent			Seafloor							
L.	Miocene			Middle-Late Miocene Boundary			SU5-d						
329	11.6				R-MLM								
M.	Early-Middle Miocene			SU5-e									
329	15.9				R-EMM								
E.							SU5-b						
329	23.03	Oligocene-Early Miocene						R-OM					
Oligocene	Paleogene						SU5-a						
511	33.9	Eocene-Oligocene			R-EO								
Eocene	Paleocene-Eocene Boundary			SU4-b									
511	56				R-PE								
Paleocene							SU4-a						
511	330	66	Cretaceous-Tertiary			R-CT	U4	244 42 112	-	Semi-continuous to partially discrete internal reflections of middle- to high-amplitude			
L.	Cretaceous						SU3	SU3	D3	Semi-continuous to continuous high-amplitude reflector. Major erosional unconformity.			
511	100.5	Middle Cretaceous			R-MC								
E.				SU2-b									
511	330	113	Aptian-Albian Boundary			R-AA							
E.				SU2-a									
511	330	145	Jurassic-Cretaceous			R-JC	U2	610 328	-	Medium to occasionally low amplitude reflector			
L.	Jurassic						SU1-b						
330	157.3	Oxfordian-Kimmeridgian Boundary			R-OK								
L.				SU1-a									
330	541	Precambrian-Jurassic						Top basement R-TB	U1	615	-		
Precambrian							Basement						
* Lorenzo and Mutter, 1988.													

5.4.2.3 Seismic expression of contourites

The observed sedimentary features (erosional patches/surfaces, moats, sediment mounds) are interpreted within the concept of current-controlled sedimentation, as practiced and adopted similarly within other study areas (e.g. Müller-Michaelis et al., 2013; Nielsen et al., 2008; Steinbrink et al., 2020; Uenzelmann-Neben et al., 2007). Bottom currents and water masses erode and transport sediments, depositing the material where the flow velocity is reduced. This concept of sediment drift formation

has been defined and summarized by a number of authors (e.g., Esentia et al., 2018; Faugères and Stow, 2008; Faugères et al., 1999; Nielsen et al., 2008; Rebisco et al., 2014; Stow et al., 2002). A three-scale approach is proposed to best define the diagnostic criteria for the contourite drift systems, as shortly presented below.

- Typical geometries, mostly mounded, as an interactive product of the nature of the bottom current flow, topographic features, and sediment supply.
- Along-slope (down-current) elongation.
- Basal (ocean-wide) and internal (sub-regional) erosional discontinuities, marked by high-amplitude continuous reflectors, indicating changes in the bottom-current conditions.
- Uniform subunits with middle- to low-amplitude reflections in between the discontinuities, marking the temporal and spatial persistence of the bottom-current conditions.
- Medium-scale seismic criteria are indicative of periodic deposition, non-deposition, and erosion marking the history of drift construction. These include:
- Mostly lenticular, upward-convex formed units.
- Progradational, aggradational, or uniform stacking pattern, in response to different drift systems, prone to change along the development of the drift.
- Down-current to oblique migration direction. Lateral migration is attributable to the action of Coriolis Force (increasingly at high latitudes).
- Reflector terminations in form of downlapping and sigmoidal progradational patterns.
- Small-order seismic criteria reflect changes in the depositional facies, processes, and sediment types, these are however very dependent on the seismic acquisition and processing schemes and therefore should be integrated with other methods.

We thus interpret the observed sediment mounds as sediment drifts and together with moats and erosional patches/surfaces as the result of bottom current and bottom water mass activity.

5.5 Results

Five widespread seismic units were distinguished on the MEB, which are bound by unconformities sampled and biostratigraphically dated at DSDP Sites 327, 329, 330, and 511 (Figure 5.2). The drilling data from DSDP Sites are correlated with observations of the reflection characteristics for both reflectors and seismic units. Several seismic horizons with distinct characters distinguish subunits of these sequences, as listed in Table 5.1.

5.5.1 Basement

The top of the basement, reflector R-TB, exhibits a twofold character. On the shoulder of the MEB, towards the F/MB, it forms a low dip reflection of low-amplitude (Figure 5.4, CDPs 800-1800). On

top of the MEB, however, it exhibits a rough and indented topography, with semi-continuous, middle-to high-amplitude reflections (Figure 5.5, CDPs 1-1500). Reflector R-TB occasionally reaches a maximum depth of more than 2500 msbsf TWT towards the shoulder of the MEB (Figure 5.4, CDPs 1200-1600) and shoals towards the top of the MEB, where it lies at an average depth of 600 msbsf TWT (Figure 5.5, CDPs 1-1600). Basement highs are common across the MEB and exhibit different sizes. At their base, these show a width ranging from less than 5 km (Figure 5.5, CDPs 1-200) to more than 22 km (Figure 5.6, CDPs 600-1500). Some rise less than 200 ms TWT relative to the adjacent basement (Figure 5.5, CDPs 1600-1900), while others rise up to 1000 ms TWT. Locally, these highs can be traced close to the seafloor.

5.5.2 Seismic units

5.5.2.1 Unit SU1, Reflectors R-TB to R-JC (Precambrian-Jurassic to Jurassic-Cretaceous)

Unit SU1 is bound at the top by reflector R-JC, an approximately 25-million-year non-depositional unconformity of late Jurassic-early Cretaceous age (Shipboard_Scientific_Party, 1974c, 1980), sampled at DSDP Sites 511 and 330 (Figure 5.2, Table 5.1). Reflector R-JC is of continuous middle- to high-amplitude character and can be tracked well across the MEB (Figure 5.7). Reflector R-TB forms the base reflector for unit SU1 (Figure 5.7, Table 5.1).

Unit SU1 is split into the lower subunit SU1-a and the upper subunit SU1-b by reflector R-OK, which marks the Oxfordian-Kimmeridgian boundary at DSDP Site 330 (Shipboard_Scientific_Party, 1974c) (Figure 5.2). Reflector R-OK appears as a low- to middle-amplitude reflector, sub-parallel to the basement topography, which onlaps onto basement in more elevated regions where the top basement rises to a depth of less than 3200 ms TWT (Figure 5.7, CDP≈14500). Subunit SU1-a has subparallel continuous wide-spaced reflections of middle- to high-amplitude, while subunit SU1-b shows subhorizontal semi-continuous to discrete moderate-spaced internal reflections of medium- to low-amplitude (Figure 5.7).

Unit SU1 follows the topography of the basement and wedges out at the crest of the MEB, and its thickness is a function of the basement depth and varies between 50 ms TWT (≈ 47 m) and more than 1800 ms TWT (≈ 1687 m) in the vicinity of the MEB. Unlike subunit SU1-a, which shows a very variable thickness between 0 and 1700 ms TWT (≈ 1658 m), subunit SU1-b has an average thickness of 150 ms TWT (≈ 139 m) on the shoulder and top of the MEB (Figures 5.4- 5.9).

Unit SU1 is mainly characterized by a hemipelagic depositional system, that fills the topographic troughs within the basement and exhibits a retrogradational character on the MEB (Figure 5.7). Towards the north, approaching the Falkland/Malvinas Escarpment, subunit SU1-a is heavily distorted (Figure 5.6, CDPs 1500-2500, TWT > 3800 ms TWT).

5.5.2.2 Unit SU2, Reflectors R-JC to R-MC (Jurassic-Cretaceous to middle Cretaceous)

Unit SU2 is bound at the base by reflector R-JC and at the top by reflector R-MC, which correlates to a middle Cretaceous hiatus as reported at DSDP Site 511 (Shipboard_Scientific_Party, 1980a) (Figure 5.2, Table 5.1). Reflector R-MC appears as a semi-continuous middle- to high-amplitude reflector across the MEB, which erosionally truncates reflections as old as the Albian (Figure 5.4, CDPs 1600-2000, 700 msbsf TWT).

Reflector R-AA of semi-continuous low- to middle-amplitude, which marks the Aptian-Albian boundary (Shipboard_Scientific_Party, 1974a, c, 1980), separates unit SU2 into subunits SU2-a and SU2-b. Subunit SU2-a exhibits subparallel middle-amplitude reflections, while subunit SU2-b has subparallel semi-continuous to discrete reflections of low- to middle-amplitude (Figures 5.7 and 5.8). Unit SU2 shows a thickness between 50 ms TWT (52 m) and more than 350 ms TWT (364 m) in the vicinity of the MEB, with subunit SU2-a showing a constant thickness of ca. 100 ms TWT (118 m) and subunit SU2-b showing a more variable thickness, ranging from less than 50 to 200 ms TWT (45-180 m) (Figures 5.7 and 5.8). Towards the MEB crest unit SU2 thins and occasionally disappears (Figure 5.7), it thickens again towards greater water depths. This unit wedges out on the crest of the MEB once the top basement rises to less than ca. 2300 ms TWT (Figure 5.8).

Unit SU2 is strongly affected by erosion in depths of 3200-3800 ms TWT (2400-2850 m) at the western flank of the MEB (Figure 5.6, CDPs 1500-2000) and in depths of 4100-4700 ms TWT (3075-3525 m) in the depression north of the MEB.

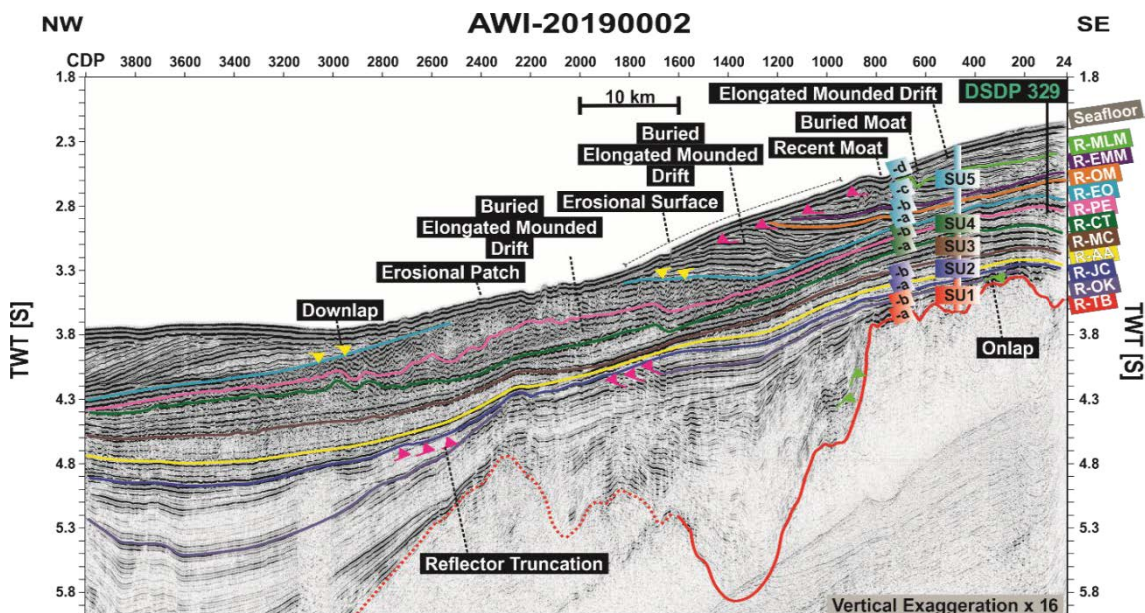


Figure 5.4: Interpreted seismic profile AWI-20190002. Location of profile is shown in Figure 5.1b. Superimposed are the seismic stratigraphy and the marker horizons (for more details, refer to Table 5.1 and Section 5.5).

5.5.2.3 Unit SU3, Reflectors R-MC to R-CT (Middle Cretaceous to Cretaceous-Tertiary)

Seismic unit SU3 is bound by reflector R-MC at its base and a major regional erosional unconformity, reflector R-CT, identified at DSDP Sites 511, 330, and 327 (Shipboard_Scientific_Party, 1974a, c, 1980) (Figure 5.2, Table 5.1), at its top. Reflector R-CT mostly has a semi-continuous to continuous high-amplitude character and can be traced very well across the MEB and truncates reflections as old as unit SU2 (Figure 5.7, CDPs 12100-13500 and Figure 5.6, CDPs 600-1600).

Unit SU3 shows sub-parallel semi-continuous to continuous internal reflections of middle- to high-amplitude. Lower reflections of unit SU3 lie conformably on reflector R-MC, while reflections within the upper part are erosionally truncated by the top reflector R-CT (Figure 5.6, CDPs 12100-14800). Unit SU3 shows slightly variable thickness of ca. 200 ms TWT (\approx 173 m) across the MEB, but drops to less than 50 ms TWT (\approx 44 m) on the western flank (Figure 5.7, CDPs 12000-12800). The unit thickens again westward into the F/MB.

Onlap and erosional truncation characterize unit SU3 in the west in depths of 3200-3800 ms TWT (2400-2850 m) where it thins strongly and appears to be affected by erosion (Figure 5.7, CDPs 12000-13000 and Figure 5.4, CDPs 1100-1600). There, unit SU3 forms the youngest present unit (Figure 5.7, CDPs 12100-12300, location of DSDP Site 330). The unit is further strongly affected by erosion in depths of 4100-4700 ms TWT (3075-3535 m) at the northern flank of the MEB (Figure 5.5, CDPs 4300-4800) and in the depression in the north. In the northwestern corner of the depression, a filled moat is identified, which shows an updip westward migration (Figure 5.5, CDPs 3200-4700).

5.5.2.4 Unit SU4, Reflectors R-CT to R-EO (Cretaceous-Tertiary to Eocene-Oligocene)

Unit SU4 is bound at the top by reflector R-EO, a prominent undulated, semi-continuous, middle- to high-amplitude reflector (Figure 5.7), which marks an early to middle Eocene hiatus recorded at DSDP Site 329 (Shipboard_Scientific_Party, 1974c) (Figure 5.2, Table 5.1). Unit SU4 unconformably lies on the base reflector R-CT.

Reflector R-PE is a semi-continuous high-amplitude reflector marking the Paleocene-Eocene Boundary (Shipboard_Scientific_Party, 1974a, b) and separates unit SU4 into subunits SU4-a and -b. Reflector R-PE mostly is sub-parallel to reflector R-CT and displays a semi-continuous high-amplitude reflection across the MEB (Figure 5.7). Subunit SU4-a shows sub-parallel semi-continuous to partially discrete internal reflections of middle- to high-amplitude, and subunit SU4-b has more continuous internal reflections (Figure 5.5). The internal reflections of subunit SU4-a are subparallel to reflector R-CT, while the reflections of subunit SU4-b are erosionally truncated by reflector R-EO at the top (Figures 5.4-5.9).

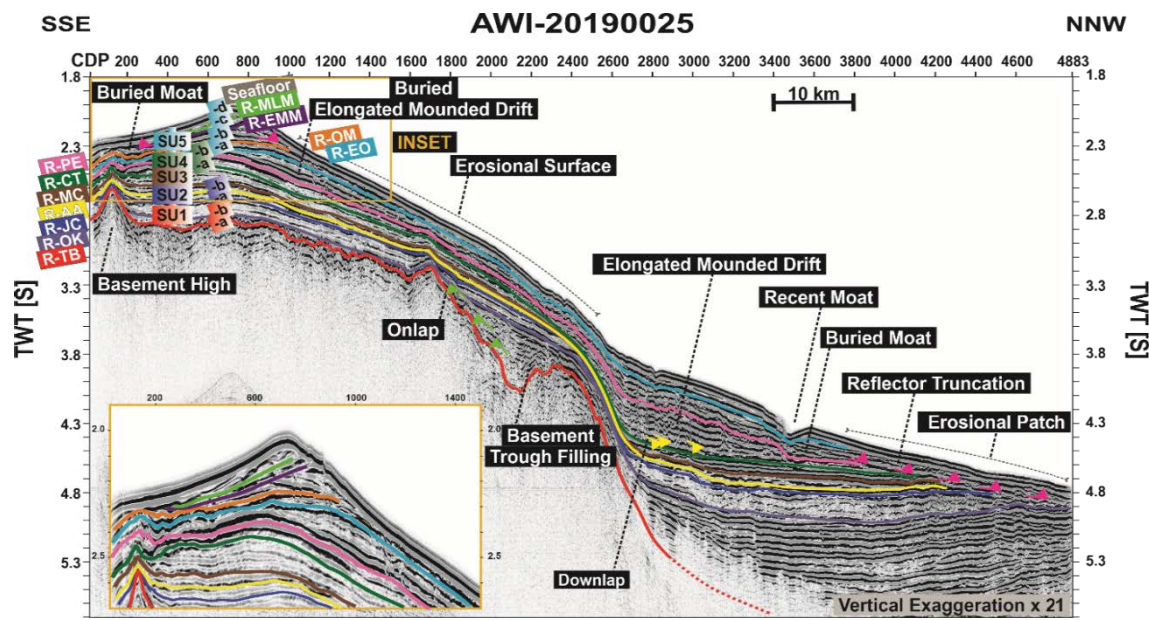


Figure 5.5: Interpreted seismic profile AWI-20190025. Location of profile is shown in Figure 5.1b. Superimposed are the seismic stratigraphy and the marker horizons (for more details, refer to Table 5.1 and Section 5.5).

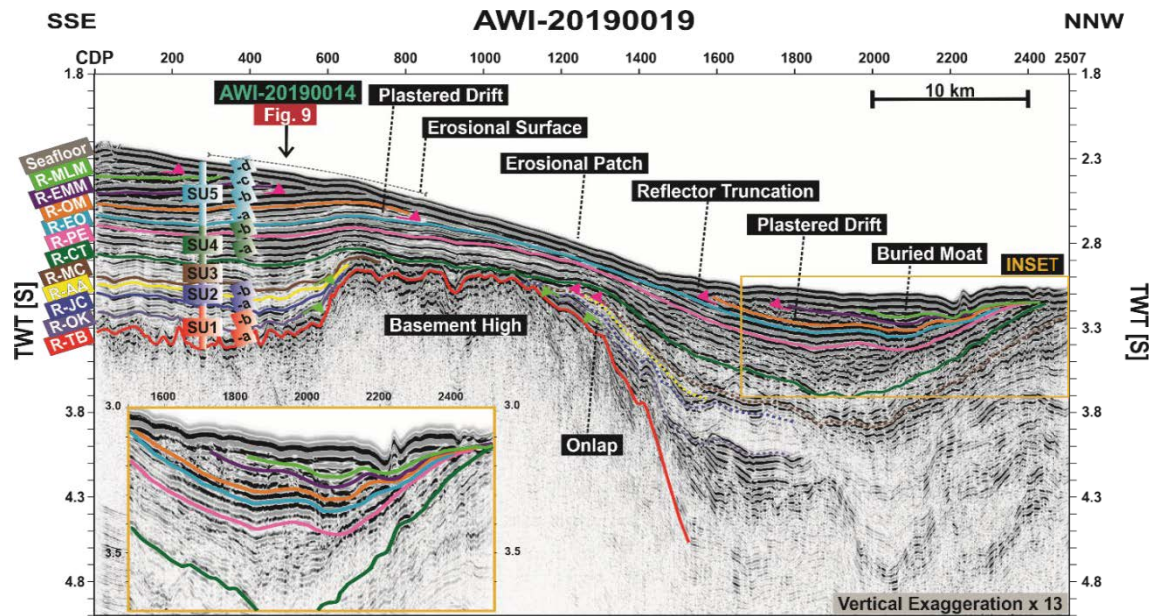


Figure 5.6: Interpreted seismic profile AWI-20190019. Location of profile is shown in Figure 5.1b. Superimposed are the seismic stratigraphy and the marker horizons (for more details, refer to Table 5.1 and Section 5.5). Arrow shows the location of the crossing seismic profile.

Unit SU4 shows limited thicknesses on top of the MEB with an average of ca. 200 ms TWT (≈ 165 m) (Figure 5.4- 5.9). This unit shows thinning towards the flanks of the MEB and can therefore be mostly distinguished on the deeper shoulder or within the northern depression, where it thickens again and shows an average thickness of 400 ms TWT (≈ 330 m) (Figures 5.4- 5.9).

On the western flank of the MEB, subunit SU4-a locally shows a mounded structure with an average thickness of 200 ms TWT (\approx 155 m) developed to the west of an erosional patch lain against the western flank of the MEB at a depth range of 3200-3800 ms TWT (2400-2850 m) (Figure 5.4, CDPs 1200-3000). The mounded body shows sub-parallel internal reflections, extends northwards, and further develops into subunit SU4-b to an average of 250 ms TWT (\approx 219 m) (Figure 5.10, SU4-a and -b). Within this sediment body, the internal reflections of subunit SU4-a onlap reflector R-CT, while internal reflections of subunit SU4-b are terminated by reflector R-EO (Figure 5.4).

A mounded sediment body, with an average thickness of 100 ms TWT (\approx 78 m), develops within subunit SU4-a on top of the MEB, which extends towards the east (Figure 5.5, CDPs 1-2000 and Figure 5.10, SU4-a). This structure further persists within subunit SU4-b with the crest migrating northwards, showing an average thickness of 150 ms TWT (\approx 132 m), (Figure 5.5, CDPs 1-2000 and Figure 5.10, SU4-b). A filled moat limits this asymmetric sediment mound at a depth range of 2400-2500 ms TWT (1800-1850 m) and displays a gradual updip northward migration, where the internal reflections of this mounded body downlap onto reflector R-CT (Figure 5.5, CDP \approx 200, 400 msbsf TWT).

The two subunits of SU4 show strong thinning at the northern flank of the MEB within a depth interval of 3200-3800 msbsf TWT (2400-2850 m) (Figure 5.5, CDPs 2000-2500). Occasionally, subunit SU4-b thins abruptly and partly disappears leaving subunit SU4-a exposed at the seafloor. On the northern flank of the MEB, erosion further affects subunits SU4-a and SU4-b at depths between 2500 and 3000 ms TWT (1875-2250 m) (Figure 5.6, CDPs 1000-1500 and Figure 5.10, SU4-a and -b). There, an asymmetrical mounded structure builds up within subunit SU4-b, showing an average thickness of 75 ms TWT (\approx 66 m) and a westward elongation, with a moat carved at a depth of ca. 3300 ms TWT (2475 m) to its north (Figure 5.10, SU4-b). This sediment body further persists within unit SU5 (Figure 5.10, SU5-a to -d), where it builds up to an average thickness of 400 ms TWT (\approx 298 m).

Extreme erosion is observed at a depth interval of ca. 4100-4700 ms TWT (3075-3525 m) within the southernmost section of the northern depression (Figure 5.5, CDPs 2600-4800). There, subunit SU4-a outcrops in the central and western sections. However, younger sediments are present on top of subunit SU4-a on the shallower eastern section. Subunit SU4-a locally shows prominent downlaps onto base reflector R-CT in the northern depression, where the subunit shows an average thickness of 200 ms TWT (\approx 155 m) (Figure 5.5, CDPs 2800-4400). This sediment buildup persists in subunit SU4-b, showing a westward extension (Figure 5.10, SU4-a and -b). A moat is identified north of this sedimentary structure at a depth interval of 4600-4700 ms TWT (3450-3525 m) with its steeper flank towards the northern flank of the MEB and a gradual southward updip migration (Figure 5.5, CDPs 3400-3700 and Figure 5.10, SU4-a and -b). Here, a recent moat is carved into the seafloor and sediments of unit SU5 in depths of ca. 4400 ms TWT (3300 m) (Figure 5.5, CDP \approx 3500 and Figure 5.10, SU4-b).

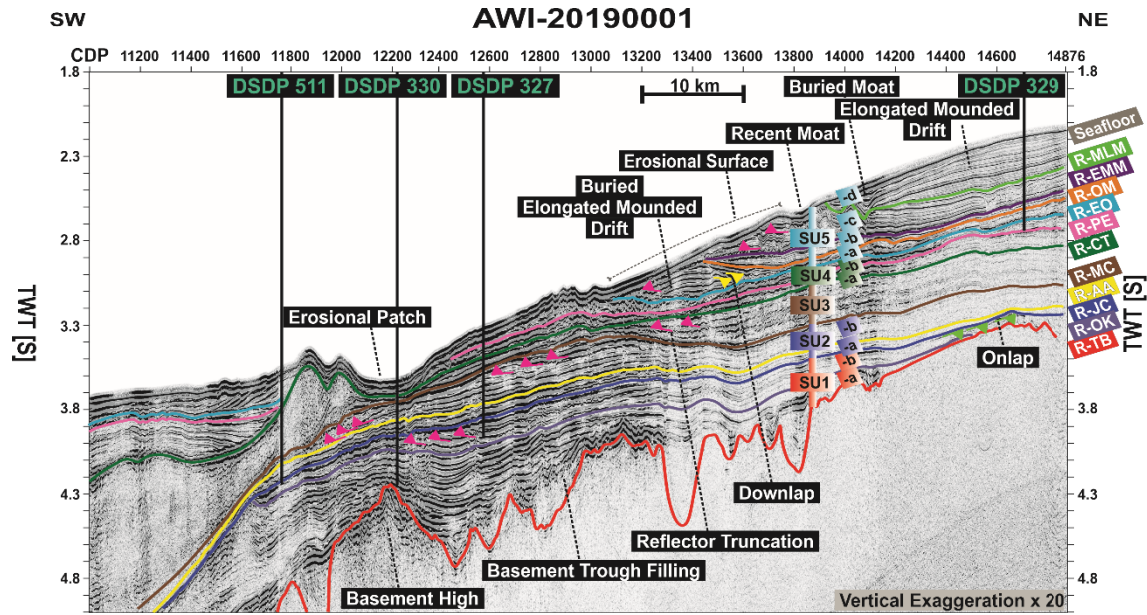


Figure 5.7: Interpreted seismic profile AWI-20190001. Location of profile is shown in Figure 5.1b. Superimposed are the defined seismic stratigraphy and the marker horizons (for more details, refer Table 5.1 and Section 5.5). Arrow shows the location of the crossing seismic profile.

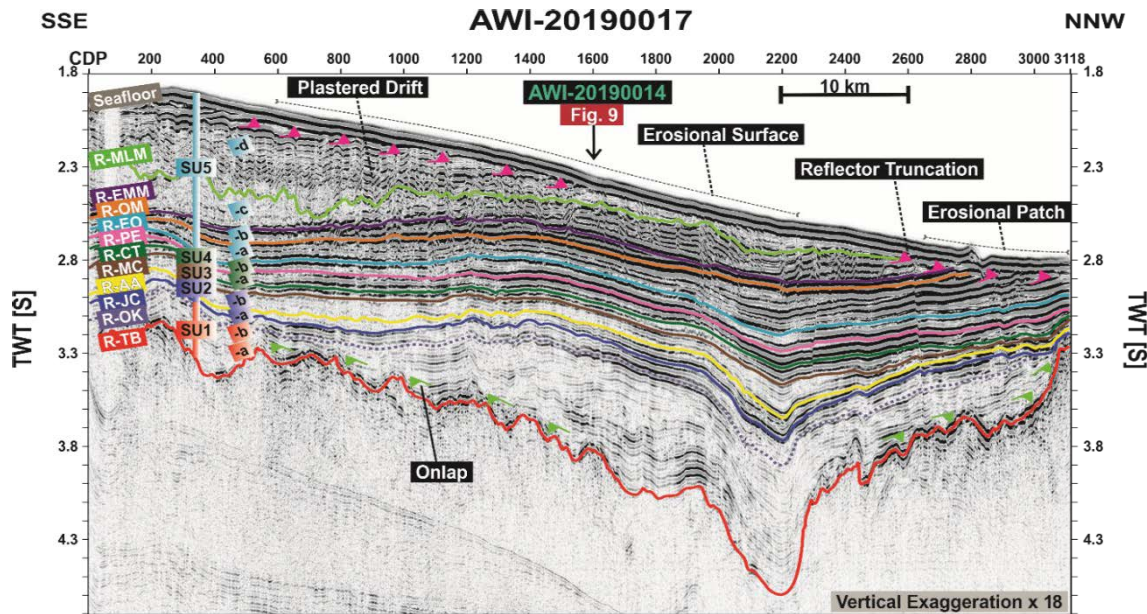


Figure 5.8: Interpreted seismic profile AWI-20190017. Location of profile is shown in Figure 5.1b. Superimposed are the defined seismic stratigraphy and the marker horizons (for more details, refer to Table 5.1 and Section 5.5). Arrow shows the location of the crossing seismic profile.

5.5.2.5 Unit SU5, Reflectors R-EO to Seafloor (Eocene-Oligocene to Recent)

Unit SU5 lies unconformably on base reflector R-EO and is bound at the top by the seafloor (Figure 5.4-5.9). This unit is separated into four subunits SU5-a, -b, -c, and -d by reflectors R-OM, R-EMM, and R-MLM.

Subunit SU5-a is bound by base reflector R-EO and top reflector R-OM. Reflector R-OM forms a subhorizontal to wavy, continuous, high-amplitude reflector (Figure 5.7) and at DSDP Site 329 is referred to as an Oligocene to early Miocene hiatus (Shipboard_Scientific_Party, 1974c) (Figure 5.2, Table 5.1). Reflector R-OM can be tracked well over most of the MEB, truncating reflections of subunit SU5-a and occasionally onlapping reflector R-EO, the top reflector of subunit SU4-b (Figure 5.6). The internal structure of subunit SU5-a is composed of sub-horizontal to wavy, high-continuity moderate to wide-spaced middle- to high-amplitude reflections (Figures 5.4-5.9).

Subunit SU5-b is bound by the base reflector R-OM and the top reflector R-EMM. Reflector R-EMM is a continuous high-amplitude reflector across the top of the MEB, that marks an early to middle Miocene hiatus at DSDP Site 329 (Shipboard_Scientific_Party, 1974c) (Figure 5.2, Table 5.1). Subunit SU5-b shows sub-horizontal, semi-continuous to discrete, narrow- to moderately-spaced, middle- to high-amplitude reflections (Figures 5.4- 5.9).

Subunit SU5-c is bound by the base reflector R-EMM and the top reflector R-MLM. Reflector R-MLM displays a continuous to discrete high amplitude reflection on the MEB (Figure 5.4-5.9), which marks the boundary between middle and late Miocene (Shipboard_Scientific_Party, 1974c) (Figure 5.2, Table 5.1). Subunit SU5-c shows sub-horizontal, continuous to discrete, narrow- to moderately-spaced, middle- to high-amplitude reflections and includes moats and wavy reflections (Figure 5.4- 5.7). Internal reflections of subunit SU5-c show abrupt changes of reflection amplitude and are mostly moderately-spaced (Figure 5.7).

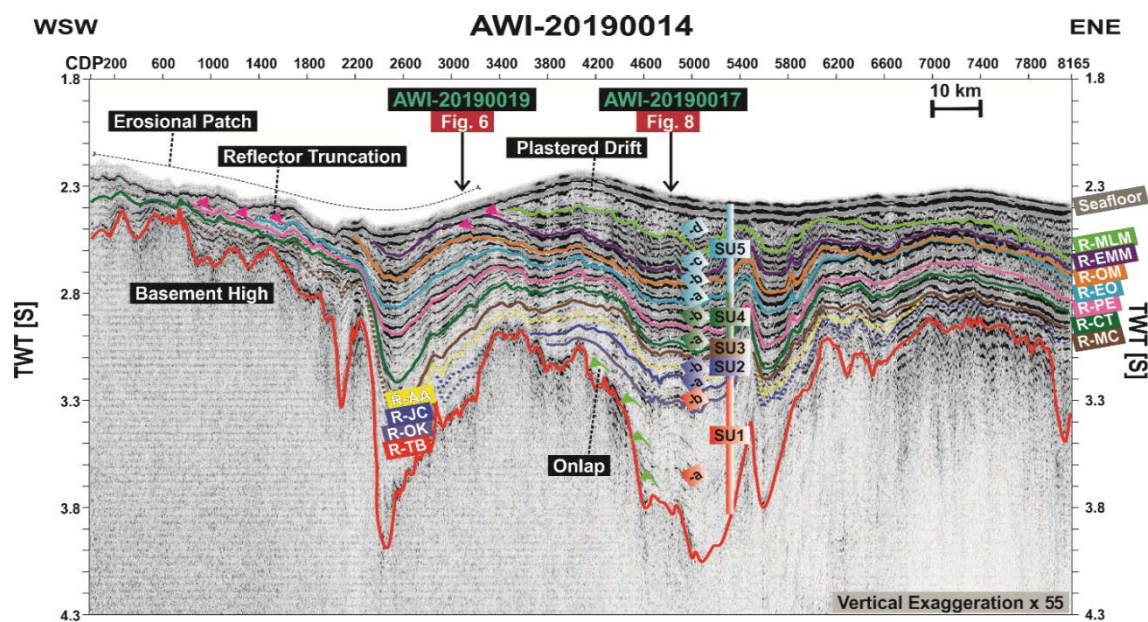


Figure 5.9: Interpreted seismic profile AWI-20190014. Location of profile is shown in Figure 5.1b. Superimposed are the seismic stratigraphy and the marker horizons (for more details, refer to Table 5.1 and Section 5.5). Arrows show the location of the crossing seismic profile.

Subunit SU5-d is bound by reflector R-MLM at the base and the seafloor at the top and shows subhorizontal, locally wavy, continuous to semi-continuous, narrow- to moderate-spaced, high-amplitude reflections (Figures 5.7 and 5.8). Within the internal reflections of SU5-d, abrupt changes of the amplitude can be observed.

Unit SU5 forms asymmetric mounded sediment packages and can mostly be traced on the elevated part of the MEB. From 500 ms TWT (\approx 373 m) thickness on the western flank (Figure 5.4, CDPs 200-1800), the unit thins towards the crest of the MEB to about 300 ms TWT (\approx 224 m) (Figure 5.5, CDPs 1-1000) and thickens again on the eastern flank, where it reaches its maximum thickness of 1000 ms TWT (\approx 745 m) (Figure 5.8, CDPs 1-1000).

In the west, a prominent erosional surface limits the occurrence of unit SU5 in depths of 3000-3800 ms TWT (2250-2850 m) (Figure 5.7, CDPs 12200-13100 and Figure 5.10, SU5-a to -d). The one seismic profile at the southern flank of the MEB also highlights thinning and erosion of unit SU5 in depths of 3300-3700 ms TWT (2475-2775 m) (Figure 5.10, SU5-a to -d). Towards the east, strong erosion has taken place in depths of 2700-3000 ms TWT (2025-2250 m) (Figure 5.8, CDPs 2600-3100 and Figure 5.6, CDPs 800-1600). At the northern flank of the MEB, the unit also shows strong thinning and is severely affected by erosion in depths of 2400-3900 ms TWT (1800-2925 m) (Figure 5.5, CDPs 1000-2600 and Figure 5.10, SU5-a to d). Here, the MEB is locally devoid of sediments younger than unit SU5-a at an average depth of 2200-2400 ms TWT (1650-1750 m) (Figure 5.9, CDPs 1-1400).

An asymmetrical mounded sediment body onlapping reflector R-EO is observed on the western flank of the MEB within subunit SU5-a (Figure 5.7, CDPs 13100-13600, Figure 5.4, CDPs 1000-1800). The deposit forms an elongated sediment body, lying against the western flank of the MEB, in a depth range of ca. 2900-3300 ms TWT (2175 -2475 m). It measures ca. 15 km in width with a maximum thickness of ca. 200 ms TWT (\approx 160 m) at about 50.8°S, shows larger width and thickness towards the north (ca. 25 km wide and ca. 400 ms TWT at about 50.5°S) and is accompanied by a filled moat to its east (Figure 5.4, CDPs \approx 1100 and Figure 5.10, SU5-a). The moat has its steeper flank against the western flank of the MEB. The apex of the concave sediment body as well as the filled moat show an updip migration.

On top of the MEB, an asymmetrical slightly mounded sediment pile flanked by a moat in the south is located within subunit SU5-a in a depth range of 2200-2400 ms TWT (1650-1800 m) (Figure 5.5, CDPs 1-2000 and Figure 5.10, SU5-a). On the northern flank of the MEB, the continued presence of a slightly mounded sediment pile, already identified in subunit SU4-b, can be observed within similar water depths (Figure 5.6, CDPs 1-800 and Figure 5.10, SU5-a). At its base, this sediment pile measures an average of 10 km and shows a maximum thickness of 200 ms TWT (\approx 150 m) (Figure 5.6). The apex of the mounded sediment body, as well as the concavity of the adjacent moat, show an updip southward migration. On the southern flank of the MEB, a sediment body is present within subunit SU5-a, showing channels within its structure and extensive erosion at the top.

The asymmetric mounded sediment body observed in subunit SU5-a on top of the MEB further persists into subunit SU5-b. The deposit is strongly affected by erosion, within a depth of 2400-3900 ms TWT (1800-2925 m) (Figure 5.5, CDPs 1-1100 and Figure 5.10, SU5-b). The sediment mound attached to the northern MEB flank in the northern depression, which was already observed in subunits SU4-b and SU5-a, persists in subunit SU5-b (Figure 5.6, CDPs 1600-2200 and Figure 5.10, SU5-b). A semi-symmetrical sediment body unconformably occurs in subunit SU5-b on the southwestern flank of the MEB in depths of 2300-2900 ms TWT (1725-2175 m). At its base, it is about 35 km wide and builds up to an average thickness of 100 ms TWT (\approx 75 m).

On the western flank and top of the MEB, subunit SU5-c shows a wavy character with an average length and height of ca. of 200 m and 30 ms TWT (Figure 5.7, CDPs 13600-14000). Similar to subunit SU5-b, subunit SU5-c also shows extensive erosion at the crest of the MEB within depths of 2200-2400 ms TWT (1650-1750 m) (Figure 5.5, CDPs 1-1000 and Figure 5.9, CDPs 1-2400). This subunit is also eroded to a great extent at the northern flank of the MEB within a depth of 2200-3900 ms TWT (1650-2925 m). Deeper on the southern flank of the MEB, the attached sediment mound, which was initially observed in subunit SU5-b, persists in subunit SU5-c (Figure 5.10, SU5-c). The symmetric mounded sediment body, first identified within subunit SU4-b in the northern depression, prevailed into subunits SU5-a and -b, is further maintained with an average thickness of 75 ms TWT (\approx 55 m) in subunit SU5-c (Figure 5.10, SU5-c).

Subunit SU5-d is the youngest and by far the thickest subunit of unit SU5 (Figures 5.7 and 5.8). On the western part, subunit SU5-d shows a mounded sediment body with an average thickness of ca. 200 ms TWT (\approx 140 m) and includes a filled moat, with an average width and height of 850 m and 100 ms TWT, showing an eastward updip migration (Figure 5.7, CDPs 13800-14800). Here, a recent moat is carved into the seafloor (Figure 5.7, CDP \approx 13820, Figure 5.6, CDP \approx 770, and Figure 5.10, SU5-d). Towards the crest of the MEB, subunit SU5-d thins to less than 50 ms TWT (Figure 5.5, CDPs 800-400). Similar to other subunits of unit SU5, subunit SU5-d also shows extensive erosion/non-deposition on the southern flank of the MEB, where reflector R-MLM onlaps reflector R-EMM at depths of 2100-2200 ms TWT. This deposit is strongly eroded at the northern flank of the MEB within a depth of 2100-3900 ms TWT (1575-2925 m).

Towards the east, however, subunit SU5-d thickens enormously and displays an average thickness of 200 ms TWT (\approx 140 m) at the northern flank and an average thickness of 500 ms TWT (\approx 350 m) towards the crest (Figure 5.8). Here, extensive erosion has taken place at an average depth of 2600-2700 ms TWT (1950-2025 m) (Figure 5.8, CDP 2800-3100 and Figure 5.10, SU5-d). A recent moat is observed on the northern flank of the MEB at depths of 3100 ms TWT (\approx 2325 m) (Figure 5.10, SU5-d). There, the mounded sediment body, observed in subunits SU5-a, SU5-b, and SU5-c on the southern flank of the MEB, persists in subunit SU5-d.

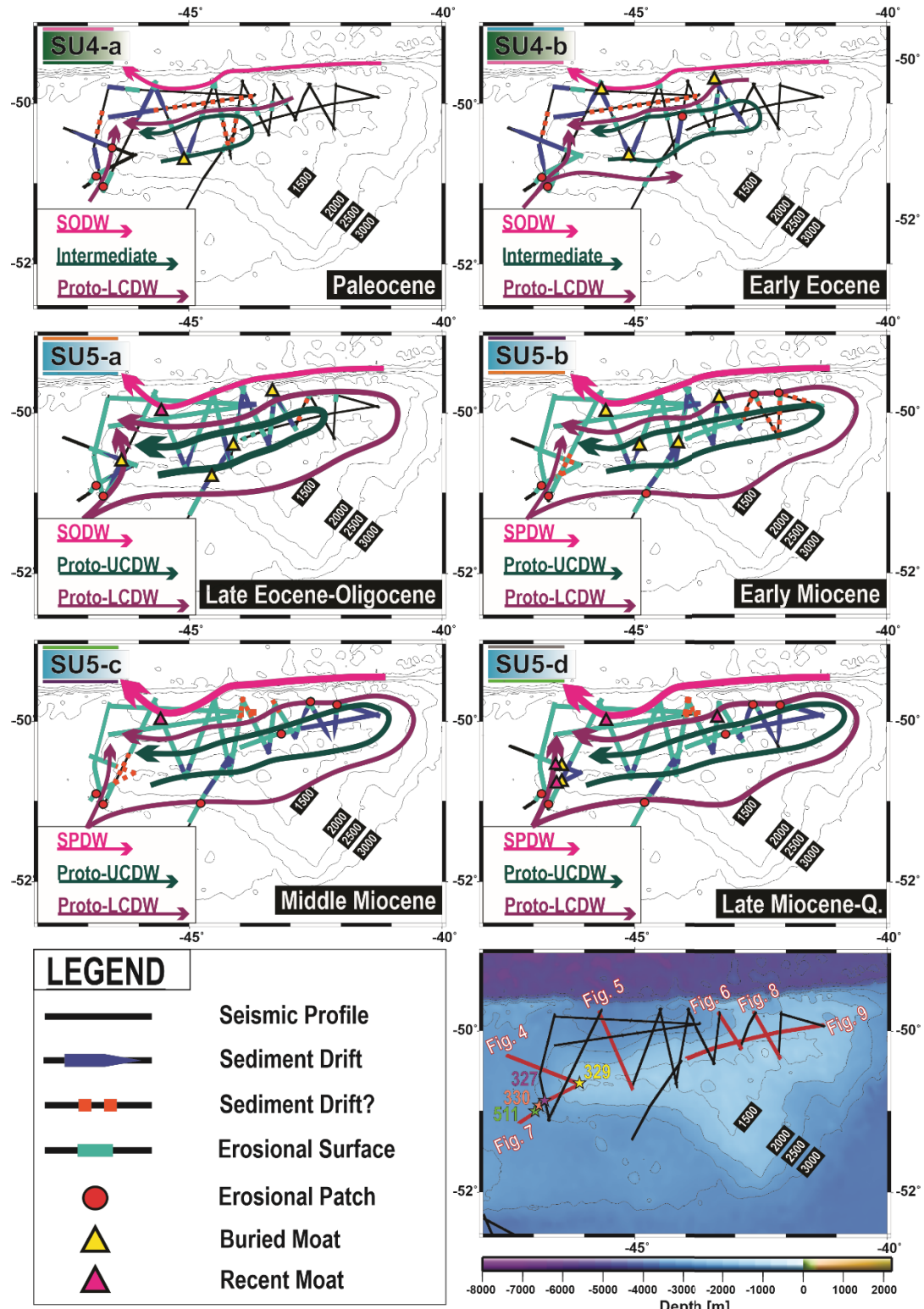


Figure 5.10: Evolution of the palaeocirculation in the study area. Erosional and depositional features for the labeled seismic subunits SU4-a, SU4-b, SU5-a, SU5-b, SU5-c, and SU5-d, as observed along the seismic profiles are color-marked (see the legend). For each subunit, respectively corresponding to Paleocene, Eocene, late Eocene-Oligocene, early Miocene, middle Miocene, and late Miocene times, the arrows schematically show the inferred flow paths of water masses (arrow thickness qualitatively shows the postulated acceleration/deceleration). Also illustrated in the bottom right, is the bathymetry map of the Maurice Ewing Bank (Smith and Sandwell, 1997), superimposed by the location of the seismic profiles and DSDP Leg 36 Sites 327, 329, and 330 and Leg 71, Site 511.

5.6 Discussion

The sedimentary units of the MEB exhibit morphological and internal reflection characteristics similar to contourite drifts, which in turn provide good archives for palaeoceanographic reconstructions. Observations of current-controlled erosional and depositional (e.g., mounded) features are interpreted in order to gain insights into the evolution of the palaeoceanographic circulation (Figure 5.10).

The thickness of the Mesozoic sequences (seismic units SU1, SU2, and SU3) on the MEB directly ties to the topography of the basement, which principally rises towards the MEB, there showing isolated cone-shaped local highs. In contrast, sedimentary sequences of the Cenozoic (seismic units SU4 and SU5) shape thick packages on top of the MEB while thinning towards the flanks due to erosion. We here concentrate on sedimentary features observed in seismic units SU4 and SU5 since those document the activity of oceanic currents since the Paleocene. According to Pérez-Díaz and Eagles (2017), the F/MP had reached its present depth in the Paleocene and thus the younger sedimentary deposits on the MEB represent an archive of the oceanic circulation influenced by the opening of the Drake Passage and the modifications of the Tertiary climate.

5.6.1 Pre-Tertiary circulation (seismic units SU1, SU2, and SU3)

The distinct lithological change at the Aptian-Albian boundary at DSDP Sites 327, 330, and 511, marks a change in the oceanic setting from a restricted basin to open marine conditions (Dummann et al., 2021; Shipboard_Scientific_Party, 1974a, d, 1980a). Faunal studies at DSDP 327 and 511 suggested an increase in paleodepths from a few hundred meters in Albian to more than 1500 m in the Maastrichtian (Holbourn et al., 2001; Shipboard_Scientific_Party, 1974a). Palaeobathymetric reconstructions of the South Atlantic support water connections between the Southern Ocean and the southern South Atlantic across the F/MP prior to Albian times (Pérez-Díaz and Eagles, 2017). Uenzelmann-Neben et al. (2017) suggested shallow (Upper Pacific Water) and intermediate (Intermediate Southern Ocean Water) water masses for the Albian and early late Cretaceous to have entered the growing Argentine Basin.

Taking the suggested paleodepths into account, our the spatially restricted observations of the erosional features in the sedimentary sequence of the Cretaceous (subunit SU2-b and unit SU3) (Figure 5.6, CDPs 1500-2000 and Figure 5.4, CDPs 12000-13000), to the west and southwest of the MEB hint at a shallow-intermediate (Upper Pacific Water) northward-flowing current. This complies with an opening of the Drake Passage for shallow water mass exchange between the Pacific and the South Atlantic in the Albian as suggested by Sewall et al. (2007) and Dummann, Steinig, et al. (2020). The F/MP would have played a barricading role between the Southern Ocean and the South Atlantic, except for shallow-intermediate circulation at least until the late Cretaceous.

Pérez-Díaz and Eagles (2017) suggested depths of above 3000 m (their Figure 3) for the southernmost part of the Argentine and Cape basins (north of the present F/MP-MEB), within the early stage of opening of the South Atlantic (\approx Aptian). Their simulation accounts for a post-Albian deep connection between the Southern Ocean and the southern South Atlantic across the Georgia Basin, confirmed by Nd isotope studies (Dummann, Steinig, et al., 2020). The detachment of the MEB from Africa at about the Albian may have favored the development of a deep seaway and exchange of deeper water masses (König and Jokat, 2010; Martin et al., 1982). Our observations of the erosional traces north of the MEB, in sedimentary units of the late Cretaceous (seismic units SU2-b and SU3) within depths of 4100-4700 ms TWT (3075-3525 m) can therefore support the development of a deeper water mass entering the deepening South Atlantic from the Indian Ocean.

5.6.2 Paleocene and early Eocene circulation (seismic unit SU4)

The Paleocene and early Eocene sequences on the MEB are characterized by the increased formation of sediment drifts, moats, and erosion (Figure 5.10, SU4-a and SU4-b). These contourite features indicate an enhanced circulation compared to the Cretaceous since a possible growing sediment supply can only result in contourite features if the circulation increases. These sedimentary features can be observed in three different depth intervals: a) 1800-2200 m, b) 2400-2850 m, and c) 3075-3525 m. This indicates that different water masses were responsible for the formation of the contourite features.

Accompanied by erosional patches in depths of 3200-3800 ms TWT (2400-2850 m), the presence of a Paleocene-Eocene elongated mounded drift in unit SU4 (Figure 5.4, CDPs 1200-3000, Figure 5.10, SU4-a and -b, and Figure 5.11) points to the long-term sedimentation under the influence of a deep water mass attempting to overspill the area west of the MEB. The activity depth is similar to the present LCDW (2000-3000 m) (Arhan et al., 1999; Arhan et al., 2002; Orsi et al., 1999). We thus interpret a water mass with properties similar to LCDW (proto-LCDW) to have formed this sediment drift.

On top of the MEB, an eastward extending mounded sediment drift with an adjacent moat at depths of 2400-2500 ms TWT (1800-1850 m) (Figure 5.5, CDPs 150-2000, Figure 5.10, SU4-a and -b, and Figure 5.11) is likely the result of an eastward flowing intermediate water mass. The seismic evidence of early Paleogene accentuated current-controlled deposition argues for rather quiet circulation conditions, which is consistent with steady hydrographic conditions reported by Uenzelmann-Neben et al. (2017). Their ocean-atmosphere dynamics simulations suggest domination of Antarctic Intermediate Water (AAIW), reaching velocities of 5 cm/s in 1750 m water depth in the early Eocene South Atlantic sector of the Southern Ocean. AAIW or a proto-UCDW (UCDW occupies water depths of 1000-2000m) is suggested to have shaped the observed sediment drift.

Erosion extending from 2500 to 3800 ms TWT (1875-2850 m depth) characterizes the northern flank of the MEB indicating the bank has acted as an obstacle, guiding both the intermediate/proto-UCDW as well as the deep water mass proto-LCDW towards the west (Figure 5.10, SU4-a and -b). An even

deeper flowing water mass shaped a drift deposit (3900-4700 ms TWT \cong 2925-3525 m depth) against the northern flank of the MEB in an east-west direction (Figure 5.5, CDPs 2800-4400, Figure 5.10, SU4-a and -b, and Figure 5.11). The presence of a recent moat there at the seafloor in depths of ca. 4400 ms TWT (3300 m) and the thin sedimentary sequences younger than Eocene (seismic unit SU5) in this northern depression hint at the continuous action of a deep-water mass at least since the early Paleogene (Figure 5.5, CDPs 2500-4800). Today, Southeast Pacific Deep Water (SPDW) flows around the MEB at water depths of 2500-3500 m (Arhan et al., 2002). However, the Drake Passage was closed for deep water masses during the Paleocene and early Eocene (Eagles and Jokat, 2014). It opened for shallow water mass exchange at \sim 41 Ma and for deep water mass exchange at \sim 30 Ma (Eagles and Jokat, 2014; Scher and Martin, 2006a). A precursor of SPDW thus cannot have shaped the deep sediment drift observed at the northern flank of the MEB. This deep water mass may have originated in the Southern Ocean (Figure 5.11), possibly in the Indian Ocean sector (Thomas et al., 2003).

Extensive thinning and erosion, observed within sedimentary sequences of Paleocene-early Eocene (subunit SU4-a and -b) or even older (unit SU3), refer to the action of deep oceanic currents since at least the late Eocene. Erosional events of similar age are also identified via seismic reflection studies in other areas of the South Atlantic (e.g., Gruetzner and Uenzelmann-Neben, 2016; Gruetzner et al., 2012; Nicholson and Stow, 2019; Schlüter and Uenzelmann-Neben, 2008; Uenzelmann-Neben, 2001). It is thus logical to relate these extensive modifications in the oceanic setting to the tectonic events of opening of the Southern Ocean gateways during the late Eocene-early Oligocene, allowing for a circum-Antarctic full pathway and the establishment of a proto-ACC and deep water production under the expanding Antarctic ice sheets (Katz et al., 2011).

5.6.3 Oligocene-Quaternary circulation (seismic unit SU5)

The remarkable increase in current-related erosional/non-depositional features on the transition from the early Eocene (SU4-b) to the late Oligocene (SU5-a) points to a change towards a highly dynamic circulation regime (compare Figure 5.10, SU4-b and SU5-a). Sediment drift formation in the depression north of the MEB and on the western shoulder, however, is significantly reduced (Figure 5.11).

Geological records from DSDP Sites 327 and 329 relate the early Eocene-Oligocene hiatus to the opening of the Southern Ocean gateways (Shipboard_Scientific_Party, 1974a, c). The complete opening of the Tasman gateway (Lawver and Gahagan, 2003; Scher et al., 2015) and the Drake Passage (Brown et al., 2006; Eagles and Jokat, 2014) in the Oligocene are believed to have contributed to the establishment of a proto-ACC (Scher and Martin, 2006a; Uenzelmann-Neben et al., 2017). A modern four-layer ocean structure including deep and bottom waters developed in the early Oligocene as a result of this and the development of continental-scale Antarctic glaciation (Goldner et al., 2014; Katz et al., 2011).

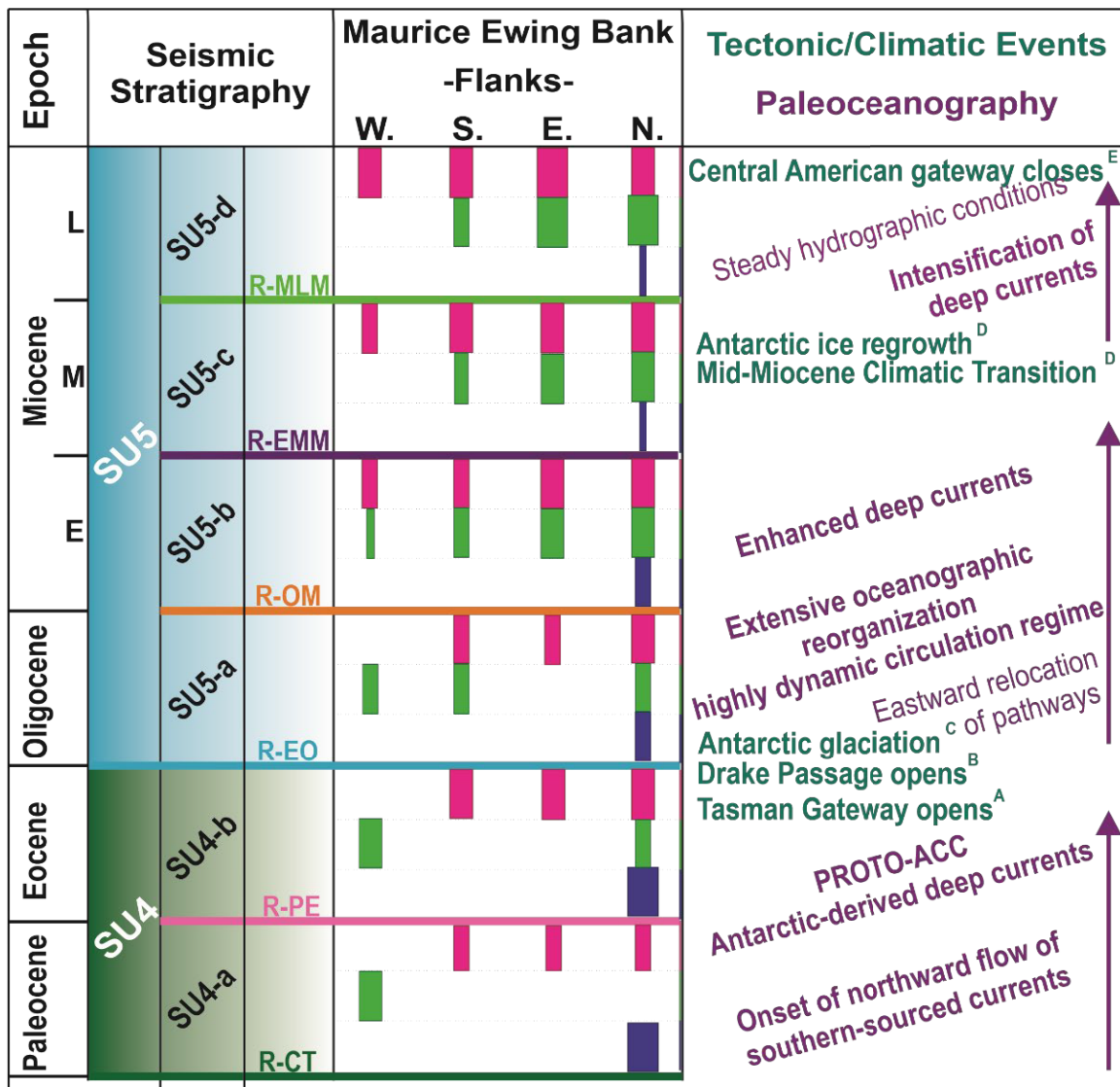


Figure 5.11: Schematic representation of contourite sedimentary features' distribution across the Maurice Ewing Bank within different seismic subunits, color-marked by their depth of occurrence below the sea surface as intermediate (<2000 m) in pink, deep (3000 m < < 2000 m) in green, and abyssal (>3000 m) in blue. The width of the bars qualitatively depicts the increased/decreased buildup of the sedimentary features. The rightmost column summarizes the main tectonic and climatic events and the reconstructed palaeoceanography. Refer to Figure 5.10 and section 5.6 for details. [A: (Lawver and Gahagan, 2003; Scher et al., 2015)], [B: (Brown et al., 2006; Eagles and Jokat, 2014)], [C: (Goldner et al., 2014; Katz et al., 2011)], [D: (Flower and Kennett, 1994; Zachos et al., 2001)], [E: (Gruetzner and Uenzelmann-Neben, 2016; Gruetzner et al., 2014; Nisancioglu et al., 2003)].

Since the Oligocene, erosion has affected mainly two water depth ranges in the area of the MEB: a) 1575-2250 m, and b) 2475-2975 m. Today, these water depths correspond to the activity levels of UCDW and LCDW (Arhan et al., 1999; Arhan et al., 2002; Naveira Garabato et al., 2002). We thus suggest a proto-UCDW and a proto-LCDW to have formed the observed erosional surfaces. An elongated mounded drift aligned with the western flank of MEB extends north-south at water depths of 2900-3300 ms TWT (2175 -2475 m) (Figure 5.4, CDPs 1000-1800, Figure 5.10, SU5-a, and Figure 5.11). A similar water mass could be held responsible for the drift which developed coevally and within the same water depth on the southern flank of the MEB (Figure 5.10, SU5-a and Figure 5.11) as well

as building up a sheeted drift at the northern flank (Figure 5.6, CDPs 1500-2200, Figure 5.10, SU5-a, and Figure 5.11). Physical Oceanography studies locate a branch of the PF at the southeastern flank of the MEB. Within this eastbound branch, LCDW is constrained by the bathymetry of the MEB within a depth range of ca. 2000-3000 m flowing around it (Arhan et al., 2002; Naveira Garabato et al., 2002). From the similar circulating behavior and depth-character, we suggest a component of proto-LCDW to overspill the F/MP west of and skirting the bathymetry south and east of the MEB, causing erosion, non-deposition, and shaping the sediments since at least the late Eocene.

The formation of sediment drifts has shifted to the east mostly abandoning the maintenance of the sediment drifts shaped during the Paleocene and early Eocene (Figures 5.10 and 5.11, compare SU4-a and -b and SU5-a to -d). We observe the build-up of a large sediment drift on top of the MEB within depths of 2200-2400 ms TWT (1650-1800 m) until the middle Miocene (Figure 5.5, CDPs 1-2000), which is further maintained until the present (Figures 5.10 and 5.11, SU5-b to -d). The depth points to the activity of proto-UCDW. The same current could be accounted for at the northern flank of the MEB, resulting in erosional/non-depositional surfaces, leaving the Oligocene strata as the youngest sedimentary unit present (Figure 5.8, CDPs 1-2200, Figure 5.10, SU5-a to -d).

Numerical simulations put forward oceanic circulations dominated by an ACC for the early Miocene (Herold et al., 2012; Von der Heydt and Dijkstra, 2006). The North Atlantic Deep Water (NADW) has been suggested to have flowed into the Pacific via the open Central American Seaway until the late Miocene (~6 Ma) (Gruetzner et al., 2016; Gruetzner et al., 2014; Nisancioglu et al., 2003) and thus could not have shaped sediment drifts on the F/MP. The water mass shaping the sediment drifts in depths up to 2000 m thus can only have been proto-UCDW.

The inception of the ACC is believed to have in turn favored the thermal isolation of Antarctica, leading to enlargement of the ice sheets and production of the AABW by the Oligocene (Diester-Haass et al., 1996; Katz et al., 2011; Scher and Martin, 2004). We observed a transition from relative quiescence bottom water conditions in the early Eocene (subunit SU4-b) towards vigorous bottom water conditions in the middle Miocene (SU5-c) with an increase of erosion in the depression north and the area west of the MEB and enhanced sediment drift formation on the eastern MEB (Figures 5.10 and 5.11, compare SU4-b and SU5-a to -d). This is interpreted as the pronounced deep/bottom water production due to renewed growth of Antarctic ice sheets during the mid-Miocene Climatic Transition (Flower and Kennett, 1994; Zachos et al., 2001), which agrees with a northward movement of the PF towards the Argentine Basin in the Miocene proposed by Ciesielski and Wise Jr (1977). Indications for increased bottom-current activity in the middle Miocene have also been reported in other sections of the Southern Ocean (e.g., Fischer and Uenzelmann-Neben, 2018b; Horn and Uenzelmann-Neben, 2015; Schlüter and Uenzelmann-Neben, 2008; Steinbrink et al., 2020; Uenzelmann-Neben, 2019b; Uenzelmann-Neben et al., 2009).

The observation of extensive erosional surfaces fully devoid of sedimentary sequences younger than late Oligocene (subunit SU5-a) within two distinct depth intervals hints at persistent and simultaneous action of a shallower and a deeper water mass since the early Miocene. These erosional patches generally lie within depths of 2200-2400 ms TWT (1650-1750 m) (Figure 5.8, CDPs 1-2200) and 2600-3100 ms TWT (1950-2325 m) (Figure 5.6, CDPs 800-1600), respectively on the top and the flanks of the MEB. In the present oceanic setting of the western South Atlantic, the PF is suggested to undergo a horizontal and vertical branching across the sill of the F/MP (Arhan et al., 2002; Naveira Garabato et al., 2002). The hydrographic data places the shallower western velocity core comprising UCDW (within depths of about 500-2000 m) northward across the F/MP, with an excursion to flow across the MEB, while a deeper eastern branch comprising LCDW lies at the southeastern flank of the MEB. An anticyclonic LCDW skirts the MEB within a depth range of ca. 2000-3000 m (Arhan et al., 2002; Naveira Garabato et al., 2002). Based on analogies in depth-character and flow path between the described erosional features and today's UCDW and LCDW, we infer the continuous action of these water masses (or precursors) in shaping the morphology of the MEB since the early Miocene along similar pathways as recognized today. This is consistent with the palaeocirculation simulation for the Miocene/Pliocene (Uenzelmann-Neben et al., 2017).

West of the MEB, the sediment drift formation stopped and erosion commenced in the middle Miocene within depths of 2500-2700 ms TWT (1875-2025 m) (Figure 5.7, CDPs 13400-14100, Figure 5.10, and Figure 5.11), documenting the impact of a proto-UCDW on sediment deposition. Ocean-atmosphere models indicate a much stronger influence of the NADW within the study area (Uenzelmann-Neben et al., 2017). On the western shoulder of the MEB, distinct erosional surfaces devoid of sediments younger than the late Oligocene-early Miocene developed (Figure 5.4, CDPs 1800-2600 and Figure 5.10, SU5-c) pointing towards overspill of proto-LCDW, perhaps diluted by NADW within a depth interval of 2250-2850 m, similar to today's hydrographic measurements (Arhan et al., 2002; Naveira Garabato et al., 2002).

Proto-UCDW could be held responsible for shaping the thick mounded contourite drift on the western flank of the MEB in the late Miocene within water depths of 2100-2500 ms TWT (1575-1650 m) (Figure 5.7, CDPs 13400-14100, Figure 5.4, CDPs 1-700, Figure 5.10, SU5-d, and Figure 5.11). The presence of recent moats at water depths of ca. 2500 ms TWT (1875 m) on top of this drift (Figure 5.4, CDP≈13800, Figure 5.6, CDP≈770, and Figure 5.10, SU5-d) in today's activity level of proto-UCDW (500-2000 m) endorses this interpretation.

The giant mounded drift deposit on the eastern MEB within water depths of 1700-2700 ms TWT (1275-2025 m) (Figures 5.8 and 5.11), which mainly formed in middle-late Miocene times, attests to deposition at steady hydrographic conditions beneath proto-UCDW and -LCDW, bathymetrically controlled by the MEB (Figure 5.10, SU5-d). Traces of water mass activity in depths > 3000 m, which could be attributed to SPDW, can only be identified in the depression north of the MEB. During the

Paleocene/early Eocene Southern Ocean Deep Water was interpreted to have flowed in from the Indian Ocean and along the northern flank of the MEB. Following the opening of a deep Drake Passage in the Oligocene, we now infer SPDW to be the shaping water mass in water depths > 3000 m.

The DSDP drillings (Shipboard_Scientific_Party, 1974a, b, c, d, 1980a, b) as well as the piston corings (Ciesielski and Wise Jr, 1977) across the MEB report only a thin veneer (less than a few meters) of Plio-Pleistocene sediments across the MEB, which is beyond the resolution of the seismic reflection data. Studies on the recovered cores, however, do report sharp biostratigraphic hiatuses within the Pliocene-Quaternary sedimentary sections (Ciesielski and Wise Jr, 1977), which have been related to the history of bottom current activity over the MEB. These include late Gilbert to mid-Gauss, Gauss-Matuyama boundary, and late Matuyama-early Brunhes time spans (Ciesielski and Weaver, 1980). However, our study cannot add to the Quaternary development.

5.7 Conclusions

The study of a set of new high-resolution seismic reflection profiles combined with information from DSDP Leg 36 Sites 327, 329, and 330 and Leg 71 Site 511 within the scheme of current-controlled sedimentation provided information on the Tertiary development of the oceanic circulation in the area of the MEB, southwestern South Atlantic (Figures 5.10 and 5.11).

- In contrast to restricted erosion indicating a quiet circulation for the late Cretaceous, the increased formation of sediment drifts and large erosional surfaces point towards an enhanced circulation in the Paleocene/early Eocene. Three activity levels of water masses are observed and interpreted to correspond to proto-UCDW, proto-LCDW, and Southern Ocean Deep Water. This provides evidence for a multi-layered ocean already in the Paleocene/early Eocene.
- Sediment drift formation bears witness to overspill of the F/MP by proto-LCDW already in the Paleocene/early Eocene. Erosion of the southern and northern flanks shows that the MEB has acted as an obstacle steering the water masses.
- A significant increase in erosional surfaces in the late Eocene/Oligocene indicates the onset of a highly dynamic circulation regime mainly in two activity levels corresponding to proto-UCDW and proto-LCDW.
- Overspill of the F/MP appears increased in the late Eocene/Oligocene but decelerated in the early Miocene resulting in sediment drift formation. A deceleration of proto-UCDW in combination with an eastward relocation can also be observed in the early Miocene. Since the middle Miocene both water masses, proto-UCDW and –LCDW, appear to have remained uniform in intensity (within the limits of seismic resolution), maintaining both erosional features and sediment drifts but extending farther eastward.
- The study as shown attests to the strong control of the MEB's topography on the pathways of deep water masses flowing within the ACC.

CHAPTER 6. Fossilized silica diagenetic fronts: Implications for palaeoceanographic evolution across the Falkland/Malvinas plateau

Najjarifarizhendi, Banafsheh*; Uenzelmann-Neben, Gabriele

Alfred Wegener Institute, Helmholtz Centre for Polar and Marine Research, Am Alten Hafen 26, 27568 Bremerhaven, Germany

- The formatting has been adapted to the dissertation and differs slightly from the publication.

6.1 Abstract

A set of newly collected 2D seismic reflection data allows the mapping of two distinct cross-cutting reflectors across the Falkland/Malvinas Plateau. Reflector XR-F/MB in the Falkland/Malvinas Basin appears as a bottom simulating reflector that mimics the geometry of the present seafloor, whereas reflector XR-F/MT in the Falkland/Malvinas Trough is a non-bottom simulating reflector that mimics a shallower reflector representing the early-middle Miocene unconformity. The discordant geometry of these two reflectors with respect to the host stratigraphy is argued to be associated with Opal-A to Opal-CT diagenesis, which is primarily a function of temperature. However, the estimated temperature at the present depth for reflector XR-F/MB lies below the minimum temperature for the onset of silica diagenesis. Based on their geometry and seismic characteristics, the two reflectors are interpreted to be fossilized silica diagenetic fronts, formed under palaeo-thermal conditions different from today. We hypothesize that the erosional action of intensified deep and bottom water masses subsequent to Antarctic glaciation during the early-middle Miocene may have driven the fossilization of the diagenetic front in the study area. It is estimated that erosion of a minimum of 270 m of overburden would account for the temperature drop driving the fossilization of the silica diagenetic front.

6.2 Introduction

Cross-cutting reflectors of positive or negative polarity are distinctive features on seismic reflection profiles due to their discordance with host stratigraphic reflections (e.g. Berndt et al. 2004). Cross-cutting reflections may be a function of seafloor geometry (bottom simulating reflector, or BSR), or may show no geometrical similarity to the seafloor (non-bottom simulating, or NBSR) (Bohrmann et al. 1992; Berndt et al. 2004; Varkouhi et al. 2022). Cross-cutting reflectors are interpreted to be associated with secondary (post-depositional) geochemical processes, most notably silica diagenesis or gas hydrate (GH) formation (Berndt et al., 2004; Shedd et al., 2012). These two processes involve very different lithological and thermobaric conditions within the sedimentary successions, resulting in

distinctive seismic characteristics that provide a means to distinguish the origin of cross-cutting reflectors (Somoza et al., 2014). In particular, silica diagenesis results in positive amplitude reflections, whereas GHs are associated with negative amplitude reflections (Bohrmann et al., 1992; Davies et al., 2002; Hein et al., 1978; Shipley et al., 1979).

Diagenesis in silica-rich sediments involves conversion of biogenetic Opal-A to micro-crystalline Opal-CT at a transition zone known as $TZ_{A/CT}$ (Hesse, 1988; Wise Jr, 1972), which is usually tens of meters thick (Varkouhi et al., 2020). Further in the diagenesis process, Opal-CT transforms to micro-crystalline Quartz known as Opaline Chert (e.g. Hesse, 1988; Kastner et al., 1977b; Wise Jr, 1972; Wrona et al., 2017). Silica transformation is a function of temperature (Grützner and Mienert, 1999; Kastner et al., 1977b), therefore $TZ_{A/CT}$ extends (sub)parallel to the seafloor. Silica transformation across the $TZ_{A/CT}$ is accompanied by a noticeable decrease in porosity, permeability, and water content and an increase in density and the P-wave velocity values (e.g. Guerin and Goldberg, 2002; Hesse, 1988; Isaacs, 1981; Meadows and Davies, 2010; Nobes et al., 1992). Therefore, $TZ_{A/CT}$ appears as a BSR of positive polarity that cross-cuts the host strata, known as Opal-A to Opal-CT BSR (O_{A/CT_BSR}) (Bohrmann et al., 1992; Davies and Cartwright, 2002; Hein et al., 1978). Since sediments beneath the O_{A/CT_BSR} contain Opal-CT, they show higher amplitude reflectors compared to those above (Berndt et al., 2004). O_{A/CT_BSR} s tend to decline in terms of sub-bottom depth with increasing water depth, due to favored diagenesis at higher pressures (Berndt et al., 2004).

Table 6.1: Summary of the features used for discerning the status of a silica diagenetic front (active vs. arrested), modified from Varkouhi et al. (2022) (for details, see sections 6.5.2 and 6.6.2. The colors indicate the degree of reliability attributed to each feature for characterizing an active vs. an arrested silica diagenetic front; red (low reliability), yellow (reliability), and green (high reliability).

Criteria		Argument for		Reliability
		Active diagenetic front	Fossilized diagenetic front	
Geometrical	1. a. TZA/CT appears as a BSR	✓		
	1. b. $TZ_{A/CT}$ appears as an NBSR	x	✓	
	1. c. TZA/CT terminates at the seafloor	x	✓	
Structural	2. a. Regional anticlines/synclines above the $TZ_{A/CT}$		✓	
	2. b. Differential compaction folding above the $TZ_{A/CT}$		✓	
	2. c. Polygonal faulting in the vicinity of the $TZ_{A/CT}$		✓	
Combination of 1.b., 2. a., 2. b., and 2. c.		x	✓	

Studies have shown that TZ_{A/CT} can extend inclined to the present-day seafloor, and instead mimic other stratigraphic boundaries (e.g. Brekke et al., 1999; Davies and Cartwright, 2002; Roaldset and He, 1995; Rundberg, 1989). These are referred to as Opal-A to Opal-CT transition non-bottom simulating reflector (O_{A/CT}_NBSR). The difference between an O_{A/CT}_BSR and an O_{A/CT}_NBSR is explained by introducing the concept of the so-called fossilized versus active silica diagenetic fronts. An ‘active’ TZ_{A/CT}, which corresponds to an O_{A/CT}_BSR on seismic profiles, is defined as one with a recent transition across the sedimentary column (Neagu et al., 2010) and is conformable to the present isotherm. A ‘fossilized’ (or ‘arrested’) TZ_{A/CT}, which corresponds to an O_{A/CT}_NBSR on seismic profiles, on the contrary, was formed under a palaeo-thermal regime other than that of the present-day and therefore appears inclined to the present seafloor bathymetry. It is hypothesized that a fossilized TZ_{A/CT} is either a product of an abrupt change in temperature regimes or a consequence of major discontinuities in the sediment accumulation (Meadows and Davies, 2010; Varkouhi et al., 2022). Table 6.1 summarizes the reviewed criteria (Varkouhi et al., 2022) to discern between active and fossilized TZ_{A/CT}.

Gas hydrates are clathrate of methane (or higher- and non-hydrocarbons) and water which form under low temperature (<25°C) and high pressure (>0.6 MP) (Kvenvolden, 1994; Sloan Jr, 1998). Sediments hosting GHs show increased P-wave velocity values due to the solidification effect of GHs (e.g. Sloan Jr, 1998; Whalley, 1980). Below the base of the GHs stability zone (BGHS), free gas and/or dissolved gas account for a drastic drop in the P-wave velocity values (e.g. Domenico, 1977; Lee, 2004) and in the seismic frequency content (Carcione and Picotti, 2006; Taner et al., 1979; Taner et al., 1994). BGHS appears as a negative polarity reflector on seismic profiles (Shipley et al., 1979). The depth-dependent thermobarometric conditions for the formation of GHs cause BGHS to lie (sub)parallel to the seafloor on the seismic sections (GH-BSR) (Shipley et al., 1979). GH-BSRs tend to slightly deepen as the water depth increases, since under increased hydrostatic pressure and decreased water bottom temperature, GHs are stable to a greater depth below the seafloor (Berndt et al., 2004).

Analysis of seismic diagnostic criteria has been used to identify diagenetic fronts and gas-hydrate intervals in basins worldwide (e.g. Berndt et al., 2004; Geletti and Busetto, 2011; Lodolo et al., 1993; Nouzé et al., 2009; Sain et al., 2000; Shedd et al., 2012). In turn, the cross-cutting reflections associated with these occurrences can provide information on the evolutional history and the paleoenvironmental conditions of the host sedimentary basin (e.g. Davies, 2005; Davies and Clark, 2006; Neagu et al., 2010; Nicholson and Stow, 2019). Geometrical, morphological, and depth characteristics of diagenetic – and gas-hydrate related reflectors provide a basis to learn about basin-wide (palaeo)thermal conditions (e.g. Kuramoto et al., 1992; Meadows and Davies, 2010; Minshull and Keddie, 2010; Ohde et al., 2018). Popescu et al. (2006) discussed the potential of using characteristics of BSRs on seismic data from the Black Sea as proxies for paleoclimatic conditions. Pérez et al. (2021) held a thicker-than-present

sedimentary cover in Pennell Basin responsible for the silica diagenesis in the basin; they suggested that the overburden underwent extensive erosion and thinning due to recurrent ice advances in this basin.

Previous studies from the Falkland/Malvinas Plateau (F/MP) have mentioned the presence of cross-cutting reflectors that have been suggested to be of diagenetic origin (Cunningham, 1999; Koenitz et al., 2008). However, an in-depth review of the morphostructural characteristics of the reflectors as silica diagenetic fronts have not been addressed. An important aspect regarding the silica diagenesis, namely the concept of active vs. fossilized silica diagenetic fronts (e.g. Davies and Cartwright, 2002; Meadows and Davies, 2010; Neagu et al., 2010; Varkouhi et al., 2022), which contributes to a better understanding of the basin's evolutional processes, is further missing in available studies of the study area. On the Falkland/Malvinas Terrace, Nicholson and Stow (2019) attribute the depth character of an identified BSR to the erosive action of the core of the Subantarctic Front (SAF).

The aim of this study is to investigate the nature of cross-cutting reflectors across the F/MP through analysis of their seismic characteristics and with reference to lithological, thermal and velocity information available from Deep Sea Drilling Project (DSDP) Sites 327, 329, 330, and 511 (Figure 6.1). We argue the seismic character of the cross-cutting reflectors to be consistent with silica diagenesis, and examine their formation in relation to present-day geothermal conditions versus past changes that could have led to fossilization of the diagenetic front. Our findings have implications for the thermal, sedimentary and oceanographic evolution of this area of the South Atlantic.

6.3 Geological and oceanographic background

The F/MP is an elongated submarine plateau in the southwest South Atlantic, some 600 km east of the South American mainland. It comprises three distinct provinces, from west to east: the Falkland/Malvinas Islands (F/MI), the Falkland/Malvinas Basin (F/MB), and the Maurice Ewing Bank (MEB) (e.g., Lorenzo and Mutter, 1988; Shipboard Scientific Party, 1974a, c, d, 1980a) (Figure 6.1). The F/MB lies between the more elevated F/MI and MEB, with average water depths of 2600m, and forms a 500 km-wide basin containing a sedimentary column up to ca. 3000 m thick above basement (Lorenzo and Mutter, 1988; Najjarifarizhendi and Uenzelmann-Neben, 2021; Richards, Gatliff, Quinn, Fannin, et al., 1996).

The F/MP is confined to the north by the Falkland Escarpment, a basement ridge that is the result of strike-slip motion along transform faults (Ludwig, 1983) , which gives way to the Falkland-Agulhas Fracture Zone (Ben Avraham et al., 1997; Lorenzo and Mutter, 1988; Ludwig, 1983) (Figure 6.1). To the south, the west-east trending Falkland/Malvinas Trough (F/MT) is a 1000 km-long bathymetric depression formed by transform movement between the South American and Scotia plates (Figure 6.1). The seabed in the F/MT deepens into the Georgia Basin in the east while it shoals westwards towards the South American continental shelf (Schreider et al., 2010). The F/MT extends 1300 km from the South American continental shelf where it lies at ca. 3250 m water depth with a width of less than

9 km at about 49°W , while eastwards it deepens to more than 3750 m and widens to ca. 50 km at 46°W , as it gives way to the Georgia Basin at ca. 41°W (Cunningham and Barker, 1996).

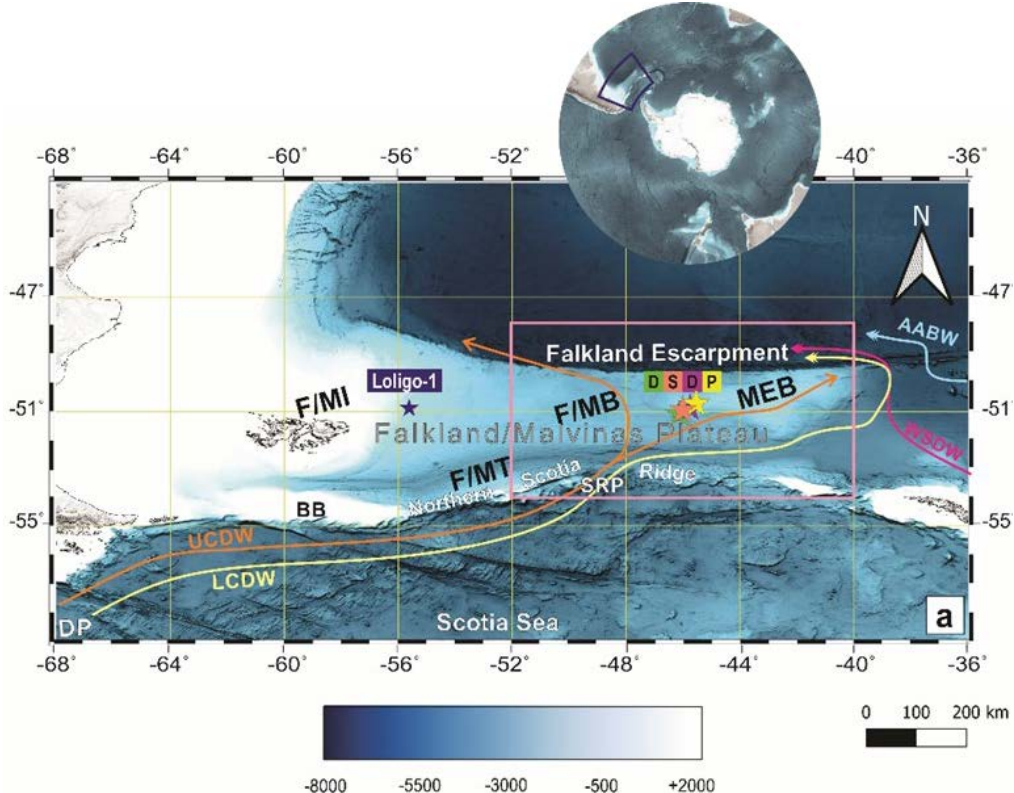


Figure 6.1: (a) Bathymetric map showing the location of the Falkland/Malvinas Plateau in the Southern Ocean (General Bathymetric Chart of the Oceans (Dorschel et al., 2022)). Arrows schematically show the pathways of the southern-sourced deep/bottom water masses in the present oceanic scheme (Arhan et al., 1999; Arhan et al., 2002; Orsi et al., 1999; Shipboard_Scientific_Party, 1980a). Upper Circumpolar Deep Water (UCDW) in orange, Lower Circumpolar Deep Water (LCDW) in yellow, South Pacific Deep Water (SPDW) in orange, Weddell Sea Deep Water (WSDW) in pink, and Antarctic Bottom Water (AABW) in blue. BB=Burdwood Bank; DP=Drake Passage; F/MB=Falkland/Malvinas Basin; F/MI=Falkland/Malvinas Islands; F/MT=Falkland/Malvinas Trough; MEB=Maurice Ewing Bank; SRP=Shag Rocks Passage. Stars mark the location of DSDP Leg 36 Sites 327, 329, and 330 and Leg 71, Site 511 and the commercial borehole Loligo-1 in the study area. (b) Superimposed are the locations of the seismic profiles used for this study, shown as solid lines. Dark red lines illustrate the location of profiles shown in figures. Light dashed lines illustrate part of the dataset across the MEB, which have been the focus of the publication by Najjarifarizhendi and Uenzelmann-Neben (2021). Stars mark the location of DSDP Leg 36 Sites 327, 329, and 330 and Leg 71, Site 511 in the study area.

The sedimentary history of the F/MB has been inferred from DSDP drill sites in its easternmost sector (Figure 6.1). Middle to late Jurassic sediments rest unconformably on granitic basement and characterize an open shelf environment, in which sapropelic claystone was deposited under euxinic conditions by Oxfordian times (Shipboard_Scientific_Party, 1977). A combination of rapid subsidence and early connections between the Indian and Proto-Atlantic oceans led to open marine conditions by the Albian (e.g. Barker, 1977a; Dummann, Steinig, et al., 2020; Ludwig, 1983; Shipboard_Scientific_Party, 1974a, d, 1980a). A Cretaceous-Tertiary unconformity that spans 25 My has been associated with a carbonate-poor ocean, as well as oceanographic changes in the Southern Ocean (e.g. Barker, 1977a; Ciesielski and Wise Jr, 1977; Dummann, Steinig, et al., 2020; Ludwig, 1983; Shipboard_Scientific_Party, 1974a, d, 1980a). The Paleogene and Neogene sequences include erosional and/or non-depositional unconformities that record major hiatuses (for details see Figure 2 in Najjarifarizhendi and Uenzelmann-Neben (2021)). The two most prominent unconformities, the Eocene-Oligocene and middle-late Miocene, have been linked to the onset of a proto-Antarctic Circumpolar Current (ACC) and intensified deep and bottom water production consequent to the perennial glaciation of Antarctica (e.g. Barker, 1977a; Barker and Thomas, 2004; Scher and Martin, 2006a; Shipboard_Scientific_Party, 1974a, c, d, 1980a).

In the oceanographic setting of the Southern Ocean, the southwest South Atlantic forms an important gateway for interoceanic exchanges of mass and energy. The F/MP lies in the pathway of the ACC (Figure 6.1a) and accommodates the transfer of a total of ~100 Sv of deep and bottom water masses (Arhan et al., 2002; Orsi et al., 1995). The water masses in the area are of different origins and comprise Weddell Sea Deep Water (WSDW), Antarctic Bottom Water (AABW), Lower Circumpolar Deep Water (LCDW), and Upper Circumpolar Deep Water (UCDW) (Arhan et al., 1999; Arhan et al., 2002; Orsi et al., 1999) (Figure 6.1a). Downstream of the Drake passage, at about 66°W, the major part of the ACC transport is diverted northward by the SAF and Polar Front (PF), which then form a western and an eastern branch after skirting the Burwood Bank (Fetter and Matano, 2008). The F/MB takes in the western branch on its way towards the Argentine Basin, while the eastern branch flows along the PF and rounds the MEB before merging with the western branch at 48°W to form the Falkland/Malvinas Current (Figure 6.1a).

6.4 Data and methods

6.4.1 Seismic reflection data

This study uses a subset (ca. 3300 km) of 2D seismic reflection data from the 2019 RV *Maria S. Merian* cruise MSM81 (Uenzelmann-Neben, 2019a), covering the central and the eastern sections of the F/MB and F/MT (solid lines in Figure 6.1b). The seismic source comprised an array of 4 GI-guns (Generator/Injector-gun) with a total volume of ca. 9.6 l and was fired every 25 m, producing signals with frequencies of up to 300 Hz and a dominant frequency of 80 Hz. For a reflector at depth of ca.

3000 m with an average velocity of 2500 m/s, considering signal frequency of 80 Hz, this implies $\cong 10$ m vertical resolution. Each individual GI-gun consisted of a generator chamber (0.72 l volume) and an injector chamber (1.68 l volume), the latter triggered with a 33 ms delay to minimize the bubble effect. The data were acquired using a 240-channel digital seismic streamer (SERCEL SEAL[©]) with a hydrophone array spacing of 12.5 m (total active length 3 km) and a 141.4 m-long lead-in cable. Data were recorded at a 1 ms sampling rate over a record length of 9 s.

Pre-processing of the seismic data included navigation merge, geometry definition, and common depth point (CDP)-sorting with a 25 m CDP spacing. Normal moveout (NMO) corrections were applied based on a precise velocity analysis (at least every 50 CDPs or ~ 1.25 km), using root-mean-square (RMS) velocity values in semblance method. Amplitude attenuation due to geometric spreading was accounted for in producing the stacked data. In order to reconstruct a true subsurface image, especially in areas with high reflector inclinations, an Omega-X post-stack time migration step (Yilmaz, 2001) was applied. In order to preserve amplitudes, no Automatic Gain Control filter (AGC) was used in the processing sequences or for display. Displayed sections include a bandpass filter with a Hanning Window taper with low and high boundaries of 5-30 Hz and 200-250 Hz, respectively. Appendix A summarizes the seismic data processing workflow.

Semblance velocity attribute as a means of RMS velocity analysis sweeps CDP gathers for a range of velocities along the time axis; where for matching velocities with reflector', semblance attribute gives higher correlation values (Yilmaz, 2001b). Seismic attributes were derived from the original seismic data using mathematical methods. These quantify the changes in characteristics of seismic waves, such as amplitude, frequency, phase, velocity, as they propagate throughout the earth layers and are subjected to varying physical properties (Aminzadeh and Dasgupta, 2013). Trace attributes are considered as convenient display forms, however they can also be used as analytic geophysical tools that provide information on lithological properties(Taner, 2001). In this study we use three post-stack geometrical attributes. Instantaneous frequency is the time derivative of the phase, which responds both to wave propagation effects as well as depositional characteristics. It is known as an indicator of lower frequency zones such as fracture zones or gas accumulations (Subrahmanyam and Rao, 2008). The first envelope derivative shows the variation of the energy of reflected events and is a good discriminator of absorption effects (Subrahmanyam and Rao, 2008). Energy attribute is a measure of reflectivity in specified time windows, which is useful for amplitude anomaly detection. meaning higher energy correlates with higher reflectivity (Johnston, 2010) .

6.4.2 Drilling data and age model

DSDP Legs 36 and 71 drilled four Sites 327, 329, 330, and 511 in the westernmost MEB (Figure 6.1b). Results from each drill site, including water depth, total drilled and cored depths, total core recovery, and lithological information, are summarized in Figure 6.2 (Shipboard_Scientific_Party, 1974a, c, d,

1980a). Results from each site, including water depth, total depths drilled and cored, total core recovery, and lithological information, are summarized in Figure 6.2. No downhole geophysical logs were acquired at the four DSDP Sites, but velocity measurements on cored sections yielded interval velocities which we used to convert from the depth to time domains (Najjarifarzhendi and Uenzelmann-Neben, 2021). The velocity data were used to correlate information from the drill sites with seismic profiles in order to construct an age-constrained stratigraphic model for the eastern part of the F/MP (see Appendix B).

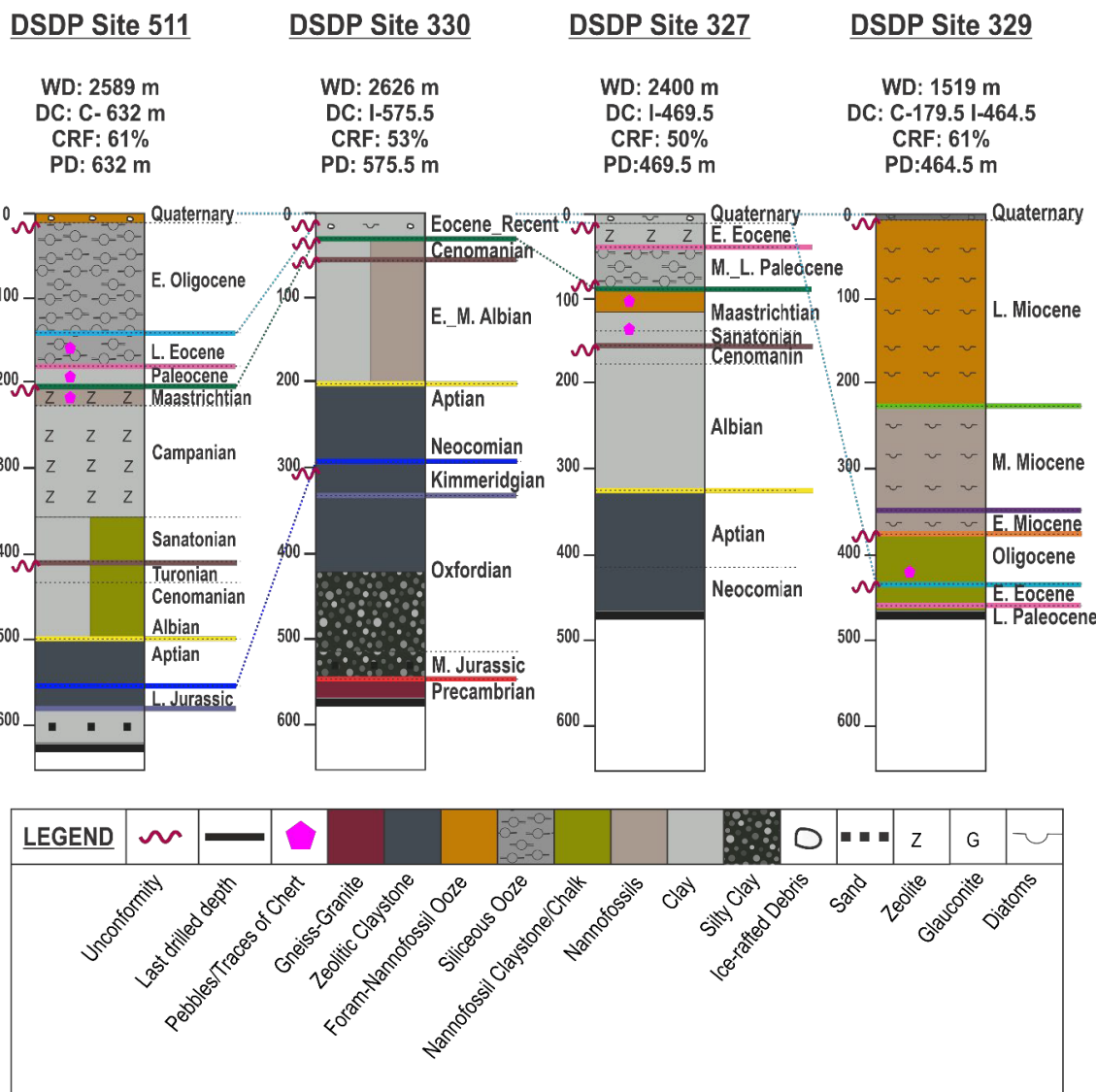
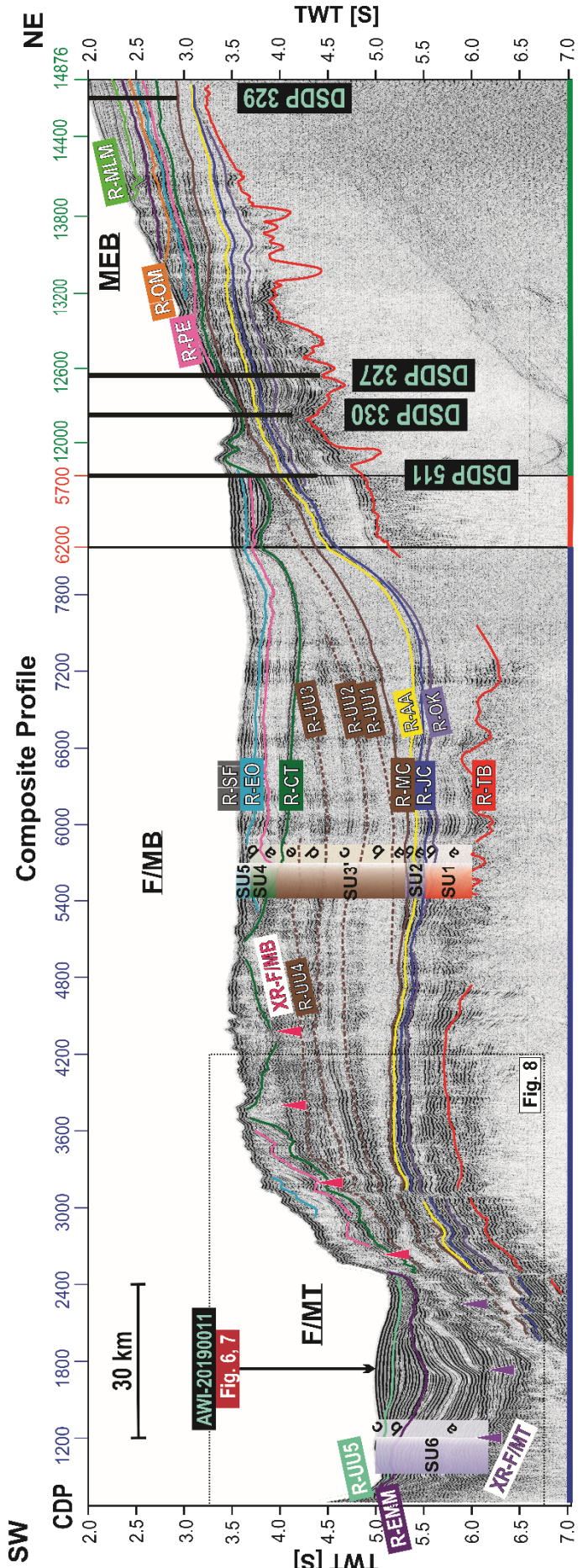


Figure 6.2: Summary of results from DSDP Leg 36 Sites 327, 329, and 330 and Leg 71, Site 511 (Shipboard_Scientific_Party, 1974a, c, d, 1980a). Schematically shown are the lithological information, hiatuses, and geological ages reported at each site plotted against depth below seafloor. WD, DC (C or I), PD, and CRF values stated for each site respectively represent Water Depth, Drilled Core (Continuously Cored or Intermittently Cored), penetration depth, and Core Recovery Factor. The marker horizons defined in the seismostratigraphic model are also color marked (for details, see Figure 6.4, Section 6.5.1, and Appendix B).



AWI-20190004 **AWI-20190008** **AWI-20190001**

Figure 6.3: Interpreted composite seismic profile (from profiles AWI-20190001, AWI-20190008, AWI-2019004). Location of profile is shown in Figure 6.1b. Superimposed are the marker horizons defined in the seismostratigraphic model (for details, see Figure 6.4, Section 6.5.2, and Appendix B). The location of DSDP Sites 327, 329, and 330 and Leg 71, Site 511 crossed by the seismic lines are marked with thick black lines. The pink and purple triangles respectively mark the cross-cutting reflectors XR-F/MB and XR-F/MT (for details, see Section 6.5.2). The black box marks the zoomed section shown in Figure 6.8. Arrow shows the location of crossing seismic profile.

6.5 Results

6.5.1 Stratigraphic context

Seismic reflection profiles correlated to drilling data show the study area to consist of Precambrian basement overlain by a sedimentary succession up to 3 km thick, that records deposition since the middle-late Jurassic (Figures 6.3 and 6.4) (Najjarifarizhendi and Uenzelmann-Neben, 2021). Previous work by Najjarifarizhendi and Uenzelmann-Neben (2021) on the MEB, has divided the succession into five main units , shown in Figure 6.3 on a composite profile crossing DSDP Sites. The stratigraphic model is detailed in Appendix B, including modifications adopted in this study in extending it towards the F/MB and F/MT. Unit SU3 has been modified to SU3' to represent late Cretaceous strata within the F/MB, which unlike the MEB includes thick packages subdivided into five subunits separated by four unconformities. Furthermore, the distinct mounded morphology of Post-Oligocene strata within the F/MT, which is dissimilar with strata of the same age elsewhere on the F/MP, called for introducing Unit 6.

6.5.2 Cross-cutting reflectors

6.5.2.1 Reflector XR-F/MB

In the F/MB, a very high amplitude, continuous to discontinuous reflector extends (sub)parallel to the seafloor (reflector R-SF) and cross-cuts reflectors of (sub)units SU3'-e, SU4 and SU5 (Figure 6.3, AWI-20190004, CDPs 2500-5000, Figure 6.5a, CDPs 2000-5000, and Figure 6.6, CDPs 600-8000). The reflector is identified on seismic profiles southwards from ca. 50°S in the F/MB and in places can be traced onto the northern flank of the F/MT. Reflector XR-F/MB is mostly recognized within the western and central parts of the F/MB, whereas towards the east it becomes difficult to trace (Figures 6.3 and 6.5a). Reflector XR-F/MB has the same polarity as seafloor reflector R-SF (Figure 6.5b) and appears as a high-energy interface using the seismic attribute energy, which is proportional to the reflection coefficient of the reflecting interface (Figure 6.5d). Reflector XR-F/MB lies 500-550 ms TWT below seafloor (msbsf TWT) and shoals slightly towards the south with increasing water depth (Figure 6.6a). Reflector XR-F/MB in places shows serrated reflection patterns (Figure 6.6b),including asymmetrical saw-tooth morphologies with heights ranging from 20-60 ms TWT.

6.5.2.1 Reflector XR-F/MT

Reflector XR-F/MB can in places be traced onto the northern flank of the F/MT , where it gives way to a continuous and very high amplitude reflector (hereafter called reflector XR-F/MT) that cross-cuts the host strata of subunit SU6-a within the F/MT (Figure 6.3, AWI-20190004, CDPs 1200-2400 and Figure 6.6, CDPs 8600-10600). Reflector XR-F/MT has high reflectivity (Figure 6.5d) and the same polarity as the seafloor reflector R-SF (Figure 6.5c). Reflector XR-F/MT is not parallel to the seafloor

reflector in the F/MT; instead, it seems to replicate the geometry of reflector R-EMM (Figure 6.3, AWI-20190004, CDPs 1000-2500 and Figure 6.6, CDPs 8600-10600). This reflector is identified between ca. 46- 49°W across the F/MT.

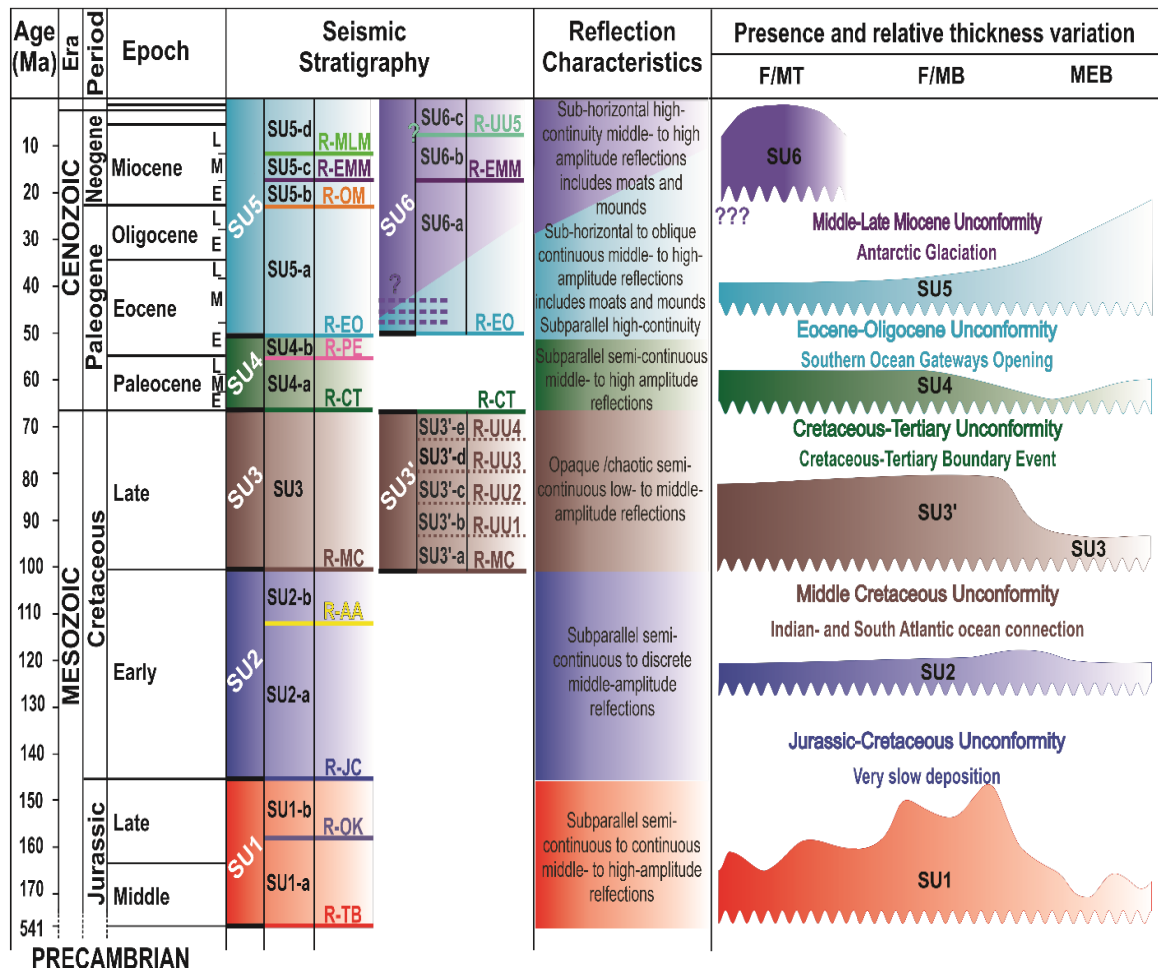


Figure 6.4: Summary of the seismostratigraphic model for the Falklands/Malvinas Plateau, showing units and marker horizons (at left), generalized reflection characteristics (middle column) and relative thickness variations (right-hand column). Left column is the seismostratigraphic model and seismic units across the Falkland/Malvinas Plateau . The marker horizons and seismic units for the eastern sector of the Falkland/Malvinas Plateau, after Figure 2 in Najjarifarizhendi and Uenzelmann-Neben (2021) have been modified to include the new seismic unit SU3' in the F/MB (for more details, see Figure 6.5, section 6.5.1 and Appendix B.2) and the new seismic unit SU6 in the F/MT (for details, see Figure 6.3 and 6.5, section 6.5.1 and Appendix B.2). Unit SU3' is introduced to represent late Cretaceous strata in the F/MB, which unlike its coeval strata on the MEB (SU3), comprises 5 distinct subunits. Unit SU6, has been introduced to include the strata of post-Oligocene with a unique mounded morphology, restricted to F/MT, and differentiable from underlying unit SU5 elsewhere on the Falkland/Malvinas Plateau.

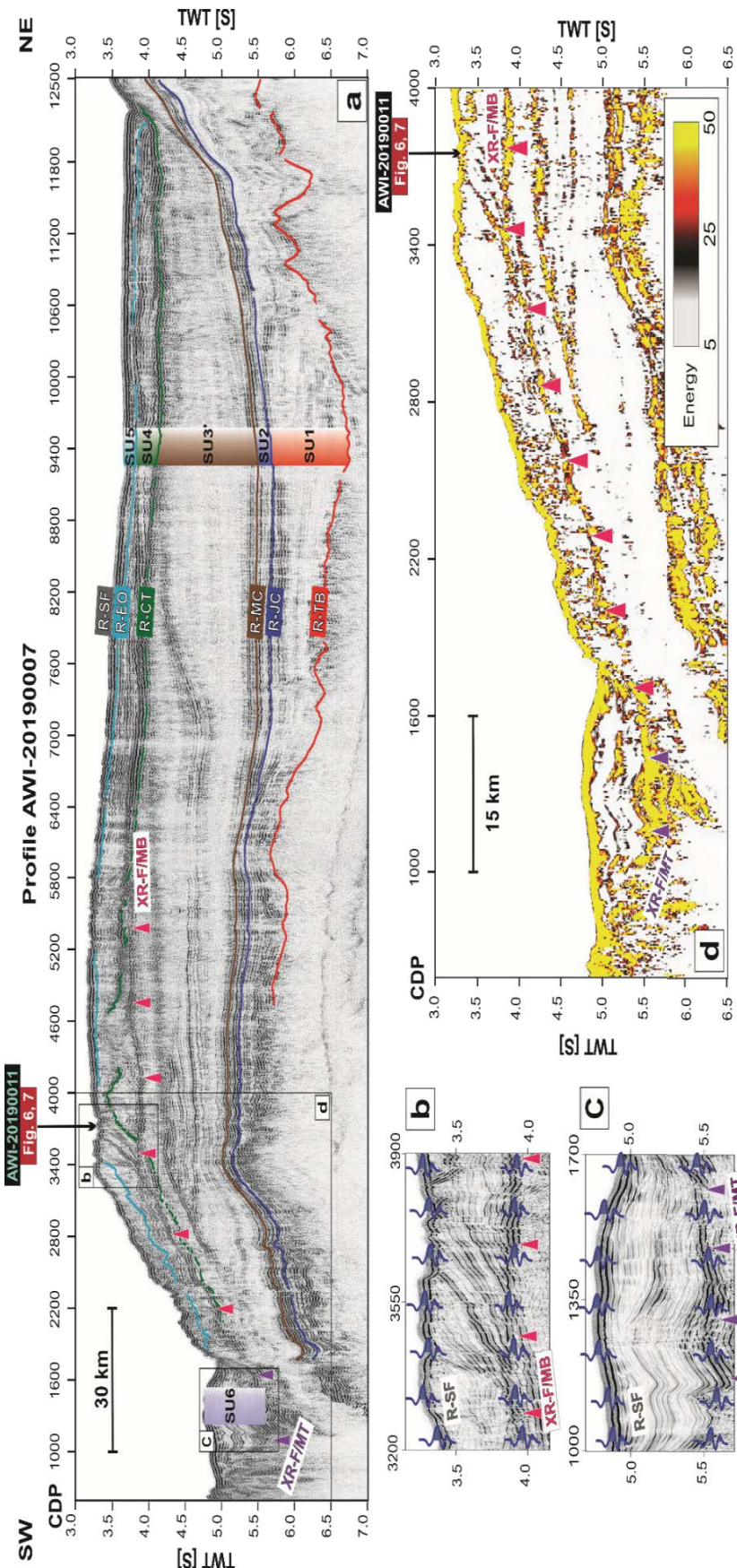


Figure 6.5: (a) Interpreted seismic profile AWI-20190007. Location of profile is shown in Figure 6.1b. Superimposed is the defined seismic stratigraphy and the marker horizons (for details, see Figure 6.4, Section 6.5.2 and Appendix B). The pink and purple triangles respectively mark the cross-cutting reflectors XR-F/MB and XR-F/MT (for details, see Sections 6.5.2 and 6.5.3). Black boxes mark the zoomed sections shown in (b), (c), and (d). Arrow shows the location of crossing seismic profile. (b) and (c) Zoomed sections respectively showing the cross-cutting reflectors XR-F/MB and XR-F/MT; schematically shown are the polarity of the cross-cutting reflector compared to the seafloor reflector, typical of a positive polarity (for details, see Sections 6.5.2 and 6.5.3). (d) Zoomed section showing the seismic attribute “energy” (for details, see Section 6.5.3). Arrows show the location of crossing seismic profile.

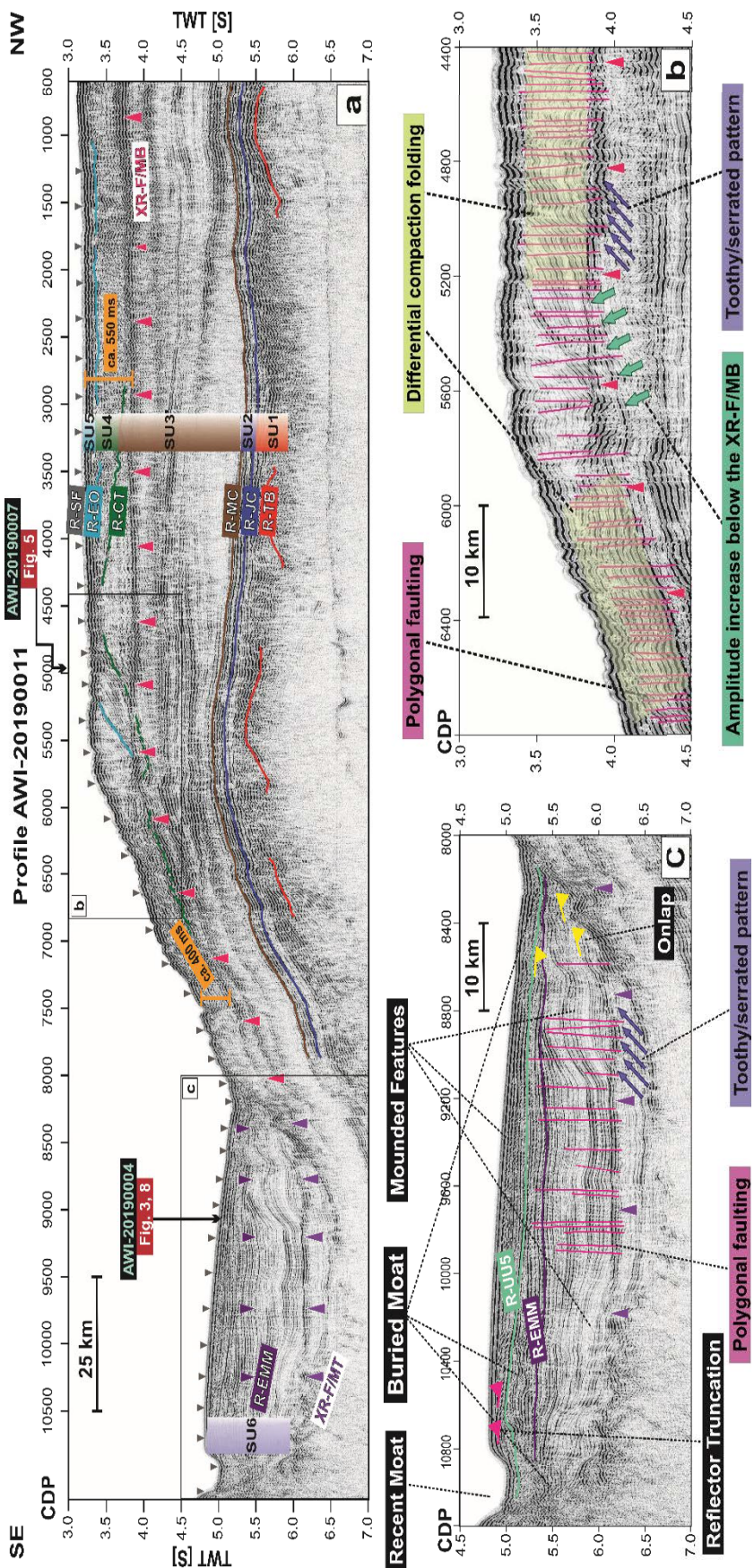


Figure 6: (a) Interpreted seismic profile AWI-20190011. Location of profile is shown in Figure 6.1b. Superimposed is the defined seismic stratigraphy and the marker horizons (for details, see Figure 6.4, Section 6.5.1 and Appendix B). The gray and violet triangles respectively mark the seafloor reflector (R-SF) and the early-middle Miocene unconformity (R-EMM). The pink and purple triangles respectively mark the cross-cutting reflectors XR-F/MB and XR-F/MT (for details, see Sections 6.5.2 and 6.5.3). The black boxes mark the zoomed sections shown in (b) and (c). Arrows show the location of crossing seismic profiles. (b) and (c) Zoomed sections respectively showing the peculiar structural features in proximity of the cross-cutting reflectors XR-F/MB and XR-F/MT (for details, see Section 6.5.3).

6.5.3 Distinctive features associated with cross-cutting reflectors

In the presence of reflector XR-F/MB, adjacent strata, including (sub)units SU3'-e, SU4 and SU5, in places are highly affected by faulting (Figure 6.6b). Numerous small-scale faults with average throws of about 40 ms TWT have deformed the strata surrounding reflector XR-F/MB, where partially serrated reflection patterns are formed (Figure 6.6b). The fault displacements decrease throughout subunits SU3'-a to SU3'-d and most do not propagate into underlying strata (compare the strata below and above reflector XR-F/MB in Figure 6.6b, CDPs 6000-6800). In comparison, reflector XR-F/MT is less affected by fault sets, yet the faults have similar characteristics to those in the F/MB (Figure 6.6c, CDPs 8600-10000). These faults show small throws, no systematic orientation, and mainly deform strata above reflector XR-F/MT including subunits SU6-a and SU6-b.

Considering reflectors from the same stratal units, successions below the cross-cutting reflector XR-F/MB show higher amplitudes than those above (Figure 6.6b). Above reflector SR-F/MB, internal reflectors of (sub)units SU3'-e, SU4, and SU5 locally show irregular deformation features as product of faulting (Figure 6.6b). These include a series of anti- and synclinal folds, with an average wavelength of ca. 1250 m, that are not characteristic of these units elsewhere on the F/MB.

Seismic attributes provide information on the cross-cutting reflectors (Figures 6.7 and 6.8). Reflectors XR-F/MB and XR-F/MT both appear as high-velocity reflections on semblance attribute sections, which provide a measure of the RMS velocity values (Figure 6.7). Across both reflectors, an average velocity increase of about 75 m/s is observed on semblance profiles. Interval velocity sections also indicate a noticeable increase across these two reflectors (Figure 6.7a).

Instantaneous frequency attribute sections show no significant change across reflectors XR-F/MB and XR-F/MT, indicating that they are not associated with strong changes in frequency content (Figure 6.8a). The low absorption effect of reflectors XR-F/MB and XR-F/MT is also inferred from the seismic attribute first envelope derivative, which indicates little change in energy across the reflecting interfaces (Figure 6.8b).

6.6 Discussion

The cross-cutting character of reflectors XR-F/MB and XR-F/MT (Figures 6.3, 6.5a and 6.6a) clearly indicate them to be products of post-depositional processes. Below, we present arguments for their origin as fossilized silica diagenetic fronts and their palaeoceanographic implications.

6.6.1 Diagenetic origin of cross-cutting reflectors

DSDP Sites 327 and 511 documented the prevalence of siliceous ooze in the Post-Tertiary sediments and traces of chert in late Cretaceous sediments (Ciesielski and Wise Jr, 1977; Shipboard_Scientific_Party, 1974a, d, 1980a) (Figure 5.2). Piston and Kasten cores also provide

evidence for Neogene silica-rich sediments across the F/MT (Allen et al., 2011; Allen et al., 2005; Cunningham, 1999; Rivas, 2018; Saito et al., 1974). From a lithological perspective, supports the diagenetic nature of reflectors XR-F/MB and XR-F/MT, since silica diagenesis can only take place in presence of silica-rich sediments (Berndt et al., 2004).

The two cross-cutting reflectors have the same positive (normal) polarities as the seafloor reflector (Figures 6.5b and 6.5c). This observation rules out their origin as GH-BSRs, which are associated with negative (reversed) polarities due to the presence of gas beneath the BGHS. The very high positive amplitudes of reflectors XR-F/MB and XR-F/MT (Figures 6.3, 6.5a, and 6.6a) are instead consistent with the expected characteristics of a TZ_{A/CT}, for which silica diagenesis causes porosity and water content to drop considerably, leading to decreased acoustic impedance (Bohrmann et al., 1992; Davies and Cartwright, 2002; Hein et al., 1978).

In general, reflections from the same seismic event show an increase in amplitude below reflector XR-F/MB (Figure 6.6b). This observation could be due to the presence of Opal-CT below the TZ_{A/CT}, which leads to higher acoustic impedance and thus to stronger reflectivity (Berndt et al., 2004; Bohrmann et al., 1992; Davies and Cartwright, 2002; Hein et al., 1978). The serrated character of the cross-cutting reflector observed in some places is considered to be due to variations in Opal-A content of the overlying strata which result in preferential upward advancement of TZ_{A/CT} in zones with Opal-A-rich content (Varkouhi et al., 2022).

Semblance profiles and interval velocity sections (Figure 6.7) indicate a noticeable velocity increase below reflectors XR-F/MB and XR-F/MT, typical of diagenetic fronts (e.g. Guerin and Goldberg, 2002; Hesse, 1988; Isaacs, 1981; Meadows and Davies, 2010; Nobes et al., 1992). Moreover, no significant lateral variations in interval velocities are observed within the top 1500 msbsf TWT, inclusive of units SU4 and SU5 and reflector XR-F/MB (Figure 6.7a). Hence, the observation that reflector XR-F/MB shoals in greater water depth on the seismic profiles (Figure 6.6) is not velocity dependent and can be attributed to the actual subsurface geometry. This phenomenon has been explained for TZ_{A/CT} by the higher effective pressure of the water column as the water depth increases (Berndt et al., 2004).

The instantaneous frequency attribute has been used to identify free-gas zones, for example below the BGHS (e.g. Geletti and Busetti, 2011; Kim et al., 2013; Taylor et al., 2000; Vanneste et al., 2002). No drastic drop in frequency content is observed below reflectors XR-F/MB and XR-F/MT, as expected for a GH-BSR (Figure 6.8). The seismic attribute first envelope derivative displays rapid changes across reflectors XR-F/MB and XR-F/MT indicating a wide bandwidth and weak absorption effects (Figure 6.8ig). Seismic units SU4 and SU5 are extremely affected by small-scale fault sets (throw values \approx 40 ms TWT), especially where reflectors XR-F/MB and XR-F/MT are present (Figure 6.5d, 6.6b and 6.6c). Since these faults do not show a particular orientation and are layer-bound (confined to specific stratigraphic units) without any indication for a deeper tectonic origin, we categorize these as polygonal faults associated with the abrupt compaction across the TZ_{A/CT} (Bünz et al., 2003; Davies et al., 2009;

Nouzé et al., 2009; Volpi et al., 2004). Folds, observed above reflectors XR-F/MB and XR-F/MT within seismic units SU4 (Figure 6.6b), interpreted as features of differential compaction, as observed in other areas associated with silica transformation (Davies, 2005; Neagu et al., 2010; Varkouhi et al., 2022).

6.6.2 Cross-cutting reflectors as fossilized silica diagenetic fronts

Reflector XR-F/MB is a BSR observed at a constant depth of 500-550 msbsf TWT, while reflector XR-F/MT is an NBSR that varies in depth relative to the seafloor (Figure 6.6a). A BSR does not necessarily indicate an active diagenetic front (Varkouhi et al., 2022), while an NBSR clearly points to the presence of a fossilized diagenetic front (Table 6.1) and allows interpretation of reflector XR-F/MT as a fossilized TZ_{A/CT}. A BSR does not necessarily indicate an active diagenetic front (Varkouhi et al., 2022), and the structural peculiarities associated with reflector XR-F/MB, including polygonal faults and differential compaction folds (Figure 6.6b), argue in favor of its fossilized nature.

Fossilized diagenetic fronts in disequilibrium with present-day isotherms have been hypothesized to be the products of rapid changes in the regional thermal regime, or of long-lasting erosional phases within sedimentary basins (Meadows and Davies, 2010; Varkouhi et al., 2022). The fossilization time can be estimated from identification of the shallowest horizon with the same geometry as reflector XR-F/MT, which would have been the seafloor at the time of fossilization (arrest of the diagenetic front). This approach has been applied in several studies to estimate the time when upward migration of the TZ_{A/CT} ceased (Davies and Cartwright, 2002; Meadows and Davies, 2010; Neagu et al., 2010). The seafloor in the F/MB, which we interpret to be an erosional surface, is formed by a middle-late Miocene reflector that dips southwards below younger strata in the F/MT (Figures 6.3 and 6.6a). Piston and gravity sampling in the F/MB retrieved sediments of Oligocene-Miocene ages at seafloor (Saito et al., 1974).

The study of the processes which could contribute to the development of fossilized diagenetic fronts is still in its infancy, but such features are recognized to represent regional palaeo-isotherms (Meadows and Davies, 2010). Both reflectors XR-F/MB and XR-F/MT show good correspondence with the geometry of reflectors dated as middle-late Miocene (R-SF in F/MB and R-EMM in F/MT), suggesting this surface to have been the palaeo-isotherm that resulted in the formation of the fossilized TZ_{A/CT} across the F/MB and F/MT (Figures 6.3 and 6.6a).

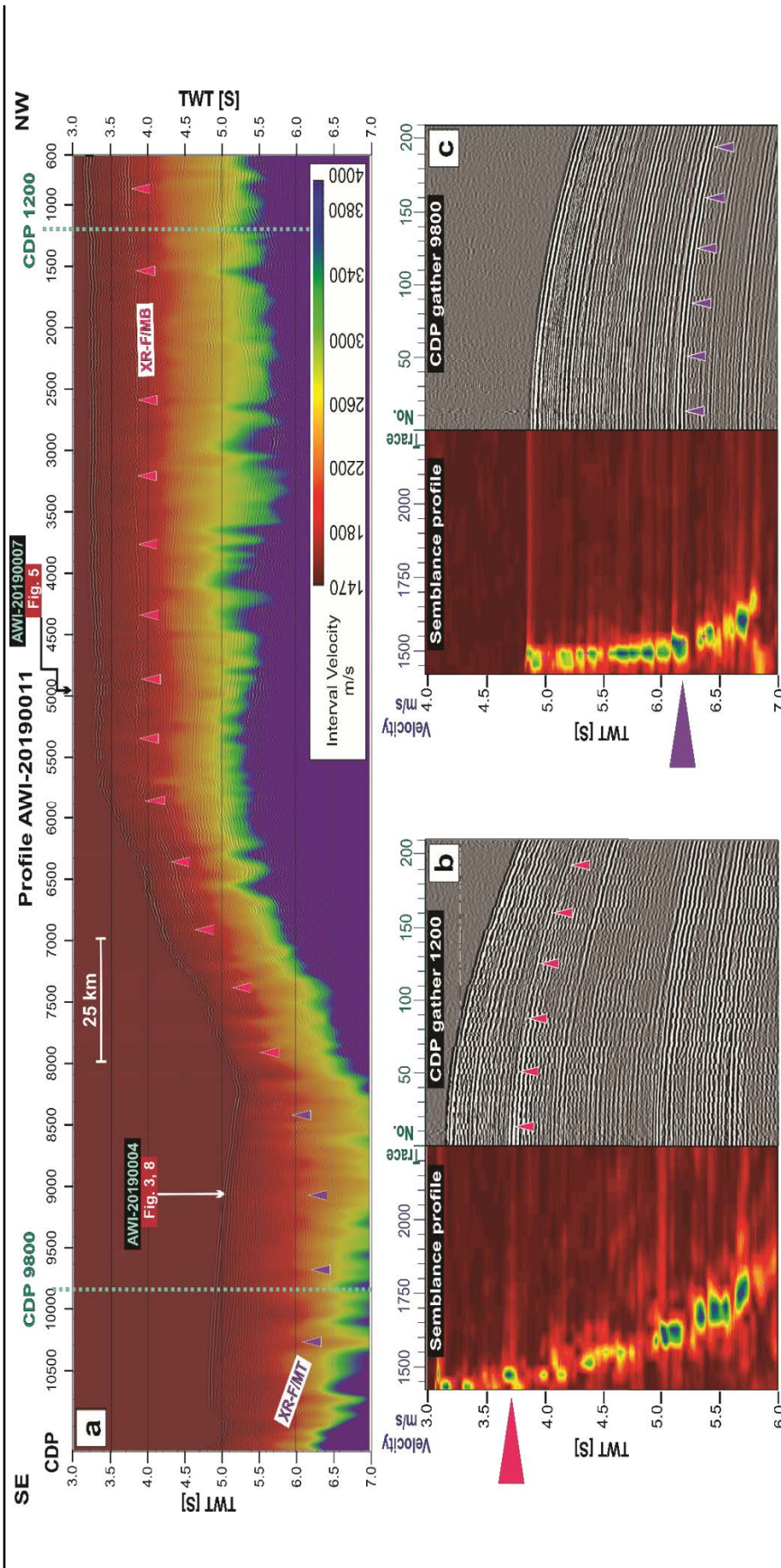


Figure 6.7: (a) Seismic profile AWI-20190011. Location of profile is shown in Figure 6.1b. The pink and purple triangles respectively mark the cross-cutting reflectors XR-F/MB and XR-F/MT (for details, see Section 6.5.2). Superimposed on the seismic section is the interval velocity section calculated from the seismic stacking velocity data, where the color scale gives the velocity values. Dashed cyan lines show the location of CDP 1200 and 9800. (b) and (c) respectively show the extent of reflectors XR-F/MB and XR-F/MT on the CDP gathers and semblance profiles (for details, see Sections 6.5.2 and 6.5.3). Arrows show the location of crossing seismic profiles

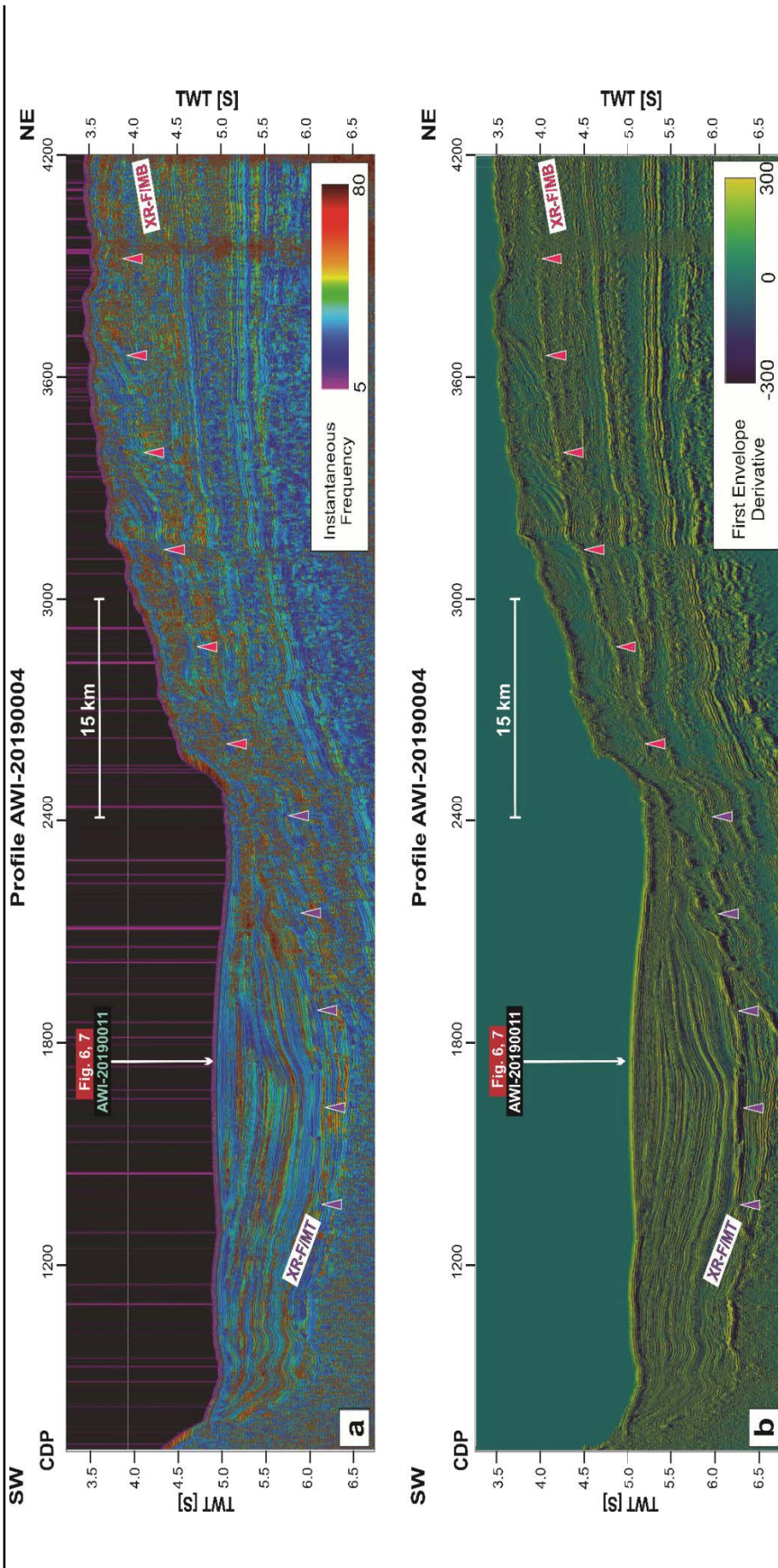


Figure 6.8: Section from seismic profile AWI-2019004. Location of profile is shown in Figure 6.1b. The pink and purple triangles respectively mark the cross-cutting reflectors XR-F/MB and XR-F/MT (for details, see Section 6.5.2) and (b) Superimposed on the seismic profiles are respectively the instantaneous frequency and the first envelope derivative attribute section calculated from the seismic data, where the color scale gives the corresponding values (for details, see Sections 6.5.2 and 6.5.3). Arrows show the location of crossing seismic profiles.

6.6.3 Implications for regional palaeoceanographic evolution

The process of Opal-A to -CT (Opal-A/CT) conversion is primarily controlled by temperature (e.g. Hein et al., 1978; Kastner et al., 1977a; Nobes et al., 1992; Varkouhi et al., 2020). In sedimentary basins where observed O_{A/CT}_BSRs were validated by borehole data, the reported temperatures for the Opal-A/CT conversion exceeded 35°C (Berndt et al., 2004; Kuramoto et al., 1992; Neagu et al., 2010). Based on a study of progressive siliceous ooze diagenesis at Leg 19 DSDP Sites, Hein et al. (1978) also found that temperatures exceeding 35°C, effective at least for 10 My, were required for Opal-A/CT conversion in shallow marine sediments.

Geothermal gradients are available from temperature measurements in two boreholes within the study area. DSDP Site 511 in the easternmost sector of the F/MB yielded a value of 74°C/km (Langseth and Ludwig, 1983), and commercial borehole Loligo-1 in the westernmost sector of the F/MP reported 38.5°C/km (Nicholson and Stow, 2019) (Figure 6.1). In addition, based on analysis of a gas hydrate BSR, Baristeas et al. (2012) estimated a value of 23.9±2.0 °C/km in the Malvinas Basin, southwest of the F/MI. These values give an average thermal gradient of 45°C/km. Seafloor temperature measurements at the locations of DSDP Site 511 (Langseth and Ludwig, 1983) and Loligo-1 (Nicholson and Stow, 2019), respectively, were 0.7 and 2 °C. These are in good agreement with oceanographic data from the F/MB, which indicate bottom water temperatures below 1.8 °C for the F/MB at water depths > 2000 m, where influenced by LCDW (Arhan et al., 2002).

The temperature T (°C) at depth z (meters below seafloor (mbsf)) for a supposed temperature gradient $\frac{dT}{dz}$ (°C/km) and seafloor temperature T_{SF} (°C) is given by $T(z) = \frac{dT}{dz} * \frac{z}{1000} + T_{SF}$. The depth z (mbsf) of an observed reflector on the seismic section can be estimated by means of P-wave velocity v (m/s) and Two-way travel-time (msbsf TWT), given by $z = vt/2$. Reflector XR-F/MB lies on average 550 msbsf TWT (Figure 6.6a), and interval velocities average 1900 m/s for the shallow marine sediments in the F/MB (Figure 6.7). Using an average thermal gradient of 45 °C/km and seafloor temperature of 1 °C for the F/MB, the estimated temperature at the TZ_{A/CT} equals 22.3 °C. Taking 35 °C as the minimum required temperature for onset of Opal-A/CT conversion (Berndt et al., 2004; Hein et al., 1978; Kuramoto et al., 1992; Neagu et al., 2010), the calculated temperature at the present depth of TZ_{A/CT} in the F/MB cannot account for this transition.

One possible explanation for the cessation of upward movement of the TZ_{A/CT} at the F/MB is a rapid temperature drop at the seafloor in response to the onset of the ACC, when southern-sourced cold water masses reached the plateau at about the Eocene-Oligocene boundary (e.g. Barker, 1977a; Najjarifarizhendi and Uenzelmann-Neben, 2021; Scher and Martin, 2006a; Scher and Martin, 2006b; Uenzelmann-Neben et al., 2017). Benthic foraminiferal proxy records at DSDP Site 511 suggest a temperature drop from 8-12.5 °C in the Eocene to ca. 2 °C in Oligocene times (Muza et al., 1980).

Although a 10°C temperature variation at the seafloor is significant, it cannot account for the thermal conditions required for the Opal-A/CT conversion in the F/MB. This implies a temperature of 32.3°C at depth of reflector XR-F/MB, which is below the minimum temperature 35°C suggested in the literature (Berndt et al., 2004; Hein et al., 1978; Kuramoto et al., 1992; Neagu et al., 2010) for the initiation of silica diagenesis.

A past regime of higher geothermal gradients could account for the present depth of the arrested silica diagenetic front across the F/MB. However, the present-day geothermal gradient measured at DSDP 511 (74 °C/km) is already higher than those reported in neighboring areas, such as Malvinas Basin (23.9 ± 2.0 °C/km) (Baristeas et al., 2012) and westernmost sector of the F/MP (38.5 °C/km) (Nicholson and Stow, 2019). An alternative means to account for the arrest of the silica diagenetic front is the removal of overburden, the presence of which would have implied higher temperatures at depth. Taking 45 °C/km as the thermal gradient in the F/MB, an excess of ca. 270 m overburden would account for the minimum thermal requirement for Opal-A/CT conversion. This explanation is supported by analysis of the organic carbon content in sediments of Jurassic to Recent age at DSDP Site 511, which indicate an unusually high rate of maturation vs. burial depth (Dick et al., 1983). These authors relate this to either higher palaeo-thermal gradients of up to 100 °C/km or the removal of up to 400 m of overburden above the Cretaceous-Tertiary unconformity, or a combination of both. From seafloor exposures of Mesozoic sediments containing traces of well-lithified chert, Ciesielski and Wise Jr (1977) inferred erosion of a minimum of 150-200 m of sediments on the shoulder of the MEB near DSDP 330 (Figure 6.3, AWI-20190001, CDPs 12100-12400).

The major erosional and non-depositional unconformities within the post-Tertiary sections at DSDP Sites 327, 329, 330, and 511 on the F/MP have been linked to the influx of deep and bottom water masses subsequent to the opening of the Drake Passage (Barker, 1977a; Ciesielski and Wise Jr, 1977; Shipboard_Scientific_Party, 1974a, d, 1980a). The most extensive erosional phase has been attributed to the late Miocene, with intensified deep and bottom water formation in response to the growth of ice sheets in Antarctica (Shipboard_Scientific_Party, 1974a, c). The absence of sedimentary strata younger than the Miocene in drill core data in the F/MB (Shipboard_Scientific_Party, 1980a), the exposure of the early-middle Miocene horizon at the seafloor as observed on seismic data, and the abraded/hummocky texture of the seafloor on seismic (Figure 6.3, AWI-20190004, CDPs 2500-5500) and Parasound profiles (Uenzelmann-Neben, 2019a), together suggest that oceanic circulation on the F/MP has been relatively stable since at least the middle-late Miocene. Palaeoceanographic investigations using contouritic features across the MEB also concluded a relatively uniform intensity and pathway for LCDW since at least the middle Miocene (Najjarifarizhendi and Uenzelmann-Neben, 2021). In today's oceanic setting, the oceanographic data place the velocity core of the LCDW at depths of 2000-3000 m, overspilling the F/MB and entering the Argentine basin (Arhan et al., 1999; Arhan et al., 2002; Orsi et al., 1999).

We thus hypothesize that the large-scale reorganization of oceanic circulation following the opening of the Southern Ocean gateways and the onset and intensification of the ACC was responsible for the scouring and removal of at least 270 meters of sediment across the F/MB. The prominent erosional phase in the early-middle Miocene may have driven the fossilization of the silica diagenetic fronts in the F/MB and the F/MT. We interpret the early-middle Miocene erosional surface, which seems to have defined the present-day seafloor at the F/MB, as the palaeo-seafloor in the F/MB and F/MT at the time of fossilization of silica diagenetic fronts.

6.7 Conclusions

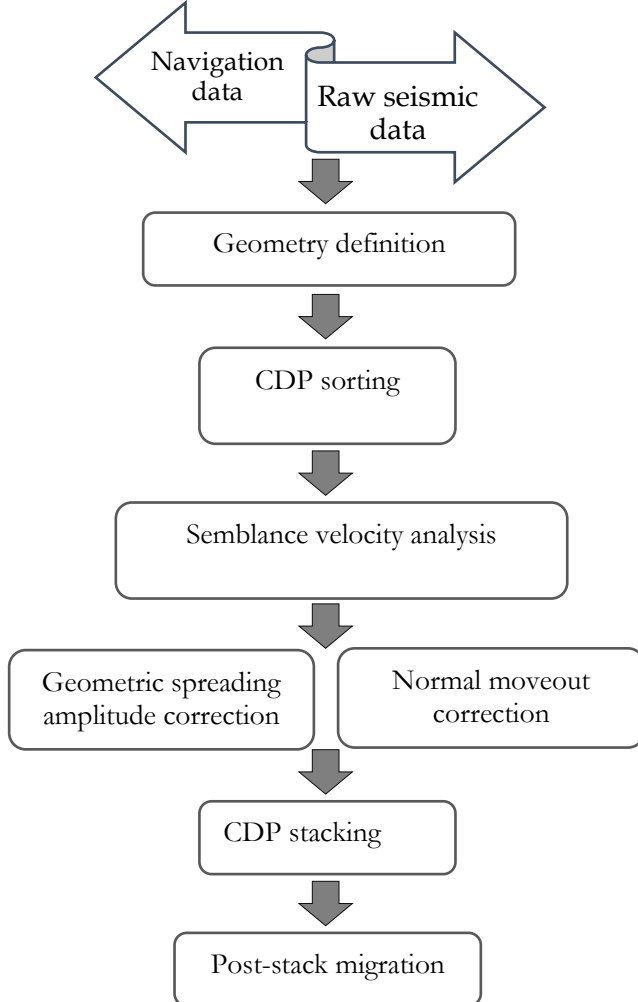
Two high amplitude cross-cutting reflectors of normal (non-reversed) polarity are identified across the F/MB and F/MT using a set of new high-resolution seismic reflection profiles. Reflector XR-F/MB appears as a BSR, observed at about 500 msbsf TWT. In contrast, reflector XR-F/MT is an NBSR, which shows correlation with the geometry of a shallower reflector (reflector R-EMM), an early-middle Miocene unconformity that also shapes the seafloor in the F/MB.

The seismic and geometrical properties of reflectors XR-F/MB and XR-F/MT, together with lithological indications from DSDP Sites 327, 329, 330, and Site 511, allow these two cross-cutting reflectors to be associated with the Opal-A to Opal-CT transition zone. However, estimated temperatures at the present depth for these two reflectors based on regional geothermal gradients lie below the minimum temperatures known for the onset of silica diagenesis.

The geometrical characteristics of the two cross-cutting reflectors relative to the seafloor, as well as the presence of deformation features in strata between these reflectors and the seafloor reflector (polygonal faults and differential compaction folds) supports their interpretation as fossilized or arrested silica diagenetic fronts. The arrest of this boundary can be explained by a temperature drop due to widespread erosion and sediment removal by the action of abyssal water masses. It is hypothesized that the erosional action of intensified deep and bottom water masses at early-middle Miocene subsequent to Antarctic glaciation may have driven the fossilization of the diagenetic front in the study area. Erosion of a minimum of 270 m of overburden is estimated to have occurred, accounting for thermal conditions leading to the fossilization of the silica diagenetic fronts.

Appendices

Appendix A: Seismic processing Workflow.



Appendix B:

Appendix B.1. is a review of the stratigraphic model of five units developed for the MEB by (Najjarifarizhendi and Uenzelmann-Neben, 2021). In appendix B.2., modifications to the stratigraphic model by Najjarifarizhendi and Uenzelmann-Neben (2021) is presented to extend the model towards the F/MB and F/MT. The modified model introduced units SU3' and SU6, which are unique and restricted to the F/MB and F/MT.

B.1. Seismic stratigraphy.

Unit SU1 is bound by base reflector R-TB and top reflector R-JC, which respectively represent the top of the acoustic basement and the Jurassic-Cretaceous unconformity, and has semi-continuous to continuous middle-amplitude internal reflections (Figures 6.3 and 6.5a). This unit wedges out on more

elevated parts of the MEB (Figure 6.3, AWI-20190001, CDPs 12000-14800), while it shows a variable thickness of up to 2000 ms TWT towards the F/MB. Unit SU1 fills basement troughs and follows the topography of the basement (Figure 6.5a, CDPs 5000-12500).

Units SU2 and SU3 represent the Cretaceous strata, separated by a middle Cretaceous unconformity (reflector R-MC) (Figures 6.3 and 6.5a). Reflectors R-JC and R-MC respectively are the base and top boundaries of unit SU2. This unit has subparallel semi-continuous reflections within the F/MB and shows a constant thickness of ca. 250 ms TWT throughout the basin. Unit SU2 forms wedges up to 400 ms TWT thick on the shoulder of the MEB, which thin across more elevated parts of the MEB (Figure 6.3, AWI-20190004, CDPs 6500-8170).

Unit SU2 is overlain by Unit SU3 with reflector R-MC at the base and reflector R-CT, a regional Cretaceous-Tertiary unconformity, at the top (Figures 6.3 and 6.4). In the proximity of the MEB, Unit SU3 shows semi-continuous middle- to high-amplitude internal reflections and has its minimum thickness (less than 100 ms TWT) (Figure 6.3, AWI-20190001, CDP 12000-14800). Within the F/MB, however, unit SU3 thickens strongly to more than 2000 ms TWT and shows distinct internal structures (Figure 6.3, AWI-20190004, CDP 3000-7000). These strata developed in a different depositional setting in the F/MB compared to the MEB. Therefore, the stratigraphic model is modified for seismic unit SU3 in the F/MB (Unit SU3'). For details see Appendix B.2.1 and Figure 6.4.

Units SU4 and SU5 comprise the Cenozoic strata (Figure 6.4). Reflector R-EO, which represents the Eocene-Oligocene unconformity, bounds Unit SU4 at the top (Figures 6.4 and 6.5). Unit SU4 includes subparallel, semi-continuous to continuous, high-amplitude, undulated internal reflections which onlap Reflector R-CT at the base and are erosionally truncated at the top by Reflector R-EO (Figure 6.5a, CDPs 2000-12000). Unit SU4 shows extreme thinning on the shoulder of the MEB (Figure 6.3, AWI-20190001, CDPs 12000-13000) but is present in the F/MB with up to 400 ms TWT in thickness (Figure 6.5a, CDPs 2000-12000).

Unit SU5 lies unconformably on reflector R-EO and is bounded at the top by the seafloor reflector (R-SF) (Figures 6.3 and 6.4). This unit has its largest thickness (up to 1000 ms TWT) on top of the MEB. In general, it shows sub-horizontal to oblique, middle- to high-amplitude, high continuity, and wavy internal reflections (Figures 6.3 and 6.5). Within the F/MB, Unit SU5 has similar reflection characteristics, with a thickness less than 350 ms TWT (Figure 6.3, AWI-20190004, CDPs 3000-8000). Here, the Miocene subunits of unit SU5 (SU5-c and SU5-d) become indistinct and cannot be mapped on the seismic sections. In the southern parts of the F/MB, unit SU5 exhibits variable-amplitude and deformed reflections (Figure 6.5a, CDPs 2000-4000). Reflector R-EMM, which represents the early-middle Miocene unconformity, truncates at the seafloor in the F/MB (Figure 6.3, AWI-20190004, CDP 2400). Reflector R-SF has a very high-amplitude, continuous character and shows a rugged/abraded character in central and southern parts of the F/MB, whereas elsewhere it represents a smooth seafloor (Figure 6.3, AWI-20190004, CDPs 2500-5500).

B.2. Modified Seismostratigraphic Model in F/MB and F/MT

In extending the seismostratigraphic model from the MEB by Najjarifarizhendi and Uenzelmann-Neben (2021) towards the F/MB and F/MT, two new units SU3' and SU6 have been introduced. Unit SU3' in F/MB, unlike its coeval unit SU3 on MEB includes thick strata including five distinct subunits. Unit SU6 in F/MT is a new unit unique in the F/MT, restricted to this area, including distinct mounded strata above the youngest unit SU5.

B.2.1. Unit SU3', Reflectors R-MC to R-CT (Middle Cretaceous to Cretaceous-Tertiary).

As with unit SU3 on the MEB, Unit SU3' within the F/MB is bound at the base by reflector R-MC and at the top by reflector R-CT, in contrast, unit SU3' shows distinct internal subunits (Figure 6.3). Four previously undated (middle -/Upper Cretaceous) unconformities R-UU1 to R-UU4 separate unit SU3' into subunits SU3'-a, -b, -c, -d, and -e (Figures 6.3 and 6.4).

Subunit SU3'-a is bound by base reflector R-MC and top reflector R-UU1 (Figures 6.3 and 6.4). Reflector R-UU1 has a sub-horizontal, semi-continuous, low-amplitude character (Figure 6.3, AWI-20190004, CDPs 5000–8000). Subunit SU3'-a forms wedges up to 800 ms TWT thick, on the eastern and northern margins of the F/MB. Elsewhere in the F/MB, this subunit has a constant thickness of ca 100 ms TWT (Figure 6.3). Subunit SU3'-a displays subhorizontal, semi-continuous, low-amplitude, widely-spaced internal reflections, which are erosionally truncated at the top by reflector R-UU1. Reflector R-UU2, which bounds subunit SU3'-b at the top, is a middle-to high-amplitude, semi-continuous to discrete reflector (Figure 6.3). Subunit

SU3'-b, which unconformably lies on reflector R-UU1, in general is seismically opaque, but occasionally includes medium-amplitude, discrete, and widely-spaced reflectors. It forms wedges in northern parts of the F/MB with up to 1000 ms TWT thickness. In central parts of the M/FB, subunit SU3'-b includes lens-shaped structures with minimum and maximum thicknesses of respectively ca. 150 and 1000 ms TWT, which are truncated on the top by reflector R-UU2 (Figure 6.3, AWI-20190004, CDPs 3000–6000).

Subunit SU3'-c unconformably lies on base reflector R-UU2 and is bound at the top by reflector R-UU3, which is a sub-horizontal, high-amplitude, continuous reflector across the F/MB (Figure 6.3). This subunit shows middle-to high-amplitude, semi-continuous internal reflections and a constant thickness of ca. 400 ms TWT across the F/MB (Figure 6.3). Southwards towards the F/MT, subunit SU3'-c can reach a thickness of up to 700 ms TWT. Internal reflections of SU3'-c are erosionally truncated in northern and eastern parts of the F/MB by reflector R-CT (Figure 6.3, AWI-20190004, CDPs 6000–7000), and in the southern F/MB by the younger unconformity R-UU4 (Figure 6.3, AWI-20190004, CDP 2500–3500).

Subunit SU3'-d is bound at the base and top by Reflectors R-UU3 and R-UU4 respectively. The latter is a sub-horizontal, low-to middle-amplitude, semi-continuous reflector within the F/MB (Figure 6.3). Subunit SU3'-d shows mainly chaotic internal reflections overall in the F/MB, except for the eastern and western F/MB where it shows oblique, high-amplitude, semi-continuous internal reflections (Figure 6.3, AWI-20190004, CDPs 3300–3700). Here, internal reflectors show lateral displacement towards the south, where the upper reflectors downlap onto lower reflectors. Subunit SU3'-d has a relatively constant thickness of ca. 350 ms TWT across the F/MB. Reflections of this subunit are truncated by reflector R-CT in eastern and northern parts of the F/MB (Figure 6.3, AWI-20190004, CDPs 5400–5800). In the southern parts of the F/MB, internal reflections of SU3'-d terminate against reflector R-UU4 (Figure 6.3, AWI-20190004, CDPs 3100–3400).

Reflectors R-CT and R-UU4, respectively from the top and base reflector of subunit SU3'-e. Within the F/MB, reflector R-CT shows a twofold character. In northern and eastern parts, reflector R-CT is a subhorizontal, high-amplitude, continuous reflector (Figure 6.3, AWI-20190004, CDPs 2400–5400), whereas elsewhere in the basin it shows a tangential, middle-amplitude, wavy, and highly scattered reflection (Figure 6.3, AWI-20190004, CDPs 6000–8100). The lower part of this unit exhibits middle-amplitude, semi-continuous to discrete, widely-spaced reflections; towards the upper part, reflections of SU3'-e have disturbed and wavy character (Figure 6.3, AWI-20190004, CDPs 2600–4600). SU3'-e shows extreme thinning in northern and eastern parts of F/MB. It shows variable thickness elsewhere within the F/MB, where it forms cone-shaped features truncated on the top by reflector R-CT (Figure 6.3, AWI-20190004, CDPs 3500–5200).

B.2.2. Seismic unit SU6, Reflectors R-EMM to Seafloor (early-middle Miocene to Recent).

Bounding reflectors of Units SU1 and SU2, reflectors R-TB, RJC, and R-MC, are very well trackable southwards from the F/MB towards the F/MT as they plunge below the northern margin of the F/MT (Figure 6.3, AWI-20190004, CDPs 2000–3000). For the Cretaceous Unit SU3' and Tertiary Unit SU4, however, the bounding reflectors R-CT and R-EO become indistinct in the southernmost extremity of the F/MB and are hardly trackable into the F/MT (Figure 6.3, AWI-20190004, CDPs 2500–2900). Units SU1SU4 show tilting and faulting in the F/MT, and younger F/MT fill lies unconformably on these strata on the northern flank of the F/MT (Figure 6.3, AWI-20190004, CDPs 2000–2500).

The sedimentary sequence resolved in the F/MT cannot be dated with confidence, however partial tracking of reflector R-EO from the F/MB into the F/MT locates it below this sedimentary sequence on the northern flank of the F/MT (Figure 6.5a, CDP 1900). This provides a hint on the age of the filling strata being younger than the Eocene-Oligocene, suggesting that these strata are coeval to unit SU5 in F/MB. These strata however show different seismic characteristics compared to those of unit SU5, since they build up as a thick and conforming package. Therefore, the seismostratigraphic model is expanded to include an additional unit SU6 with three subunits.

Subunit SU6-a includes mostly horizontal and sub-horizontal internal reflections which onlap the acoustic basement on the southern flank of the M/FT and the southward dipping strata of units SU3'-SU5 on the northern flank (Figure 6.3, AWI-20190004, CDPs 700–2400 and Figure 6.6c). This subunit occasionally includes transparent strata. Reflector R-EMM, which is an early-middle Miocene erosional unconformity, truncates reflections of subunit SU6-a at the top (Figure 6.3). Reflections of subunit SU6-a show high-continuity, middle-to high-amplitude, and middle- to high-frequency reflections. This subunit shows its maximum thickness of up to 1200 ms TWT in the central section of the F/MT, while it thins and pinches out on the southern and northern flanks and occasionally includes moats and mounded sediment bodies (Figure 6.6c).

An undated erosional unconformity (hereafter called R-UU5) bounds subunit SU6-b at the top. Reflector R-UU5 is a continuous, middle-amplitude reflector that truncates reflections of subunit SU6-a (Figure 6.3, AWI-20190004, CDPs 700–2400). Reflections of subunit SU6-b lie sub-parallel to but occasionally onlap reflector R-EMM (Figure 6.6c, CDP 8600). Subunit SU6-b shows a variable thickness across the F/MT, ranging from less than 100 ms TWT towards the northern and southern F/MT flanks to more than 300 ms TWT in central parts of F/MT. This subunit has sub-parallel, continuous, middle-to high-amplitude internal reflections and includes moats close to the northern (Figure 6.3, CDP 8600) and southern (Figure 6.6c, CDP 10400) flanks of the F/MT that show a gradual up-dip migration.

Subunit SU6-c is the youngest subunit in the F/MT. It lies sub-parallel to the base reflector R-UU5 and is bound at the top by the seafloor reflector (R-SF). This unit has sub-parallel, continuous, low-to middle-amplitude internal reflections, which are truncated by reflector R-SF. This subunit forms a well-developed symmetric mounded sediment body in central parts of the F/MT, which reaches a thickness of up to 250 ms TWT and wedges out on the southern and northern flanks of the F/MT. Subunit SU6-c includes moats at the flanks of the F/MT which extend up-dip and are seen at the seafloor (Figure 6.6c, CDP 1150–1800).

CHAPTER 7. Falkland/Malvinas Trough: Indications for Cenozoic tectonic and oceanographic evolution in the southwestern South Atlantic

Najjarifarizhendi, Banafsheh*; Uenzelmann-Neben, Gabriele; Gruetzner, Jens

Alfred Wegener Institute, Helmholtz Centre for Polar and Marine Research, Am Alten Hafen 26, 27568 Bremerhaven, Germany

7.1 Abstract

The Falkland/Malvinas Trough bounds the southern extremity of the Falkland/Malvinas Plateau. This bathymetric depression developed as the Cenozoic orogenic foreland basin of the North Scotia Ridge. The sedimentary infill of the Falkland/Malvinas Trough carries a history of a development in a transpressional setting along the South American-Scotian plate boundary, in association with the evolution of the Drake Passage-Scotia Sea zone. Since the Falkland/Malvinas Trough is located on the pathway of the Antarctic Circumpolar Current, the current-controlled depositional and erosional features within its sedimentary infill provide valuable information on the palaeoceanographic modifications in the southwestern South Atlantic related to the opening of the Drake passage. Via a set of 2D high-resolution seismic reflection data acquired in 2019, the structural and morphological aspects of the Cenozoic strata across the Falkland/Malvinas Trough are investigated and discussed with respect to the tectonic evolutional history of the Drake Passage and the Scotia Sea. Development of the deformational folds and reactivation of Mesozoic faults during Oligocene-middle Miocene times argue for a compressional regime linked with the growth of Drake Passage-Scotia Sea zone. The onset of current-related deposition-erosion processes by action of abyssal water masses is identified for middle Miocene times. Since then, with the enhancement of abyssal circulation subsequent to the perennial Antarctic glaciation, a precursor of the Weddell Sea Deep Water has shaped a confined sediment drift at the trough's floor, in an oceanographic setting analogous to that of the present.

7.2 Introduction

The opening of the Drake Passage, along with the Tasman Gateway completed a full circumpolar pathway, and contributed to the establishment of the almighty Antarctic Circumpolar Current (ACC). The inception of the ACC is believed to be a pre-requisite for the thermal isolation of Antarctica and the onset of the continental-wide glaciation (e.g. Barker and Thomas, 2004; Ciesielski and Wise Jr, 1977; Katz et al., 2011; Kennett, 1977; Scher et al., 2015). The latter led to the increased production and reinforcement of the bottom water masses below the expanding ice-shelves (Goldner et al., 2014). The evolution of the ACC is hence important in terms of climatic and oceanographic modifications.

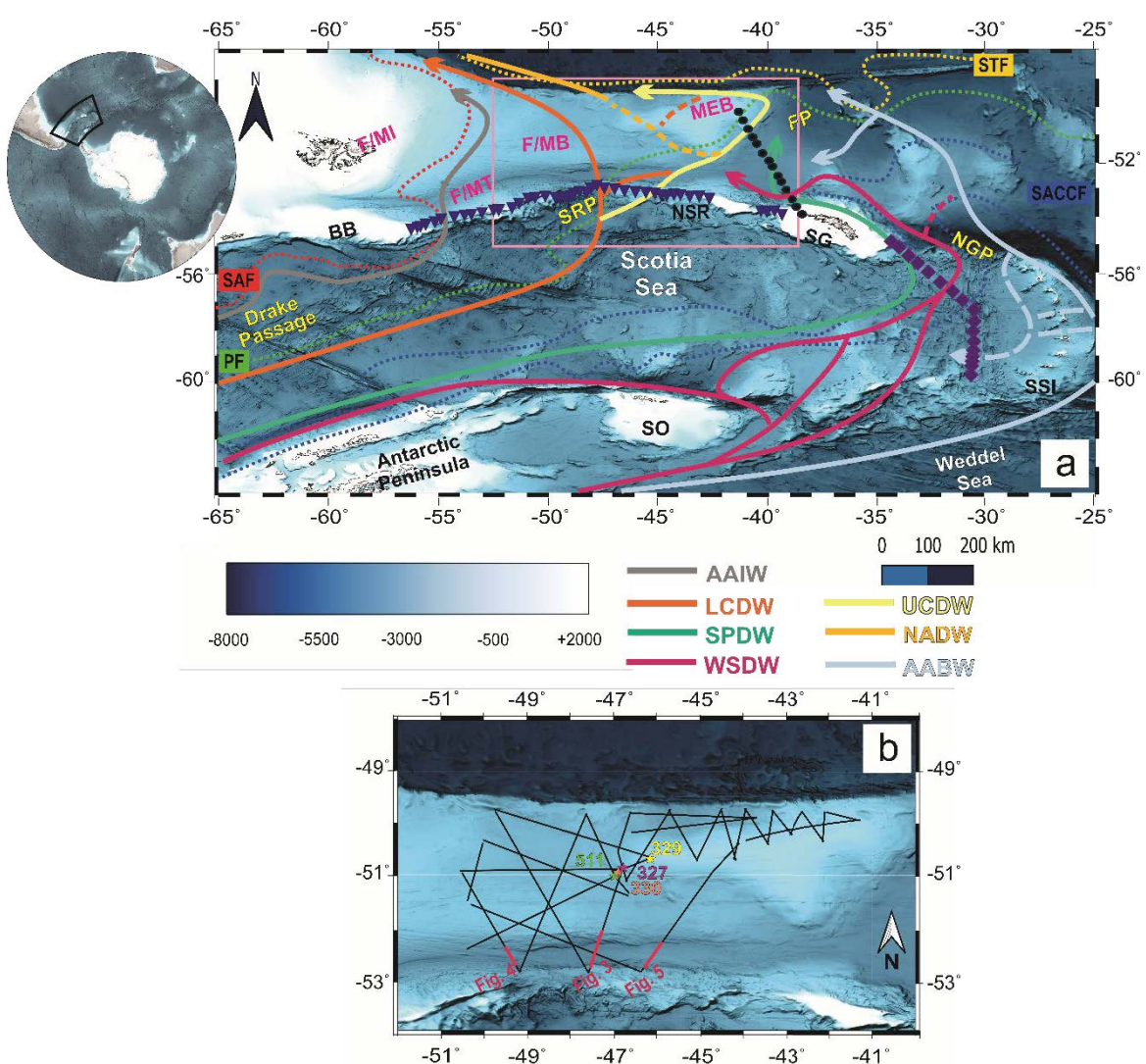


Figure 7.1: (a). Bathymetric map of the southwestern South Atlantic (Dorschel et al., 2022). Colored dotted lines are the paths for the Antarctic Circumpolar Current fronts from Orsi et al. (1995), including the Subtropical Front-STF (yellow), Subantarctic Front-SAF (red), Polar Front (green), and Southern Antarctic Circumpolar Current Front-SACCF (blue). Colored thick lines show the schematic pathway of the deep water masses in the area after Naveira Garabato et al. (2002) (see legend for the definition). Dashed lines are the sporadic or undefined pathways. Blue triangles are the CTD stations for the North Scotia Ridge Overflow Project, results are shown in Figure 7.2 (Smith et al., 2010). Black circles and purple diamonds are the station position of ALBATROSS hydrographic cruise, results are shown in Figure 7.2 (Arhan et al., 2002). Arrows show the location of the Antarctic Circumpolar Current fronts after Orsi et al. (1995) and (Arhan et al., 2002; Naveira Garabato et al., 2002). BB = Burdwood Bank; F/MB = Falkland/Malvinas Basin; F/MI = Falkland/Malvinas Islands; F/MT = Falkland/Malvinas Trough; FP = Falkland/Malvinas Passage; IOR = Islas Orcadas Rise; MEB = Maurice Ewing Bank; NGP = North Georgia Passage; SG = South Georgia; SO = South Orkney Islands; SRP = Shag Rocks Passage.

The Cenozoic development of the oceanic circulation in the Southern Ocean is however a matter of debate. Estimations for the opening of the Drake Passage are not in agreement, partly due to the complexities and uncertainties in reconstructing the tectonic evolution of the Scotia Sea and the Drake Passage (Barker et al., 2007). They reviewed that the tectonic reconstructions suggest between 34 and

16 Ma for the evolution of this gateway; whereas geo-environmental analyses provide an even wider span of 41 to 6 Ma for completion of the drake passage opening and a full-connection between the Pacific and South Atlantic.

The sedimentary infill in the Falkland/Malvinas Trough (F/MT), deposited coeval to the tectonic evolution of the Drake Passage-Scotia Sea zone, provide archives of the regional Cenozoic tectonic and oceanographic evolution in the southwestern South Atlantic. The F/MT is a bathymetric depression with an average water depth of ca. 3000 m to the south of the Falkland/Malvinas Plateau (F/MP), covering the northern boundary of the North Scotia Sea (NSR) (Figure 7.1). The F/MT is suggested to have been formed as an orogenic foreland basin, by shortening and crustal loading along the NSR, at the active margin of the South American and Scotian plates (e.g. Bry et al., 2004; Dalziel and Elliot, 1971; De Wit, 1976; Ludwig and Rabinowitz, 1982). The NSR comprises several continental blocks shaping submarine ridges/banks in form of a continuous belt, extending ca. 2000 km from Tierra del Fuego to the South Georgia Island and barricades the northward and eastwards flow of the abyssal water masses of the ACC in the Scotia Sea.

So far, research has focused mostly on the westernmost sector of the F/MT, to the south of the Falkland/Malvinas islands (F/MI). There, Esteban et al. (2020) described a fold-and-thrust Belt north of the Burdwood Bank, providing evidence of Oligocene-late Miocene northwards transgression. Syn-tectonic normal faulting in the South Falkland/Malvinas Basin has been attributed to the flexure of the F/MP below the scotia plate until the late Miocene (Bry et al., 2004; Koenitz et al., 2008). In a study of the NSR, Cunningham et al. (2002), based on seismic and sub-bottom profiler data reported current-controlled deposition on top of an inactive accretionary prism under the influence of the Weddell Sea Deep Water (WSDW) and Circumpolar Deep Water (CDW). In the easternmost sector of the F/MT, south of the Maurice Ewing Bank (MEB), Del Ben and Mallardi (2004), based on a single seismic profile, found evidence of Miocene underthrusting of the F/MP and described the filling of the F/MT as typical fabrics of current-related depositional systems.

Overall, available seismic reflection data in the central parts of the F/MT is sparse and yet of low-resolution. We present new high-resolution multi-channel seismic reflection data across the F/MT, acquired during RV Maria S. Merian expedition MSM81 in 2019 (Uenzelmann-Neben, 2019a). Our interest is in the sedimentary and structural features on the southern flank of the F/MP and in the central and eastern sector of the F/MT. In both areas, the structural peculiarities are analyzed to investigate their relevance to the regional tectonic evolution of the Drake Passage-Scotia Sea zone. We furthermore describe the current-controlled sedimentary and erosional features in the F/MT and investigate their onset and development with respect to the Cenozoic oceanographic modification of the Southern Ocean in response to tectonic and climatic modifications.

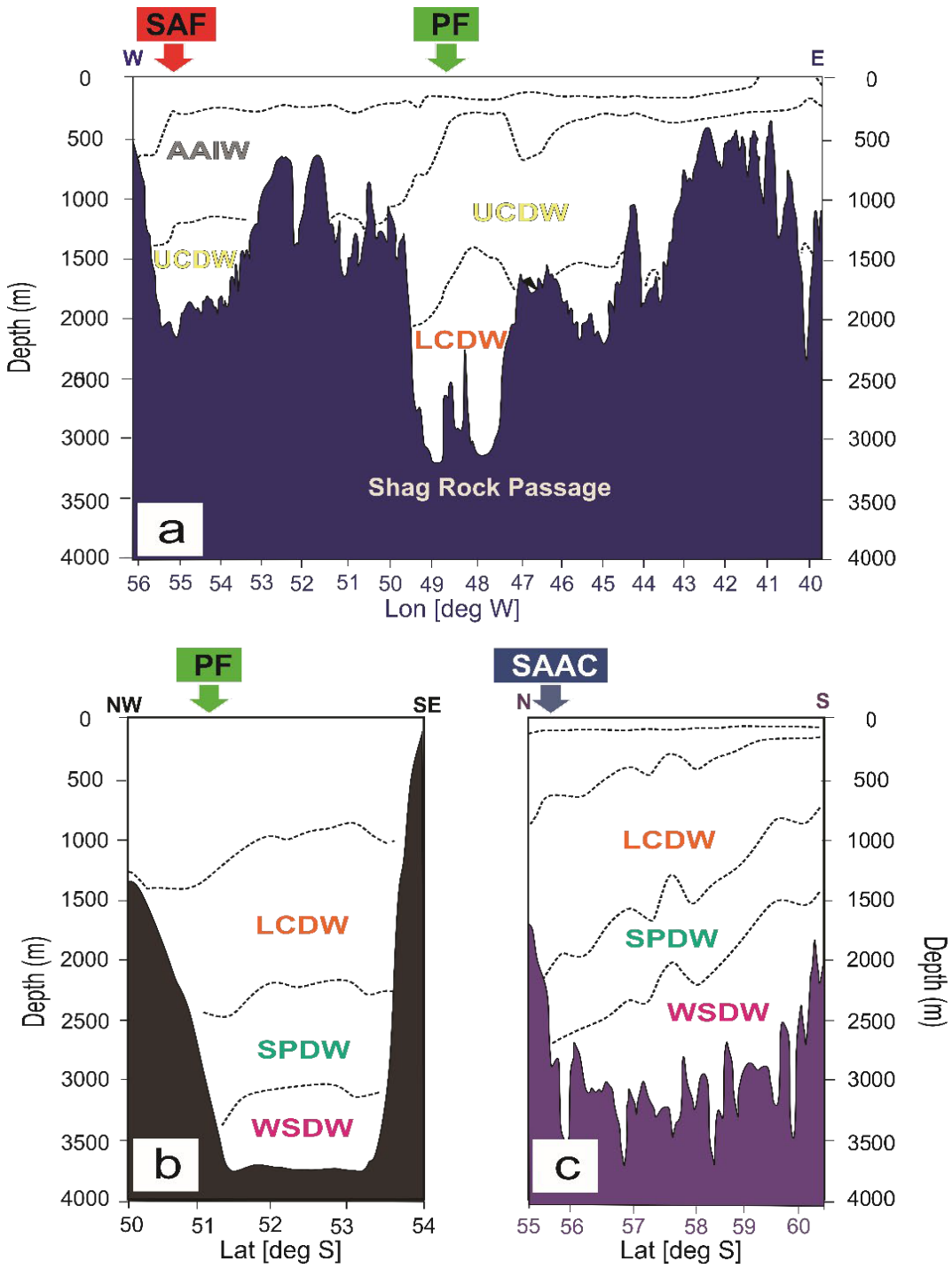


Figure 7.2: Schematic of the spatial distribution of water masses along the stations for the North Scotia Ridge Overflow Project after (Smith et al., 2010) and the ALBATROSS cruise track after Arhan et al. (2002). See Figure 7.1 for the location of these hydrographic stations. The black dashed-lines represent the water mass isopycnal limits (surfaces of constant density).

7.3 Geological and tectonic settings

The genesis of the F/MP is linked with several tectonic events. A Permian-Triassic collisional phase is responsible for the trans-Gondwanian orogenesis, indication of which is spotted onshore F/MI and

are scattered as well in South Argentina, South Africa, Antarctica (e.g. Dalziel et al., 2000; Du Toit, 1937). A Jurassic extensional system subsequent to the breakup of Gondwana and the initial phase of opening of the South Atlantic embraced the F/MP (Faulkner, 2000; Shipboard_Scientific_Party, 1974a, d, 1980a; Thompson, 1977). Later in late Jurassic to late Cretaceous times, a thermal subsidence phase accompanied the earliest open marine conditions in the Aptian in F/MB (Bry et al., 2004; Shipboard_Scientific_Party, 1977).

Since the Paleocene, due to rapid subsidence, sedimentation took place in pelagic environment across the F/MP. The Cenozoic history of the F/MP is linked with the final phase in the breakup of southwest Gondwana resulting in the opening of the Drake Passage and the Scotia Sea. This involved seafloor spreading in the Scotia Sea, starting in the Oligocene in West Scotia Sea (e.g. Dalziel et al., 2013; Eagles and Jokat, 2014; Eagles et al., 2005; Livermore et al., 2005), leading to the collision of the NSR segments with the F/MP, as well as an eastward translation along deep transform faults (Cunningham and Mann, 2007; Dalziel et al., 2021; Eagles and Eisermann, 2020). This tectonism is considered to have paved the way for the completion of a full circum-polar pathway, which conditioned the vast Cenozoic oceanographic reorganizations of the Southern Ocean (e.g. Barker, 2001a; Dalziel, 2014). The Cenozoic sedimentary strata at the F/MP provide records of these oceanographic modifications (Koenitz et al., 2008; Najjarifarizhendi and Uenzelmann-Neben, 2021; Shipboard_Scientific_Party, 1974a, c, d, 1980a)

7.4 Present oceanographic setting

In the present oceanographic setting of the Southern Ocean, the ACC, as the largest oceanic current, is responsible for the transport of ca. 140 Sv ($140 * 10^6 \text{ m}^3/\text{s}$) water, mainly through a number of high-velocity and deep-reaching circumpolar fronts (Orsi et al., 1995; Rintoul et al., 2001; Smith et al., 2010). Downstream of the Drake Passage, the Subantarctic Front (SAF), the Polar Front (PF), and the Southern ACC Front (SACCF) carry out the majority of the transport. These three fronts are bathymetrically steered in the Scotia Sea and the western South Atlantic Ocean (Figure 7.1).

The crest of the NSR lies at water depths between 200 m and 2000 m (Zenk, 1981). It therefore acts as a barrier to the deep and bottom water masses flowing within the ACC downstream of the Drake Passage and modifies these water masses on their way north and east, spilling over the F/MP into the South Atlantic (Howe et al., 1997; Smith et al., 2010). The bulk of the ACC, overspills the F/MP through a number of narrow gateways (Figure 7.1). The SAF crosses the NSR to the east of the Burdwood Bank through a pathway at around 54°W (Moore et al., 1999). The PF follows the central gap in the NSR at 48°W, called the Shag Rocks Passage, with a sill depth of ca. 3100m (Zenk, 1981); while the SACCF flows eastward around South Georgia prior to continuing northwards through the Falkland Passage (sill depth 5100) on its way into the southern South Atlantic (Smith et al., 2010). Figure 7.2 shows the depth characteristics of the water masses based on the hydrographic data.

To the East of the Burdwood Bank, the Antarctic Intermediate Water (AAIW) flows parallel to the SAF across the F/MP into the South Atlantic (Figure 7.1). The CDW is a major water mass associated with the ACC, the properties of which allow for a distinction between an Upper and a Lower component, respectively the UCDW and LCDW. In general, CDW runs parallel to the PF, extending to depths of 3500 m (Arhan et al., 1999; Arhan et al., 2002; Naveira Garabato et al., 2002). The Shag Rock Passage constrains the flow of the CDW northwards across the F/MP into the Argentine Basin, where a partitioning takes place for the LCDW. The shallower core flows north along the saddle of the F/MP into the Argentine Basin. A deeper core skirts the MEB, the elevated eastern portion of the F/MP, while entraining the southward-flowing diluted NADW (Arhan et al., 2002) (Figure 7.1).

The dense WSDW takes different paths spilling over the South Scotia Ridge, allowing for the distinction between two types (Naveira Garabato et al., 2002). A deeper component flows westward towards the Drake passage. The majority of the WSDW however, escapes eastwards in the Scotia Sea and enters along the path of the SACCFF from the eastern Scotia Sea, through the North Georgia Passage and the Georgia Basin towards the southwestern South Atlantic (Arhan et al., 1999; Mantyla and Reid, 1983; Naveira Garabato et al., 2002) (Figure 7.1).

7.5 Seismic data and seismostratigraphy

A set of 2D high-resolution seismic reflection profiles from Cruise Leg MSM81, acquired by the Alfred Wegener Institute (AWI) in 2019 covering the southern flank of the F/MP, the F/MT and partly the NSR (ca. 45.5-50.5°W), has been used in this study. Post-stack time migrated sections were the final products of an amplitude-preserved seismic processing scheme. Acquisition-geometry corrected seismic records were sorted into common depth point (CDP)-gather of 25 m distance, used for the semblance velocity analysis. These were then corrected for the geometrical spreading amplitude attenuation, followed by CDP stacking and migration sequences.

Najjarifarizhendi and Uenzelmann-Neben (2022) presented a seismostratigraphic model for the Falkland/Malvinas Basin (F/MB) and F/MT, including 6 seismic units through correlation with regional Deep Sea Drilling Project (DSDP) Leg 36 Sites 327, 329, 330 and Leg 71 Site 511 (Figure 7.1). Figures 7.3 to 7.5 present this seismostratigraphic framework and the reflection characteristics of the seismic units in the F/MB and F/MT. Lying unconformably on the acoustic basement is the seismic unit SU1, including reflections from the Jurassic strata which extend southwards and submerge below the northern flank of the F/MT. The Cretaceous strata build reflections of units SU2 and SU3', separated by a middle Cretaceous unconformity. Unit SU3' in F/MB shows variable reflection patterns and includes 5 subunits. A regional Cretaceous-Tertiary unconformity (reflector R-CT) truncates subunits SU3'-c, -d, and -e, which dip southwards below the filling strata in the F/MT.

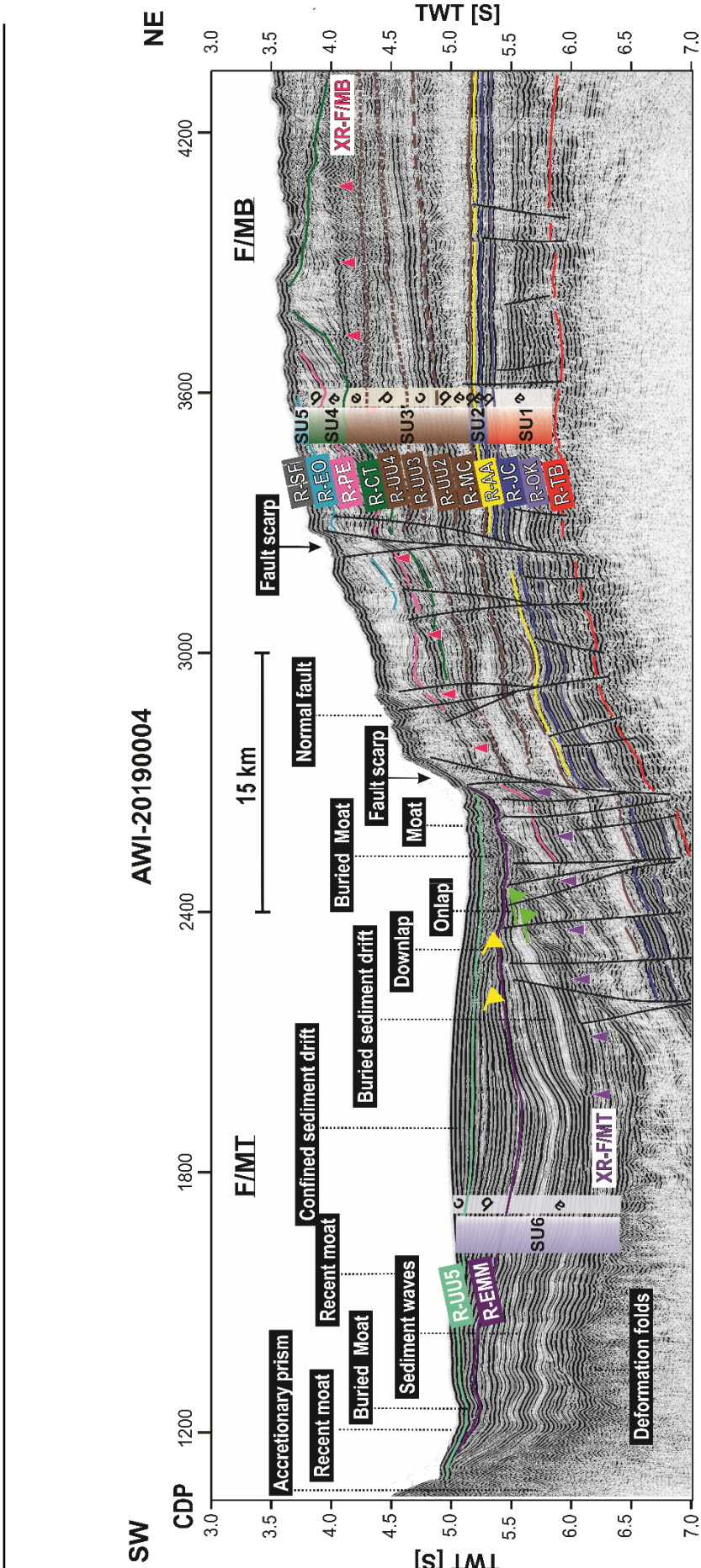


Figure 7.3: Part of the interpreted seismic profile AWI-20190004. Location of section is shown in Figure 7.1b. Superimposed is the seismic stratigraphy and the marker horizons. The pink and purple triangles respectively mark the cross-cutting reflectors XR-F/MB and XR-F/MT (for details, see Section 7.5)

Seismic units SU4 and SU5 includes reflections from the Paleogene to recent, which are separated by an Eocene-Oligocene erosional unconformity (reflector R-EO). In the F/MB, reflections of SU4 build-up unconformably on the base reflector R-CT, while southwards they mostly show scattered and disturbed reflection characteristics as they terminate at the base reflector in the F/MT. Unit SU5 shows extreme thinning on the F/MB, where the internal reflectors terminate at the seafloor. An early-middle Miocene erosional unconformity, represented by reflector R-EMM, seem to have paved the way for the present seafloor morphology in the F/MB(Najjarifarizhendi and Uenzelmann-Neben, 2022).

The age of the base reflector in the F/MT is not well constrained, however, Najjarifarizhendi and Uenzelmann-Neben (2022) infer an age younger than the Oligocene, based on the termination of an Eocene-Oligocene reflector (R-EO) at this base reflector. The filling strata in F/MT has been assigned by these authors as seismic unit SU6 due its distinct reflection characteristics, despite being somewhat coeval with the youngest strata in the F/MB. Unit SU6 is separated into 3 subunits, by an early-middle Miocene unconformity (R-EMM) and an unknown unconformity R-UU5. Reflectors XR-F/MB and XR-F/MT are cross-cutting reflectors which show discordance to the host strata from units SU3', SU4, SU5, and SU6. These reflectors, as argued by Najjarifarizhendi and Uenzelmann-Neben (2022), are to be associated with fossilized silica diagenetic fronts.

7.6 Discussion of observations

Fault reactivation. In the F/MB, in particular in the southern sectors, the basement top (reflector R-TB) as well as the sedimentary strata of unit SU1 show extensive faulting, in compliance to a history of development in an extensional system of the Jurassic (e.g. Faulkner, 2000; Shipboard_Scientific_Party, 1974a, d, 1980a; Thompson, 1977). These normal faults shape horst and graben structures and basement troughs, which are filled with the Jurassic bedforms of unit SU1 (Figures 7.3 and 7.4). To the north of the F/MT, these extensional faults are boldly present and occasionally show offsets as much as 500 ms TWT (ca. 500 m) (Figure 7.3, CDP≈2700). These faults occasionally show stratigraphic growth within the younger strata of (sub)units SU2, SU3'-a, and -b (Figure 7.3, CDP≈2800 and 4000 and Figure 7.4, CDP≈6900), as evidence of active tectonics also in the early-middle Cretaceous. The slight upward inclination of reflections from these strata on the hanging-wall relative to the assumed fault plane hint at a syn-tectonic deposition.

Towards the south, in the proximity of the F/MT, the Mesozoic faults seem to have at times affected the younger strata of units SU4 and SU5 (Figure 7.3, CDP≈2700 and 3300 and Figure 7.4, CDP≈7200). These faults show stratigraphic growth within the sedimentary succession of the Cenozoic and occasionally extend to the seafloor, resulting in abrupt changes in the reflector dips of unit SU4 and SU5 (Figure 7.3, CDPs≈3200-3300). There, down-faulting of the bedforms have shaped south-facing scarp-features on the seafloor, where up to 300 ms TWT (ca. 150 m) down-thrown can be observed (Figure 7.3, CDP≈3200 and Figure 7.4, CDP≈7250). Further south, at the edge of the F/MT, these

extensional faults affect the base strata in the trough and can be traced throughout bedforms of subunit SU6-a. In the F/MT; these faults are mostly bound to reflector R-EMM of the early-middle Miocene age (Figure 7.3, CDPs 2100-2600 and 3300 and Figure 7.5, CDPs 2400-2800).

Normal faulting of the pre-middle Miocene sedimentary sequences in the South Falkland/Malvinas basin (Bry et al., 2004; Foschi and Cartwright, 2016) and faults affecting the contourite drift further north in the westernmost parts of the F/MT (Koenitz et al., 2008; Pérez et al., 2015) have been linked with the regional Cenozoic compressional tectonic regime accompanied by flexure of the F/MP below the Burdwood Bank. Richards, Gatliff, Quinn and Fannin (1996) reported movement of Neogene strata along reactivated faults in the South Falkland/Malvinas Basin, subsequent to the opening of the Scotia Basin.

DSDP boreholes, piston and gravity coring across the F/MB have recovered core-tops of Eocene-Miocene age (Howe et al., 1997; Saito et al., 1974; Shipboard_Scientific_Party, 1980a), allowing for the interpretation that the seafloor has been erosional and/or non-depositional for much of the late Cenozoic (Cunningham et al., 1998). This absence of deposition has been attributed to the long-term action of southern-sourced deep and bottom water masses spilling over the F/MP into the southern South Atlantic (e.g. Barker, 1977a; Ciesielski and Wise Jr, 1977; Del Ben and Mallardi, 2004; Lorenzo and Mutter, 1988; Najjarifarizhendi and Uenzelmann-Neben, 2021, 2022).

Tectonic reconstruction suggests the evolution of the Scotia Sea started in an Eocene extensional system in the Central Scotia Plate, followed by a northward-propagating seafloor spreading respectively starting and ceasing around 30 and 6 Ma (Eagles and Jokat, 2014). Associated to this tectonic event, early shallow-intermediate circulation through the Drake Passage is attributed to middle-late Eocene times, where deepening of this gateway allowed for abyssal water exchange later on (Eagles and Jokat, 2014; Eagles et al., 2006).

The stratigraphic growth of sub-vertical normal faults within the Cenozoic sediments in F/MB and F/MT indicates that these were reactivated during the tectonic evolution of the Drake Passage-Scotia Sea zone. Based on our observation that these major faults reach the seafloor in F/MB and are bound to the reflector R-EMM of early-middle Miocene age in the F/MT (Figure 7.3, CDPs 2100-2600 and 3300 and Figure 7.5, CDPs 2400-2800), the underthrusting and loading of the F/MP in association with the transpressive system at the NSR during the opening of the Scotia Sea is inferred to have ceased at around the early-middle Miocene.

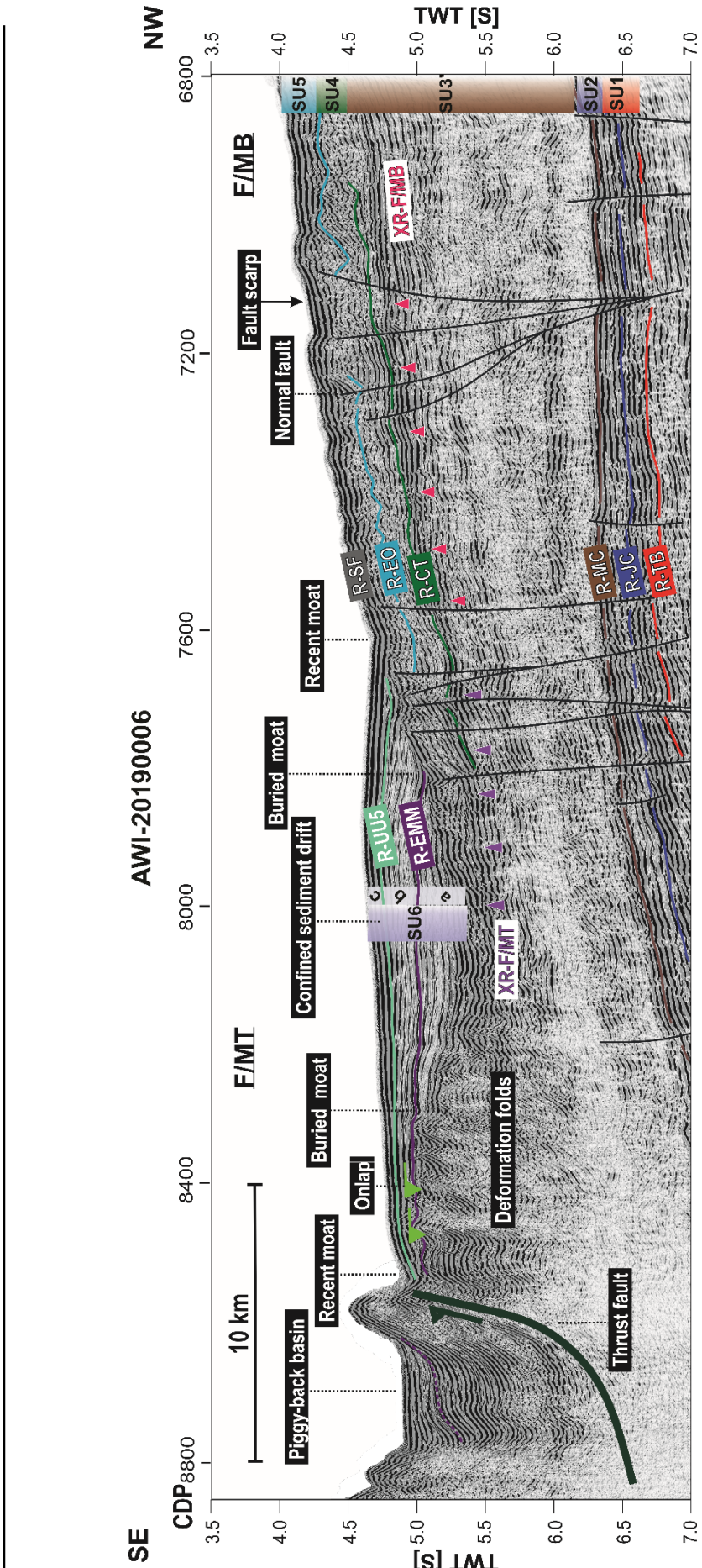


Figure 7.4: Part of the interpreted seismic profile AWI-20190006. Location of section is shown in Figure 7.1b. Superimposed is the seismic stratigraphy and the marker horizons. The pink and purple triangles respectively mark the cross-cutting reflectors XR-F/MB and XR-F/MT (for details, see Section 7.5).

Deformational folds.

The northern flank of the NSR is described as a massive accretionary prism (collision complex), formed by the South American and Scotian plate conversion during the middle-late Cenozoic (e.g. Cunningham and Barker, 1996; Ludwig and Rabinowitz, 1982; Tassone et al., 2008). There, a series of southerly dipping thrust faults have been held responsible for the tertiary deformation of the Mesozoic strata and the formation of the NSR (Bry et al., 2004; Tassone et al., 2008).

Further north, at the foot of the NSR, a series of asymmetrical folds lie below the sedimentary fill in the F/MT (Figures 7.3 to 7.5). In our study, these folded structures are identified almost on every seismic profile in the area between 46°W to 49.5°W, where they advance on average 10 km northwards below the F/MT sedimentary infill. Seismic profiles show that these folding features affect the strata representing unit SU6-a (Figure 7.4, CDPs 8100-8600). In the F/MT, reflector R-EMM can be traced southwards, where it onlaps onto these folded structures (Figures 7.4 and 7.5), whereas the overlying strata from SU6-b seem rather undisturbed. Similar deformed structures described as a fold-and-thrust Belt, embracing the Mesozoic sediments to the north of the Burdwood Bank (Esteban et al., 2020; Foschi and Cartwright, 2016; Koenitz et al., 2008) are suggested to have formed under the regional compressional tectonics of the Oligocene-late Miocene.

The deformational folding in our study area provide evidence of the northward compressional system acting at the plate boundary of the South America and Scotia below the NSR, synchronous with the seafloor spreading within the Scotia Sea. The consideration that these accreted strata are bound to the early-middle Miocene within the F/MT (reflector R-EMM) allows for temporally constraining the tectonism and to suggest that the regional compressional setting has ceased at about these times. This interpretation complies with the proposed timing for the cease of the seafloor spreading in the Scotia Sea and the shift of the South American-Scotian Plate boundary from a convergent margin to a rather transform one at about late Miocene times (Eagles and Jokat, 2014; Esteban et al., 2020).

On seismic profile AWI-20190006, imaging the northernmost sector of the NSR at around 49-49.5°W, an expression of a thrust fault can be very well observed at the seafloor, adjacent to the filling bedform of the F/MT (Figure 7.4, CDP≈8600). Here a south dipping thrust fault has overridden the sedimentary strata updip to shape a bathymetric feature at the seafloor. In the hanging-walls of the thrust fault, this propagation has produced a typical piggy-back (detached) basin (Figure 7.4, CDPs 8650-8800). Such minor sedimentary basins are also reported north of the Burdwood Bank (Bry et al., 2004; Fish, 2005). Correlation of the reflection characteristics of the strata across this thrust fault surface shows that the youngest dragged bedforms which were deposited coevally with the progressive tectonics, should be approximately of middle-late Miocene age, in accordance with the termination of the conversational phase of the South-American-Scotian plate margin (Eagles and Jokat, 2014; Esteban et al., 2020).

The present location of the South Georgia Islands, somewhat 1600 km east of its assumed location in the Mesozoic close to Tierra del Fuego, is mainly attributed to strike-slip faults south the NSR (e.g.

Carter et al., 2014; Cunningham and Mann, 2007; Cunningham et al., 1995; Dalziel and Elliot, 1971; Dalziel et al., 2021). The strike-slip motion is considered to be still an ongoing process based on the evidence from regional earthquake distributions (Pelayo and Wiens, 1989). In the westernmost parts of the F/MT and the western sector of the Scotia Sea, the left-lateral strike-slip tectonics in the western segment of the South America-Scotian Plate boundary is suggested since ca. 7 Ma (Esteban et al., 2020; Lodolo et al., 2006). According to the seismic data, we cannot report direct indication of this transpressive tectonic system within the sedimentary strata; if so, there should be a strike-slip component superimposed on the sub-vertical basement faults as suggested by Cunningham et al. (1998).

Current-related sedimentary features.

Bedforms of unit SU6-a, in particular in the eastern sector of the F/MT, show wavy structure towards the southern flank (Figures 7.3 and 7.5), building-up on top of the accreted strata at the toe of the NSR. These asymmetric sinusoidal waveforms have an average width of ca. 2 km and show heights of up to ca. 40 m, lying unconformably on the fold-and-thrust structures of the NSR, showing a general up-dip migration pattern. Towards the north, these strata form mounded bedforms onlapping onto the base reflector on the northern flank of the F/MT (Figure 7.3, CDPs 2000-2400).

The identified waveforms are comparable in size and morphology to the abyssal sediment waves (Flood et al., 1993; Wynn and Masson, 2008), which can develop in quasi-stable conditions at the seafloor. Such depositional feature can be attributed to the action of sluggish along-slope bottom water masses acting on the palaeo-seafloor (Wynn and Masson, 2008; Wynn and Stow, 2002). Sediment waves in the southern ocean have been associated with the action of abyssal currents across the sediment drifts (Flood et al., 1993). These waveforms tend to form at clockwise angles, migrating up-current and left-lateral, relative to the prevailing flow direction (Flood et al., 1993).

The wavy seismofacies within SU6-a change upward into the rather well-stratified strata of SU6-b which show thinning towards the north as they downlap onto reflector R-EMM, shaping a wide buried moat feature adjacent to the flank (Figures 7.3 to 7.5). In the youngest subunit in the F/MT (SU6-c), the strata form a distinct mounded structure in the central floor of the trough, while they show thinning at the northern and southern flank. Here they downlap onto reflector R-UU4 shaping moat features which extend updip and are present at the seafloor (Figures 7.3 to 7.5).

The strata shaping units SU6-b and SU6-c exhibit the very typical seismic characteristics of a contourite drift, namely a mounded morphology, an along-slope elongation, basal and internal erosional unconformities, etc. (e.g. Esentia et al., 2018; Faugères and Stow, 2008; Faugères et al., 1999; Rebescu and Stow, 2001; Stow et al., 2002). Gaining or losing momentum on their pathways, the deep and bottom water masses shape contouritic erosional and/or depositional features by the persistent action at the seafloor (Esentia et al., 2018; Rebescu, 2014). At the floor of the F/MT, this confined sediment drift shows an east-west elongation and is restricted at the northern and southern extremities to the

erosional surfaces in shape of moats, which show a general up-dip migration and further appear at the seafloor.

Several studies have used the geometrical and spatial characteristics of the contourite drifts to learn about the responsible water masses and the oceanographic evolution in response to tectonic and climatic modifications (e.g. Alves et al., 2023; Fischer and Uenzelmann-Neben, 2018a; Gruetzner and Uenzelmann-Neben, 2016; Hernandez-Molina et al., 2006; Koenitz et al., 2008; Najjarifarizhendi and Uenzelmann-Neben, 2021; Nicholson and Stow, 2019). Based on the morphology and the depth characteristics of this confined sediment drift in the F/MT, the characteristics of the responsible water mass for shaping it can be inferred (Barker and Thomas, 2004; Koenitz et al., 2008; Lyle et al., 2007; Pfuhl and McCave, 2005).

In the F/MT, the onset of the drift formation was synchronous to the deposition in the upper part of unit SU6-a of Oligocene times (Figure 7.3, CDPs 2000-2400), along with the sediment wave structures in the southerly parts of the F/MT (Figures 7.3 and 7.5) is consistent with the proposed earliest indications of cold Antarctic deep water activities (Kennett, 1977). The sediment waves are topped by reflector R-EMM of the early-middle Miocene, above which the contouritic sedimentary expression dominates throughout units SU6-b and SU6-c. The bold erosional moat features above reflector R-EMM indicates higher current velocities at the base of the slope. A continuation of the contourite drift is seen at the present-day seafloor with clear moat features (Figures 7.3 and 7.5). According to the present oceanographic setting of the area and the water depths of ca. 3375- 3750 m (4500-5000 ms TWT), we suggest that these buried contouritic features were shaped by deep water flow of a proto-WSDW (Figures 7.1a and 7.2)

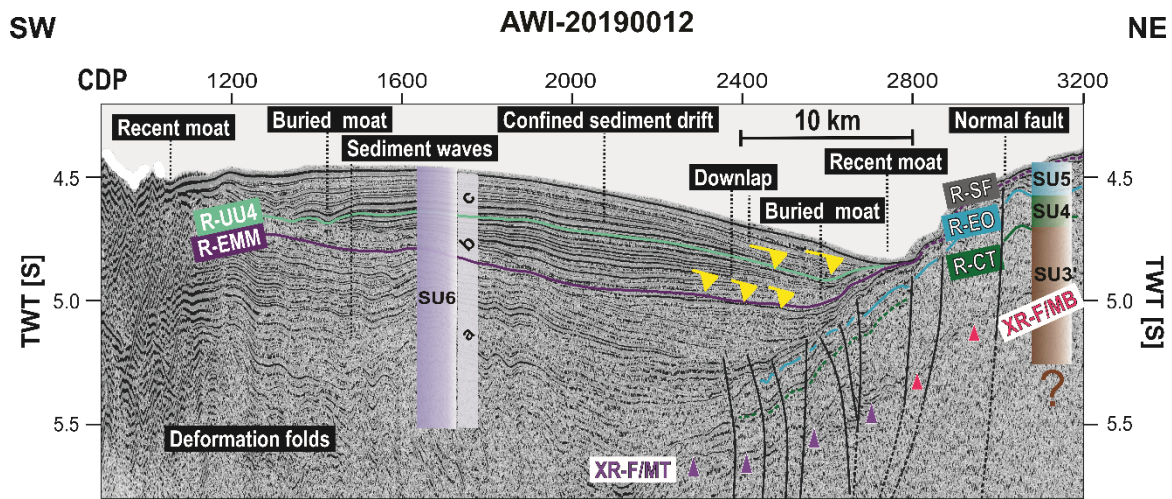


Figure 7.5: Part of the interpreted seismic profile AWI-20190012. Location of section is shown in Figure 7.1b. Superimposed is the seismic stratigraphy and the marker horizons. The pink and purple triangles respectively mark the cross-cutting reflectors XR-F/MB and XR-F/MT (for details, see Section 7.5).

Today, the northward and eastward flow of the WSDW into the South Atlantic is constricted to the bathymetry of the NSR. The outflow of the WSDW from the Scotia Sea is realized through the narrow North Georgia Passage into the Georgia basin (Figure 7.1a). From there, some WSDW enters the Argentine Basin through a deep branch overspilling the F/MP (Arhan et al., 1999), while the bulk of this water mass enters into the F/MT (Cunningham and Barker, 1996). Naveira Garabato et al. (2002) suggest that the WSDW may upwell in this bathymetric depression into CDW, leaving the Georgia Basin. Arhan et al. (1999) suggest a recirculation of the WSDW below the retroflection of the SACCF.

The shift in the sedimentary features across reflector R-EMM in the F/MT, from sediment wave structures attributed to rather quiescent bottom water conditions towards a highly dynamic one shaping the sediment drift (Figures 7.3 and 7.5), complies with a postulated post-middle Miocene intensification of bottom water production and intensified circulation of a proto-ACC (e.g. Goldner et al., 2014; Najjarifarizhendi and Uenzelmann-Neben, 2021; Shipboard_Scientific_Party, 1974a, c; Steinbrink et al., 2020). The presence of the current-related erosional features adjacent to the northern and southern slope of the F/MT is in accordance to this layout and has persisted since the late Miocene. The morphology of the confined drift at the floor of the F/MT between the 46°W to 49.5°W conforms with the westward flow of the WSDW constrained to the southern flank, while taking a clock-wise turn and flowing east along the northern flank below the LCDW to enter the Argentine Basin.

Based on the investigation of a contourite drift in the northwestern sector of the Scotia Sea abyssal plain, Pérez et al. (2015) reported a major oceanographic reorganization in the middle Miocene, involving the enhancement of the CDW, coeval with the onset of the WSDW in the Scotia Sea. Our observation in this sector of the F/MT suggests that the onset of deep water circulation was synchronous to the deposition of unit SU6-a (late Eocene-Oligocene). This implies that the Drake Passage should have cleared for the intermediate and deep water exchange by the Eocene-Oligocene, as proposed among others by Barker (1977a); Ciesielski and Wise Jr (1977); Eagles and Jokat (2014); Nicholson and Stow (2019); Scher and Martin (2006a).

Shaping of a contourite drift in units SU6-b and SU6-c since the middle Miocene, by abyssal flow of proto-WSDW in the F/MT, requires the full establishment of a four-layered ocean as a precursor of that of the present. This points to the realization of full-depth opening of the Drake Passage and intensification of bottom water production subsequent to the Antarctic glaciation by this time (Eagles et al., 2006; Goldner et al., 2014; Katz et al., 2011). Regional tectonic reconstructions as well, argue for realization of bathymetric conditions, allowing for a modern circulation regime and the onset of the abyssal frontal patterns in the scotia sea since middle Miocene times (Eagles and Jokat, 2014; Pérez-Díaz and Eagles, 2017).

7.7 Conclusions

Opening of the Drake Passage and the formation of the Scotia Sea contributed to the completion of a full circumpolar pathway, the establishment of the ACC, and consequently to the vast oceanographic and climatic modifications of the Cenozoic. Investigation of the sedimentary strata across the southern sector of the F/MB and the F/MT using newly acquired high-resolution 2D seismic reflection data, provided insight into the development of structural and morphological features, coeval to the development of the Drake Passage-Scotia Sea zone.

- At the southernmost sector of the F/MP and the northern flank of the F/MT, Mesozoic normal faults show reactivation. These subvertical faults affect the strata as young as early-middle Miocene times (reflector R-EMM); where occasionally fault-scars are shaped at the seafloor in the F/MB. This renewed tectonic activity has occurred consequent to the underthrusting of the Falkland/Malvinas Plate below the Scotian Plate, coeval to the development of the Drake Passage and the Scotia Sea.
- A package of deformational folds to the south of the F/MT, at the toe of the accreted strata of the NSR, resulted from the compressional system active in the Cenozoic at the South American and Scotian plate boundary. The strata of Oligocene-early Miocene age underwent deformation in association with the main tectonism of the evolution of the Drake Passage and the Scotia Sea.
- Prior to middle Miocene times, sediment waves and minor drift deposits in the F/MT hint at deposition under quiescent abyssal bottom water conditions. The evolution of the Drake Passage by this time, however should have enabled a full depth circulation pattern under a proto-ACC.
- Since middle Miocene times, a highly dynamic circulation with action of water masses analogous to today's WSDW has shaped a confined sediment drift at the seafloor in the F/MT. This vigorous middle Miocene abyssal current activity can be attributed to the enhanced production of the bottom water masses subsequent to the Antarctic glaciation.
- The erosional expression of this precursor water mass in the post-middle Miocene strata can be traced as recent moats adjacent to the northern and southern slopes of the F/MT at the present seafloor. Correlations with the present oceanographic setting suggests that a proto-WSDW has entered the F/MT through the Georgia Basin since middle Miocene times; taking a westward path at the southern flank, there making a turn as it overspilled the F/MP confined to the northern slope of the F/MT.

CHAPTER 8. Conclusion

Intent.

This thesis was dedicated to better understand the Cenozoic oceanographic evolution in the southwestern sector of the South Atlantic in response to the evolution of the Drake Passage-Scotia Sea and the major climatic modifications subsequent to the continental-wide Antarctic glaciation. The central goal has been to delineate the onset and the development of different water masses flowing within the Antarctic Circumpolar Current (ACC) across the F/MP. Furthermore, it was intended to constrain the variations in the pathways and intensities of these water masses following the tectonic and climatic events.

Distinctiveness of the Falkland/Malvinas Plateau (F/MP) for this study.

Having its palaeolocation in the southwest Gondwana and its present location as a submarine plateau downstream of the Drake Passage and the Scotia Sea makes F/MP ideal for the study of the palaeoceanographic evolution of the southwestern South Atlantic versus the tectonic and climatic modifications. To this end, a new set of 2D high-resolution seismic reflection data was acquired in 2019 by the Alfred Wegener Institute (AWI), which allowed for imaging and investigating the sedimentary strata across the F/MP.

Conclusive findings.

In chapters 5, 6, and 7 several arguments were provided in different sectors of the F/MP, supporting that as a bathymetric high steering the southern-sourced deep and bottom water masses, the F/MP presents a unique archive of palaeoceanographic evolution of the southwestern South Atlantic.

To conclude the study, in the following, I will relate my findings with the central research questions raised in section 2.3.

When do the earliest current-related sedimentary traces appear across the F/MP? If and how do these sedimentary manifestations link to the early phase of the evolution of the Southern Ocean?

Restricted evidence of current-controlled deposition (sediment drift deposits) and erosion (erosional patches, moat features) is present in the sedimentary sequence of the late Cretaceous in a small

depression to the north of the Maurice Ewing Bank (MEB), at average water depths 3300 m (4400 ms TWT). [See section 5.6.1 for details]. This small basin is located at the edge of the Falkland Escarpment, the westernmost extremity of the transform margin of the Falkland-Agulhas Fracture Zone (Ben Avraham et al., 1997; Lorenzo and Mutter, 1988; Ludwig, 1983), which formed as South America and Africa moved apart during the break-up of Gondwana. Palaeobathymetric reconstructions of the south Atlantic suggest water depths of more than 3000 m for the southernmost sector of the Argentine Basin, which favored the deep oceanic connections between the proto-Indian Ocean and the proto-South Atlantic already in Albian times (Pérez-Díaz and Eagles, 2017). Early Cretaceous gateway opening in the southern South Atlantic is endorsed by integrated Neodymium proxy data and general circulation modeling by Dummann, Steinig, et al. (2020) The late Cretaceous current-related erosional traces in this northern basin from my observations is linked to the earliest water mass flow between the southern proto-South Atlantic and - Indian Oceans.

Sedimentary evidence for the erosional action of water masses is present as well to the west and southwest of the MEB in the sedimentary strata of the late Cretaceous, at average water depths of 2600 m (3600 ms TWT). [See section 5.6.1 for details]. For this period, drill data from Deep Sea Drilling Project (DSDP) Sites 327, 330, and 511, suggest that the sedimentation in the Falkland/Malvinas Basin (F/MB) took place in open marine conditions, with palaeodepths of more than 1500 m (Shipboard_Scientific_Party, 1974a, d, 1980a). The major hiatus at the Maastrichtian-Tertiary boundary at DSDP Sites on the F/MP are linked to the early development of the Southern Ocean circulations (Shipboard_Scientific_Party, 1980a). It can therefore be inferred that these erosional features relate to the early action of southern-sourced intermediate water masses (Intermediate Southern Ocean Water), and probably precursors of Upper Pacific Water flowing through the shallow gateway at the Drake Passage (Dummann, Steinig, et al., 2020; Sewall et al., 2007). For the same period, Uenzelmann-Neben et al. (2017) report circulation of shallow and intermediate southern-sourced water masses in the Argentine Basin. In that respect, the F/MP should have played a barrier role for the southern deep water masses on their way to the South Atlantic until at least the late Cretaceous.

When and how do sedimentary manifestations of a multi-layered ocean appear on the F/MP? When and how has sedimentation on the F/MP recorded the overspill of the Upper- and Lower Circumpolar Deep Water (UCDW and LCDW)?

The Paleocene-early Eocene strata in the Falkland/Malvinas Basin (F/MB) and across the MEB show a clear increase in current-related sedimentary features. These appear at three distinct depth intervals with average depths of ca. 2000 m (2600 ms TWT), 2600 m (3500 ms TWT), and 3300 m (4400 ms TWT). [See section 5.6.2 for details]. Since the signature of the current activity in the sedimentary strata is rather depositional than erosional, a quiescent circulation regime will have prevailed. In addition, the distinctive activity levels hint at action of different water masses, implying circulation in an ocean with

vertical stratification of water masses already in the Paleocene-early Eocene. A continuation of deep water exchange between the proto-Indian and -South Atlantic Ocean, established in the late Cretaceous subsequent to the opening of the South Atlantic is suggested to have been responsible for the deepest traces in the small basin north of the MEB. The intermediate-depth traces which mostly appear in the F/MB, and southern flank of the MEB at average activity depth of ca. 2600 m (ca. 3500 ms TWT) imply the action of a water mass with properties similar to the present LCDW (Arhan et al., 1999; Naveira Garabato et al., 2002; Orsi et al., 1995). These observations suggest that a precursor of LCDW attempted to overspill the F/MP since the Paleocene. An elongated sediment drift is observed at water depths of ca. 2000 m (2700 ms TWT) on the MEB, analogous to the activity level of today's UCDW. This observation bears witness to the persistent action of an intermediate water mass, a precursor of the UCDW skirting the MEB towards the Argentine Basin. Tectonic reconstructions endorse that the early opening phase of the Drake Passage around 50 Ma, preceding the seafloor spreading in the Scotia Sea contributed to the establishment of the ACC (Eagles and Jokat, 2014; Livermore et al., 2007; van de Lagemaat et al., 2021). For the period of the early Paleogene in the southwestern South Atlantic, ocean-atmospheric dynamics simulations admit steady hydrographic conditions with the dominance of Intermediate Antarctic Water circulation (Uenzelmann-Neben et al., 2017).

When and how do the Cenozoic sedimentary structures on the F/MP reveal the onset of the ACC and the transition to a modern ocean? Does it correlate with the tectonic development of the Southern Ocean, and if so, in what way?

Across the early Eocene to late Oligocene, the sedimentary strata across the F/MB and the MEB show extreme current-related thinning and erosion, attesting to the transition towards a highly dynamic circulation regime. The formation of the drift deposits is clearly reduced and the dominating erosional features mainly have affected two intervals with average water depth of ca. 1900 m (2500 ms TWT) and 2800 m (3700 ms TWT). [See section 5.6.3 for details]. In addition, compared to the Paleocene-Eocene, these current-controlled erosional features further developed on the southern, as well as the northern flanks of the MEB. The spatial distribution and the depth characteristics of these sedimentary features are conformant to the pathways of the modern UCDW and LCDW according to regional hydrographic data (Arhan et al., 1999; Naveira Garabato et al., 2002; Orsi et al., 1995). In the present oceanic setting, these water masses are constrained to the bathymetry of the MEB, rounding the eastern flank and entering the Argentine Basin. DSDP Sites at the F/MP include records of several major biostratigraphic hiatus and erosional unconformities during the early Eocene-Quaternary in association with the vigorous action of the bottom currents subsequent to the opening of the Drake Passage (Shipboard_Scientific_Party, 1974a, c, d, 1980a). The establishment of the ACC is often thought to be preconditioned by the full opening of the Drake Passage (e.g. Barker, 2001b; Barker and Thomas, 2004; Kennett, 1977; Lawver and Gahagan, 2003). Plate tectonic reconstructions (Barker, 2001a; Eagles and

Jokat, 2014; van de Lagemaat et al., 2021), circum-Antarctic palaeo-bathymetric reconstructions (Pérez-Díaz and Eagles, 2014), as well as geological, geophysical, and geochemical studies (Livermore et al., 2005; Scher and Martin, 2006a; Scher et al., 2015) endorse vast late Eocene-Oligocene oceanographic modifications with the inception of the ACC subsequent to the development of the Drake Passage, the completion of a full circumpolar pathway, and the onset of Antarctic glaciation. The extensive sedimentary erosional features across the F/MB and the MEB in my study also bears witness to the scouring action of deep water masses, which according to their depth characters and pathways would correspond to proto-UCDW and -LCDW, overspilling the F/MP within a well-developed ACC since the Oligocene.

According to the contouritic features on the F/MP, how have the characteristics, pathways, and intensities of the water masses flowing within the ACC varied during the Cenozoic?

By evidence of the sedimentary features, since the early Miocene, the pathways of the proto-UCDW and -LCDW in the F/MB and to the east of the MEB in general stayed uniform, however the deceleration of these currents should have been responsible for the onset of the giant drift formation on the eastern flank of the MEB. Across the early – to middle Miocene transition, however, a clear shift towards a more dynamic ocean has reduced the current-controlled deposition accompanied by an eastward relocation of the pathways of these water masses. In addition, at the early-middle Miocene transition, very bold sedimentary indications for the action of abyssal water masses are present in the depression north of the MEB. Today the pathway of the South Pacific Deep Water (SPDW) lies to the north of the MEB according to the physical hydrology surveys (Arhan et al., 1999; Naveira Garabato et al., 2002; Orsi et al., 1995). Extreme thinning of the Miocene-Recent strata and bold erosional moat features at average water depths of 3300 m (ca. 4400 ms TWT) hint at non-depositional and erosional action of a proto-SPDW since Miocene times, which would have required enough deepening and widening of the Drake Passage by this time to allow the through-flow of pacific-sourced water masses. [See section 5.6.3 for details]. Current-related sedimentary erosional features dominate in general the entire F/MP across the early- to middle Miocene, attesting to the intensification of southern-sourced water masses, also reported at DSDP Sites (Shipboard_Scientific_Party, 1974c, d, 1980a). This major erosional event seems to have paved the way for the present seafloor topography of the F/MB. More importantly, my findings suggest that sediment removal and scouring of at least 270 m of overburden above the Opal-A to Opal-CT transition zone across the F/MB and Falkland/Malvinas Trough (F/MT) by the vigorous deep oceanic currents at early-middle Miocene times has contributed to the fossilization/arrest of the silica diagenetic front. [See section 6.6.3 for details]. Moreover, the earliest observations of sedimentary footprints from abyssal currents in the F/MT correlates well with the Miocene estimations for the full opening of the Drake Passage and development of the Scotia Sea

(Eagles and Jokat, 2014; van de Lagemaat et al., 2021) which allowed the establishment of the proto-ACC (Dalziel et al., 2013; Katz et al., 2011; Scher and Martin, 2004) and the enhanced bottom water production below the expanding Antarctic ice shelves (Barker, 2001a; Flower and Kennett, 1994; Zachos et al., 2001). A proto-Weddell Sea Deep Water (WSDW), with a similar depth signature as the one flowing today into the Georgia Basin, has shaped a well-structured mounded confined sediment drift at average depth of the ca 3750 m (5000 ms TWT) in the eastern and central parts of the F/MT since the early-middle Miocene. Additionally, the structural characteristics of the deformational folds at the toe of the North Scotia Ridge (NSR) in F/MT and reactivated faulting on the southern sector of the F/MB, which seem to be bound to early-middle Miocene, acknowledge the tectonic development of the Drake Passage-Scotia Sea zone that will have allowed the establishment of a modern four-level stratified oceanic system. Hence my findings support the interpretation that the deep and abyssal water masses have been flowing in a modern ACC at least since the middle Miocene times in the southwestern south Atlantic. [See sections 6.6.3 and 7.6 for details].

CHAPTER 9. Future direction

Quaternary palaeoceanography of the southwestern South Atlantic.

Deep Sea Drilling project (DSDP) Sites at the F/MP drilled into thin veneers (less than a few meters) of post-Miocene sedimentary strata (Shipboard_Scientific_Party, 1974a, c, d, 1980a), which indicates persistent scouring and winnowing action of deep and abyssal water masses flowing within the ACC. These sedimentary bedforms would have archived the modifications of the ACC in Pliocene-Holocene times. The limited thickness of these strata, below the vertical resolution of reflection seismology, made them invisible to the seismic reflection data (discussed in this thesis). Yet the acoustic sub-bottom profiling data, which was collected parallel to the seismic data acquisition during cruise MSM81 by the Alfred Wegener Institute (AWI), very well imaged these shallow and thin bedforms. Integrating the sub-bottom profiling data with the available shallow core information across the F/MP would provide high-resolution palaeoceanographic records of the Quaternary in the southwestern South Atlantic.

Cretaceous ocean in the western South Atlantic.

The ice-free poles of Cretaceous times are believed to have dictated oceanographic and atmospheric circulations, in which much lower temperature gradients prevailed between the poles and the equator (Hay, 2011). Synchronous low- and high- pressure systems in the northern and southern hemispheres would have hindered steady Westerlies and therefore no large ocean gyres and meridional ocean heat transport would have evolved. A chaotic circulation regime with bathymetrically steered deep-reaching eddies would be developed by variable winds (Uenzelmann-Neben et al., 2017; Viebahn et al., 2016). Integration of the seismic data from cruise MSM81, which covers mostly the eastern sector of the Falkland/Malvinas Basin (F/MB) with existing regional seismic data covering the central parts of the basin (e.g. RV Robert D. Conrad RC cruise 2106) and seismic datasets commercially available east of the Falkland/Malvinas Islands (F/MI) would allow to image the Cretaceous sedimentary bedforms basin-wide and to investigate whether Cretaceous mesoscale eddies would have shaped drift deposits in F/MB.

CHAPTER 10. References

- Adie**, R.J., 1952. The position of the Falkland Islands in a reconstruction of Gondwanaland. Geological Magazine 89, 401-410.
- Allen**, C.S., Pike, J., Pudsey, C.J., 2011. Last glacial-interglacial sea-ice cover in the SW Atlantic and its potential role in global deglaciation. Quaternary Science Reviews 30 (19-20), 2446-2458.
- Allen**, C.S., Pike, J., Pudsey, C.J., Leventer, A., 2005. Submillennial variations in ocean conditions during deglaciation based on diatom assemblages from the southwest Atlantic. Paleo 20 (2).
- Alves**, D.P.V., Maselli, V., Iacopini, D., Viana, A.R., Jovane, L., 2023. Oceanographic exchanges between the Southern and Northern Atlantic during the Cenozoic inferred from mixed contourite-turbidite systems in the Brazilian Equatorial Margin. Marine Geology 456.
- Aminzadeh**, F., Dasgupta, S.N., 2013. Chapter 3 - Fundamentals of Petroleum Geophysics, in: Aminzadeh, F., Dasgupta, S.N. (Eds.), Developments in Petroleum Science. Elsevier, pp. 37-92.
- Arhan**, M., Heywood, K.J., King, B.A., 1999. The deep waters from the Southern Ocean at the entry to the Argentine Basin. Deep-Sea research II 46, 475-499.
- Arhan**, M., Naveira Garabato, A.C., Heywood, K.J., Stevens, D.P., 2002. The Antarctic Circumpolar Current between the Falkland Islands and South Georgia. Journal of Physical Oceanography 32, 1914-1931.
- Badley**, M.E., 1985. Practical seismic interpretation.
- Baristeas**, N., Anka, Z., di Primio, R., Rodriguez, J.F., Marchal, D., Dominguez, F., 2012. Distribution of hydrocarbon leakage indicators in the Malvinas Basin, offshore Argentine continental margin. Marine Geology 332-334, 56-74.
- Barker**, P.F., 1977b. Correlations between sites on the eastern Falkland Plateau by means of seismic reflection profiles, Leg 36, DSDP, in: Barker, P.F., Dalziel, I., Wise Jr, S.W., et.al. (Eds.), Initial Reports DSDP. U.S. Govt. Printing Office, Washington, pp. 971-990.
- Barker**, P.F., 2001b. Scotia Sea regional tectonic evolution: implications for mantle flow and palaeocirculation. Earth-Science Reviews 55, 1-39.
- Barker**, P.F., Filippelli, G.M., Florindo, F., Martin, E.E., Scher, H.D., 2007. Onset and role of the Antarctic Circumpolar Current. Deep Sea Research Part II: Topical Studies in Oceanography 54, 2388-2398.
- Barker**, P.F., Thomas, E., 2004. Origin, signature and palaeoclimatic influence of the Antarctic Circumpolar Current. Earth-Science Reviews 66, 143-166.
- Bayer**, U., 1980. The Influence of Sediment Composition on Physical Properties Interrelationships, in: Ludwig, W.J., Krasheninnikov, V.A., et.al. (Eds.), Initial Reports DSDP. U.S. Govt. Printing Office, Washington, pp. 1111-1132.
- Belkin**, I.M., Gordon, A.L., 1996. Southern Ocean fronts from the Greenwich meridian to Tasmania. Journal of Geophysical Research: Oceans 101, 3675-3696.
- Ben Avraham**, Z., Hartnady, C.H.J., Kitchin, K.A., 1997. Structure and tectonics of the Agulhas-Falkland fracture zone. Tectonophysics 282, 83-98.
- Berndt**, C., Bünz, S., Clayton, T., Mienert, J., Saunders, M., 2004. Seismic character of bottom simulating reflectors: examples from the mid-Norwegian margin. Marine and Petroleum Geology 21, 723-733.
- Bohrmann**, G., Spieß, V., Hinze, H., Kuhn, G., 1992. Reflector “Pc” a prominent feature in the Maud Rise sediment sequence (eastern Weddell Sea): Occurrence, regional distribution and implications to silica diagenesis. Marine Geology 106, 69-87.
- Borrello**, A.V., 1963. Fremontella inopinata n. sp. del Cámbrico de la Argentina. Ameghiniana 3, 51-55.
- Brett**, R., 1992. The Cretaceous-Tertiary extinction: A lethal mechanism involving anhydrite target rocks. Geochimica et Cosmochimica Acta 56, 3603-3606.
- Brown**, B., Gaina, C., Mueller, R.D., 2006. Circum-Antarctic palaeobathymetry: Illustrated examples from Cenozoic to recent times. Palaeogeography, Paleoceanography, Palaeoecology 231, 158-168.

-
- Bry**, M., White, N., Singh, S., England, R., Trowell, C., **2004**. Anatomy and formation of oblique continental collision: South Falkland basin. *Tectonics* 23, n/a-n/a.
- Bünz**, S., Mienert, J., Berndt, C., **2003**. Geological controls on the Storegga gas-hydrate system of the mid-Norwegian continental margin. *Earth and Planetary Science Letters* 209, 291-307.
- Carcione**, J., Picotti, S., **2006**. P-wave seismic attenuation by slow-wave diffusion: Effects of inhomogeneous rock properties: *Geophysics*, 71, O1–O8, <http://dx.doi.org/10.1190/1.219452>.
- Carter**, A., Curtis, M., Schwanethal, J., **2014**. Cenozoic tectonic history of the South Georgia microcontinent and potential as a barrier to Pacific-Atlantic through flow. *Geology* 42, 299-302.
- Chemale Jr**, F., Ramos, V.A., Naipauer, M., Girelli, T.J., Vargas, M., **2018**. Age of basement rocks from the Maurice Ewing Bank and the Falkland/Malvinas Plateau. *Precambrian Research* 314, 28-40.
- Ciesielski**, P.F., Weaver, F.M., **1980**. Neogene and Quaternary Paleoenvironmental history of Deep Sea Drilling Project Leg 71 Sediments, Southwest Atlantic Ocean, in: Ludwig, W.J., Krasheninnikov, V.A., et.al. (Eds.), Initial Reports DSDP. U.S. Govt. Printing Office, Washington, pp. 461-477.
- Ciesielski**, P.F., Wise Jr, S.W., **1977**. Geologic history of the Maurice Ewing Bank of the Falkland Plateau (southwest Atlantic sector of the Southern Ocean) based on piston and drill cores. *Marine Geology* 25, 175-207.
- Claerbout**, J.F., Doherty, S.M., **1972**. Downward continuation of moveout-corrected seismograms. *Geophysics* 37, 741-768.
- Cunningham**, A.P., **1999**. Geophysical investigations of the North Scotia Ridge. Unpublished PhD thesis, University of London, London, England.
- Cunningham**, A.P., Barker, P.F., **1996**. Evidence for westward-flowing Weddell Sea Deep Water in the Falkland Trough, western South Atlantic. *Deep-Sea research I* 43 (5), 643-654.
- Cunningham**, A.P., Barker, P.F., Tomlinson, J.S., **1998**. Tectonics and sedimentary environment of the North Scotia Ridge region revealed by side-scan sonar. *Journal of the Geological Society* 155, 941-956.
- Cunningham**, A.P., Howe, J.A., Barker, P.F., **2002**. Contourite sedimentation in the Falkland Trough, western South Atlantic. *Geological Society, London, Memoirs* 22, 337-352.
- Cunningham**, W., Mann, P., **2007**. Tectonics of strike-slip restraining and releasing bends. *Geological Society, London, Special Publications* 290, 1-12.
- Cunningham**, W.D., Dalziel, I.W., Lee, T.Y., Lawver, L.A., **1995**. Southernmost South America-Antarctic Peninsula relative plate motions since 84 Ma: Implications for the tectonic evolution of the Scotia Arc region. *Journal of Geophysical Research: Solid Earth* 100, 8257-8266.
- Dalziel**, I.W., Lawver, L., Murphy, J., **2000**. Plumes, orogenesis, and supercontinental fragmentation. *Earth and Planetary Science Letters* 178, 1-11.
- Dalziel**, I.W., Lawver, L.A., Norton, I.O., Gahagan, L.M., **2013**. The Scotia Arc: genesis, evolution, global significance. *Annual Review of Earth and Planetary Sciences* 41.
- Dalziel**, I.W.D., **2014**. Drake Passage and the Scotia arc: A tortuous space-time gateway for the Antarctic Circumpolar Current. *Geology* 42, 367-368.
- Dalziel**, I.W.D., Elliot, D.H., **1971**. Evolution of the Scotia Arc. *Nature* 233, 246-252.
- Dalziel**, I.W.D., Macdonald, D.I.M., Stone, P., Storey, B.C., **2021**. South Georgia microcontinent: Displaced fragment of the southernmost Andes. *Earth-Science Reviews* 220.
- Davies**, R., Bell, B.R., Cartwright, J.A., Shoulders, S., **2002**. Three-dimensional seismic imaging of Paleogene dike-fed submarine volcanoes from the northeast Atlantic margin. *Science* 30, 223-226.
- Davies**, R., Cartwright, J., **2002**. A fossilized Opal A to Opal C/T transformation on the northeast Atlantic margin: Support for a significantly elevated palaeogeothermal gradient during the Neogene? *Basin Research* 14, 467-486.
- Davies**, R.J., **2005**. Differential compaction and subsidence in sedimentary basins due to silica diagenesis: A case study. *Geological Society of America Bulletin* 117, 1146-1155.

-
- Davies**, R.J., Clark, I.R., **2006**. Submarine slope failure primed and triggered by silica and its diagenesis. *Basin Research* 18, 339-350.
- Davies**, R.J., Ireland, M.T., Cartwright, J.A., **2009**. Differential compaction due to the irregular topology of a diagenetic reaction boundary: a new mechanism for the formation of polygonal faults. *Basin Research* 21, 354-359.
- de Lépinay**, M.M., Loncke, L., Basile, C., Roest, W.R., Patriat, M., Maillard, A., De Clarens, P., **2016**. Transform continental margins—Part 2: A worldwide review. *Tectonophysics* 693, 96-115.
- De Wit**, M., **1976**. THE EVOLUTION OF THE SCOTIA ARC AS A KEY TO THE RECONSTRUCTION OF SOUTHWESTERN GONDWANALAND *.
- Del Ben**, A., Mallardi, A., **2004**. Interpretation and chronostratigraphic mapping of multichannel seismic reflection profile I95167, Eastern Falkland Plateau (South Atlantic). *Marine Geology* 209, 347-361.
- Del Ben**, A.M., A., **2004**. Interpretation and chronostratigraphic mapping of multichannel seismic reflection profile I95167, Easter Falkland Plateau (South Atlantic). *Marine Geology* 209, 347-361.
- Dick**, H.v.d., Rullkötter, J., Welte, D.H., **1983**. Content, Type, and Thermal Evolution of Organic Matter in Sediments from the Eastern Falkland Plateau, Deep Sea Drilling Project, Leg 71.
- Diester-Haass**, L., Robert, C., Chamley, H., **1996**. The Eocene-Oligocene preglacial-glacial transition in the Atlantic sector of the Southern Ocean (ODP Site 690). *Marine Geology* 131, 123-149.
- Dingle**, R.V., Robson, S.H., **1992**. Southwestern African Continental Rise: Structural and Sedimentary Evolution, in: Poag, W., de Graciansky, C. (Eds.), *Geologic evolution of Atlantic Continental Rifts*. Van Nostrand Reinhold, New York, pp. 62-75.
- Dix**, C.H., **1955**. Seismic velocities from surface measurements. *Geophysics* 20, 68-86.
- Domenico**, S.N., **1977**. Elastic properties of unconsolidated porous sand reservoirs. *Geophysics* 42, 1339-1368.
- Dondurur**, D., **2018**. Acquisition and processing of marine seismic data. Elsevier.
- Dorschel**, B., Hehemann, L., Viquerat, S., Warnke, F., Dreutter, S., Tenberge, Y.S., Accettella, D., An, L., Barrios, F., Bazhenova, E., Black, J., Bohoyo, F., Davey, C., De Santis, L., Dotti, C.E., Fremand, A.C., Fretwell, P.T., Gales, J.A., Gao, J., Gasperini, L., Greenbaum, J.S., Jencks, J.H., Hogan, K., Hong, J.K., Jakobsson, M., Jensen, L., Kool, J., Larin, S., Larter, R.D., Leitchenkov, G., Loubrieu, B., Mackay, K., Mayer, L., Millan, R., Morlighem, M., Navidad, F., Nitsche, F.O., Nogi, Y., Pertuisot, C., Post, A.L., Pritchard, H.D., Purser, A., Rebesco, M., Rignot, E., Roberts, J.L., Rovere, M., Ryzhov, I., Sauli, C., Schmitt, T., Silvano, A., Smith, J., Snaith, H., Tate, A.J., Tinto, K., Vandenbossche, P., Weatherall, P., Wintersteller, P., Yang, C., Zhang, T., Arndt, J.E., **2022**. The International Bathymetric Chart of the Southern Ocean Version 2. *Sci Data* 9, 275.
- Du Toit**, A., **1927**. A geological comparison of South America with South Africa. Carnegie Institute of Washington Publications 381, 1-157.
- Du Toit**, A.L., **1937**. Our wandering continents: an hypothesis of continental drifting.
- Dummann**, W., Hofmann, P., Herrle, J.O., Wennrich, V., Wagner, T., **2020**. A refined model of Early Cretaceous South Atlantic–Southern Ocean gateway evolution based on high-resolution data from DSDP Site 511 (Falkland Plateau). *Palaeogeography, Palaeoclimatology, Palaeoecology*.
- Dummann**, W., Hofmann, P., Herrle, J.O., Wennrich, V., Wagner, T., **2021**. A refined model of Early Cretaceous South Atlantic–Southern Ocean gateway evolution based on high-resolution data from DSDP Site 511 (Falkland Plateau). *Palaeogeography, Palaeoclimatology, Palaeoecology*, 110113.
- Dummann**, W., Steinig, S., Hofmann, P., Flögel, S., Osborne, A.H., Frank, M., Herrle, J.O., Bretschneider, L., Sheward, R.M., Wagner, T., **2020**. The impact of Early Cretaceous gateway evolution on ocean circulation and organic carbon burial in the emerging South Atlantic and Southern Ocean basins. *Earth and Planetary Science Letters* 530, 115890.
- Eagles**, G., Eisermann, H., **2020**. The Skytrain plate and tectonic evolution of southwest Gondwana since Jurassic times. *Scientific Reports* 10.
- Eagles**, G., Jokat, W., **2014**. Tectonic reconstructions for paleobathymetry in Drake Passage. *Tectonophysics* 611, 28-50.

-
- Eagles**, G., Livermore, R.A., Fairhead, J.D., Morris, P., 2005. Tectonic evolution of the west Scotia Sea. *Journal of Geophysical Research: Solid Earth* 110.
- Eagles**, G., Livermore, R.A., Morris, P., 2006. Small basins in the Scotia Sea: The Eocene Drake Passage gateway. *Earth and Planetary Science Letters* 242, 343-353.
- Emery**, D., Myers, K., 2009. Sequence stratigraphy. John Wiley & Sons.
- Esentia**, I., Stow, D., Smillie, Z., 2018. Contourite Drifts and Associated Bedforms, Submarine Geomorphology, pp. 301-331.
- Esteban**, F.D., Ormazabal, J.P., Palma, F., Cayo, L.E., Lodolo, E., Tassone, A., 2020. Strike-slip related folding within the Malvinas/Falkland Trough (south-western Atlantic ocean). *Journal of South American Earth Sciences* 98.
- Faugères**, J.C., Stow, D.A.V., 2008. Chapter 14 Contourite Drifts: Nature, Evolution and Controls, in: Rebesco, M., Camerlenghi, A. (Eds.), *Developments in Sedimentology*. Elsevier, pp. 257, 259-288.
- Faugères**, J.C., Stow, D.A.V., Imbert, P., Viana, A.R., 1999. Seismic Features Diagnostic of Contourite Drifts. *Marine Geology* 162, 1-38.
- Faulkner**, P.A., 2000. Tectonic and thermal evolution of South Atlantic marginal basins. University of Cambridge.
- Fetter**, A.F.H., Matano, R.P., 2008. On the origins of the variability of the Malvinas Current in a global, eddy-permitting numerical simulation. *Journal of Geophysical Research C113*.
- Fischer**, M.D., Uenzelmann-Neben, G., 2018a. Late Cretaceous onset of current controlled sedimentation in the African-Southern Ocean gateway. *Marine Geology* 395, 380-396.
- Fischer**, M.D., Uenzelmann-Neben, G., 2018b. Neogene Modifications of Circulation in the Northeastern African-Southern Ocean Gateway. *Geochemistry, Geophysics, Geosystems* 19, 4673-4693.
- Fish**, P., 2005. Frontier South, East Falkland basins reveal important exploration potential. *Oil & gas journal* 103, 34-40.
- Flood**, R.D., Shor, A.N., Manley, P.L., 1993. Morphology of abyssal mudwaves at Project MUDWAVES sites in the Argentine Basin. *Deep-Sea research II* 40, 859-888.
- Flower**, B.P., Kennett, J.P., 1994. The middle Miocene climatic transition: East Antarctic ice sheet development, deep ocean circulation and global carbon cycling. *Palaeogeography, Palaeoclimatology, Palaeoecology* 108, 537-555.
- Foschi**, M., Cartwright, J.A., 2016. South Malvinas/Falkland Basin: Hydrocarbon migration and petroleum system. *Marine and Petroleum Geology* 77, 124-140.
- Gadallah**, M.R., Fisher, R., 2008. Exploration geophysics. Springer Science & Business Media.
- Geletti**, R., Busetti, M., 2011. A double bottom simulating reflector in the western Ross Sea, Antarctica. *Journal of Geophysical Research: Solid Earth* 116.
- Gille**, S.T., 1994. Mean sea surface height of the Antarctic Circumpolar Current from Geosat data: Method and application. *Journal of Geophysical Research: Oceans* 99, 18255-18273.
- Goldner**, A., Herold, N., Huber, M., 2014. Antarctic glaciation caused ocean circulation changes at the Eocene-Oligocene transition. *Nature* 511, 574-577.
- Gordon**, A.L., Editors-in-Chief: John, H.S., Karl, K.T., Steve, A.T., 2001. Current Systems in the Southern Ocean, in: John, A.A., Steele, H. (Eds.), *Encyclopedia of Ocean Sciences (Second Edition)*. Academic Press, Oxford, pp. 735-743.
- Gruetzner**, J., Uenzelmann-Neben, G., 2016. Contourite drifts as indicators of Cenozoic bottom water intensity in the eastern Agulhas Ridge area, South Atlantic. *Marine Geology* 378, 350-360.
- Gruetzner**, J., Uenzelmann-Neben, G., Franke, D., 2012. Variations in sediment transport at the central Argentine continental margin during the Cenozoic. *Geochem. Geophys. Geosyst.* 13, Q10003.

-
- Gruetzner**, J., Uenzelmann-Neben, G., Franke, D., **2016**. Evolution of the northern Argentine margin during the Cenozoic controlled by bottom current dynamics and gravitational processes. *Geochemistry, Geophysics, Geosystems* 17, 3131-3149.
- Gruetzner**, J., Uenzelmann-Neben, G., Franke, D., Arndt, J.E., **2014**. Slow-down of Circumpolar Deepwater flow during the Late Neogene: Evidence from a mudwave field at the Argentine continental slope. *Geophysical Research Letters* 41, 2070-2076.
- Grützner**, J., Mienert, J., **1999**. Physical property changes as a monitor of pelagic carbonate diagenesis: an empirically derived diagenetic model for Atlantic Ocean basins. *AAPG Bulletin* 83, 1485-1501.
- Guerin**, G., Goldberg, D., **2002**. Sonic waveform attenuation in gas hydrate-bearing sediments from the Mallik 2L-38 research well, Mackenzie Delta, Canada. *Journal of Geophysical Research: Solid Earth* 107, EPM 1-1-EPM 1-11.
- Gulick**, S.P.S., Barton, P.J., Christeson, G.L., Morgan, J.V., McDonald, M., Mendoza-Cervantes, K., Pearson, Z.F., Surendra, A., Urrutia-Fucugauchi, J., Vermeesch, P.M., Warner, M.R., **2008**. Importance of pre-impact crustal structure for the asymmetry of the Chicxulub impact crater. *Nature Geosci* 1, 131-135.
- Hay**, W.W., **2011**. Can humans force a return to a 'Cretaceous' climate? *Sedimentary Geology* 235, 5-26.
- Hein**, J.R., Scholl, D.W., Barron, J.A., Jones, M.G., Miller, J., **1978**. Diagenesis of late Cenozoic diatomaceous deposits and formation of the bottom simulating reflector in the southern Bering Sea*. *Sedimentology* 25, 155-181.
- Hernandez-Molina**, F.J., Larter, R.D., Rebesco, M., Maldonado, A., **2006**. Miocene reversal of bottom water flow along the Pacific Margin of the Antarctic Peninsula: Stratigraphic evidence from a contourite sedimentary tail. *Marine Geology* 228, 93-116.
- Herold**, N., Huber, M., Müller, R.D., Seton, M., **2012**. Modeling the Miocene climatic optimum: Ocean circulation. *Paleoceanography* 27, PA1209.
- Hesse**, R., **1988**. Diagenesis #13. Origin of chert: Diagenesis of biogenic siliceous sediments. *Geoscience Canada* 15, 171-192.
- Hillier**, P.C.R.a.B.V., **2000**. POST-DRILLING ANALYSIS OF THE NORTH FALKLAND BASIN-PART 2: PETROLEUM SYSTEM AND FUTURE PROSPECTS.
- Holbourn**, A., Kuhnt, W., Soeding, E., **2001**. Atlantic paleobathymetry, paleoproductivity and paleocirculation in the late Albian: the benthic foraminiferal record. *Palaeogeography, Palaeoclimatology, Palaeoecology* 170, 171-196.
- Horn**, M., Uenzelmann-Neben, G., **2015**. The Deep Western Boundary Current at the Bounty Trough, east of New Zealand: Indications for its activity already before the opening of the Tasmanian Gateway. *Marine Geology* 362, 60-75.
- Howe**, J.A., Pudsey, C.J., Cunningham, A.P., **1997**. Pliocene-Holocene contourite deposition under the Antarctic Circumpolar Current, Western Falkland Trough, South Atlantic Ocean. *Marine Geology* 138, 27-50.
- Isaacs**, C.M., **1981**. Porosity reduction during diagenesis of the Monterey Formation, Santa Barbara coastal area, California.
- Johnston**, D.H., **2010**. Methods and applications in reservoir geophysics. *Society of Exploration Geophysicists*.
- Kastner**, M., Keene, J., Gieskes, J., **1977a**. Diagenesis of siliceous oozes—I. Chemical controls on the rate of opal-A to opal-CT transformation—an experimental study. *Geochimica et Cosmochimica Acta* 41, 1041-1059.
- Kastner**, M., Keene, J.B., Gieskes, J.M., **1977b**. Diagenesis of siliceous oozes—I. Chemical controls on the rate of opal-A to opal-CT transformation—an experimental study. *Geochimica et Cosmochimica Acta* 41, 1041-1059.
- Katz**, M.E., Cramer, B.S., Toggweiler, J.R., Esmay, G., Liu, C., Miller, K.G., Rosenthal, Y., Wade, B.S., Wright, J.D., **2011**. Impact of Antarctic Circumpolar Current Development on Late Paleogene Ocean Structure. *Science* 332, 1076-1079.
- Kearey**, P., Brooks, M., Hill, I., **2002**. An introduction to geophysical exploration. John Wiley & Sons.

-
- Kennett, J.P., 1977.** Cenozoic evolution of Antarctic glaciation, the circum-Antarctic Ocean, and their impact on global paleoceanography. *Journal of Geophysical Research* 82, 3843-3860.
- Kim, H.-J., Jou, H.-T., Kang, S.-G., Lee, G.H., Yi, B.Y., Yoo, D.-G., Ryu, B.-J., Shin, C., 2013.** Seismic characterization and imaging of a gas hydrate deposit in the western part of the Ulleung Basin, the East Sea (Japan Sea). *Marine and Petroleum Geology* 47, 214-221.
- Kim, Y.S., Orsi, A.H., 2014.** On the Variability of Antarctic Circumpolar Current Fronts Inferred from 1992–2011 Altimetry*. *Journal of Physical Oceanography* 44, 3054-3071.
- Kimbell, G.S., Richards, P.C., 2008.** The three-dimensional lithospheric structure of the Falkland Plateau region based on gravity modelling. *Journal of the Geological Society* 165, 795-806.
- Koenitz, D., White, N., McCave, I.N., Hobbs, R., 2008.** Internal structure of a contourite drift generated by the Antarctic Circumpolar Current. *Geochemistry, Geophysics, Geosystems* 9, n/a-n/a.
- König, M., Jokat, W., 2010.** Advanced insights into magmatism and volcanism of the Mozambique Ridge and Mozambique Basin in the view of new potential field data. *Geophysical Journal International* 180, 158-180.
- Kuhlbrodt, T., Griesel, A., Montoya, M., Levermann, A., Hofmann, M., Rahmstorf, S., 2007.** On the driving processes of the Atlantic meridional overturning circulation. *Reviews of Geophysics* 45.
- Kuramoto, S., Tamaki, K., Langseth, M., Nobes, D., Tokuyama, H., Pisciotti, K., Taira, A., 1992.** 73. Can opal-A/opal-CT BSR be an indicator of the thermal structure of the Yamato Basin, Japan Sea. *Age* 794.
- Kvenvolden, K.A., 1994.** Natural gas hydrate occurrence and issues. *Annals of the New York Academy of Sciences* 715, 232-246.
- Langseth, M., Ludwig, W., 1983.** A heat-flow measurement on the Falkland Plateau. *Initial Reports of the Deep Sea Drilling Project* 71, 299-303.
- Lawver, L.A., Gahagan, L.M., 2003.** Evolution of Cenozoic seaways in the circum-Antarctic region. *Palaeogeography, Palaeoclimatology, Palaeoecology* 198, 11-37.
- Lazarus, D., Caulet, J.P., 1993.** Cenozoic Southern Ocean reconstructions. *Antarctic Research Series* 60, 145-174.
- Lee, M.W., 2004.** Elastic velocities of partially gas-saturated unconsolidated sediments. *Marine and Petroleum Geology* 21, 641-650.
- Levashov, S., Yakymchuk, M., Korchagin, I., Bakhmutov, V., Soloviev, V., Bozhezha, D., 2014.** The Falkland Basins-New Structural Model and Hydrocarbon Bearing Prospects (by Remote Sensing and Geoelectric Data), 76th EAGE Conference and Exhibition 2014. European Association of Geoscientists & Engineers, pp. 1-5.
- Livermore, R., Hillenbrand, C.-D., Meredith, M., Eagles, G., 2007.** Drake Passage and Cenozoic climate: An open and shut case? *Geochemistry Geophysics Geosystems* 8.
- Livermore, R., Nankivell, A., Eagles, G., Morris, P., 2005.** Paleogene opening of Drake Passage. *Earth and Planetary Science Letters* 236, 459-470.
- Lodolo, E., Camerlenghi, A., Brancolini, G., 1993.** A bottom simulating reflector on the South Shetland margin, Antarctic Peninsula. *Antarctic Science* 5(02), 207-210.
- Lodolo, E., Donda, F., Tassone, A., 2006.** Western Scotia Sea margins: Improved constraints on the opening of the Drake Passage. *Journal of Geophysical Research* B111.
- Lonardi, A., 1974.** Measurement of chemical/physical properties. U.S. Government Printing Office, Washington, D.C., 197 vol. 36.
- Lopes, F.M., Koutsoukos, E.A.M., Kochhann, K.G.D., Savian, J.F., Fauth, G., 2017.** Benthic foraminiferal paleoecology and depositional patterns during the Albian at DSDP Site 327 (Falkland Plateau). *Journal of South American Earth Sciences* 78, 126-133.
- Lorenzo, J.M., Mutter, J.C., 1988.** Seismic stratigraphy and tectonic evolution of the Falkland/Malvinas Plateau. *Revista Brasileira de Geociencias* 18, 191-200.

-
- Lovecchio**, J.P., Naipauer, M., Cayo, L.E., Rohais, S., Giunta, D., Flores, G., Gerster, R., Bolatti, N.D., Joseph, P., Valencia, V.A., Ramos, V.A., **2019**. Rifting evolution of the Malvinas basin, offshore Argentina: New constraints from zircon U–Pb geochronology and seismic characterization. *Journal of South American Earth Sciences* 95.
- Ludwig**, W.J., **1983**. Geologic framework of the Falkland Plateau, in: Ludwig, W.J., Krasheninnikov, V.A., et.al. (Eds.), *Initial Reports DSDP*. U.S. Govt. Printing Office, Washington, pp. 281-293.
- Ludwig**, W.J., Rabinowitz, P.D., **1982**. The collision complex of the North Scotia Ridge. *Journal of Geophysical Research: Solid Earth* 87, 3731-3740.
- Lyle**, M., Gibbs, S., Moore, T.C., Rea, D.K., **2007**. Late Oligocene initiation of the Antarctic Circumpolar Current: Evidence from the South Pacific c. *Geology* 35, 691–694.
- Mantyla**, A.W., Reid, J.L., **1983**. Abyssal characteristics of the World Ocean waters. *Deep Sea Research Part A. Oceanographic Research Papers* 30, 805-833.
- Marshall**, J., **1994**. The Falkland Islands: a key element in Gondwana paleogeography. *Tectonics* 13, 499-514.
- Martin**, A.K., Goodlad, S.W., Hartnady, C.J.H., Plessis, A.d., **1982**. Cretaceous palaeopositions of the Falkland Plateau relative to southern Africa using Mesozoic seafloor spreading anomalies. *Geophysical Journal International* 71, 567-579.
- Meadows**, D., Davies, R.J., **2010**. The limited suitability of silica diagenetic boundaries as isothermal markers: Insights from seismic reflection imaging, Offshore Sakhalin, Russian Far East. *Marine and Petroleum Geology* 27, 1028-1039.
- Minshull**, T.A., Keddie, A., **2010**. Measuring the geotherm with gas hydrate bottom-simulating reflectors: a novel approach using three-dimensional seismic data from the eastern Black Sea. *Terra Nova* 22, 131-136.
- Misra**, A.A., Mukherjee, S., **2018**. Seismic structural analysis. *Atlas of Structural Geological Interpretation from Seismic Images*, 15-26.
- Mitchell**, C.e., Taylor, G., Cox, K., Shaw, J., **1986**. Are the Falkland Islands a rotated microplate? *Nature* 319, 131-134.
- Mitchum Jr**, R., Vail, P., Thompson III, S., **1977**. Seismic stratigraphy and global changes of sea level: Part 2. The depositional sequence as a basic unit for stratigraphic analysis: Section 2. Application of seismic reflection configuration to stratigraphic interpretation.
- Moore**, J.A., Abbott, M.R., Richman, J.G., **1999**. Location and dynamics of the Antarctic Circumpolar Front from satellite sea surface temperature data. *Journal of Geophysical Research* 104, 3059-3073.
- Müller-Michaelis**, A., Uenzelmann-Neben, G., Stein, R., **2013**. A revised Early Miocene age for the instigation of the Eirik Drift, offshore southern Greenland: Evidence from high-resolution seismic reflection data. *Marine Geology* 340, 1-15.
- Muza**, J.P., Williams, D.F., Wise Jr, S.W., **1980**. Paleogene Oxygen isotope record for Deep Sea Drilling Sites 511 and 512, subantarctic South Atlantic Ocean: Paleotemperatures, Paleoceanographic changes, and the Eocene/Oligocene boundary event, in: Ludwig, W.J., Krasheninnikov, V.A., et.al. (Eds.), *Initial Reports DSDP*. U.S. Govt. Printing Office, Washington, pp. 409-422.
- Najarifarizhendi**, B., Uenzelmann-Neben, G., **2021**. Footprints of palaeocurrents in sedimentary sequences of the Cenozoic across the Maurice Ewing Bank. *Marine Geology* 438.
- Najarifarizhendi**, B., Uenzelmann-Neben, G., **2022**. Fossilized silica diagenetic fronts: Implications for palaeoceanographic evolution across the Falkland/Malvinas plateau. *Marine and Petroleum Geology*.
- Nanda**, N.C., **2021**. Seismic data interpretation and evaluation for hydrocarbon exploration and production. Springer.
- Naveira Garabato**, A.C., Ferrari, R., Polzin, K.L., **2011**. Eddy stirring in the Southern Ocean. *Journal of Geophysical Research: Oceans* 116.
- Naveira Garabato**, A.C., Heywood, K.J., Stevens, D.P., **2002**. Modification and pathways of Southern Ocean Deep Waters in the Scotia Sea. *Deep Sea Research Part I: Oceanographic Research Papers* 49, 681-705.
- Neagu**, R.C., Cartwright, J., Davies, R., Jensen, L., **2010**. Fossilisation of a silica diagenesis reaction front on the mid-Norwegian margin. *Marine and Petroleum Geology* 27, 2141-2155.

-
- Nicholson**, U., Libby, S., Tappin, D.R., McCarthy, D., **2020**. The Subantarctic Front as a sedimentary conveyor belt for tsunamigenic submarine landslides. *Marine Geology* 424.
- Nicholson**, U., Stow, D., **2019**. Erosion and deposition beneath the Subantarctic Front since the Early Oligocene. *Scientific Reports* 9, 9296.
- Nielsen**, T., Knutz, P.C., Kuijpers, A., Rebesco, M., Camerlenghi, A., **2008**. Chapter 16 Seismic Expression of Contourite Depositional Systems, *Developments in Sedimentology*. Elsevier, pp. 301-321.
- Nisancioglu**, K.H., Raymo, M.E., Stone, P.H., **2003**. Reorganization of Miocene deep water circulation in response to the shoaling of the Central American Seaway. *Paleoceanography* 18, 1006.
- Nobes**, D.C., Murray, R.W., Kuramoto, S.i., Pisciotto, K.A., Holler, P., **1992**. Impact of silica diagenesis on physical property variations, *Proceedings of the Ocean Drilling Program, Scientific Results*. Ocean Drilling Program, College Station, pp. 3-23.
- Nouzé**, H., Cosquer, E., Collot, J., Foucher, J.-P., Klingelhoefer, F., Lafay, Y., Géli, L., **2009**. Geophysical characterization of bottom simulating reflectors in the Fairway Basin (off New Caledonia, Southwest Pacific), based on high resolution seismic profiles and heat flow data. *Marine Geology* 266, 80-90.
- Nowlin**, W.D., Klinck , J.M., **1986**. The physics of the Antarctic Circumpolar Current. *Rev. Geophys.* 24, 469 - 491.
- Ohde**, A., Otsuka, H., Kioka, A., Ashi, J., **2018**. Distribution and depth of bottom-simulating reflectors in the Nankai subduction margin. *Earth Planets Space* 70, 60.
- Orsi**, A.H., Johnson, G.C., Bullister, J.L., **1999**. Circulation, mixing, and production of Antarctic Bottom Water. *Progress in Oceanography* 43, 55–109.
- Orsi**, A.H., Whitworth, T., Nowlin, W.D., **1995**. On the meridional extent and fronts of the Antarctic Circumpolar Current. *Deep Sea Research Part I: Oceanographic Research Papers* 42, 641-673.
- Pelayo**, A.M., Wiens, D.A., **1989**. Seismotectonics and relative plate motions in the Scotia Sea region. *Journal of Geophysical Research: Solid Earth* 94, 7293-7320.
- Pérez-Díaz**, L., Eagles, G., **2014**. Constraining South Atlantic growth with seafloor spreading data. *Tectonics* 33, 2014TC003644.
- Pérez-Díaz**, L., Eagles, G., **2017**. South Atlantic paleobathymetry since early Cretaceous. *Sci Rep* 7, 11819.
- Pérez**, L., Hernández-Molina, F.J., Esteban, F., Tassone, A., Piola, A., Maldonado, A., Preu, B., Violante, R., Lodolo, E., **2015**. Erosional and depositional contourite features at the transition between the western Scotia Sea and southern South Atlantic Ocean: links with regional water-mass circulation since the Middle Miocene. *Geo-Marine Letters* 35, 271-288.
- Pérez**, L.F., De Santis, L., McKay, R.M., Larter, R.D., Ash, J., Bart, P.J., Böhm, G., Brancatelli, G., Browne, I., Colleoni, F., Dodd, J.P., Geletti, R., Harwood, D.M., Kuhn, G., Sverre Laberg, J., Leckie, R.M., Levy, R.H., Marschalek, J., Mateo, Z., Naish, T.R., Sangiorgi, F., Shevenell, A.E., Sorlien, C.C., van de Flierdt, T., Scientists, I.O.D.P.E., **2021**. Early and middle Miocene ice sheet dynamics in the Ross Sea: Results from integrated core-log-seismic interpretation. *GSA Bulletin*.
- Pfuhl**, H.A., McCave, I.N., **2005**. Evidence for late Oligocene establishment of the Antarctic Circumpolar Current. *Earth and Planetary Science Letters* 235, 715– 728.
- Platt**, N.H., Philip, P.R., **1995**. Structure of the southern Falkland Islands continental shelf: initial results from new seismic data. *Marine and Petroleum Geology* 12, 759-771.
- Popescu**, I., De Batist, M., Lericolais, G., Nouzé, H., Poort, J., Panin, N., Versteeg, W., Gillet, H., **2006**. Multiple bottom-simulating reflections in the Black Sea: Potential proxies of past climate conditions. *Marine Geology* 227, 163-176.
- Pudsey**, C.J., Howe, J.A., **2002**. Mixed biosiliceous-terrigenous sedimentation under the Antarctic Circumpolar Current, Scotia Sea. *Geological Society, London, Memoirs* 22, 325-336.
- Rack**, F.R., **1993**. A geologic perspective on the Miocene evolution of the Antarctic Circumpolar Current system. *Tectonophysics* 222, 397-415.

-
- Ramos**, V.A., Cingolani, C., Junior, F.C., Naipauer, M., Rapalini, A., **2017**. The Malvinas (Falkland) Islands revisited: the tectonic evolution of southern Gondwana based on U-Pb and Lu-Hf detrital zircon isotopes in the Paleozoic cover. *Journal of South American Earth Sciences* 76, 320-345.
- Rebesco**, M., Camerlenghi, A., Volpi, V., Neagu, C., Accettella, D., Lindberg, B., Cova, A., Zgur, F., Magico, P., **2007**. Interaction of processes and importance of contourites: insights from the detailed morphology of sediment Drift 7, Antarctica, in: Viana, A., Rebesco, M. (Eds.), *Economic and Palaeoceanographic Significance of Contourite Deposits*. Geological Society of London, Special Publication, London, pp. 95-110.
- Rebesco**, M., Hernández-Molina, F.J., Van Rooij, D., Wählén, A., **2014**. Contourites and associated sediments controlled by deep-water circulation processes: State-of-the-art and future considerations. *Marine Geology* 352, 111-154.
- Rebesco**, M., Stow, D.A.V., **2001**. Seismic expression of contourites and related deposits: a preface. *Marine Geophysical Research* 22, 303-308.
- Richards**, P., Gatlift, R., Quinn, M., Fannin, N., **1996**. Petroleum potential of the Falkland Islands offshore area. *Journal of Petroleum Geology* 19, 161-182.
- Richards**, P.C., Gatlift, R.W., Quinn, M.F., Fannin, N.G.T., Williamson, J.P., **1996**. The geological evolution of the Falkland Islands continental shelf. *Geological Society, London, Special Publications* 108, 105-128.
- Rintoul**, S.R., Hughes, C.W., Olbers, D., **2001**. The Antarctic Circumpolar Current System, in: Siedler, G., Church, J.A., Gould, J. (Eds.), *Ocean Circulation and Climate*. Academic Press, San Diego, pp. 271-302.
- Rivas**, L., Pérez Panera, J. P., Cusminsky, G. C., **2018**. Pliocene - Holocene calcareous nannofossils from the Malvinas Trough, southwestern Atlantic Ocean. In: *Reunión de Comunicaciones de la Asociación Paleontológica Argentina*. Puerto Madryn, 92.
- Sain**, K., Minshull, T., Singh, S., Hobbs, R., **2000**. Evidence for a thick free gas layer beneath the bottom simulating reflector in the Makran accretionary prism. *Marine Geology* 164, 3-12.
- Saito**, T., Burckle, L.H., Hays, J.D., **1974**. Implications of some pre-Quaternary sediment cores and dredgings.
- Scher**, H.D., Martin, E.E., **2004**. Circulation in the Southern Ocean during the Paleogene inferred from neodymium isotopes. *Earth and Planetary Science Letters* 228, 391 – 405.
- Scher**, H.D., Martin, E.E., **2006a**. Timing and climatic consequences of the opening of Drake Passage. *Science* 312, 428-430.
- Scher**, H.D., Martin, E.E., **2006b**. Timing and climatic consequences of the opening of Drake Passage. *Science* 312, 428-430.
- Scher**, H.D., Whittaker, J.M., Williams, S.E., Latimer, J.C., Kordes, W.E.C., Delaney, M.L., **2015**. Onset of Antarctic Circumpolar Current 30 million years ago as Tasmanian Gateway aligned with westerlies. *Nature* 523, 580-583.
- Schimschal**, C.M., Jokat, W., **2018**. The crustal structure of the continental margin east of the Falkland Islands. *Tectonophysics* 724-725, 234-253.
- Schimschal**, C.M., Jokat, W., **2019**. The crustal structure of the Maurice Ewing Bank. *Tectonophysics* 769, 228190.
- Schlüter**, P., Uenzelmann-Neben, G., **2008**. Indications for bottom current activity since Eocene times: The climate and ocean gateway archive of the Transkei Basin, South Africa. *Global and Planetary Change* 60, 416-428.
- Schreider**, A.A., Mazo, E.L., Bulychev, A.A., Kulikova, M.P., Gilod, D.A., Schreider, A.A., Boiko, A.N., **2010**. Peculiarities of the Earth's Crust Sedimentary Layer Structure in the Falkland Basin. *Oceanology* 50, 961-970.
- Schulte**, P., Alegret, L., Arenillas, I., Arz, J.A., Barton, P.J., Bown, P.R., Bralower, T.J., Christeson, G.L., Claeys, P., Cockell, C.S., Collins, G.S., Deutscher, A., Goldin, T.J., Goto, K., Grajales-Nishimura, J.M., Grieve, R.A.F., Gulick, S.P.S., Johnson, K.R., Kiessling, W., Koeberl, C., Kring, D.A., MacLeod, K.G., Matsui, T., Melosh, J., Montanari, A., Morgan, J.V., Neal, C.R., Nichols, D.J., Norris, R.D., Pierazzo, E., Ravizza, G., Rebollo-Vieyra, M., Reimold, W.U., Robin, E., Salge, T., Speijer, R.P., Sweet, A.R., Urrutia-

-
- Fucugauchi, J., Vajda, V., Whalen, M.T., Willumsen, P.S., **2010**. The Chicxulub Asteroid Impact and Mass Extinction at the Cretaceous-Paleogene Boundary. *Science* 327, 1214-1218.
- Sewall**, J.O., van de Wal, R.S.W., van der Zwan, K., van Oosterhout, C., Dijkstra, H.A., Scotese, C.R., **2007**. Climate model boundary conditions for four Cretaceous time slices. *Clim. Past* 3, 647-657.
- Shedd**, W., Boswell, R., Frye, M., Godfriaux, P., Kramer, K., **2012**. Occurrence and nature of “bottom simulating reflectors” in the northern Gulf of Mexico. *Marine and Petroleum Geology* 34, 31-40.
- Sheriff**, R., Geldart, L., **1983**. Exploration seismology vol. 2, data processing. Cambridge University Press.
- Sheriff**, R.E., **1980**. Seismic Stratigraphy for Petroleum Geologists: Part I: Stratigraphic Interpretation of Seismic Data.
- Shipboard Scientific Party**, **1974a**. Site 327, in: Barker, P.F., Dalziel, I., Wise Jr, S.W. (Eds.), Initail Reports DSDP. US Government Printing, Washington, pp. 27-86.
- Shipboard Scientific Party**, **1974b**. Site 328, in: Barker, P.F., Dalziel, I., Wise Jr, S.W. (Eds.), Initail Reports DSDP. US Government Printing, Washington, pp. 87-141.
- Shipboard Scientific Party**, **1974c**. Site 329, in: Barker, P.F., Dalziel, I., Wise Jr, S.W. (Eds.), Initial Reports DSDP. US Government Printing, Washington, pp. 143-206.
- Shipboard Scientific Party**, **1974d**. Site 330, in: Barker, P.F., Dalziel, I., Wise Jr, S.W. (Eds.), Initail Reports DSDP. US Government Printing, Washington, pp. 207-257.
- Shipboard Scientific Party**, **1977**. Evolution of the Southwestern Atlantic Ocean Basin: Results of Leg 36, Deep Sea Drilling Project, in: Barker, P.F., Dalziel, I., Wise Jr, S.W., et.al. (Eds.), Initial Reports DSDP. U.S. Govt. Printing Office, Washington, pp. 993-1014.
- Shipboard Scientific Party**, **1980a**. Site 511, in: Ludwig, W.J., Krasheninnikov, V.A., et al. (Eds.), Initial Reports DSDP. U.S. Govt. Printing Office, Washington, pp. 21-109.
- Shipboard Scientific Party**, **1980b**. Site 512, in: Ludwig, W.J., Krasheninnikov, V.A., et.al. (Eds.), Initial Reports DSDP. U.S. Govt. Printing Office, Washington.
- Shipley**, T.H., Houston, M.H., Buffler, R.T., Shaub, F.J., Mcmillen, K.J., Laod, J.W., Worzel, J.L., **1979**. Seismic Evidence for Widespread Possible Gas Hydrate Horizons on Continental Slopes and Rises1. AAPG Bulletin 63, 2204-2213.
- Sloan Jr**, E.D., **1998**. Clathrate Hydrates of Natural Gases, revised and expanded. CRC press.
- Smith**, I.J., Stevens, D.P., Heywood, K.J., Meredith, M.P., **2010**. The flow of the Antarctic Circumpolar Current over the North Scotia Ridge. *Deep Sea Research Part I: Oceanographic Research Papers* 57, 14-28.
- Smith**, W.H.S., Sandwell, D.T., **1997**. Global Sea Floor Topography from Satellite Altimetry and Ship Depth Soundings. *Science* 277, 1956-1962.
- Sokolov**, S., Rintoul, S.R., **2009**. Circumpolar structure and distribution of the Antarctic Circumpolar Current fronts: 1. Mean circumpolar paths. *J. Geophys. Res.* 114.
- Somoza**, L., León, R., Medialdea, T., Pérez, L.F., González, F.J., Maldonado, A., **2014**. Seafloor mounds, craters and depressions linked to seismic chimneys breaching fossilized diagenetic bottom simulating reflectors in the central and southern Scotia Sea, Antarctica. *Global and Planetary Change* 123, Part B, 359-373.
- Stanca**, R.M., Paton, D.A., Hodgson, D.M., McCarthy, D.J., Mortimer, E.J., **2019**. A revised position for the rotated Falkland Islands microplate. *Journal of the Geological Society* 176, 417-429.
- Steinbrink**, L., Gohl, K., Rieftahl, F., Davy, B., Carter, L., **2020**. Late Cretaceous to recent ocean-bottom currents in the SW Pacific Gateway, southeastern Chatham Rise, New Zealand. *Palaeogeography, Palaeoclimatology, Palaeoecology* 546, 109633.
- Stone**, P., Kimbell, G., Richards, P., **2009**. Rotation of the Falklands microplate reassessed after recognition of discrete Jurassic and Cretaceous dyke swarms. *Petroleum Geoscience* 15, 279-287.
- Stow**, D.A.V., Faugères, J.-C., Howe, J.A., Pudsey, C.J., Viana, A.R., **2002**. Bottom currents, contourites and deep-sea sediment drifts: current state-of-the-art, in: Stow, D.A.V., Pudsey, C.J., Howe, J.A., Faugeres, J.-C., Viana, A.R. (Eds.), Deep-water contourite systems: Modern drifts and ancient series. *Geological Society of London*, London, pp. 7-20.

-
- Subrahmanyam**, D., Rao, P., 2008. Seismic attributes-A review, 7th international conference & exposition on petroleum geophysics, Hyderabad, pp. 398-404.
- Talley**, L.D., 2013. Closure of the global overturning circulation through the Indian, Pacific, and Southern Oceans: schematics and transports. *Oceanography* 26, 80–97.
- Taner**, M., Koehler, F., Sheriff, R., 1979. Complex seismic trace analysis: *Geophysics*. *Geophysics*, 1041-1063.
- Taner**, M.T., 2001. Seismic attributes. *CSEG recorder* 26, 48-56.
- Taner**, M.T., Scheuelke, J., O'Doherty, R., Baysal, E., 1994. Seismic attributes revisited. *SEG Expanded Abstract*, Annual International Meeting.
- Tassone**, A., Lodolo, E., Menichetti, M., Yagupsky, D., Caffau, M., Fe, V., 2008. Seismostratigraphic and structural setting of the Malvinas Basin and its southern margin (Tierra del Fuego Atlantic offshore). *Geologica Acta*; Vol.: 6 Núm.: 1 6.
- Taylor**, G.K., Shaw, J., 1989. The Falkland Islands: new palaeomagnetic data and their origin as a displaced terrane from southern Africa. *Deep structure and past kinematics of accreted terranes* 50, 59-72.
- Taylor**, M., Dillon, W.P., Pecher, I., 2000. Trapping and migration of methane associated with the gas hydrate stability zone at the Blake Ridge Diapir: new insights from seismic data. *Marine Geology* 164, 79-89.
- Thomas**, D.J., Bralower, T.J., Jones, C.E., 2003. Neodymium isotopic reconstruction of late Paleocene-early Eocene thermohaline circulation. *Earth and Planetary Science Letters* 209, 309-322.
- Thompson**, R., 1977. Mesozoic sedimentation on the eastern Falkland Plateau.
- Thomson**, K., 1998. When did the Falklands rotate? *Marine and Petroleum Geology* 15, 723-736.
- Timofeev**, P.P., Renngarten, N.V., Rateev, M.A., 1980. Lithologic facies and clay mineral assemblages in Mesozoic and Cenozoic sediments recovered by DEEP Sea Drilling Project LEG 71 in the South Atlantic, in: Ludwig, W.J., Krasheninnikov, V.A., et.al. (Eds.), *Initial Reports DSDP*. U.S. Govt. Printing Office, Washington, pp. 377-388.
- Trathan**, P.N., Brandon, M.A., Murphy, E.J., Thorpe, S.E., 2000. Transport and structure within the Antarctic Circumpolar Current to the north of south Georgia. *Geophysical Research Letters* 27, 1727-1730.
- Uenzelmann-Neben**, G., 2001. Seismic characteristics of sediment drifts: An example from the Agulhas Plateau, southwest Indian Ocean. *Marine Geophysical Research* 22, 323-343.
- Uenzelmann-Neben**, G., 2019a. Onset and modifications in intensity and pathways of water mass exchange between the Southeast Pacific and the South Atlantic with focus on the Falkland Plateau, Northern Scotia Ridge and the West Georgia Basin, Cruise No. MSM81, February 2 2019-March 15 2019, Valparaiso (Chile) - Montevideo (Uruguay), MARIA S. MERIAN-Berichte, Bonn, p. 30.
- Uenzelmann-Neben**, G., 2019b. Variations in ice-sheet dynamics along the Amundsen Sea and Bellingshausen Sea West Antarctic Ice Sheet margin. *GSA Bulletin* 131, 479-498.
- Uenzelmann-Neben**, G., Grobys, J.W.G., Gohl, K., Barker, D., 2009. Neogene sediment structures in Bounty Trough, eastern New Zealand: Influence of magmatic and oceanic current activity. *Geological Society America Bulletin* 121, 134-149.
- Uenzelmann-Neben**, G., Schlüter, P., Weigelt, E., 2007. Cenozoic oceanic circulation within the South African gateway: indications from seismic stratigraphy. *South African Journal of Geology* 110, 275-294.
- Uenzelmann-Neben**, G., Weber, T., Grützner, J., Thomas, M., 2017. Transition from the Cretaceous ocean to Cenozoic circulation in the western South Atlantic — A twofold reconstruction. *Tectonophysics* 716, 225-240.
- Vail, P., Mitchum Jr, R., Thompson III, S., 1977. Seismic stratigraphy and global changes of sea level: Part 4. Global cycles of relative changes of sea level.: Section 2. Application of seismic reflection configuration to stratigraphic interpretation.
- van de Lagemaat**, S.H.A., Swart, M.L.A., Vaes, B., Kosters, M.E., Boschman, L.M., Burton-Johnson, A., Bijl, P.K., Spakman, W., van Hinsbergen, D.J.J., 2021. Subduction initiation in the Scotia Sea region and opening of the Drake Passage: When and why? *Earth-Science Reviews* 215.

-
- Vanneste**, M., Mienert, J., Guidard, S., partners, H.I., **2002**. Arctic” gas hydrates offshore Western Svalbard, Norway, Proceedings of the 4th international conference on gas hydrates, Yokohama, Japan, pp. 19-23.
- Varkouhi**, S., Cartwright, J.A., Tosca, N.J., **2020**. Anomalous compaction due to silica diagenesis — Textural and mineralogical evidence from hemipelagic deep-sea sediments of the Japan Sea. *Marine Geology* 426, 106204.
- Varkouhi**, S., Cartwright, J.A., Tosca, N.J., Papineau, D., **2022**. Arrested versus active silica diagenesis reaction boundaries—A review of seismic diagnostic criteria. *Basin Research* 34, 640-661.
- Veeken**, P.P., 2006. Seismic stratigraphy, basin analysis and reservoir characterisation. Elsevier.
- Viebahn**, J.P., von der Heydt, A.S., Bars, D.L., Dijkstra, H.A., **2016**. Effects of Drake Passage on a strongly eddying global ocean. *Paleoceanography*.
- Volpi**, V., Camerlenghi, A., Hillenbrand, C.-D., Rebisco, M., Ivaldi, R., **2004**. The effects of biogenic silica on sediment compaction and slope stability on the pacific margin of the Antarctic Peninsula. *Basin Research*.
- Von der Heydt**, A., Dijkstra, H.A., **2006**. Effect of ocean gateways on the global ocean circulation in the late Oligocene and early Miocene. *Paleoceanography* 21.
- Weber**, M.E., Raymo, M.E., Peck, V.L., Williams, T., Armbrecht, L.H., Bailey, I., Brachfeld, S.A., Cardillo, F.G., Du, Z., Fauth, G., García, M., Glüder, A., Guitard, M.E., Gutjahr, M., Hemming, S.R., Hernández-Almeida, I., Hoem, F.S., Hwang, J.H., Iizuka, M., Kato, Y., Kenlee, B., Martos, Y.M., O'Connell, S., Perez, L.F., Reilly, B.T., Ronge, T.A., Seki, O., Tauxe, L., Tripathi, S., Warnock, J.P., Zheng, X., **2021**. Expedition 382 summary, Volume 382: Iceberg Alley and Subantarctic Ice and Ocean Dynamics.
- Whalley**, E., **1980**. Speed of longitudinal sound in clathrate hydrates. *Journal of Geophysical Research: Solid Earth* 85, 2539-2542.
- Wise Jr**, S.W., **1972**. Chemically precipitated sedimentary cristobalite and the origin of chert. *Eclogae Geologicae Helvetiae* 65, 157-163.
- Worsley**, T., **1974**. The Cretaceous-Tertiary boundary event in the ocean.
- Wrona**, T., Jackson, C.A.L., Huuse, M., Taylor, K.G., **2017**. Silica diagenesis in Cenozoic mudstones of the North Viking Graben: physical properties and basin modelling. *Basin Research* 29, 556-575.
- Wynn**, R.B., Masson, D.G., **2008**. Chapter 15 Sediment Waves and Bedforms, in: Rebisco, M., Camerlenghi, A. (Eds.), *Developments in Sedimentology*. Elsevier, pp. 289-300.
- Wynn**, R.B., Stow, D.A.V., **2002**. Classification and characterisation of deep-water sediment waves. *Marine Geology* 192, 7-22.
- Yilmaz**, O., **1987**. Seismic data processing: Soc. Expl. Geophys 252.
- Yilmaz**, Ö., **2001b**. Seismic data analysis: Processing, inversion, and interpretation of seismic data. Society of exploration geophysicists.
- Zachos**, J.C., Pagani, M., Sloan, L., Thomas, E., Billups, K., **2001**. Trends, Rhythms, and Aberrations in Global Climate 65 Ma to Present. *Science* 292, 686-693.
- Zenk**, W., **1981**. Detection of overflow events in the Shag Rocks passage, Scotia Ridge. *Science* 213, 1113-1114.

CHAPTER 11. Data availability

Seismic datasets related to this scientific work are hosted in Pangaea repository at www.pangaea.de, as listed below.

[AWI-20190001](#) <https://doi.pangaea.de/10.1594/PANGAEA.925462>

[AWI-20190002](#) <https://doi.pangaea.de/10.1594/PANGAEA.925250>

[AWI-20190003](#) <https://doi.pangaea.de/10.1594/PANGAEA.925467>

[AWI-20190004](#) <https://doi.pangaea.de/10.1594/PANGAEA.925468>

[AWI-20190005](#) <https://doi.pangaea.de/10.1594/PANGAEA.925469>

[AWI-20190006](#) <https://doi.pangaea.de/10.1594/PANGAEA.925470>

[AWI-20190007](#) <https://doi.pangaea.de/10.1594/PANGAEA.925472>

[AWI-20190008](#) <https://doi.pangaea.de/10.1594/PANGAEA.925473>

[AWI-20190009](#) <https://doi.pangaea.de/10.1594/PANGAEA.925474>

[AWI-20190010](#) <https://doi.pangaea.de/10.1594/PANGAEA.925476>

[AWI-20190011](#) <https://doi.pangaea.de/10.1594/PANGAEA.925477>

[AWI-20190012](#) <https://doi.pangaea.de/10.1594/PANGAEA.925478>

[AWI-20190013](#) <https://doi.pangaea.de/10.1594/PANGAEA.925479>

[AWI-20190014](#) <https://doi.pangaea.de/10.1594/PANGAEA.925480>

[AWI-20190015](#) <https://doi.pangaea.de/10.1594/PANGAEA.925481>

[AWI-20190016](#) <https://doi.pangaea.de/10.1594/PANGAEA.925639>

[AWI-20190017](#) <https://doi.pangaea.de/10.1594/PANGAEA.925486>

<u>AWI-20190018</u>	https://doi.pangaea.de/10.1594/PANGAEA.925640
<u>AWI-20190019</u>	https://doi.pangaea.de/10.1594/PANGAEA.925641
<u>AWI-20190020</u>	https://doi.pangaea.de/10.1594/PANGAEA.925642
<u>AWI-20190021</u>	https://doi.pangaea.de/10.1594/PANGAEA.925643
<u>AWI-20190022</u>	https://doi.pangaea.de/10.1594/PANGAEA.925644
<u>AWI-20190023</u>	https://doi.pangaea.de/10.1594/PANGAEA.925645
<u>AWI-20190024</u>	https://doi.pangaea.de/10.1594/PANGAEA.925646
<u>AWI-20190025</u>	https://doi.pangaea.de/10.1594/PANGAEA.925647
<u>AWI-20190026</u>	https://doi.pangaea.de/10.1594/PANGAEA.925648
<u>AWI-20190027</u>	https://doi.pangaea.de/10.1594/PANGAEA.925649
<u>AWI-20190028</u>	https://doi.pangaea.de/10.1594/PANGAEA.925650
<u>AWI-20190029</u>	https://doi.pangaea.de/10.1594/PANGAEA.925651
<u>AWI-20190030</u>	https://doi.pangaea.de/10.1594/PANGAEA.925653

CHAPTER 12. Seismic profiles

This chapter includes the migrated seismic profiles as the products of the seismic data processing of the dataset from cruise leg MSM81, across the Falkland/Malvinas Plateau (Uenzelmann-Neben, 2019a). See section 3.2.1 for details on the acquisition details. Seismic processing sequences are explained in section 3.3.1.

